
Rare earth-doped aluminum nitride thin films for optical applications

DISSERTATION

zur Erlangung des
des Doktorgrades der Ingenieurwissenschaften
der Naturwissenschaftlich-Technischen Fakultät
der Universität des Saarlandes



UNIVERSITÄT
DES
SAARLANDES

von

Alaa eldin Giba

Nancy (Frankreich) in 31 Januar 2018

Tag des Kolloquiums: 31 Januar 2018

Dekan:.....Prof. Dr. Guido Kickelbick

Berichterstatter:..... Prof. Frank Mücklich

Prof. Ralf Busch

Prof. David Horwat

Vorsitz:

Mr. Fabrice Goubilleau

Mitglieder des

Prüfungsausschusses:

Prof. Anna Vedda

Prof. Bruno Masenelli

Dr. Stéphanie Bruyère

Prof. Hervé Rinnert

Professor, Lehrstuhl für Funktionswerkstoffe,
Universität Des Saarlandes,
Saarbrücken, Germany

Professor, Lehrstuhl für Metallische
Werkstoffe, Universität des Saarlandes, Saarbrücken
Germany

Professor, IJL,
Université de Lorraine,
Nancy, France

Directeur de recherche,
CIMAP, Caen , France

Professor, dipartimento di scienza dei materiali,
Università degli Studi di Milano-Bicocca,
Milano, Italy

Professor, Institut national des sciences
appliquées (INSA), Lyon, France

Maître de Conférences, IJL,
Université de Lorraine,
Nancy, France

Professor, IJL, Université de Lorraine,
Nancy, France



THÈSE

Pour l'obtention du titre de
DOCTEUR de L'UNIVERSITÉ DE LORRAINE

Physique

Présentée par:

Alaa eldin Giba

Films minces de nitrure d'aluminium dopés par des terres rares pour applications optiques

Thèse soutenue publiquement le (31 janvier 2018) à Nancy devant le jury composé de:

Membres du jury

Mme. Anna Vedda	Professeur, dipartimento di scienza dei materiali, Università degli Studi di Milano-Bicocca, Milano, Italy	Rapporteur
M. Bruno Masenelli	Professeur, Institut national des sciences appliquées (INSA), Lyon, France	Rapporteur
M. Ralf Busch	Professeur, Lehrstuhl für Metallische Werkstoffe, Universität des Saarlandes, Saarbrücken Germany	Examineur
M. Fabrice Gourbilleau	Directeur de recherche, CIMAP, Caen, France	Examineur
M. David Horwat (Directeur de Thèse)	Professeur, IJL, Université de Lorraine, Nancy, France	Examineur
Mme. Stéphanie Bruyère (Co-Directeur de Thèse)	Maître de Conférences, IJL, Université de Lorraine, Nancy, France	Examineur
M. Frank Mücklich (Co-Directeur de Thèse)	Professeur, Lehrstuhl für Funktionswerkstoffe, Universität Des Saarlandes, Saarbrücken, Germany	Examineur
M. Hervé Rinnert	Professeur, IJL, Université de Lorraine, Nancy, France	Invité

Institut Jean Lamour – UMR 7198- Département CP2S – Equipe 202 EFCM

Université de Lorraine – Pôle M4 : matière, matériaux, métallurgie, mécanique

To only one person.....my wife....,

Hanan Sharafeldin

TABLE OF CONTENTS

CONTENT	I
ACKNOWLEDGEMENT	IV
RÉSUMÉ ÉTENDU	VI
ERWEITERTE ZUSAMMENFASSUNG	XI
MOTIVATION	1
CHAPTER I General introduction	
1. Aluminium nitride (AlN):Basic properties	4
1.1 AlN crystal structure	4
1.2 Electronic structure of AlN	6
1.3 Type of defects in AlN	9
1.4 AlN: Preparation methods	10
1.5 AlN: Applications	10
2. Rare-earth elements	11
2.1 Electronic structure and transitions of REs	11
2.2 Luminescence principles	14
2.3 Rare earth doped in solid hosts (semiconductor/insulators)	19
2.3.1 Issues related to the luminescence of RE-doped solids	19
2.3.2 Rare earth-doped semiconductors (RE-Sc)	22
2.3.3 Cerium in AlN	26
2.3.4 Ytterbium in AlN	28
CHAPTER II Experimental techniques	
1. Thin film synthesis	31
1.1 Sputtering	31
1.2 Thermal annealing of the thin films	36
2. Thin film characterization	36
2.1 Structural characterization	36
2.1.1 X-ray diffraction (XRD)	36
2.1.2 Transmission electron microscopy (TEM)	38
2.1.3 Rutherford Backscattering Spectrometry (RBS)	32
2.2 Optical characterization	43

2.2.1	Fourier transform infrared spectroscopy (FTIR)	43
2.2.2	Ellipsometry	45
2.2.3	Photoluminescence (PL) spectroscopy	47
CHAPTER III Synthesis and characterizations of AlN thin films		
1.	Introduction	54
2.	Sputtering conditions	56
2.1	Crystallographic orientations	57
2.2	Microstructures and morphology	66
2.3	Optical properties	71
3.	The optimum deposition conditions	74
4.	Conclusion	77
CHAPTER IV Rare earth-doped AlN: Cerium-doped AlN		
1.	Introduction	80
2.	Results and discussion	82
2.1	Structures and compositions	82
2.2	Structures and optical analyses of Ce-doped AlN	84
2.2.1	X-ray diffraction (XRD)	84
2.2.2	Fourier Transform Infrared Spectroscopy (FTIR)	87
2.2.3	Microstructure and composition	88
2.2.4	Photoluminescence (PL)	91
2.2.5	The role of oxygen	96
2.3	Intentionally doping oxygen during Ce AlN growth	101
2.4	Low temperature photoluminescence dependence (LTPL)	112
3.	Application perspective	116
4.	Conclusion	120
CHAPTER V Yb-doped AlN and (Ce, Yb) co-doped AlN		
1.	Introduction	122
2.	Structures and compositions	124
3.	Photoluminescence (PL)	126
4.	Structure of (Ce,Yb) co-doped Al(O)N sample	137
5.	Photoluminescence	138
6.	Low temperature photoluminescence	147

7. Conclusion	149
GENERAL CONCLUSION	151
FUTURE PERSPECTIVES	153
ANNEXES	155
REFERENCES	163
ABSTRACT	175
RÉSUMÉ	176
ZUSAMMENFASSUNG	178

Acknowledgement

After three years of work, it is really difficult in few words to acknowledge the people who helped me, and without them this work couldn't be completed smoothly. Therefore, I would like to express my appreciation to all of them.

Firstly, I would like to express my gratitude to my advisor David Horwat for providing me the opportunity to collaborate together within this project. I also thank his patience and continued guidance during the last three years in both scientific and administrative levels. Although my office was placed away from his office (~ 3 km), we were in contact every day and I found him was always available to come to my site and ready for discussion and exchange his new ideas.

I also would like to thank my co-supervisor Stéphanie Bruyere for her very helpful assistance, especially, in the structure characterization part of this work and her great effort for doing a lot of TEM measurements for my samples.

Very special thank to Philippe Pigeat, who welcomed me in his laboratory to prepare all of my samples and offered all the facilities under my request. Not only that, Mr Pigeat guided me step by step in the practical work as well as his office was always opened for me at any time for the discussion. I cannot forget that sometimes he came to the laboratory at midnight to follow my experiment. Thank you Pigeat!

Also I'd like to express my very special thank to Hervé Rinnert for welcoming me in his team and giving me the access to all the several photoluminescence experiments in his laboratory. Mr. Rinnert is involved in this work from the first day and sharing his invaluable ideas and experience in the field of optics with us. Thank you again for the great contribution.

I would like to thank my co-supervisor in Saarland University, Prof. Frank Mücklich for his important contribution in this project, as well as the great help during my presence in Saarbrücken.

I want to particularly express my thanks to Flavio Solidera for his many FIB preparations and his assistance during my stays in Saarland University.

I'd like further thank Thomas Easwarakhanthan for his collaboration in Ellipsometry measurements.

Many thanks to Alexandre Bouche for doing rapid thermal annealing for many samples and he also showed rapid and nice response.

I thank also Mr Pascal Boulet and Ms Sylvie Robert for their assistance in X-ray diffraction measurements. I also acknowledge Ms Sylvie Migot for teaching me how to use the TEM equipment in the beginning of my thesis.

I want to express my appreciation to Ms Valérie Tamburini, 202 team secretary, with her effort all the financial issues related to conferences and travel abroad costs went smooth.

Particular thank to Raul Gago, Instituto de Ciencia de Materiales de Madrid, for doing Rutherford backscattering spectrometry (RBS) measurement of many samples. The financial support for such measurement from Grant P2013/MIT-2775 (Comunidad Autónoma de Madrid, Spain) is also greatly acknowledged.

Great thank to the 202 team, in IJL, for hosting me three years during this thesis and offering an excellent environment to work.

I'd like also to thank all of my friends and colleagues in IJL and UDS; Fahad, Abdullah, Hiba, Florian, Claudia, Alejandro, Martin, Katherine, Emile, Manuel, Idriss, Jiaqi, Hisham, ... for the very enjoyable time we had together. Special thank to my friend Hany, in Egypt, for his great assistance during my travel.

It is the time to thank my parents, my brother and sister in Egypt for supporting me during my work abroad.

Special thank to my children, *Hamza* and *Noreen*. By looking to them I realize that life has other meanings than doing PhD.

No words can be found to express my love and appreciation to my wife, *Hanan*. She is the only one truly cares about me in this life.

Finally, I thank Erasmus mundus scholarship that financially funded this work within the DocMASE program. I also thanks the Université franco-allemande (UFA) for supporting my travel and stay to Saarland University within the Ph.D. track in Materials Science and Engineering.

Résumé étendu

Ce travail de thèse est dédié à l'étude des propriétés optiques de films minces de nitrure d'aluminium dopé avec des terres rares. Plus particulièrement, il est focalisé sur l'investigation des mécanismes de luminescence de terres rares spécifiques pour une future application des films minces synthétisés dans des dispositifs d'éclairage. Les composés III-V qui incorporent des terres rares attire une attention particulière depuis les années 1980 période à laquelle ces systèmes ont été proposés comme des solutions alternatives pour résoudre les problèmes observés avec le silicium dopé avec des terres rares.[1] D'une part, le silicium présente un faible gap optique qui limite le choix des terres rares à celles qui émettent dans l'infrarouge. D'autre part, ce gap optique est indirect, ce qui induit une très faible luminescence de la terre rare incorporée. Par contre, les composés III-V possèdent dans la plupart des cas un large gap optique direct dans la gamme 2 à 6 eV, ce qui offre la possibilité d'accueillir des terres rares émettrices dans les domaines du visible et de l'ultraviolet.[1] Ces matériaux présentent également une très bonne compatibilité avec les technologies de la microélectronique, permettant d'envisager une intégration dans des dispositifs microélectroniques. Parmi les composés III-V le nitrure d'aluminium (AlN) de structure hexagonale wurtzite présente le gap direct le plus élevé, autour de 6 eV. Par ailleurs, il présente des propriétés chimiques et physiques tout à fait remarquables et intéressantes pour ce domaine telles qu'une très bonne résistance aux agressions chimiques et une conductivité thermique élevée. Ainsi, il s'agit d'un candidat prometteur pour une intégration au sein de dispositifs travaillant à haute puissance.[2] Cependant, les mécanismes optiques en jeu dans l'AlN dope avec des terres rares (RE-AlN) ne sont pas clairement établis. Ceci nous a motivé à initier cette étude visant à explorer le comportement de ce système prometteur.

La méthode de pulvérisation cathodique magnétron réactive a été utilisée au cours de cette thèse pour synthétiser des films minces d'AlN non dopés et dopés par des terres rares. Cette méthode fait partie des méthodes de dépôt physique en phase vapeur (PVD) et est largement utilisée dans le cadre d'applications industrielles de fait de coût et de sa simplicité de mise en œuvre. Les caractéristiques de cette méthode et la procédure de synthèse des films sont détaillées afin de révéler le rôle des conditions d'élaboration sur les propriétés optiques, microstructurales et structurales. La stratégie menant au développement des conditions expérimentales de synthèse optimales utilisée tout au long de ce travail est détaillée.

Les analyses structurales et chimiques des échantillons ont été réalisées par l'intermédiaire de différents moyens incluant la microscopie électronique en transmission (TEM), la diffraction des rayons X (XRD), la spectroscopie de dispersion en énergie des photons X (EDS), la spectrométrie de rétrodiffusion de Rutherford (RBS) et la spectroscopie de perte d'énergie des électrons (EELS). Les propriétés optiques ont été caractérisées par spectrophotométrie UV-Visible en transmission, ellipsométrie spectroscopiques et la spectroscopie de photoluminescence.

Des films minces d'AlN non dopés et présentant une bonne qualité cristalline et une forte orientation structurale préférentielle selon l'axe c de la structure hexagonale wurtzite ont pu être préparés par pulvérisation cathodique magnétron réactive d'une cible d'aluminium dans un mélange gazeux Ar + N₂. Les résultats obtenus montrent qu'il est possible de contrôler le degré d'orientation préférentielle par l'intermédiaire de la composition du mélange gazeux. Une orientation prononcée selon l'axe c est favorisée lorsque la teneur en azote moléculaire est augmentée dans la phase gazeuse. Une assistance thermique pendant la croissance ou l'augmentation du courant de décharge ont également une influence bénéfique sur la cristallinité des films déposés dans une atmosphère d'azote pure et orientés selon l'axe c. Des mesures de température auto-induite au niveau de la surface des substrats ont été réalisées pour différentes valeurs du courant de décharge à l'aide d'une sonde thermique développée pour l'étude. Elles ont permis d'interpréter l'amélioration de la cristallinité et de l'orientation préférentielle sur la base d'une mobilité améliorée des adatoms assistée thermiquement. Les constants optiques (n, k) et le gap optique des films synthétisés ont été modélisés à partir de mesures par spectroscopie ellipsométrique en transmission et en réflexion modes. Les résultats obtenus mettent en évidence la possibilité de faire varier l'indice de réfraction par l'intermédiaire de l'orientation préférentielle alors que le gap optique reste constant. Ainsi, nos résultats montrent que les propriétés optiques des films d'AlN peuvent être modifiées par l'intermédiaire de la microstructure des films qui est elle-même dépendante de la composition en azote dans la phase gazeuse. Par ailleurs, un dichroïsme et une birefringence ont été démontrés à partir de la modélisation des mesures de spectroscopie ellipsométrique, ce qui ouvre des perspectives d'application de nos films d'AlN comme constituants de dispositifs à guide d'onde.

Les films d'AlN dopés par des terres rares ont été préparés par pulvérisation cathodique réactive. Les terres rares utilisées sont le cérium (Ce) et l'ytterbium (Yb) et elles ont été incorporés soit individuellement soit simultanément dans la matrice d'AlN.

Dans le cas d'un dopage simple au cérium, il est observé que la présence d'oxygène est essentielle pour stimuler la luminescence. Le rôle majeur de l'oxygène est double. Il intervient d'une part pour modifier l'état du cérium, naturellement présent dans AlN à l'état +4 inactif optiquement, vers un état +3 actif optiquement. D'autre part, sa présence est accompagnée de la formation de complexes de défauts impliquant des lacunes d'aluminium et de l'oxygène en substitution de l'azote. Nous avons observé que ces complexes de défauts participent aux mécanismes d'excitation du cérium. Ce rôle double de l'oxygène est vérifié par EELS (identification de l'état d'oxydation du cérium) et par spectroscopie d'excitation de la photoluminescence (PLE) en ce qui concerne la contribution des complexes de défauts. Les mécanismes d'excitation de la photoluminescence que nous proposons permettent d'interpréter les résultats observés. Par ailleurs, l'introduction d'oxygène en quantités variables dans la matrice d'AlN dopée au cérium a permis de manipuler les caractéristiques de l'émission optique et, par conséquent, de faire varier la couleur émise entre le bleu et le vert. Ces variations sont expliquées à partir des mécanismes d'excitation proposés et de la possibilité de faire varier l'intensité du champ cristallin autour des ions Ce^{3+} en ajustant le rapport O/N. Un mécanisme permettant d'expliquer l'extinction de la luminescence avec la température est également proposé à partir des données de photoluminescence à basse température. Les données ont été modélisées à partir de l'équation d'Arrhenius faisant intervenir deux fonctions exponentielles afin de déterminer l'énergie d'activation des processus mis en jeu. Deux énergies d'activation de 475 et 35.5 meV ont été déterminées. La première correspond à un phénomène d'ionisation thermique par transfert électronique depuis le niveau $5d_2$ de Ce^{3+} vers le minimum de la bande de conduction. La seconde correspond à la transition d'électrons de $5d_1$ vers $5d_2$. Finalement nous présentons une approche permettant d'obtenir une émission blanche observable à l'œil nu en ajustant les paramètres de dépôt.

Dans le cas des films dopés à l'ytterbium et des films co-dopés ytterbium-cérium, une excitation optique indirecte des ions Yb^{3+} émetteurs dans le proche infrarouge a pu être obtenue et les mécanismes d'excitation de ions Yb émetteurs dans l'infrarouge sont discutés. Une comparaison avec le comportement des films dopés au cérium est également proposée. La similarité des spectres d'excitation du cerium et de l'ytterbium s'accompagne de la possibilité de réaliser un transfert énergétique entre les deux ions au sein des films co-dopés. Ce transfert est mis en évidence par comparaison du comportement des films co-dopés et dopés avec uniquement de l'ytterbium ainsi qu'à partir du constat de l'augmentation des temps de montée et descente des signaux de photoluminescence résolue en temps. Nos

résultats indiquent que le transfert énergétique est de type one-to-one down conversion et s'appuie vraisemblablement sur un mécanisme de transfert de charge. Un mécanisme d'extinction de la photoluminescence de l'ytterbium activé thermiquement est proposé sur la base d'un échange d'énergie vers d'autres états luminescents peuplés thermiquement. Dans le cas des échantillons d'Al(O)N dopés à l'ytterbium deux énergies d'activation $E_{a1}=11.2$ meV et $E_{a1}=1200$ meV peuvent être déduites de la modélisations des données de photoluminescence résolues en température. Par ailleurs, nous avons observé que l'énergie transférée entre la transition de plus forte énergie (1262 meV) parmi les pics désactivés thermiquement et les transitions activées thermiquement à 1274.6 meV (972.2 nm) et 2479 meV (500 nm) est de 12.2 et 1217 meV. Ces valeurs présentent un accord remarquable avec les valeurs de E_{a1} et E_{a2} , respectivement. Ceci indique que la désactivation de l'émission par Yb^{3+} dans l'infrarouge se fait par transfert énergétique vers les niveaux localisés à 500 et 972.2 nm. Dans le cas du dopage mixte avec Ce et Yb, l'émission par Yb^{3+} dans le proche infrarouge est caractérisée par une seule énergie d'activation proche de 28.5 meV. La désexcitation de l'émission dans le proche infrarouge correspondant au pic localisé à 976 nm (1270 meV) peut ainsi être expliquée par la population d'un état radiatif émettant à 953 nm (1300 meV). Par ailleurs, la décroissance de l'émission dans le visible liée à Ce^{3+} est caractérisée par deux énergies d'activation, respectivement de 18 et 508 meV dont la somme (526 meV) est proche de l'énergie d'activation de 513 eV obtenue dans le cas des films présentant un dopage simple au cérium. Ainsi, nous pouvons considérer que le mécanisme de désexcitation thermique de la luminescence de Ce^{3+} intervient par transfert électronique de niveaux 5d excités du cérium vers la bande de conduction de la matrice que ce soit pour les échantillons dopés au cérium uniquement ou pour les échantillons co-dopés Ce, Yb.

Ce manuscrit est organisé en cinq chapitres et une conclusion générale comme suit :

Le chapitre un introduit les propriétés physiques, chimiques et optiques, la structure cristalline et la structure électronique du nitrure d'aluminium. Une brève description des défauts structuraux du nitrure d'aluminium et propose et les applications de ce matériaux sont mentionnées. Les mécanismes d'excitation de la luminescence au sein d'AlN généralement proposés sont décrits à la fin de ce chapitre. Les propriétés des terres rares sont également présentées avec un intérêt particulier pour le cérium et l'ytterbium. Les configurations électroniques des ions libres de ces terres rares sont alors introduites et leurs propriétés de luminescence généralement observées sont discutées ainsi que les mécanismes associés de transfert énergétique et d'excitation généralement proposés lorsque ces éléments sont placés

dans des matrices solides. Finalement, la nécessité de mener une étude sur les propriétés d'émission et d'excitation du cérium et de l'ytterbium dans AlN est motivée.

Le second chapitre décrit les méthodes et techniques expérimentales utilisées pour synthétiser et caractériser les films d'AlN non dopés et dopés. Ces méthodes sont détaillées en veillant à faire apparaître les principes fondamentaux et les caractéristiques utiles pour ce travail.

Le troisième chapitre présente et discute les résultats liés à la préparation des films d'AlN non dopés et d'appliquent à sélectionner les conditions idéales de croissances des films utilisées pour le reste de l'étude. Une attention particulière est portée sur l'optimisation des propriétés structurales et optiques. Un modèle de croissance est notamment proposé qui fait intervenir la manipulation de la mobilité des adatoms par l'intermédiaire de la teneur en azote dans la phase gazeuse et du flux d'atomes se condensant pour former les films.

Le quatrième chapitre corréle la luminescence aux propriétés microstructurales et chimiques locales des films de nitrure d'aluminium dopés avec du cérium. Il propose également des modèles permettant d'expliquer la luminescence de ce matériau, éventuellement applicables à d'autres matrices. L'émission optique des films AlN et Al(O)N dopés au cérium est étudiée à partir de deux longueurs d'onde d'excitation. Des mesures de PLE, de PL résolue en temps et en température sont présentées et analysées. La luminescence est également manipulée par l'intermédiaire de l'épaisseur des films et de la composition de la matrice, plus particulièrement du ratio O/N, de façon à obtenir de façon contrôlée des émissions bleue, verte et blanche.

Le cinquième chapitre vise à comprendre les mécanismes optiques dans les films de nitrure d'aluminium co-dopés sur la base d'une étude comparative des films dopés au cérium et/ou à l'ytterbium. La microstructure et la composition des échantillons préparés sont caractérisées et les propriétés optiques mesurées en utilisant la spectroscopie de photoluminescence à température ambiante, la PLE, la photoluminescence résolue en temps et thermiquement. Les mécanismes d'extinction de la photoluminescence de transfert énergétique entre le cérium et l'ytterbium ont notamment été mis en évidence en utilisant la photoluminescence à basse température et les mécanismes d'excitation ont été déterminés à partir de la PLE.

Erweiterte Zusammenfassung

Dieses Projekt widmet sich der Untersuchung der optischen Eigenschaften von Seltenerd-dotierten Aluminiumnitrid-Dünnschichten. Insbesondere sollen die Lumineszenzmechanismen ausgewählter Seltenerdelemente in AlN-Dünnschichten untersucht werden. Die reaktive Magnetronsputter-Technik (RMS) wird verwendet, um die undotierten und dotierten AlN-Dünnschichten zu synthetisieren. Der Einfluss der Sputterbedingungen auf die Struktur und die optischen Eigenschaften der hergestellten Proben wird untersucht. Zusätzlich werden die optimalen experimentellen Bedingungen bestimmt, die während dieser Arbeit verwendet werden. Die Struktur- und Zusammensetzungsanalysen wurden mit verschiedenen Methoden wie Transmissionselektronenmikroskopie (TEM), energiedispersive Röntgenspektroskopie (EDS) und Rutherford-Rückstreu-Spektrometrie (RBS) durchgeführt. Die optischen Eigenschaften der Filme wurden durch Spektralphotometrie, Ellipsometrie und Photolumineszenz-Spektroskopie (PL) charakterisiert.

Für undotiertes AlN wurden gut kristallisierte AlN-Dünnschichten mit hohem c-Achsen-Orientierungsgrad hergestellt. Die bevorzugte Orientierung konnte durch das Einstellen des N_2 -Anteils in der Gasphase kontrolliert werden. Es wurde herausgefunden, dass die Synthese von c-Achsen-orientiertem kristallinem AlN begünstigt wird, indem die Beschichtungen in einer stickstoffreichen reaktiven Umgebung abgeschieden werden. Die Ergebnisse wurden auf der Grundlage einer verbesserten Beweglichkeit von Adatomen interpretiert, die durch das Bombardieren der Filme mit schnellen Teilchen unterstützt wurde. Die optischen Konstanten (n , k) und die Bandlücke der hergestellten Filme wurden aus spektroskopischen Ellipsometriemessungen in Transmission und Reflexion modelliert. Es wurde gefunden, dass der Brechungsindex mit der Kristallorientierung abgestimmt werden kann, während die Bandlücke konstant gehalten wird. Unsere Ergebnisse legen nahe, dass die optischen Eigenschaften der AlN-Filme über ihre kristallographische Orientierung abgestimmt werden können, die wiederum durch die Menge an Stickstoff in der Gasphase variiert wird.

Für dotiertes AlN wurde kristallines Ce-dotiertes AlN hergestellt. Die Kristallstruktur der hergestellten Proben und deren Zusammensetzung wurde durch TEM-, RBS-, EDS- und EELS-Analysen untersucht. Es wurde herausgefunden, dass die Anwesenheit von Sauerstoff

in diesem Material für die Sensibilisierung der Photolumineszenz wesentlich ist. Es hat sich herausgestellt, dass Sauerstoff nicht nur bei der Umwandlung von Ce-Ionen vom optisch inaktiven Zustand +4 zum optisch aktiven Zustand +3 eine wichtige Rolle spielt, sondern auch zur Bildung von Defektkomplexen mit Al-Leerstellen führt. Diese Defektkomplexe tragen zum Anregungsmechanismus von Ce-Ionen bei. Daher wurden optische Anregungs- und Emissionsmechanismen basierend auf der Rolle von Sauerstoff vorgeschlagen. Auf dieser Grundlage wurde eine Manipulation der PL erreicht und verschiedene Farben (blau und grün) wurden mit bloßem Auge deutlich beobachtet. Zusätzlich wurde ein Weißlichtemissionsansatz vorgestellt und ein starkes weißes Licht wurde beobachtet. Es werden Yb-dotierte und (Ce, Yb) co-dotierte Al(O)N-Systeme hergestellt. Die Kristallstrukturen und Zusammensetzungen der hergestellten Proben wurden untersucht. Es wird eine indirekte optische Anregung der NIR-Emission von Yb-Ionen erreicht. Die Anregungsmechanismen des NIR und die sichtbare Emission von einfach dotierten und co-dotierten Proben werden diskutiert. Es wurde herausgefunden, dass die Ähnlichkeit zwischen den PLE-Spektren von Ce und Yb ermöglicht, einen Energietransfer zwischen den zwei Ionen in dem Codotierungssystem zu erreichen. Die Art des Energietransfer mechanismus ist konsistent mit der Eins-zu-Eins-Abwärtsumwandlung über den Ladungsübertragungszustandsmechanismus. Die PL-Löschung wurde untersucht, indem die Entwicklung der PL mit niedrigen Temperaturen verfolgt wurde.

Motivation

Rare earth-doped III-V compounds attracted great attention since reported for the first time in 1980s as alternative solution to address the rare earth-doped silicon materials' drawbacks.[1] The small and indirect optical bandgap of silicon not only limits the choice of REs to those emit in IR region but also exhibits low luminescence efficiency due to the indirect bandgap feature of silicon. In contrast, III-V compounds in most cases show direct and large optical bandgap in the range 2 eV to 6 eV, providing good opportunity to host the RE ions emit in ultraviolet-visible (UV-Vis) range.[1] Also, it offers the possibility of integration with semiconductor microelectronics. Among III-V compounds, hexagonal wurtzite AlN exhibits the largest direct optical bandgap (6 eV). In addition, it shows very interesting chemical and physical properties such as strong chemical resistance and large thermal conductivity. Thus, it is a promising candidate for integration in devices working at high power operation.[2] Nevertheless, the optical mechanism of RE-doped AlN is still under debate, which motivates us to start this study in order to explore the optical behavior of this system. Hopefully, we can provide a significant contribution and enhance our understanding in this field.

This work, in general, is devoted to study the luminescence properties of selected RE elements incorporated in AlN thin film prepared by reactive magnetron sputtering as a candidate for lighting devices. More particularly, cerium (Ce) and ytterbium (Yb) ions have been selected as a case study in this thesis for two main reasons.

Firstly, from fundamental understanding point of view, Ce is the first lanthanides element containing only one electron in the $4f$ orbital and its luminescence properties are characterized by $f-d$ electronic transition. So, it is considered as an example for other RE ions that have the same kind of transition (Eu^{2+} , Sm^{2+} ...). Yb is located at the end of lanthanides, and contains 13 electrons in the $4f$ orbital and its luminescent properties are mainly characterized by $f-f$ transition (in Yb^{3+}). It can be used as an example representing other REs that have the same electronic transition. In addition, the $f-d$ transition in Ce^{3+} is the outermost shell electronic transition, while $f-f$ transition in Yb^{3+} is lying in the core levels of valence electrons. This makes the $f-d$ transition is unshielded from the surrounding medium unlike $f-f$ transition. This unshielded property of $f-d$ transition results in strong influence of the local environment on the luminescence of Ce^{3+} . Whereas, the shielded property of $f-f$ transition in Yb^{3+} significantly reduces the interaction with the local environment. Thus, the excitation mechanisms in both

ions are expected to be different. Therefore, by studying and comparing the luminescence properties of Ce^{3+} and Yb^{3+} , we will have the chance to test two different electronic transitions in AlN. Moreover, Ce ions emit in the UV-Vis light spectrum, while Yb^{3+} ions emit in NIR. Hence, large part of light spectrum can be covered within this work.

Secondly, from application point of view, Ce^{3+} ions are used to produce blue light in order to fabricate blue or white light emitting devices. It is also very useful in scintillation and thin film flat panel light devices (TFFPLD) fields. On the other hand, Yb attracts a lot of attention in photonic systems mainly based on light confinement (e.g. planar, waveguide optical fibers and lasers). Thanks to the high AlN refractive index, about 2.1, it is expected to enhance the confinement efficiency of Yb based devices integrated in AlN. Moreover, AlN as a III-V compound is excellent to match with the silicon technology, which is additional advantage for silicon integration technology approaches. Furthermore, the piezoelectric properties of AlN open a promising way for realizing piezo-phototronic integrated chips technology. Hopefully our study of Ce and Yb doped in AlN will drop new and important seed in this regard.

This manuscript is organized into five chapters and general conclusion as follows:

Chapter one: is a general introduction about the basic physical, chemical and optical properties of AlN and rare earth with particular focusing on Ce and Yb-doped AlN. The crystal and electronic structure of AlN are described. Brief section about the structure defects in AlN is stated. In addition, some AlN applications are mentioned. Regarding the RE ions, the electronic configurations of the free ions are described. Also, a brief introduction about the luminescence, energy transfer, excitation mechanisms of RE in solid hosts will be provided. At the end of this chapter, description of the types of the excitation mechanisms in AlN is explained. Finally, the importance of studying Ce and Yb in AlN systems will be highlighted.

Chapter two: is dealing with the experimental methods and techniques that have been used in preparation and characterization of our samples.

Chapter three: is devoting to the results and discussion of the prepared AlN films and selecting the optimum experimental condition for the doping step. More precisely, the structure and the optical properties of AlN thin film prepared by reactive magnetron sputtering technique are examined. The correlation between the sputtering conditions, the crystallographic orientation, the morphology, the microstructure and the optical properties

will be presented. The optimum experimental conditions that will be used during this work are discussed. Finally, chapter's conclusion has been stated.

Chapter four: shows the result and discussion of prepared Ce-doped AlN films at different conditions and the correlation of the microstructure with the luminescence properties. It also provides a significant guideline for understanding the optical behavior of such material. The optical response of Ce-doped AlN and Cerium doped aluminum (oxy)nitride (Ce-doped Al(O)N) has been examined by photoluminescence (PL) under optical excitation with different wavelengths. The photoluminescence excitation measurements (PLE) have been performed in order to explore the excitation mechanisms. In addition, the PL intensity evolution with low temperature variation was used to gain more information about the PL thermal quenching mechanisms. A comprehensive study is presented to understand the optical mechanisms of Ce doped aluminum nitride and aluminum (oxy) nitride materials. Based on the proposed approach, PL manipulation has been achieved offering different emission colors (blue, green and white) that can be used as candidates for lightening applications.

Chapter five: is dedicated to understand the optical mechanisms of Yb-doped AlN and (Ce, Yb) co-doped AlN samples. The main goal of this part of the work is to establish a comparative study between two different rare earth ions doped AlN in order to explore the similarities and the discrepancies, particularly in the optical behaviors. The microstructure and the compositions of the prepared samples have been investigated. The optical properties have been also examined using the steady state PL at room temperature, PLE, and time resolve photoluminescence (TRPL). The PL thermal quenching mechanism for Yb and (Ce, Yb) co-doped AlN is presented by probing the PL evolution at low temperatures. In addition, energy transfer (ET) mechanism between Ce and Yb has been established.

Chapter I

General Introduction

In this chapter, a general introduction about the basic characteristics of aluminum nitride (AlN) and rare earth elements (REs) is presented. We will focus and highlight on the properties relevant to this study and used in our results' interpretations and discussion. This chapter is classified as follows; the first part is dealing with AlN related features; crystal and electronic structures, types of defects, preparation methods and applications. Secondly, it is focusing on some luminescence issues related to REs (electronic transitions, energy transfer and...etc). After that, general discussion about the optical behavior of REs-doped semiconductors is given. Finally, a survey on the application of Ce and Yb-doped AlN is presented.

1- Aluminum nitride (AlN): Basic properties

AlN is a III-V compound and crystallizes in the hexagonal wurtzite structure where each Al atom is tetrahedrally connected to the nitrogen atoms by covalent bonds. This particular crystal structure of AlN exhibits high chemical and thermal stabilities, high hardness and large thermal conductivity and melting temperature of 2200 °C.[2] It also shows a remarkable high optical bandgap of 6.2 eV. All these promising features allow AlN falling under intense research activities. During the last decade, several works have been dedicated to exploit the excellent properties of AlN to put it directly in the industrial field. On the one hand, many potentials have been reported on different synthesis methods in order to obtain well crystalline AlN in bulk,[3] thin films,[2] and even in nanopowders forms.[4] On the other hand great efforts have been spent to characterize and understand the chemical and physical properties of AlN in order to serve the technological development especially in acoustic [5-6] and optoelectronic fields.[7-8] In the following sections, a background required to get through this work is discussed.

1.1- AlN crystal structure

AlN belongs to the III-nitrides group which includes the compounds consisting of nitrogen with the elements of column III in the periodic table. Terminologically, III-nitrides usually point to GaN, InN, AlN and their alloys InGaN, AlGaN, AlInN, and AlInGaN, which are the most important compounds obtained from this group in semiconductor technology. These

compounds are found in wurtzite (WZ), zinc blende (ZB) and rocksalt atomic structures.[9] AlN exists in WZ and ZB, however the WZ structure is more stable than ZB. The main difference between WZ and ZB structures in AlN is the ions stacking sequence inside the crystal lattice.[10] Specifically, hexagonal WZ-AlN (H-WZ) structure is the stable and the easy growing one under normal conditions. Fig (1.1) shows the crystal structure of hexagonal WZ-AlN.

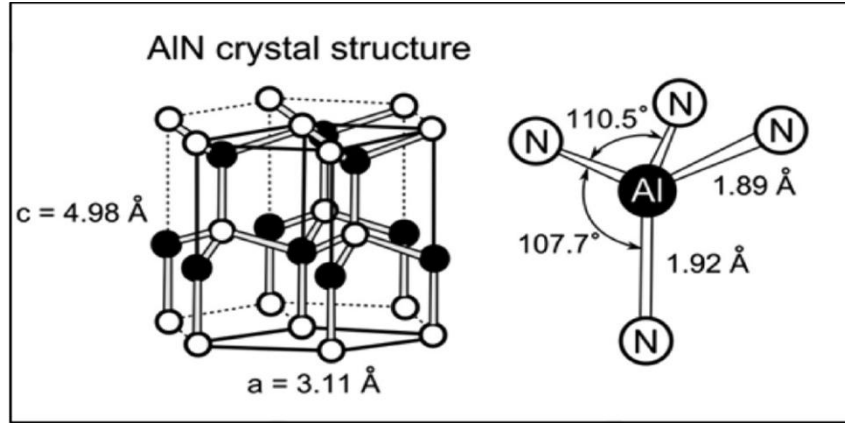



Fig. (1.1): Crystal structure of wurtzite AlN.[11]


The average lattice parameters of hexagonal wurtzite AlN $a = 3.11 \text{ \AA}$ and $c = 4.98 \text{ \AA}$ are mainly depending on the lattice strains and the oxygen content, which is an unavoidable contamination. The ideal c/a ratio for wurtzite structure is 1.63 with an internal coordinate $u = (a/c)^2 = 0.375$. [9] It was found that the specific stacking sequence of hexagonal w-AlN result in attracting pairs of cations and anions by electrostatic forces.[9] These electrostatic forces lead to decrease the c/a ratio and promote the ionic character of AlN, which makes the WZ phase more stable than the ZB. As a result, an internal spontaneous polarizability is initiated inside AlN crystal lattice. This spontaneous polarizability is the key point behind using AlN crystals in the piezoelectricity field. Furthermore, the difference between the lattice parameters (c and a) results in an anisotropic property along each axis. For instance, the ordinary and the extraordinary refractive index of AlN are not the same, which is an important property in the field of microchips nonlinear optics.[12]

The lattice structure of w-AlN consists of tetrahedron units where each Al atom is connected with four N-atoms by two kinds of bonds, sometimes referred as B1 and B2. B2 bonds are parallel to the c -axis while B1 bond are the other three legs in the tetrahedron terminals as shown fig. (1.1). In addition, the bond length of B2 (0.1917 nm) is longer than B1 (0.1885 nm).[13] Al and N atoms form four sp^3 hybridization orbitals in the crystalline structure. The

Aluminum

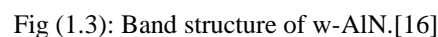


Nitrogen



1.2-Electronic structure of AlN

The electronic structure of semiconductor material is mainly governed by the bonding system and the crystal structure of the material.[15] Wurtzite AlN is considered as a direct bandgap, whose band edge is located at the Γ point, see fig (1.3).



Large direct bandgap can be realized between the minimum of the conduction band and the maximum of the valence band to reach to 6.2 eV in crystalline w-AlN. This bandgap makes AlN a promising material to host emitting centers with light emission in UV-Vis ranges with low thermal quenching of the luminescence. In addition, the direct feature of this band structure maximizes the benefit from the excitation energy avoiding any phonon consumption that occurs in other indirect bandgap semiconductors e.g. Silicon.

- ***The density of states (DOS)***

The partial density of states (DOS) of w-AlN is presented in fig (1.4). It can be observed that the valance band formed by two sub-bands of N atoms 2s and 2p, while conduction band raises from hybridization of the s and p orbitals of the Al atoms. [17-18]

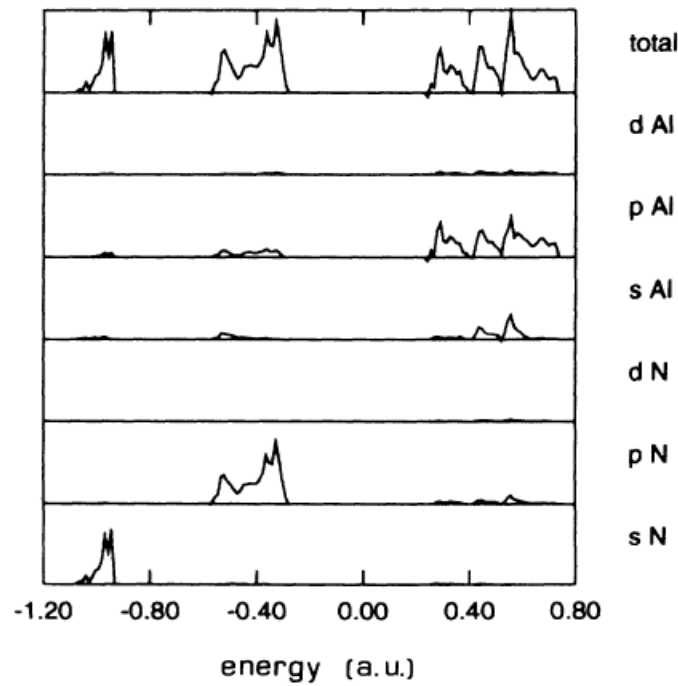


Fig (1.4): the partial and total DOS of w-AlN.[17]

- ***The optical- Phonon frequencies***

Studying the optical phonons of AlN is of great interest due to its application in optoelectronic field. Complementary measurements of Raman and FTIR have been used to obtain the full information about the optical phonons. AlN with wurtzite structure exhibits six optical phonon modes[19-20] classified as shown in fig (1.5). As it has large number of atoms, the analysis of the optical phonons is complex, however the representation at the point Γ is reducible into $\Gamma = A_1 + E_1 + 2E_2 + 2B_1$; A_1 and E_1 are Raman and IR active, $2E_2$ branches are

Raman active only while B1 branches are inactive (forbidden in Raman and IR). The phonon frequencies are listed in below table (1.1).[19] However, it can be shifted and/or broadened depending on the microstructure (crystal or amorphous), the lattice strain and the impurities in particular the oxygen contamination.[21] That is why Raman and FTIR can be used as a tool to give information about the degree of disorder and the lattice strain of a given material.[22]

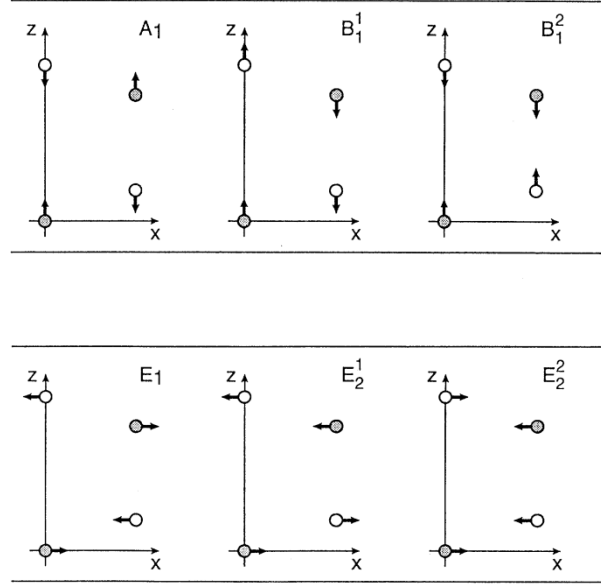


Fig (1.5): Schematic diagram for the optical phonon modes of w-AlN.[19]

Table (1.1): The optical phonon modes values in w-AlN compared to several other works from [19] and the references wherein.

Mode	Present work	Other calc.		Experiment					
		Miwa ^a	Ruiz ^b	Carlone ^c	Sanjuro ^d	Brafman ^e	Hayashi ^f	Perlin ^g	McNeil ^h
Wurtzite									
E_1	649	650	734	614	671	667	672	—	673
E_2^1	236	228	301	303	—	—	—	241	252
E_2^2	631	638	704	426	—	665	—	660	660
A_1	629	601	668	—	659	667	660	607	614
B_1^1	553	534	723	—	—	—	—	—	—
B_1^2	717	703	772	—	—	—	—	—	—
Zinc blende									
TO	652	648	—	—	—	—	—	—	—

For instance, Khan, S., et al.[23] showed how the FTIR and the Raman modes of nanocrystalline AlN can be modified by the experimental conditions and used as tools reflecting the microstructure picture. In the same line, Jagannadham, K., et al.[24] displayed the use of relative intensity of phonon peaks associated to the crystalline and amorphous phases to identify the volume fraction of the amorphous phase. They also referred the shift of the peaks in FTIR to the residual stress. Moreover, according to [25], The ratio of integrated

areas of Al(TO) and E1(TO) absorption bands in FTIR can be related to the degree of preferential orientation of AlN thin film.

1.3- Type of defects in AlN

AlN, like any semiconductor materials can't be formed without avoiding defects in its structure. The word defect is used here to point to imperfection in the crystalline material that interrupts the regular pattern of the material crystallography. This interruption locally alters the atomic and the electronic structure and results in modifications in the macroscopic properties of such material. The type and density of the defects depend mainly on the preparation methods and conditions. The functional properties and the electronic structure of semiconductor devices critically rely on the type of these defects. Therefore, controlling the performances of such devices can be achieved by understanding and managing the native and impurities defects. It has been reported that the type of defects can be classified into[26]: point defects (e.g. vacancies, interstitial and anti-sites), line defects (e.g. dislocations), planar defects (e.g. grain boundaries) and Bulk defects (e.g. pores, cracks and voids). Line, planar and bulk defects can be strongly minimized and avoided by taking care and optimizing the experimental conditions. However, the point defects as well as some impurities can't be totally avoided. Thus, it is of great importance to understand their behavior. It has been noticed that the existence of point defects/impurities to certain limit is not detrimental. In contrast, in some cases, the defects are intentionally added to the semiconductor materials to enhance a desired functional property. For example, small amount of boron or phosphorous impurities are added to pure silicon to increase the concentration of the charge carriers (holes or electrons respectively) and improve the electric conductivity of silicon.[27-28] Alternatively, generation of point defects can be used as a mediator to transfer the energy, radiatively or nonradiatively, to optically activate rare earth ions inside semiconductor. Hence, the optical properties can be enhanced.[29-30] Therefore, understanding the behavior of defects opens the door to control and tailor the material properties.

More precisely, the effect of point defects and their complexes in AlN on electronic and atomic structures have been extensively studied.[31] Stampfl et al used the density functional pseudopotential method calculations to investigate the native and impurities defects in AlN. The formation energy and the charges of the defects have been considered during their study. They found that the most pronounced native defects that have lowest formation energy in n-type and p-type AlN are V_{Al} and V_N especially the triply negatively and triply positively

charged; respectively. In wurtzite AlN, V_{Al} acts as an acceptor center near the valance band maximum (VBM) while V_N acts as a deep donor level below the conduction band minimum. In addition, the authors also demonstrated that both kind of defects induce the same geometrical interruption in the atomic structure that leads to outward moving for the nearest neighboring atoms with different percentage from the ideal position depending on the defect charge state. Moreover, the two defects act as compensation centers that prevent to achieve successful n-type or p-type doping. Regarding the impurities defects, the dominant unintentional impurity in AlN is Oxygen. It was found that oxygen in AlN matrix substitutes nitrogen site to form O_N^{+} defect that has low formation energy. In addition, when O-atoms incorporated inside AlN, each 3 O-atoms that substitute N-atoms generate one Al vacancy (V_{Al}), since they enter as ($V_{Al} Al_2 O_3$) phase. After that, the two defects V_{Al} and O_N form an energetically favorable defect complex $(V_{Al}-O_N)^{2-/-}$. [32-33] There are many reports on the influence of oxygen in AlN on the optical properties of AlN. For instant, G. A. Slack et al [34] reported on how the oxygen concentration can influence on the optical and thermal conductivity of AlN material. It is found that understanding the behavior of such oxygen related defects is essential for manipulating the properties of AlN, in particular the optical response.

1.4- AlN: Preparation methods

There are many growth methods that can be used to prepare AlN thin films. Researchers everywhere have screened several techniques in order to study the different growth mechanisms and the correlation with the functional properties of AlN. For instance, the most common methods are pulsed laser deposition (PLD)[35-36], chemical vapor deposition (CVD)[37] and physical vapor deposition (PVD).[38] Within PVD method, reactive magnetron sputtering (RMS) attracted more attention particularly in the industrial field thanks to its low cost, simplicity, large scale production applicability, and the high quality of coatings that can be achieved at low temperature.[39] More about reactive magnetron sputtering technique and how it works will be addressed in details in the experimental chapter.

1.5- AlN: Applications

Thanks to the physical, chemical, mechanical and optical properties of AlN, many applications can be found. For instance, AlN shows excellent acoustic properties due to its high piezoelectric coefficients, in particular d_{33} , that provide a chance to enhance the performance of MEMS devices. In addition, for opto-electronic purposes, the wide optical

bandgap of AlN of 6.2 eV allows emission of a deep UV wavelength around 200 nm to be obtained. Indeed, an AlN LED with emission of 210 nm has already been reported.[40] Moreover, the high thermal conductivity of AlN, about 300 [41] and 130 W/mK [2] in bulk and thin film respectively, is of particular interest in high temperature working devices. Furthermore, manipulation of optical properties of this optically transparent material represents an important challenge for future applications, especially in optical quantum circuits. Three functional properties are of primary importance for this purpose. First, c-axis out of plane orientation of AlN thin film is essential for exploiting its largest second order nonlinearity for wavelength conversion and electro-optical effects. Second, the high ordinary refractive index (typically 2.1) of AlN deposited on Si wafer is a prerequisite for realizing low loss in silicon integrated AlN photonic circuits.[42] This high refractive index allows to strongly confine the light for long distance leading to emergence a non-linear optical effect on chip scale.[12] Third, the wide range of AlN transparency (bandgap close to 6 eV) can be exploited for wide operation band devices from UV to IR wavelengths. Combining the above features together make AlN an excellent candidate for integrated nonlinear optics. Exploiting the high transparency in UV-visible range of AlN combined with its dielectric properties, make AlN is an excellent host material for transition and rare earth elements for magnetic and optical investigations. Therefore, the following sections will be dedicated to the characteristics of doped AlN.

2-Rare-earth elements

The name *rare-earth* consists of two parts; the first part ***rare*** refers to the difficulty to find these elements in pure minerals or free metals phases not to its relative abundances in the earth's crust. It is more abundant than silver and lead. In addition, these materials co-exist in oxides which indicate the difficulty to separate them from each other. This is the meaning of the second part of the name; ***earth***, where the Greeks defined earth as the material that couldn't be further changed by heat.[43]

2.1- Electronic structure and transitions of REs

Rare-earth metals defined as the 15 lanthanides located below the main body of the periodic table plus Scandium and Yttrium elements as shown in fig. (1.6).

The image shows a 3D periodic table of elements. The elements are arranged in rows and columns, with their chemical symbols and atomic numbers displayed on the blocks. The Lanthanide and Actinide series are shown as separate rows below the main table. The Lanthanides are labeled 'Lanthanides' and the Actinides are labeled 'Actinides'.

H 1																	He 2
Li 3	Be 4											B 5	C 6	N 7	O 8	F 9	Ne 10
Na 11	Mg 12											Al 13	Si 14	P 15	S 16	Cl 17	Ar 18
K 19	Ca 20	Sc 21	Ti 22	V 23	Cr 24	Mn 25	Fe 26	Co 27	Ni 28	Cu 29	Zn 30	Ga 31	Ge 32	As 33	Se 34	Br 35	Kr 36
Rb 37	Sr 38	Y 39	Zr 40	Nb 41	Mo 42	Tc 43	Ru 44	Rh 45	Pd 46	Ag 47	Cd 48	In 49	Sn 50	Sb 51	Te 52	I 53	Xe 54
Cs 55	Ba 56	La 57	Hf 72	Ta 73	W 74	Re 75	Os 76	Ir 77	Pt 78	Au 79	Hg 80	Tl 81	Pb 82	Bi 83	Po 84	At 85	Rn 86
Fr 87	Ra 88	Ac 89															

Lanthanides

Ce 58	Pr 59	Nd 60	Pm 61	Sm 62	Eu 63	Gd 64	Tb 65	Dy 66	Ho 67	Er 68	Tm 69	Yb 70	Lu 71
Th 90	Pa 91	U 92	Np 93	Pu 94	Am 95	Cm 96	Bk 97	Cf 98	Es 99	Fm 100	Md 101	No 102	Lr 103

Fig (1.6): The periodic table.[43]

These lanthanide elements are characterized by occupancy of the $4f$ level by electrons (from 0 in La to 14 in Lu). The properties that depend mainly on the occupancy of $4f$ level make the interest of lanthanides. Although, the term Lanthanides in general is restricted to the 14 elements from Ce to Lu that contain partially or totally filled $4f$ electrons, Scandium (Sc), Yttrium (Y) and lanthanum (La) can be considered in the same group. They exhibit similar chemical and physical properties to the 14 lanthanides elements although they haven't any electrons in the $4f$ level. The reason behind joining these three elements is the analogy of their electronic configuration of the outer shell three electrons with the lanthanides; $(3d4s)^3$ for Sc, $(4d5s)^3$ for Y and $(5d6s)^3$ for La. Thus, it shares all the lanthanides properties that are not depend on the $4f$ electrons. As we are interested in this work by the optical properties of cerium and ytterbium, we will focus our attention on the properties of the 14 lanthanides elements that contain electrons in its f orbital.[44] Although, the lanthanide elements have similar basic electronic structures, the small differences between the individual elements result in diversity in their properties, in particular the optical behaviors. Therefore, in order to understand the basic characteristics of lanthanides, the electronic configuration should be considered. In the following table (1.2), all the lanthanides' electronic configurations in metallic and ionic forms have been stated.

Table (1.2): Lanthanides electronic configuration of the metal and the valence states +3,+4,+2.[45]

	Atom	Ln^{3+}	Ln^{4+}	Ln^{2+}
La	$[\text{Xe}] 5d^1 6s^2$	$[\text{Xe}]$		
Ce	$[\text{Xe}] 4f^1 5d^1 6s^2$	$[\text{Xe}] 4f^1$	$[\text{Xe}]$	
Pr	$[\text{Xe}] 4f^3 6s^2$	$[\text{Xe}] 4f^2$	$[\text{Xe}] 4f^1$	
Nd	$[\text{Xe}] 4f^4 6s^2$	$[\text{Xe}] 4f^3$	$[\text{Xe}] 4f^2$	$[\text{Xe}] 4f^4$
Pm	$[\text{Xe}] 4f^5 6s^2$	$[\text{Xe}] 4f^4$		
Sm	$[\text{Xe}] 4f^6 6s^2$	$[\text{Xe}] 4f^5$		$[\text{Xe}] 4f^6$
Eu	$[\text{Xe}] 4f^7 6s^2$	$[\text{Xe}] 4f^6$		$[\text{Xe}] 4f^7$
Gd	$[\text{Xe}] 4f^7 5d^1 6s^2$	$[\text{Xe}] 4f^7$		
Tb	$[\text{Xe}] 4f^9 6s^2$	$[\text{Xe}] 4f^8$	$[\text{Xe}] 4f^7$	
Dy	$[\text{Xe}] 4f^{10} 6s^2$	$[\text{Xe}] 4f^9$	$[\text{Xe}] 4f^8$	$[\text{Xe}] 4f^{10}$
Ho	$[\text{Xe}] 4f^{11} 6s^2$	$[\text{Xe}] 4f^{10}$		
Er	$[\text{Xe}] 4f^{12} 6s^2$	$[\text{Xe}] 4f^{11}$		
Tm	$[\text{Xe}] 4f^{13} 6s^2$	$[\text{Xe}] 4f^{12}$		$[\text{Xe}] 4f^{13}$
Yb	$[\text{Xe}] 4f^{14} 6s^2$	$[\text{Xe}] 4f^{13}$		$[\text{Xe}] 4f^{14}$
Lu	$[\text{Xe}] 4f^{14} 5d^1 6s^2$	$[\text{Xe}] 4f^{14}$		

It is noticed that all the lanthanides share the xenon core electrons' configuration. Then, the rest of electrons are placed in $6s$ and $4f$ orbitals except four elements, namely La, Ce, Gd and Lu that sharing one electron in the d orbital lead to more energetic stability and result in empty $4f$ (La), half-filled $4f$ (Gd) and fully-filled $4f$ (Lu). The filling sequence of electrons from La to Lu in the outer-shells follows energetic stability concept. In addition, It was found that $4f$ electrons are spatially localized lying in the core of the REs while $5s$ and $5p$ orbitals are spatially extended, see for example fig (1.7) for Gd.[44]

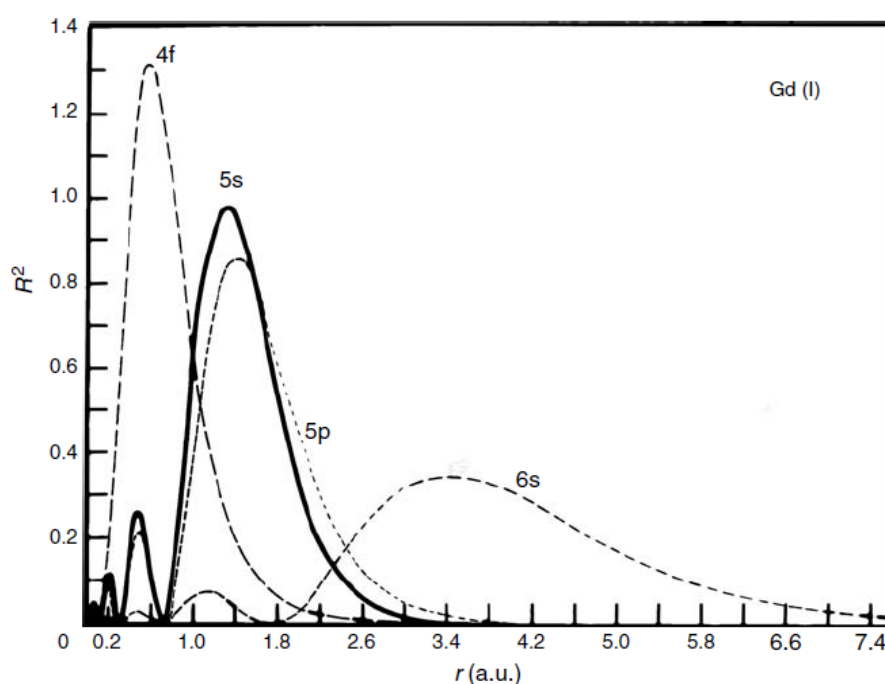


Fig (1.7): Radial charge density of valence orbitals of Gd^+ . [44]

In addition, the filled $5s$ and $5p$ outer shells are efficiently shield the $4f$ electrons from the surrounding ligands result in weak crystal field strength that can be strongly perturbed the $4f$ states. Moreover, this shielding property results in the f orbitals don't participate in the formation of valence bonds, hence the valence of REs is determined by s and p orbitals.[46] As a consequence, $f-f$ absorption spectra are very narrow which raises questions about the lanthanides' energy levels. It is worth noting that $4f-4f$ transition are exhibiting electric dipole transition although its parity is forbidden.[47-48] There are experimental evidences showing that the $4f-4f$ transition strongly matches with the electric dipole transition principle. Therefore, Judd[47] and Ofelt [48] reported that there is a probability of mixing states with the higher electronic levels of opposite parity (e.g. d -orbital). This arises from the asymmetric local environment around the RE results in perturbation in the crystal field that lead to partially allowed the electric dipole of these transitions. As a consequence, models for the $4f$ energy levels transitions became necessary. The most effective model used up to date was reported by Dieke [49] and is called Dieke diagram, provides the energy of the sub-splitting levels of RE^{3+} in different matrices. Hence, the origin of the electronic transition of lanthanides has been addressed and matched with the experimental luminescence results obtained from these ions.

In the following section some general basic concepts about the luminescence will be given before getting through the luminescence characteristics of lanthanides.

2.2- Luminescence principles

- **Terminology**

The difference between the common terms luminescence and incandescence is that, both are refereeing to emission of light but luminescence is related to emission of light from a cold body while incandescence is related to hot body (like sun or tungsten lamp). Hence, a cold body can be undergo luminescence process if stimulated by any means (except heat) to emit light. This stimulation process is called excitation. As a result, the type of luminescence action is classified according to the kind of excitation process. For example, the excitation can be performed by light (*Photoluminescence*), injection of electric current (*Electroluminescence*), bombardment of electron (*Cathodoluminescence*), bombardment by ionizing radiation (*Radioluminescence*), chemical reaction (*Chemoluminescence*) or by mechanical stress (*Triboluminescence*).....etc.[50] Therefore, the excitation process determines the type of

luminescence as well as the mechanism by which the light is emitted. The following section is focused on the photoluminescence process as it is the main subject of this work.

- **Photoluminescence (PL)**

PL is the most popular method for obtaining light from a luminescent material and usually divides into two main categories: fluorescence and phosphorescence.[51] Both are concerning to light emission from a sample after absorbing (excitation by) light, but the main difference between them is the decay time, i.e. how long time takes between the excitation and emission. Phosphorescence is a slower process than fluorescence. The reason behind the difference in the time scale between the two processes is the occupancy of forbidden state by the excited electron in the case of phosphorescence materials. Fig (1.8) shows a schematic diagram illustrates the two processes.

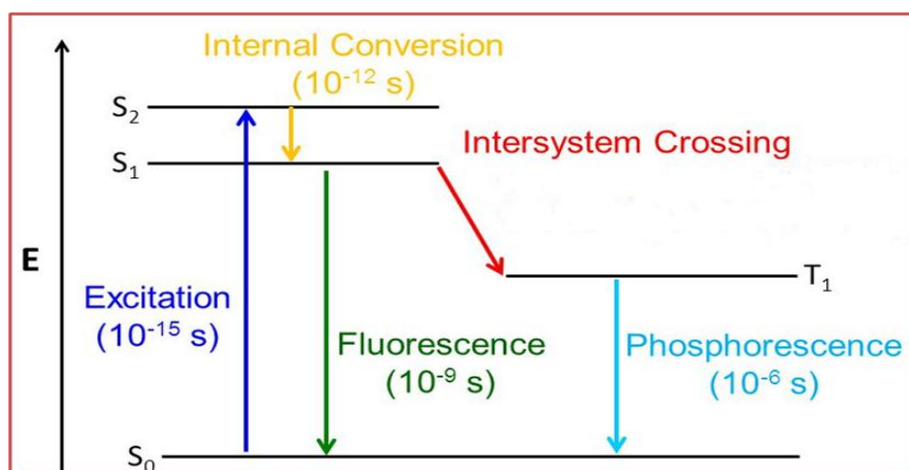


Fig (1.8): Schematic diagram revealing the absorption, fluorescence and phosphorescence process.

Luminescent materials should be excited by absorbing energy equal to the energy difference between the ground and excited state. In case of fluorescence, a deactivation (relaxation) process occurs from the excited singlet state to the ground singlet state (spin allowed process i.e. $S_{1,2}$ states to S_0). In contrast, phosphorescence is a transition from excited triplet state to the singlet ground state after a non-radiative intersystem crossing process. That is why phosphorescence process takes longer time.[52] The probability of which process is dominating or which mechanism will be followed by the substance mainly depends on the electronic structure of the material and how it can be modified under the experimental conditions. Since, the luminescence properties are strongly dependent on the electronic structure for each material. So, the luminescence characteristics are unique property for each

substance. Therefore, one can find a group of elements that share the same electronic structure having quite similar luminescence properties. This is the case of our study on lanthanides.

As mentioned before, all Lanthanides have similar electronic structure except the slight differences of Ce, Gd and Lu. Also, all the RE^{3+} ions- the most stable valence state- exhibit luminescence through $f-f$ transitions except Ce^{3+} that shows $f-d$ transition. There are other elements like Eu^{2+} , Yb^{2+} and Sm^{2+} with stable +2 state exhibiting $f-d$ transitions under certain conditions. Thus, Ce^{3+} is a unique RE^{3+} with luminescence properties originated from the $f-d$ transition.

- **Luminescence mechanism**

As seen in the previous section, how luminescence takes place, is very simple way as follows: the radiation absorbed by the material under investigation results in excitation of its electrons to excited states. Then after a certain characteristic time (excited state lifetime) it returns to the ground state by losing the absorbed energy through radiative process (emission) and/or nonradiative process (heat). The competition between the radiative and nonradiative processes determines the luminescence efficiency of the emitting species. However, finding and understanding the correct mechanism explaining how a specific emitting center (activators like REs, transition metals or even semiconductors materials) behaves and emits light is quite complicated. Many parameters should be considered to study a luminescent material. Some of these parameters are basic like the excitation spectra, radiative and nonradiative probabilities, the absorption cross section, the lifetime of the excited states and the energy transfer mechanisms. For example, in some cases the activator doesn't absorb the excitation energy directly but via different indirect ways. For instance, energy transfer process is the well established mechanism used to excite some activators indirectly. In such systems, another species called sensitizer (S) (sometimes the host material or another ions) is responsible to absorb then transfer the excitation energy to the activator (A) that , in turn, emits the light, as shown in the simple schematic diagram fig (1.9). This illustrates the rather complicated nature of the luminescence process. It is essential to understand the physical role of the above processes in order to explain the luminescence results. Particularly with REs, It was found that the luminescence of most of lanthanides comes from the partially allowed electric dipole $4f-4f$ transitions which are shielded by the outermost valence orbitals as mentioned in (beginning of rare earth section). This results in very weak direct absorption cross section of these ions. Hence, another indirect excitation method is needed.

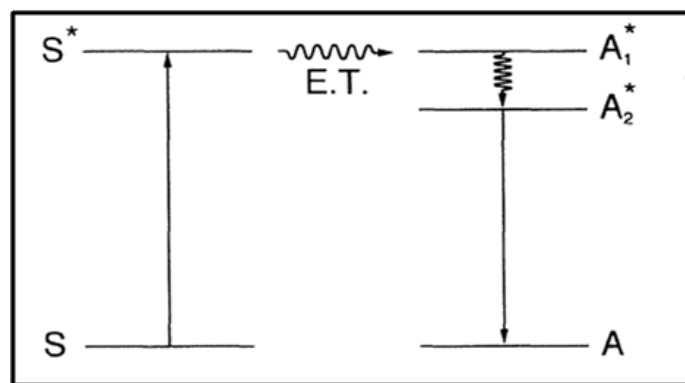


Fig (1.9): schematic diagram illustrates the energy transfer process from sensitizer to activator.

For this reason, in order to efficiently excite the lanthanides, another species is required to absorb the excitation energy and transfer it to the lanthanides ions. This process is called "sensitization" and the species used for the energy transfer is called "sensitizer" (energy donor) while the emitting lanthanide ion is called "activator" (energy acceptor).

The energy transfer mechanism is the most acceptable process used to explain the indirect excitation of rare earth ions doped in different hosts. Therefore, a brief introduction about the energy transfer phenomenon is given in the following section.

- **Energy transfer mechanisms**

Two energy transfer mechanisms are proposed for donor-acceptor energy transfer, the *Dexter* and *Förster energy transfer* mechanism.[53-54] In the case of *Dexter* mechanism, the energy is transferred via electrons exchange between the donor and acceptor. The electron in the excited state of the donor can be exchanged by one in the ground state of the acceptor, resulting in excited acceptor. In other word, the electron in the excited donor hops to the excited state of the acceptor result in excited acceptor and an electron from the ground state of the acceptor hops to the ground state of the donor.

In this case of *Förster energy transfer*, the energy is transferred from the excited donor to the acceptor nonradiatively via dipole coupling. Figure (1.10), illustrates the two kinds of mechanisms. It is worth mentioning that both mechanisms are mainly depending on the spectral overlapping and the inter-distance between the donor and the acceptor.

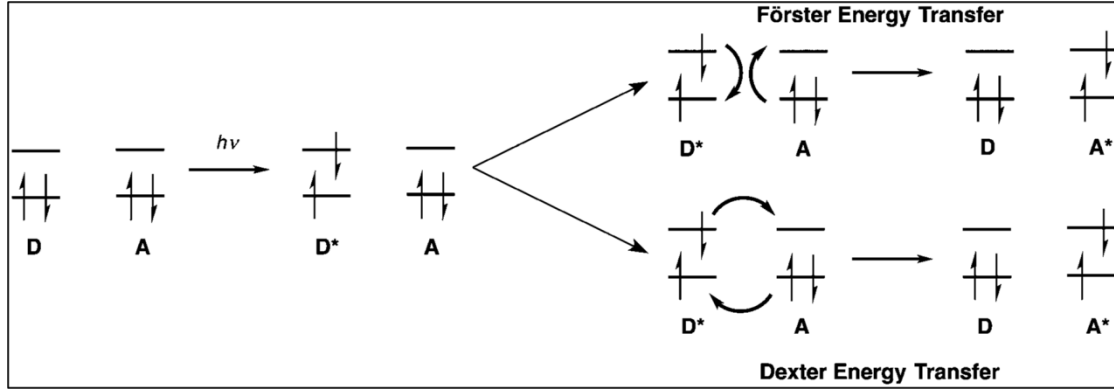


Fig (1.10): Schematic diagram for the Förster and Dexter energy transfer.

- **Luminescence decay rates**

One of important characteristic emission features is the luminescence deactivation (decay) rate. According to the quantum mechanics theory, it is noticed that the luminescence loses its intensity *spontaneously* after the excitation and returns back to the ground state after certain time. This process, called the luminescence decay rate, is characteristic for each luminescent species and brings many information about the excited level and the way this level deactivates.[55] As there are two pathways for a substance to deactivate the excited state either radiatively and/or nonradiatively, knowing the decay rate can lead to estimate the quantum efficiency of the material as well as the energy transfer efficiency if any. One popular way to figure out the decay rate is the time resolved photoluminescence experiment (TRPL). In this case, the evolution of the PL intensity is recorded as a function of time after pulse excitation. After that, by fitting the experimental results of the TRPL, the deactivation constant corresponding to the observed decay rate (called the total decay rate k_{tot}) can be estimated. The total decay rate is considered as a summation of the radiative k_{rad} and the nonradiative decay k_{nonrad} , as in the equation (1.1),[55]

$$k_{tot} = k_{rad} + k_{nonrad}, \quad (1.1)$$

The radiative decay rate can be calculated by solving the rate equation of the spontaneous emission.[55] Then, the nonradiative decay rate can be estimated. The quantum efficiency **QE** of the emitting material, which is the relative amount of emitting photons to the absorbed photons, can be calculated using the following equation:[55]

$$QE = k_{rad} / (k_{rad} + k_{nonrad}), \quad (1.2)$$

QE tells us about the amount of absorbed energy transformed to emitted light.

After the above information about the basic characteristics of the luminescence process, in the following we are going to focus on the REs behavior as luminescence centers in solid hosts.

2.3- Rare earth doped in solid hosts (semiconductor/insulators)

Rare earth-doped solid hosts attract great attention from luminescence devices point of view by combining the luminescence properties of REs with the electronic features of the host matrix. It also attracts a particular interest in the field of integrated optoelectronic devices. Rare earth based-devices have extended to cover many sectors from energy harvesting (e.g. solar cell) moving on telecommunications to lighting devices (e.g. lasers and displaying units). Although, the trivalent REs are of a great technological interest due to their sharp emission lines, some divalent REs ions that exhibit broad emission (e.g. Sm^{+2} and Eu^{+2}) find their way to the devices required broad band emission such as w-LEDs. As consequence of shielding the $4f$ electrons by $5s$ and $5p$ electrons, it is believed that the electronic energy levels of the $4f$ are influenced mainly by the spin-orbit interaction while the electron phonon coupling with the host becomes weak. Nevertheless, the energy levels of intra- f electrons have been found slightly affected by the applied crystal field.[30] For instance, this can be observed in the difference of the emission lines and photoluminescence excitation of Er doped hexagonal and cubic GaN, which referred to the difference in the local symmetry around Er ions.[56] Hence one can conclude that, although the strong shielding of the intra- f electrons of the REs, the significant influence of change in the local environment around it cannot be excluded.

2.3.1- Issues related to the luminescence of RE-doped solids

Beside the luminescence behavior, incorporation of rare earth in solid hosts raises some key questions about the lattice location of the RE inside the host and the kind of interaction with the host material. In the following section some of these points will be briefly covered.

- ***RE site location in the host lattice structure***

As mentioned before, the local environment around the RE in the host material can induce modifications in the electronic structure of the RE. These modifications, sometimes, are of great importance such that it can modify the optical response of the RE by altering the transition probabilities of the electronic levels. For example, Steckl, A.J. et al[57-58], demonstrated how the Eu lattice site can play a role in changing the emission wavelength,

emission cross section and the PL decay rate of two different Eu sites in GaN, as shown in fig (1.11). [58] They attributed their results to the different local environment for each site.

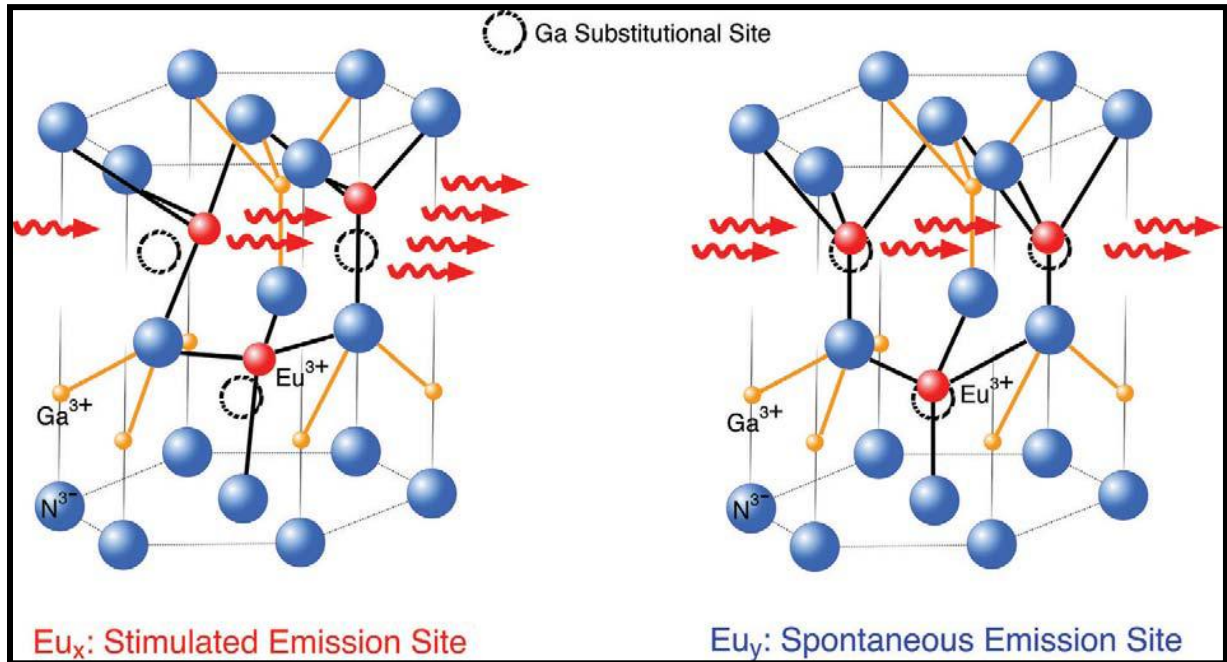


Fig (1.11): Schematic diagram for the two proposed sites of Eu in GaN.[58]

More precisely, the Eu ions located very close to the center of Ga substitution site (Eu_y) are subjected to the local symmetry and participate to the spontaneous emission with low emission cross section. In contrast, the Eu ions located in interstitial-like site (Eu_x) suffer from a distorted local environment and contribute in stimulation emission with high emission cross section. Furthermore, Gan, L., et al[59] attributed the effect of the crystallographic site of Ce on the structure and the luminescence properties of β -SiAlON:Ce phosphor to the different number of coordination with the surrounding N(O) atoms. Their experimental observations proposed three locations for Ce ions in this phosphor: two of them are in the interstitial sites with 6 and 9 coordination numbers and the third one is in substitution site for Si(Al) atoms. These different coordinations with Ce lead to structure and luminescence wavelength modifications. However, in general the common location of RE in the crystal hosts, in particularly at high concentration of RE, is segregation close to the grain boundaries due to the large ionic sizes of the REs and the less rigid structure at the crystal grain boundaries.[60-62] Therefore, the dependency of the luminescence of such phosphors on the local structure of the RE opens the door for intensive structure investigations in order to better understand the luminescence from atomic scale point of view.

- ***RE ion- host interaction***

One of the most important process results from the RE ions-host interaction is the multiphonon relaxation. In this process, the emitting photons energy are used to excite the vibration modes of the host material instead of de-activate via radiative pathways which, in turn, lead to luminescence quenching or suppression some of optical transitions in the activator. Generally speaking, the contribution of multiphonon relaxation can be estimated considering the phonon cut off energy of the matrix relative to the energy of the emitting photons of the activator. If the phonon cut off energy is higher than 25% of the photon energy, complete luminescence quenching can be occurred. In contrast, if the phonon cut off energy less than 10% of the photon energy, the multiphonon relaxation can be neglected. Between 10% and 25%, quenching is temperature dependent. Thus, the prior knowledge about the phonon energy of the matrix and the optical transition of the activators is essential for appropriate selection of good matrix for certain activator. For example, in case of erbium doped silica matrix, the phonon cut off energy of silica is 1100 cm^{-1} then erbium optical transition $I_{13/2} - I_{15/2}$ emitting at 1535 nm (6500 cm^{-1}) is weakly quenched at room temperature ($1100/6500 = 16\%$). In contrast, the erbium transition $I_{11/2} - I_{13/2}$ at 2700 nm (3700 cm^{-1}) is totally quenched by multiphonon (non-radiative) relaxation ($1100/3700 = 30\%$). [63] Therefore, low phonon cut off energy host matrices are desirable to avoid such unwanted multiphonon relaxation. It is worth to note that the maximum phonon energy of AlN material is about 700 cm^{-1} , which is low and compatible with many of rare earth ion transitions. In other words, the multiphonon relaxation process in AlN starts to have a very weak role for optical transitions at 7000 cm^{-1} (i.e. 10% of the optical transition energy).

- ***RE ion- ion interactions***

Ion- ion interaction process is a well known and characteristic phenomenon taking place with the RE ions. [64] This process can occur between similar RE ions, for instance at high RE concentrations, and in some case leads to luminescence quenching due to re-absorption process or can lead to RE oxidation conversion by electron exchanges. [65] On the other hand, the same process can occur between two different RE ions in order to sensitize one RE ion by another one. In a well managed sample doped by two different REs, one of them can absorb the excitation pump and transfer the energy to the other ion, which opens several pumping schemes for the sample. [66-69]

2.3.2- Rare earth-doped semiconductors (RE-Sc)

RE-doped semiconductors have attracted great attention from the scientific and industrial societies in order to integrate the RE emission in microelectronic technology. Combining the advantages of the electronic structure of semiconductor as well as its compatibility to the chip technology with the emission properties of the RE will open the door to new and wide spread lightening technology. Exploiting these features has been reflected in many applications especially in color displays and flat panel technologies. RE-doped silicon is the most studied system in this direction due to the compatibility of silicon with silicon microelectronic fields. However, silicon has serious drawbacks like having indirect bandgap which leads to significant unwanted non-radiative processes. Moreover, its low bandgap value (1.12 eV) makes the doping with RE ions is limited to few elements that emit in the IR region.[70] Therefore, intensive research for new semiconductor hosts has been stimulated to overcome the silicon drawback points. The main characteristics that should be considered during searching for new hosts are: the compatibility with the silicon substrates, the direct bandgap (to reduce the non-radiative process) and the wide bandgap value (to cover the visible light range). It was found that III-V semiconductor compounds efficiently offer the integration compatibility with the silicon microelectronic technology.[71] Among them, III-nitride compounds attract particular interest, especially GaN and AlN due to their direct and wide bandgap properties, see fig (1.12).

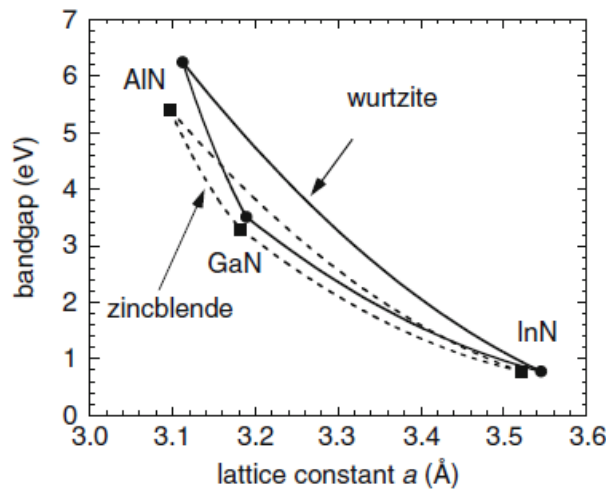


Fig (1.12): Bandgap values for wurtzite and zinc blend structures of InN, GaN and AlN and their alloys as a function in the lattice constant (a). [9]

It can be seen that, wurtzite AlN has a large bandgap close to (6.2 eV) that gives the advantage to cover the UV-visible range with less thermal quenching of the luminescence.

Therefore, many research groups exploited this advantage of AlN to start to figure out the behavior of RE in AlN, especially to promote UV-Vis light emission. Many rare earth elements have been used as activators in AlN host materials. Most of lanthanide elements-doped AlN have been reported and cover the light spectrum from UV (Gd),[72] blue (Ce, Eu, Tm),[73-74] green (Tb),[75] yellow (Dy),[76] red (Sm, Eu)[76] to IR (Yb, Nd)[77-78] which highlights the versatility and the efficiency of AlN host material. Also, AlN has been conducted to several final forms such as thin films, powders[74] and bulk ceramics.[41] Moreover, from microstructure point of view, RE-doped AlN has been reported in different microstructures; amorphous,[79] polycrystalline[80] and single crystal.[81] With these many reports of using RE-doped AlN for lightening purposes, the need to gain deep understanding of the optical behavior of these RE inside AlN and III-nitrides in general became highly desired. The most important process that allows exploring the luminescence behavior of phosphor is the excitation mechanisms. However, the buried nature of f - f levels in the core of most of RE ions makes the excitation mechanisms of the REs became a hot debate topic. Different theories have been established to understand and explain how these levels can be excited, which will be the main point of discussion in the following section.

- **Excitation mechanisms of REs-doped III-V semiconductors**

Understanding the excitation mechanism of rare earth doped III-nitrides is essential for better interpretation of the luminescence properties and enhances our fundamentals about these materials. Although, large part of research in this regard was devoted to find and draw a general excitation mechanism responsible for the excitation of the optically active rare earth ions in semiconductors, the exact mechanism is still ambiguous. However, we believe that the excitation mechanism of RE-doped III-nitrides shouldn't be generalized. It can be studied case by case due to the various possible ways to deliver the excitation energy to the REs ions. One of the highest obstacle to understand the excitation mechanism of the core $4f$ levels in RE^{3+} is the deep lying position of these levels shielded by the outer $5s$ and $5p$ orbitals, which make the energy delivering process is quite difficult.

However, in general, the excitation mechanisms can be divided into main categories: direct and indirect processes.

I- Direct excitation mechanism:

In this procedure, the pumping is chosen to be resonant with the energy difference between the ground and excited states of the $4f$ levels in the RE. But as mentioned earlier, due to bury these $4f$ levels in the core of the RE, results in very low absorption cross section. This makes the direct method is inefficient for the excitation. However, in some cases it can be used because of its simplicity as well as due to the advances in diode laser technology providing several wavelengths at different areas in the light spectrum that can directly pump many REs ions.[82-83]

II- Indirect excitation mechanism:

In this method, the excitation energy can be delivered via a mediator called sensitizer. This is a common way used to transfer the energy to the emitting "activator" species. For example, when the absorption cross section of the activator is low in a certain spectral range, an appropriate sensitizer with high absorption cross section in that range can be chosen in order to efficiently transfer the excitation energy to the activator from such spectral region. In RE-doped semiconductor, the host and/or another transition metals or RE ions can play the role of sensitizer. In this case, the excitation mechanism becomes quite difficult to understand due to the involvement of different excitation pathways. In the simple approach, the host lattice is used to play the role of sensitizer instead of incorporating other ions because the structure and the optical picture in co-doping system become more complicated.

Here, we focus mainly on the indirect excitation mechanisms by energy transfer from the matrix to the REs in III-nitrides.

- **Excitation mechanisms of rare earth-doped III-nitride**

Several attempts have been reported to figure out the kinetics of energy transfer from the host lattice to the localized core excited states ($4f$) of the RE. It has been established and proved by several experimental measurements that RE in III-V compounds replaces the III ion site and acts as isoelectronic structured traps (REI-traps).[84] Isoelectronic traps, are such impurities that contain the same outer electronic configurations as the replaced native ions.[85] For example, all RE^{3+} exhibit $5s^2 5p^6$ outershell electron configuration and the III-column ions have the same $s^2 p^6$ outer electronic configuration.[86] Thus, RE^{3+} is called isoelectronic impurity when replacing the III-column ions in their compounds. There are two types of isoelectronic impurities; "simple" and "structured".[86] The simple isoelectronic impurity is

considered when the III-column ions are replaced by another ion of the same III-group. For example, it occurs when Al substitutes the Ga site in AlGaN compound. The simple isoelectronic impurities introduce only effective -mass-like states in the forbidden bandgap. In contrast, the structured isoelectronic impurities (e.g. RE³⁺) introduce local structure and electronic disturbance due to the size and the electronegativity mismatch with the replaced native ion.[86] Hence, because of this potential disturbance, the REI-traps centers can be electrically active and can trap carriers.

The different excitation mechanisms possibilities can be summarized as follows:[87]

I- Direct excitation using light source with photon energy equal the exact energy difference between the ground and excited states of the core level of RE as in path.

II- Indirect excitations from the host lattice to the RE which can be classified to:

❖ *band to band excitation:*

In this case, free carriers (e-h pairs) are generated by exciting the electrons from the valance band (V.B.) to the conduction band (C.B.) of the host using either hot electrons (e.g. cathodluminescence and electroluminescence) or resonant pumping photons with energy equal at least the bandgap energy of the host. Hence, free excitons can be formed and interact with the RE by energy transfer. Alternatively, the free exciton energy can be transferred to other localized or extended defects that would play the role of the sensitizer.

❖ *Below bandgap excitation:*

Using excitation photons with energy less than the host bandgap energy (below bandgap excitation) would lead to excite localized or extended defects. The excited electrons and/or holes can be captured by the impurities (RE or localized or extended defects) and form bound excitons (BEs) or trapped carrier coupled with free carrier (B-F). The recombination of these BEs or trapped carrier (B-F) can lead also to REs excitation if the released energy is at least equal to the energy difference of the core lying levels of the RE and if the recombined defects are close enough to the RE. In all cases, the RE trap can also participate in formation of the bound exciton or the bound-free carrier mechanisms inside its trap zone.[86]

Hence, one can conclude that the presence of core empty levels buried in the REs ions opens the door for several and new excitations schemes that depend on the pumping regime and the

kind of carriers (bound or free or mixed) which determined by the type of impurities and defects. This supports the previous mention of the importance of impurities/defects in the semiconductors that can be turned on to a useful thing. Without these defects, the excitation of RE would be inefficient in most cases.

This work will mainly focus on the optical behaviors of two REs ions (Ce and Yb) doped in AlN as a case study for REs-doped III-nitrides.

2.3.3- Cerium in AlN

As mentioned in the beginning of this chapter, cerium is a unique RE element. It is the first lanthanide element containing one electron in the $4f$ -orbital. The luminescence properties of its optically active ion (Ce^{3+}) are characterized by fully allowed electric dipole moment $5d-4f$. [88] Thus, it has large absorption cross-section $\sim 10^{-18} \text{ cm}^2$ compared to the other rare earths characterized by $f-f$ transition $\sim 10^{-20} \text{ cm}^2$. [89] Moreover, It absorbs in UV and emits in UV-VIS range, which is suitable for many applications in this range. Furthermore, involving the unshielded outer d -orbitals in the optical transitions makes the excited electron strongly sensitive with the local field of the environment and leads to the possibility to tune the Ce^{3+} luminescence from UV to blue-green-yellow by changing the local environment using different host compositions. [90-92] This property is very interesting in terms of luminescence engineering technology. Particularly, the promising luminescence property of cerium is the ability to emit blue light that can be used in white light generation technology. So, great potentials have been directed in this regard using Ce in different hosts (glasses, garnet, ceramics and semiconductors). [41, 93-94]

The types of hosts can be classified from the elemental composition point of view into several categories: phosphors including oxides (aluminates, silicates, phosphates and borates), sulfides/oxyulfids, fluorides/oxyfluorides and nitrides/oxy-nitride. The common key questions raised about the quality of the phosphors are mainly on the thermal and chemical stabilities as well as the optical stability of the phosphor under the operating conditions. These stabilities limit the selection of the phosphors composition in order to fit the practical applications. For instance, although Ce ions have been mostly used in oxide hosts for lightening purposes, Ce-doped nitrides and (oxy)-nitrides offer additional important advantages over the oxide counterpart. Thanks to the low electronegativity of nitrogen atoms compared to the oxygen atoms, the covalent character of nitrides or (oxy)nitride compounds is higher than that of pure oxide counterpart compounds. This makes, in turn, the crystal network structure becomes

more rigid and enhances both the thermal and chemical stabilities.[95] Moreover, due to the higher formal charge of N^{3-} than O^{2-} , a stronger crystal field splitting is induced and affects the surrounding cations, resulting in shifting the lowest d -orbital of Ce to lower energy.[96-97] Hence, the excitation and emission of Ce ions can be tuned by modifying N/O ratio and shift it to longer wavelengths, which is suitable for w-LEDs. Among nitrides/oxy-nitrides compounds, aluminum nitride/(oxy) nitride represents promising candidates as host material activated by the RE, especially that emit in UV-VIS range thanks to its wide bandgap (6 eV). Moreover, its high thermal conductivity about 300 W/mk [41] in bulk and 130 W/mk [98] in thin film forms is considered as a large advantage to avoid the thermal degradation under high power working devices. These features of AlN serve our target of generating blue emission using Ce doped AlN in order to be a candidate for w-LEDs. In addition, there is little knowledge on Ce-doped AlN. Amorphous Ce-AlN thin films were prepared by DC magnetron co-sputtering at substrate heated up to 350°C.[99] Their structure and microstructure was studied but the assignment of the PL signal was not clear. Liu et al, studied in more details the blue emission from a polycrystalline powder of AlN phosphor co-activated by Ce^{3+} and Si^{4+} synthesized by gas pressure sintering under high temperature (2050 °C for 4 hr) and high nitrogen pressure (0.92 MPa).[74] An intense luminescence at 600 nm from Ce-doped single bulk AlN crystal synthesized by reactive flux method under high pressure/temperature was also reported.[81, 100] The authors succeeded to directly observe the diffusion of single Ce atoms.[100] Recently, in 2015 and 2016, Majid A. et al[101-102] theoretically demonstrated the modification of the electronic structure of Ce-doped AlN using first principle calculations. More recently, broad band emission from Ce doped AlN ceramic bulk material sintered at (1700 C and 105 MPa) has been reported^[41] but experimental evidence of the influence of Ce oxidation state on the emission of Ce-doped AlN is still missing. Hence, deep investigation of Ce-doped AlN thin films, compatible with the chip technology, is particularly desired. Therefore, this work is dedicated to the synthesis and study of the optical properties of crystalline Ce-doped AlN thin films at room temperature deposited on silicon substrate.

2.3.4- Ytterbium in AlN

Yb^{3+} is the RE ion that contains 13 electrons in the $4f$ orbital and its electronic transition is relatively simple compared to other lanthanides. The electronic configuration of Yb^{3+} consists of two energy terms $F_{7/2}$ and $F_{5/2}$ generated by spin-orbit interaction. Although, the core f - f levels are slightly perturbed by the host environment, the $F_{7/2}$ and $F_{5/2}$ of ytterbium can be splitted into possible 25 sublevels according to theoretical calculations.[78] The emission lines of excited Yb^{3+} fall in the near infrared region (NIR) around 1000 nm which is promising for lightening solid state applications in that region e.g. laser devices. Although Nd ions emit in the same spectral range about 1064 nm and are widely used in laser devices in this region, the luminescence properties Yb ions have advantages over the Nd ions. These advantages can be summarized as follows: Simplicity of the electronic levels of Yb ions facilitates the understanding and interpretation of excitation and emission process. In addition, the absence of excited state absorption in Yb (considered as a quasi-three level system) reduces the effective loss cross section. Unlike Nd ion, Yb exhibits no absorption in the green region which is favorable in frequency doubling laser conversion.[103] Thus, Yb ions have emerged in several lighting applications such as optical fiber lasers and waveguides.[104-107] Yet recently, Yb has been also reported for down-conversion solar cells by exploiting the advantage of Yb emission line at 1000 nm (1.2 eV) that matches with silicon bandgap.[108-110] In this regard, researches have been focused on the way to transfer the UV-VIS photons of the solar spectrum by down conversion the energy of these photons using another mediator (Ce, Tb,...etc) to the Yb. Then, the excited electrons in Yb ions transferred to silicon which is supposed to enhance the solar cell efficiency. However, ytterbium is one of few lanthanides that have not been experimentally investigated as an optically active center in *crystalline* AlN host. It has been reported in few works in GaN and amorphous AlN but deep investigation of doping Yb in crystalline AlN is still unavailable.[76, 78, 111-112]

But, why Yb-doped AlN should have our attention although it is available in different hosts? Two reasons motivate us to study this system. First, there is a special interest for us to figure out the influence of the presence of another RE in addition to Ce in AlN in order to have a wide view about the different mechanisms of REs inside AlN. As described earlier, the luminescence properties of all the REs^{3+} in semiconductors are mostly characterized by a core lying f - f (e.g. Yb^{3+}) transition and sometimes characterized by d - f transition (Ce^{3+}). By studying and comparing the optical behaviors of Ce^{3+} and Yb^{3+} , we will have the opportunity

to test both electronic transitions mechanisms, which will provide us a better understanding about the optical properties for all the RE in AlN. Secondly from application point of view, Yb exhibits a great attention in solid state lightening systems that mainly based on light confinement concept (e.g. waveguide devices). By knowing that, crystalline AlN has high refractive index (about 2.1); this supposed to enhance the confinement efficiency if integrated in such devices. Moreover, AlN, as III-V compound, presents excellent match with silicon technology, which is additional advantage for silicon integration technology approaches. Furthermore, the piezoelectric properties of AlN open a promising path to piezo-opto-electronic integrated chips technology.

Chapter II

Experimental techniques

This chapter is dedicated to describe the experimental techniques that have been used during this thesis. The following sections are focusing on the preparation and samples' characterization techniques. A brief description of the basic principles and set up of the instruments are given. All samples have been prepared in thin film form deposited either on silicon and/or sapphire substrates. The chapter is organized in 3 parts dealing with film synthesis, structure and composition analysis and, finally, optical analysis.

All the used techniques are listed as follows:

For thin film synthesis

- Reactive magnetron sputtering (RMS) has been used.
- Thermal annealing process for optical activation

For structure and composition analysis

- X-ray diffraction (XRD)
- Transmission electron microscopy (TEM)
- Energy-dispersive X-ray spectroscopy (EDS)
- Electron energy loss spectroscopy (EELS)
- Rutherford backscattering spectrometry (RBS)

For optical analysis

- Fourier transform infrared spectroscopy (FTIR)
- Ellipsometry spectroscopy (SE)
- Photoluminescence measurements (PL) at room and low temperature (LTPL)
- Photoluminescence excitation (PLE)
- Photoluminescence power dependent
- Time resolved photoluminescence (TRPL)

After film deposition using reactive magnetron sputtering, the samples were cut into several parts some of which underwent rapid thermal annealing in different atmospheres (e.g. Ar, N₂ and N₂/H₂) in order to investigate on the possibility to induce strong luminescence. X-ray diffraction (XRD) and transmission electron microscopy (TEM) were employed to determine

the film structure and microstructure. Energy dispersive electron microscopy (EDS) and Rutherford backscattering (RBS) allowed investigating the film composition. The bonding state was studied using Fourier transform infrared spectroscopy (FTIR) and electron energy loss spectroscopy (EELS) embedded to the TEM. Optical absorption properties were measured using UV-visible spectrophotometry and spectroscopic ellipsometry while photoluminescence(PL), time resolved (TRPL), low temperature (LTPL) and photoluminescence excitation spectroscopies have been carried out to investigate the emission and related mechanisms in the films.

1-Thin film synthesis

1.1-sputtering

All the undoped and rare earth-doped AlN samples have been prepared using reactive magnetron sputtering technique (RMS). Fig (2.1) shows a schematic diagram of magnetron sputtering discharge processes of Al target and gas phase composition of Ar and N₂.

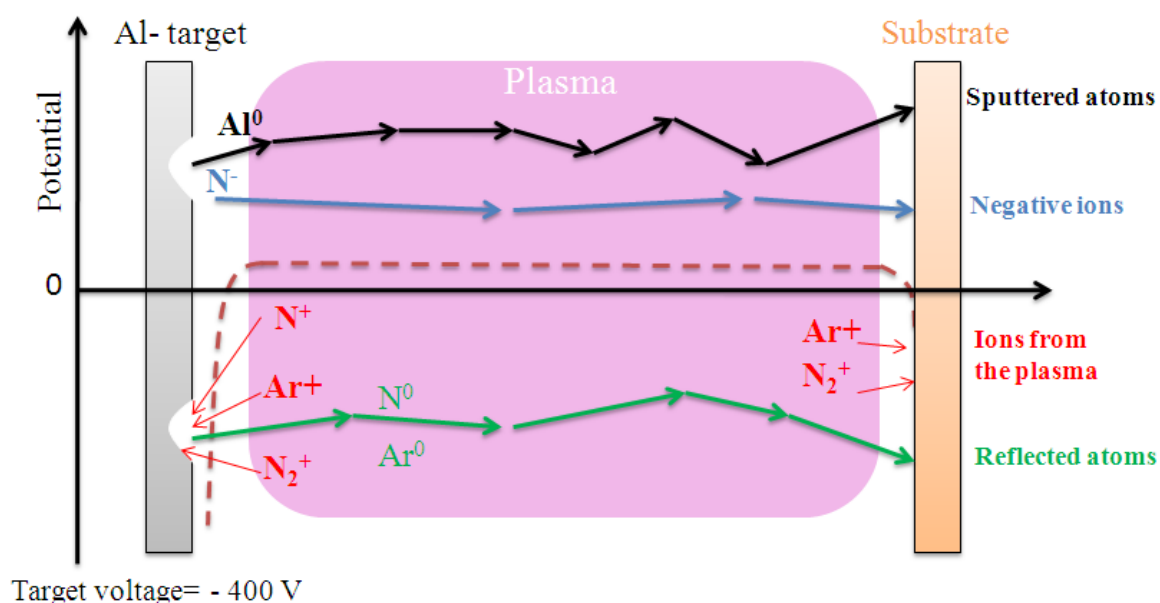


Fig. (2.1): Schematic diagram showing the different energetic species involve in the DC sputtering discharge, adapted from. [113]

The principle of sputtering operation is based on discharge plasma, in high vacuum background, by applying a difference of electrical potential between a cathode (usually where the source material, called “target” is placed) and the anode constituted by the chamber walls in presence of inert (e.g. Ar) and/or reactive gases (e.g. N₂, O). This induces ionization of part of the atoms in the gas phase. The discharge current controls the flux of positive ions (e.g.

Ar^+) impinging the target while the discharge voltage controls their kinetic energy. Thanks to bombardment of the target material by positive ions from the gas phase (ionized), several processes occur with varying probabilities depending on the discharge voltage. The target atoms sputtered from the target are emitted in all directions; some of them can condensate at the surface of the substrate to form a thin film. Then, the sputtering yield can be defined as the number of sputtered atoms per bombarding particle. In addition, impinging of the positive ions induces electron emission (called secondary electron emission) from the surface of the metallic target. This electron emission is described as a result of neutralization of the ionized ions. This neutralization process released an energy that can be transferred to the target's atoms and results in emission of some electrons to the vacuum. The secondary electron emission is of great importance in understanding the several processes happening inside the plasma and sustaining the discharge.[113-114] Other species are formed when highly energetic ions accelerated to the target and neutralize. These atoms experience collision with the target atoms leading to their backscattering towards the substrate. Other negative ions are generated near to the target's surface and accelerated cross the plasma towards the substrate with high energy equal approximately the target voltage. These very energetic negative ions show significant influence on the growth of deposited film.[114]

The term *reactive*, in reactive magnetron sputtering, is pointing to the gas composition of the plasma, when at least one of its components is reactive. Reactive sputtering allows to produce compound thin films resulting from the chemical reaction between the sputtered atoms and the reactive gas(es) during the condensation process. This is also accompanied by chemical reaction at the surface of the sputtering target. The term *magnetron* is referring to two magnets of opposite polarities placed under the target. The function of these magnets is to produce above the target surface a magnetic field parallel to the target surface and perpendicular to the electric field. Thereby, due to Lorentz forces, secondary electrons are forced to follow a complex trajectory and experience more collisions with the background gas before they can be collected by the anode. This will serve the ionization process to be more efficient and to sustain the plasma glowing. The electric field needed for the discharge process can be provided commonly by means of direct current (DC), pulsed direct current (pulsed DC), radiofrequency (RF) or High-power impulse magnetron sputtering (HIPIMS). Then, sputtering process can be named referring to the way by the plasma is discharging, e.g. DC-RMS, pulsed-DC RMS, RF-RMS, or HIPIMS, RMS standing for reactive magnetron sputtering.

The schematic of our reactive magnetron sputtering setup is described in fig (2.2). Argon (inert), nitrogen (reactive) and sometime oxygen gases can be used when it is needed. The type of gases and ratios between them are depending on the desired material composition in the final coatings, as well as the stoichiometry of its elements.

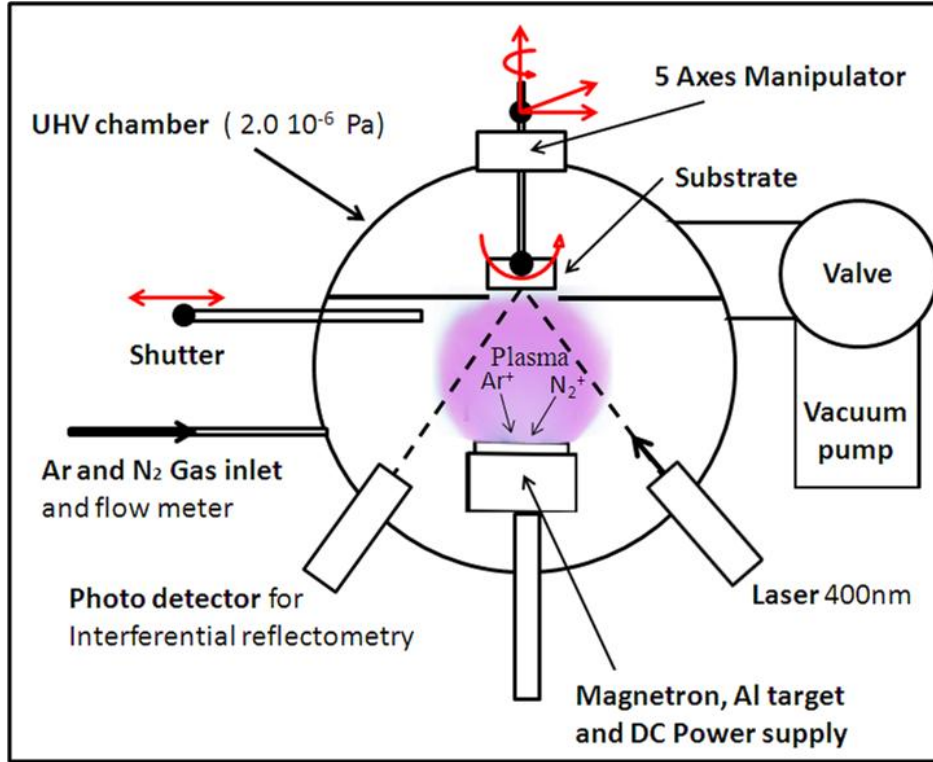


Fig. (2.2): Schematic diagram for our reactive magnetron sputtering experiment.

As we are interested in the preparation of AlN and Al(O)N coating, N₂ and O₂ have been chosen as reactive gases, and Al discs were used as target material. In case of AlN coatings, the sputtered Al atoms interact with nitrogen ions in the gas to form AlN on the substrate. The composition of the AlN coating is determined by the gas composition ratio Ar/N₂. Adjusting the argon and nitrogen gas flow rates have been achieved using MKS mass flow controller. The gas composition during this work is defined as $N_2\% = \frac{N_2}{(N_2 + \text{Ar})} \times 100$. The working pressure is controlled by the partial pressure of the gases resulting from an equilibrium between the individual gas flows and the pumping speed. A high vacuum base pressure of 1×10^{-6} Pa was obtained by using a turbo molecular pump (BOC EDWARDS EXT 255HI) coupled to a mechanical primary pump. The thin films were deposited sometimes using RF (Dressler, CESAR RF power generator) or direct current DC power supply. An aluminum disk (99.99% purity, neyco vacuum & materials) of 2 inch diameter was used as sputtering target for the AlN film preparation. For doped AlN films, a modified Al target was used, that

incorporates a thin bar of metallic Ce or Yb or both (99.9% purity, neyco vacuum & materials) in the case of co-doped samples. Appropriate relative surface areas between the RE and the Al part was defined, an example is shown in fig (2.3).

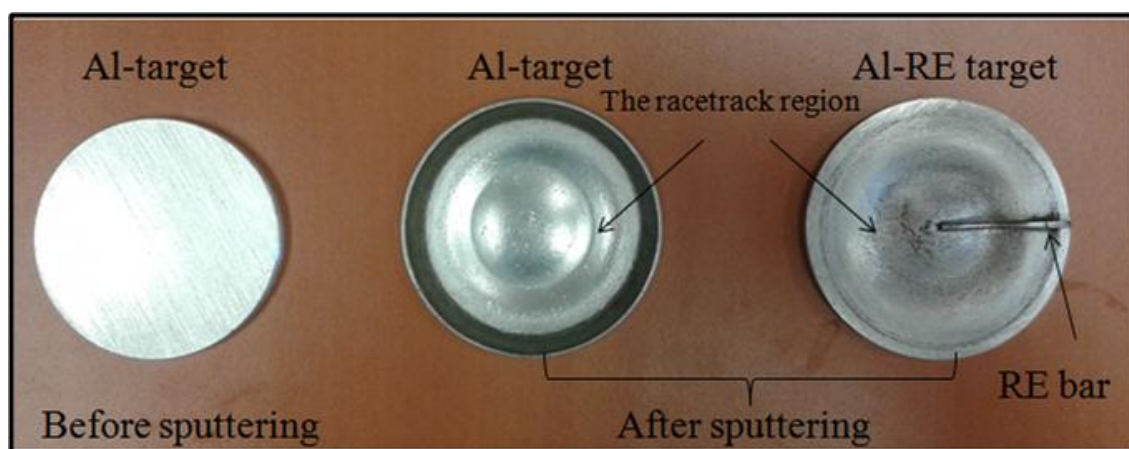


Fig. (2.3): Photo of the used Al and Al/RE targets.

The observed circular depth area in the middle of the sputtered targets is known as the racetrack region. This is a preferential sputtering area of the target resulting from the high plasma density along this path. The reason behind the circular shape is refereeing to the shape of magnetic field generated above the target due to the planar circular magnetron.

Silicon (100) and Sapphire (0001) substrates have been ultrasonically cleaned in ethanol and fixed at 5 cm distance from the target, facing the target axis. The deposition time was adjusted for each deposition condition and the films thickness was monitored *in-situ* by laser interferential reflectometry.

In sputtering experiment, several parameters should be considered and controlled in order to adjust and manipulate the growth mechanism of the coating layers. The most common sputtering parameters and their effect on the film processing are given in the following table (2.1).

Table (2.1): sputtering parameters and their effect on the plasma and film processing.

Sputtering parameter	Effect
Discharge current (A)	Flux of projectile ions to the target – sputtering rate
Discharge voltage (V)	Kinetic energy of projectile ions to the target – sputtering rate, energy of fast particles impinging the growing film
Composition of gas phase (%)	Film composition, flux of fast particles impinging the growing film
Working pressure (Pa)	Microstructure and morphology of the film
Substrate temperature (°C)	Microstructure of the film
Substrate bias (V)	Film microstructure

It has been well established that, the experimental parameters of sputtering strongly influence the film growth mechanism that modify the functional properties of the final product. For instance, the crystallites orientation can be modified by tuning the gas composition $N_2\%$. Fig (2.4) shows x-ray diffractograms AlN thin films deposited using different $N_2\%$ for the same total pressure. Obviously, the crystallites orientation, normal to the substrate is modified from (101) to (002) crystallographic planes of AlN parallel to the film surface by tuning the gas composition.

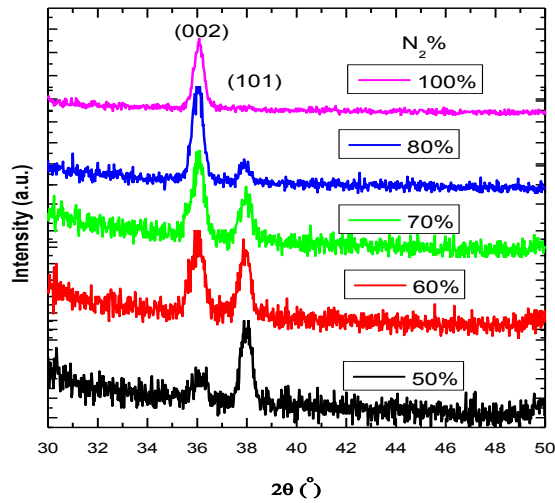


Fig. (2.4): XRD of AlN thin films deposited at different gas compositions $N_2\%$.

This clearly shows how the sputtering conditions are of great importance for manipulating the coating properties. Therefore, the strategy of our work is based on fixing all the experimental conditions but one to examine the influence of this parameter on the film properties. Most of samples have been prepared with 200 nm thickness and few of them with higher thicknesses according to each case.

A thermal probe has been established to measure the substrate temperature at different sputtering conditions. Fig (2.5) displays a schematic diagram of such thermal probe experiment and the incident/dissipating energy flux contributes in the self-heating of the substrate.

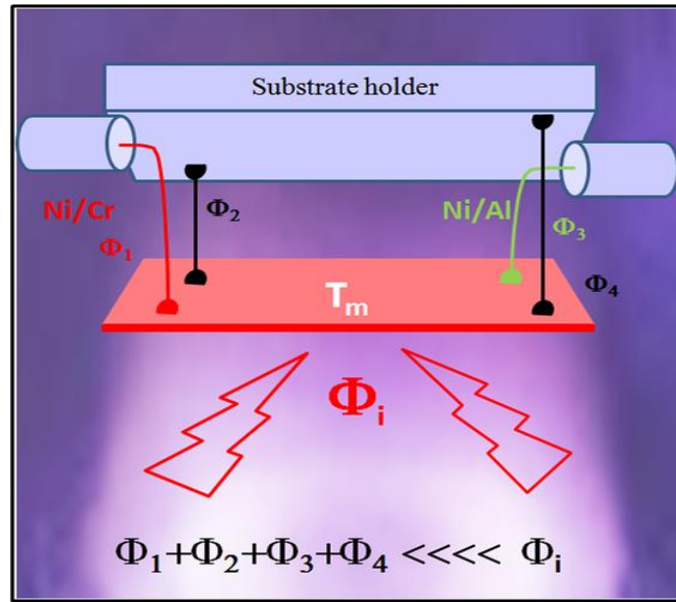


Fig (2.5): Schematic of the home made thermal probe. Φ_i corresponds to the incident energy flux while (Φ_1, Φ_3) and (Φ_2, Φ_4) correspond to the energy dissipated by the thermocouple and holding wires, respectively.

1.2-Thermal annealing of the thin films

A post-deposition rapid thermal annealing (RTA) was used to thermally activate the deposited RE-doped AlN thin films. The annealing process was performed under different atmospheres (nitrogen, argon or forming gas $N_2/H_2 = 90/10$) using an oven (RTA Jipelec Jetfirst). The films underwent RTA at 1000 °C for 5 min with rising temperature rate (400 °C/min) and cooling rate (250 °C/min).

2-Thin film characterization

2.1- Structural characterization

2.1.1- X-ray diffraction (XRD)

X-ray is considered as an electromagnetic radiation with very high photon energies (i.e. very short wavelength of few angstroms). Thanks to these very short wavelengths which are comparable to the size of atoms, X-rays are suited for probing the structural arrangement of atoms and molecules in a wide range of materials. When rays incident to a material, some photons are elastically scattered and deflected ‘diffracted’ from their original direction. These diffracted x-rays carry information about the atomic arrangement in the material. The diffracted waves from different atoms can interfere, and the resultant spatial intensity distribution is controlled by the atomic arrangement. Thus, X-ray diffraction (XRD) technique

is considered as a powerful tool to explore the crystal structure of materials. The atomic spacing of crystalline material can be also extracted from (XRD) data. In addition, the shape, intensity, peak width and position of the XRD signal can be used to extract information about the crystal size and the internal stress of sample. The physical concept behind XRD principle is based on Bragg's diffraction phenomenon. The distribution of the diffracted waves is governed by the Bragg's law:

$$2d \sin\theta = n \lambda, \quad (2.1)$$

Where d is the inter-planar distance, λ is the wavelength of the x-ray, θ the scattering angle, and n an integer representing the order of the diffraction peak. Fig (2.6) shows the ideal graphical representation for the Bragg's diffraction process.

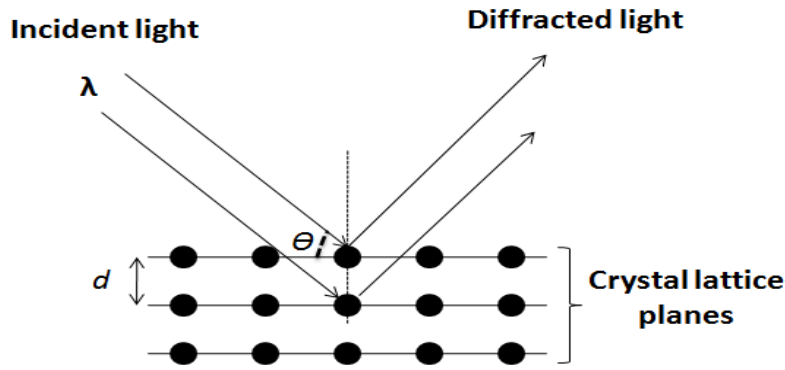


Fig (2.6): Schematic representation of Bragg's diffraction process.

The constructive interference of the diffracted rays occurs when the previous Bragg's condition, equation (2.1), is valid. Then, the inter-planar distance for specific crystallographic planes d can be estimated. The average size of crystallites can be also estimated from the XRD data by using Scherrer's equation:[23]

$$\text{Average crystallite size} = \frac{k \lambda}{\beta \cos\theta}, \quad (2.2)$$

where k is the dimensionless shape factor, λ the X-ray wavelength, β the line broadening at half the maximum intensity (FWHM) in radians, θ the Bragg angle.

The basic construction of an XRD apparatus (diffractometer) consists of a source of radiation (x-ray tube) followed by a monochromator to select the X-ray wavelength. Set of slits to adjust the shape and size of the x-ray beam are used to illuminate the sample with an X-ray beam of specific section. A sample holder is placed on a goniometer circle to control the

sample's center position with respect to the position of the incident x-ray and the detector. This allows accessing to different geometrical configurations of the measurements.

In this thesis, the crystal structure and growth orientation of the films were analyzed by X-ray diffraction (XRD) in a Bruker D8 Advance system with Cu K $_{\alpha 1}$ radiation ($\lambda = 0.15406$ nm) in Bragg-Brentano geometry. A LINXEYE XE linear detector was used that exhibits excellent filtering of K $_{\beta}$ radiation without the need of secondary monochromator. All samples were positioned on substrate holders and aligned with a reference plane of the holders. Holders were enabled to spin around their vertical axis during measurement with a total integration time of 1 hr.

2.1.2- Transmission electron microscopy (TEM)

TEM is an electron microscopy technique used for material imaging and diffraction purposes. Electrons are the main probe used in the processes. The TEM principle of work is based on the transmission of electron beam through an ultra-thin specimen. Interactions between these transmitted electrons and the specimen bring specific information about the microstructure, the atomic arrangements, the crystallographic and sometimes the morphology of the investigated materials. The main components of a TEM apparatus are a source of electrons (electron gun), a sample holder, electromagnetic lenses and detectors. Set of electron lenses and apertures are placed before and after the sample holder to control and manipulate the emitted and the transmitted electron beams. All the setup has to be operated under high vacuum conditions in order to avoid scattering of the electrons by the background gas. The schematic diagram of the ray path in TEM is presented in fig. (2.7a). The electrons are generated by electron gun and accelerated to the required high energy directed to the **specimen**. Then, the transmitted and scattered electrons are collected by **objective lens** forming a diffraction pattern (DP) in the **back focal plane** and **intermediate image** in the image plane. Therefore both the image and the diffraction pattern (DP) are present simultaneously in the TEM. Switching between the two modes (image and DP) can be achieved by changing the strength of **the intermediate lens** and inserting aperture called (**objective aperture**) in the back focal plane in case of image mode or inserting aperture called (**SAED aperture**) in the image plane in case of DP mode.

In imaging mode, the position of the objective aperture can be used to select different imaging modes (e.g. bright field or dark field) as shown in fig (2.7b, c). In **bright field (BF)** mode the objective aperture is placed such that allows only the transmitted beam to pass and form the

image. Whereas, in the case of **dark field (DF)** the transmitted beam is blocked and one or more diffracted beams are allowing to pass.

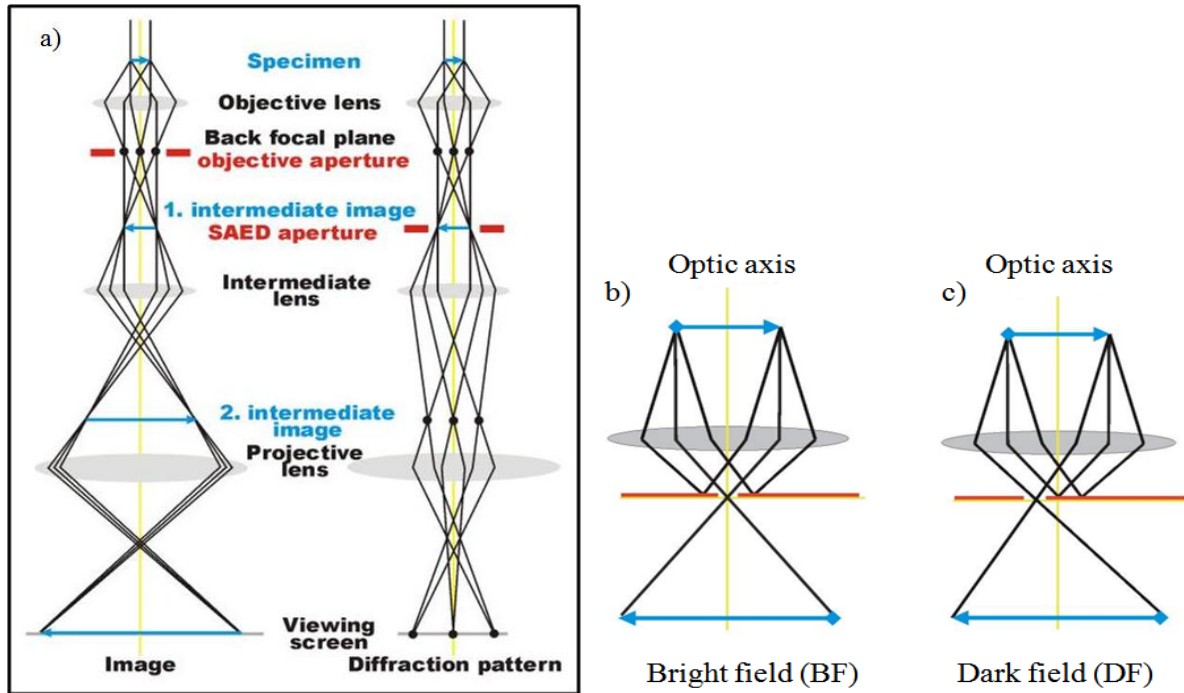


Fig. (2.7): Schematic diagram showing cross section view of the ray path in a) all the TEM column, b) bright field mode c) dark field mode. [115]

In this work, details of the microstructure were investigated using a JEOL ARM 200-Cold TEM equipped with a field-emission gun (FEG) fitted with a GIF Quantum ER. Most of samples have been pre-prepared in Saarland University (Saarbrücken, Germany) with a focused ion beam (FIB)-scanning electron microscope (SEM) dual beam system (FEI Helios 600) using the ‘in situ’ lift-out technique.

In the following section, example images obtained with of the abovementioned tools of TEM applied to one of our AlN samples are presented. **Bright field and dark field** images and **SAED** are shown in fig. (2.8). It can be observed the difference between the bright and dark field images from the same region. In the dark field image, the bright regions point to the crystallites of same orientation direction to (002) after a diaphragm has been placed to select only this orientation on the SAED. This helps to identify the grains that exhibit the same orientation direction, as well as confirms the growth directions of the prepared AlN films. The SAED itself was obtained by placing a diaphragm limiting the electron-matter interaction to a specific volume of the Bright field image.

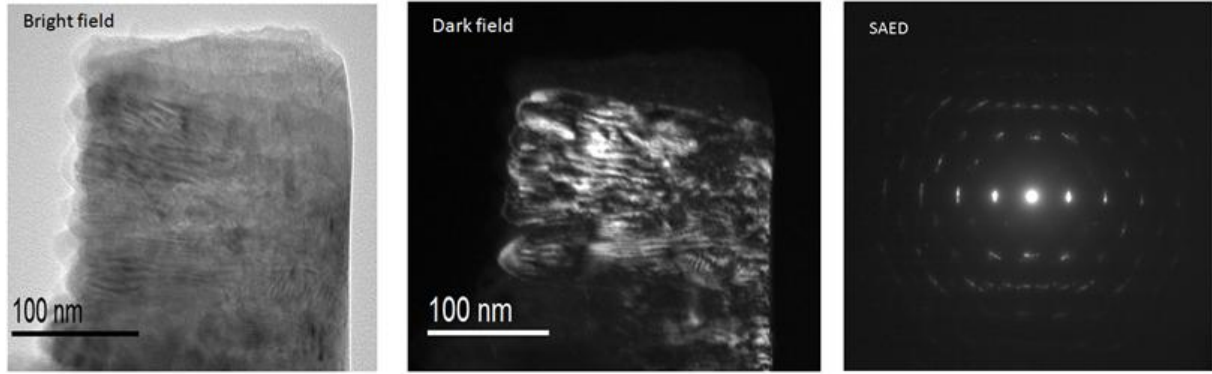


Fig. (2.8): Bright and dark images as well as SAED pattern of a prepared AlN thin film sample.

The SAED pattern exhibits small bright spots representing the diffracted electrons beam from the crystal lattice planes.

Regarding the composition analysis, the *Energy-Dispersive X-ray Spectroscopy (EDX)* embedded to the microscope can be used for semi-quantitative composition analysis for our samples. Energetic electron beam is used to penetrate the sample and interact with the core electrons by exciting them to upper energy levels. Then, the relaxation of these electrons results in characteristic x-ray emission with fingerprints of each element. The EDX spectrum of an Ce-doped Al(O)N sample is shown in fig (2.9).

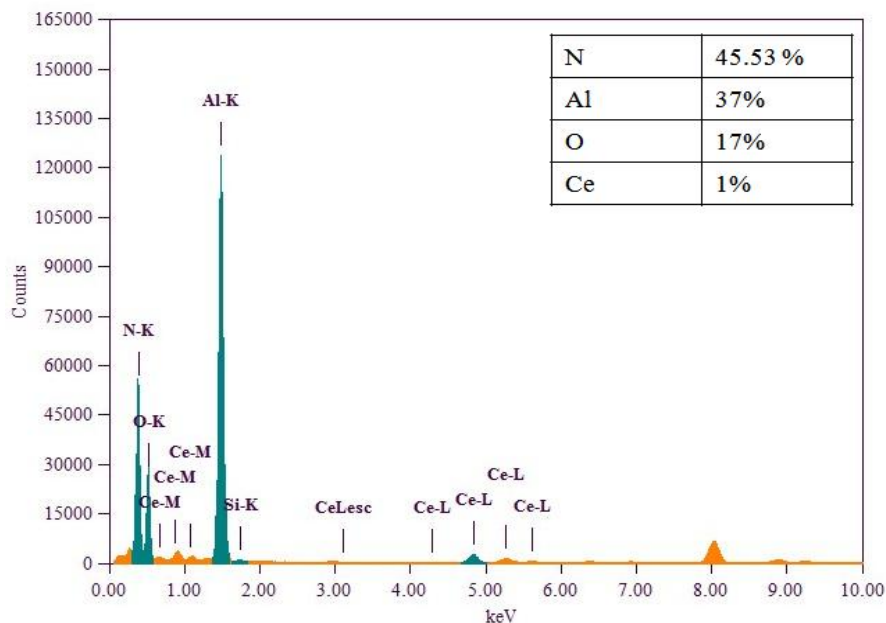


Fig. (2.9): EDS spectrum of Ce-doped Al(O)N sample.

Then, a qualitative analysis for the area under each peak is corresponding to the amount of each element in the material as shown in the inset table, fig (2.9), for the atomic percentage of (N, Al, O and Ce) elements.

In addition, the inelastically scattered electrons in TEM are used in **Electron energy loss spectroscopy (EELS)**. EELS is a technique dealing with measuring the distribution in energy loss owing to inelastic scattering interactions during exposure of the specimen to a beam of electrons with specific kinetic energy. The amount of measured energy loss provides useful information about the material composition, valence and bonding system, material thickness, and bandgap...etc. Using the advantages of electron beam manipulation in TEM such as focusing to very high spatial resolution, EELS analyses of very small volume of material can be implied.

A typical EELS spectrum can be divided into three main regions, see for example an EELS spectrum from an AlN sample in fig (2.10).

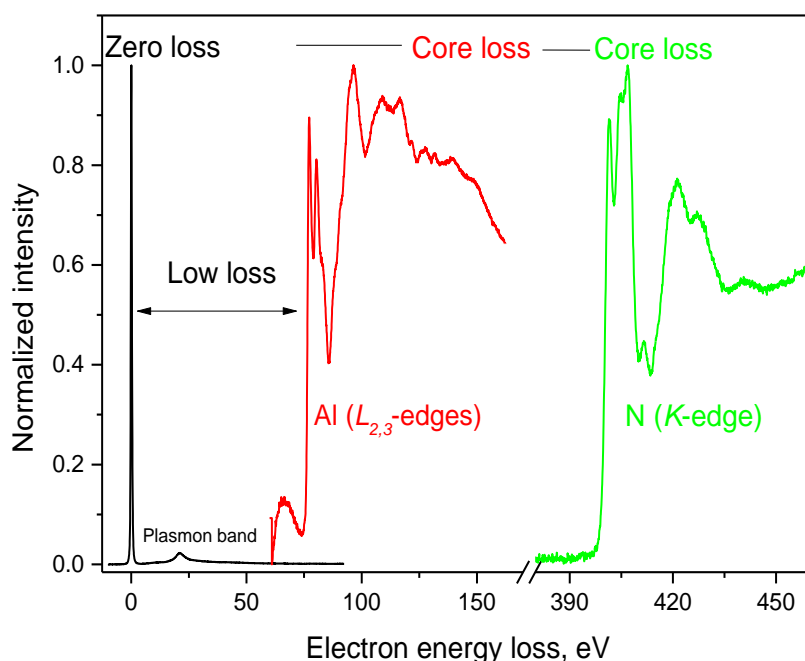


Fig. (2.10): Typical EELS recorded from an AlN sample

Each region falls in specific energy loss range and contains different information about the material.

The first region occurring around 0 eV and characterized by a very narrow peak (0.2-2 eV width) is called the *zero loss* peak. This peak represents the amount of electrons transmitted without energy loss.

These electrons didn't undergo inelastic interaction with the specimen. Narrower width of this peak means better spectrometer resolution and small energy dispersion of the primary electrons.

The second region is called *low-loss region*. This region is typically located between 2 and 100 eV and results from inelastic scattering interactions of electrons with conduction or valence band electrons. Under specific experimental conditions, useful information about the electronic structure of material can be extracted from this region. The most predominant band results from plasma resonance of the valence electrons and called bulk plasmon peaks. This appears when the electron beam interacts, and excites the weakly bound outer shell electrons. **The third region**, the *high-loss region* (e.g. *core-loss*) (ionization edges) contains information about the electrons interacting with core shell electrons of a specimen atom. This core shell interaction causes excitation to the higher unoccupied levels. The EELS signal in this region appears in form of edges and the fine structure of these edges carries information about the chemical bonding with the surrounding.

In this work, the Electron Energy Loss Spectroscopy (EELS) coupled to the TEM instrument has been mainly used to investigate the oxidation states of Ce ions in AlN thin films. For the acquisition of EELS spectra, an acceleration voltage of 200kV, an emission current of 15 μ A and an energy dispersion of 0.05eV/ch were employed. All EELS spectra were recorded in image mode, with an energy resolution of 0.55eV defined by the full width at half maximum (FWHM) of the zero loss peak.

2.1.3- Rutherford Backscattering Spectrometry (RBS)

RBS is a nuclear analytical technique used to measure the composition of materials. In this technique, a primary ion beam consisting of protons or alpha particles of high energy interact with a sample and is backscattered by the material. The energy distribution of backscattered ions is measured. The backscattering energy depends from two factors: the backscattering cross-section of the primary ion by the elements constituting the sample and the stopping power of the sample electrons. The backscattering cross-section increases with the mass of the nucleus of target atoms and defines the backscattering energy. Elements with different mass scatter ions with different energies, generating separated peaks in the RBS spectra. The peak intensity being proportional to the number of events, it can be used to calculate the elemental composition. On the other hand, the stopping power of electrons decreases gradually the kinetic energy of the primary ions as they penetrate into the material. Therefore, in-depth backscattering occurs at lower energy than at the extreme surface.

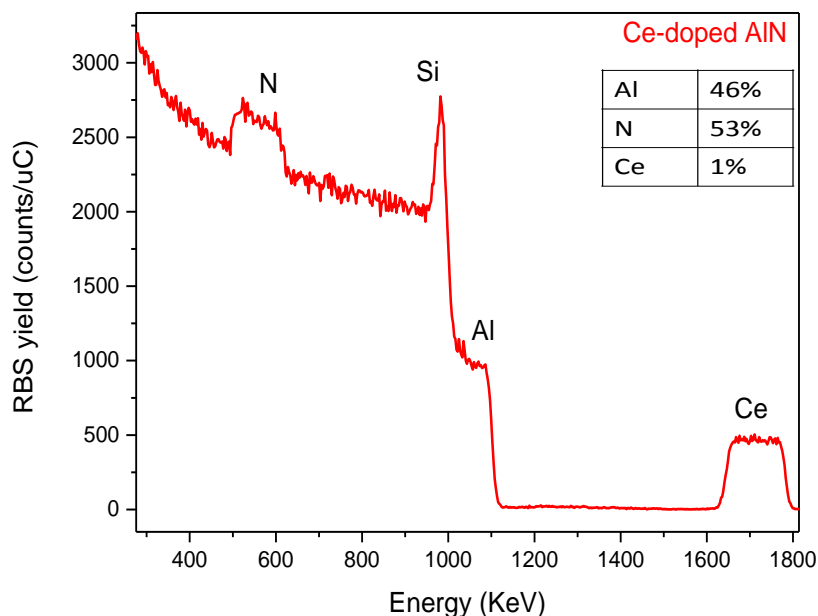


Fig. (2.11): RBS spectra of Ce-doped AlN thin film.

Consequently, instead of sharp peaks RBS spectra exhibit a plateau for each element whose width and shape is characteristic of its composition profile. The energy spectrum undergoes simulation in order to extract information about the composition of the material with depth resolution as show in fig (2.11).

In this thesis, the compositional analysis was performed by Rutherford backscattering spectrometry (RBS) with a 2 MeV He^+ beam. The experiments were performed with the 5MV accelerator available at *Centro de Microanálisis de Materiales* (CMAM) from Universidad Autónoma de Madrid (Madrid, Spain).

2.2- Optical characterization

2.2.1- Fourier transform infrared spectroscopy (FTIR)

FTIR is a spectroscopic technique dealing with the optical absorption of substances in wide range of IR spectrum. A typical FTIR spectrometer consists of an IR source, interferometer, sample holder, detector (amplifier and analog-to-digital converter) and computer. The generated radiation from the source passes the sample through the interferometer to the detector. Then, the signal is amplified and converted to digital. After that Fourier transform analysis is performed. FTIR is a very useful tool to obtain information about the vibration frequencies of the bonding system of materials. These frequencies are fingerprints for the qualitative analyses. The typical IR region used in FTIR is from 400 cm^{-1} to 4000 cm^{-1} , which

is corresponding to photons with enough energy to excite group of atoms to vibrate with respect to their bonds. These vibration motions consist of vibrational transitions with distinct energies. Therefore, each molecule with different type of bonds absorbs certain wavelengths. Thus, FTIR is widely used in identification of unknown materials. The main component of an FTIR apparatus is the interferometer. The most common interferometry configuration used in FTIR is the Michelson interferometer. Fig (2.12) displays the basic component of Michelson interferometer. It consists of two mirrors (moving and stationary), beam splitter, sample holder and detector. The incident light shines on the interferometer and is split into two beams by a beam splitter. One beam is directed to a stationary mirror and used as a reference. The second beam is directed to a mirror moving at specific speed. The reflected two beams recombine at a specific point at the beam splitter and are then directed to the detector. As this mirror moves, each wavelength of light in the beam is periodically blocked and transmitted by the interferometer, due to wave interference. Different wavelengths are modulated at different rates, so that at each moment the beam coming out of the interferometer has a different spectrum. Then, a computer processing (Fourier transform) is applied to obtain the absorption spectrum of the material.

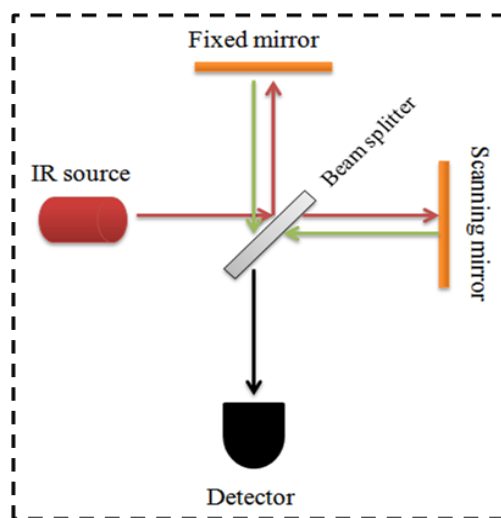


Fig. (2.12): Schematic diagram of a Michelson interferometer.

For example, FTIR spectrum of prepared AlN thin film is displayed in fig (2.13). The spectrum consists of a main peak at 681 cm^{-1} and small peaks from 1050 to 1400 cm^{-1} corresponding to the different stretching vibrations of Al-N bonds and some other small peaks around 1650 and 3000 cm^{-1} corresponding to the C-O and H-O bonds vibration due to the surface adsorption of CO_2 and water vapor from the atmosphere, respectively.[116]

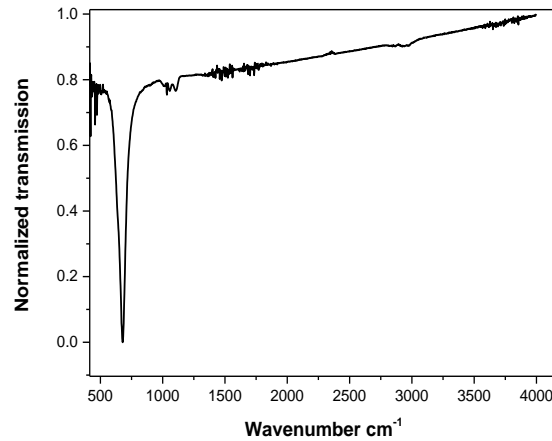


Fig. (2.13): FTIR spectrum of prepared AlN thin film.

2.2.2-Ellipsometry

Ellipsometry is an optical technique measuring the change in the polarization of transmitted or reflected light from a material. This polarization change is represented as amplitude ratio, Ψ , and phase difference, Δ , which are linked to the dielectric properties of a thin layer of material. Therefore, ellipsometry is used to determine the dielectric functions, thicknesses, roughness, anisotropy and crystalline nature.....etc. Spectroscopic ellipsometry (SE) is considered as an indirect method as it is based on measuring the ellipsometry parameters (Ψ , Δ), then propose a model and fit the data till obtaining the best fit by modifying the model. After that, several informations about the material such as the dielectric constants, the roughness, thickness and uniformity of a thin film can be obtained. The experimental configuration of ellipsometry can be found in two modes: transmission or reflection. The basic components of Experimental setup (reflection mode) are shown as in fig (2.14).Simply, a beam of light emitted from light source (lamps) falls on the sample after passing through a polarizer. After the reflection (or transmission) of the light beam from the sample, it reaches to the detector via passing through a second polarizer called "analyzer". The change in the phase difference and the amplitude of the incident polarized light after reflection from the sample are recorded.

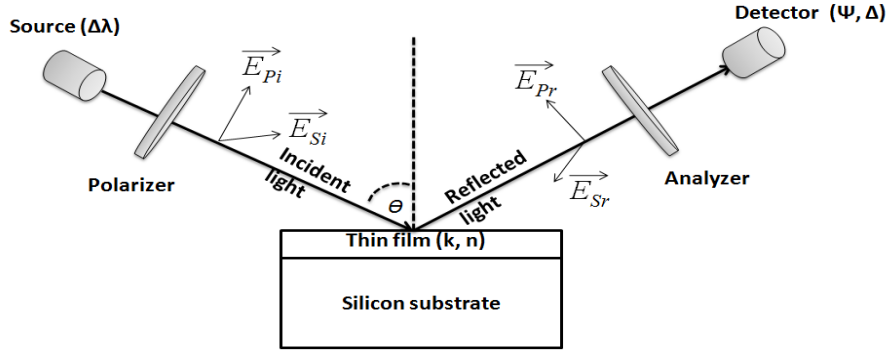


Fig. (2.14): Experimental setup of ellipsometry measurement in reflection mode.

In this thesis, a Woollam M-2000 ellipsometer has been used in reflection and transmission configuration mode. For instance, the UV-Vis analysis "transmittance" has been performed by setting the ellipsometer to its transmission mode at normal incidence. The dielectric properties of the films have been determined by fitting the modeled data to its measured data assuming the simple three-phase optical model: air/isotropic and uniform film/ substrate. The optical constants (n, k) of substrates that used in fitting process were taken from the library of Woollam WVase software. The measured and fitted ellipsometry parameters (Ψ, Δ) for a thin film of AlN are presented in fig (2.15). It is observed that the proposed model exhibits good fit to the measured data, see Annex A for more details.

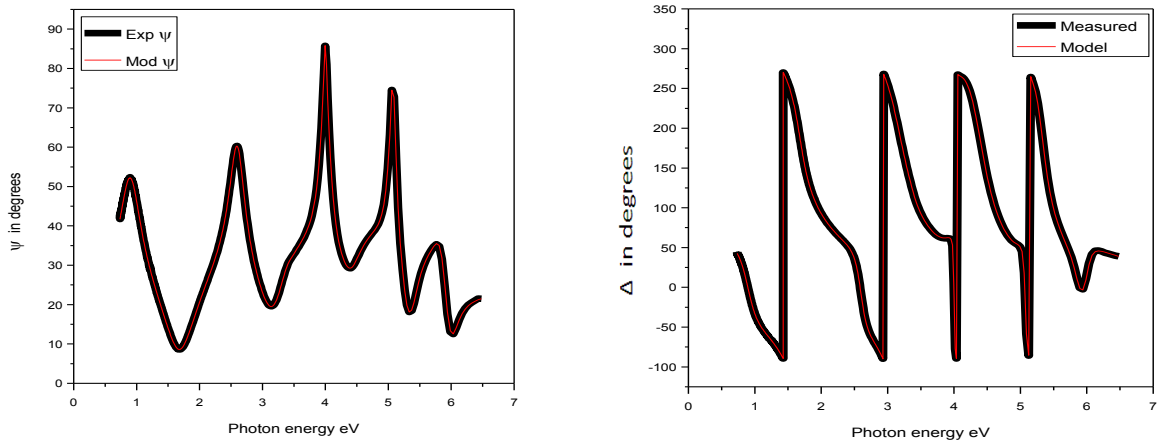


Fig. (2.15): Measured and fitted ellipsometry parameters (Ψ, Δ).

2.2.3- Photoluminescence (PL) spectroscopy

❖ Principles

PL Spectroscopy is an efficient technique in optical materials studies, where the material can be subjected to excitation by photons. PL is considered as a powerful tool to investigate the electronic structure of materials. PL is a spontaneous emission of light when an optical material undergoes optical excitation. Then, the emitted light can be collected and analyzed by several ways such as:

- Spectrally: as a function of the emission wavelength (PL) or as a function of the excitation wavelength (PLE)
- Spatially: as a function of the emission or excitation angles.
- Temporally: as a function of time after excitation; *Time-resolved PL (TRPL)*
- As a function of temperature; *Low temperature PL (LTPL)*
- As a function of excitation power

➤ PL measurements

The PL mechanism is dealing with exciting, giving energy to, some electrons to move from the ground state to excited state (electronic states in the material with different specific energies). After a characteristic time, the excited electrons relax to the ground state and release the absorbed energy in form of light emission (radiative process) and/or heat dissipation (nonradiative process). It is worth to mention that, the optical excitation energy should be equal at least the energy difference between the two transition states. In semiconductor materials, the radiative transition can occur between the valence and conduction bands with energy difference equal to the bandgap or, alternatively, the radiative transitions involve localized defects and impurities. Therefore the PL experiments can help in the identification of specific defects and impurities and to define the characteristics of the bandgap.

The radiative and nonradiative recombination rates determine the PL efficiency of the optical material. Based on the fact that the nonradiative recombination rate is strongly affected by the system temperature, the competition between radiative and nonradiative rates can be studied by analyzing the measured PL intensity under different temperatures, as shown in fig (2.16a). By plotting the PL intensity as a function of temperature, a temperature-dependent PL curve

can be obtained. Then, the obtained data can be fitted, fig (2.16b), with exponential functions using Arrhenius equation[117-118] in order to estimate the so-called activation energy(s).

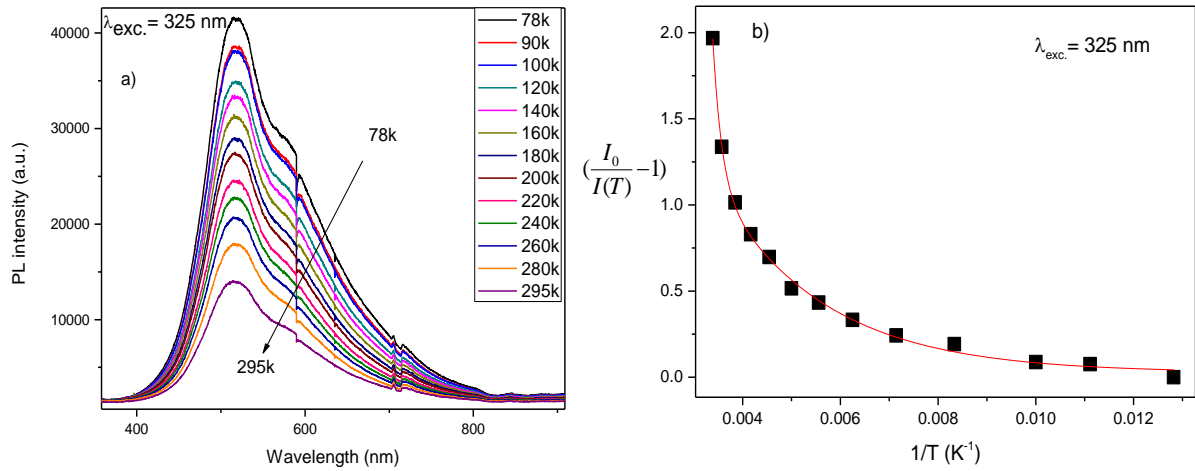


Fig. (2.16): a) PL spectra as a function of temperature and, b) is $(\frac{I_0}{I(T)} - 1)$ versus T^{-1} for Arrhenius guiding of 1% Ce-doped Al(O)N sample performed by excitation wavelength 325 nm.

Steady state PL experiments have been carried out using a continuous wave laser excitation setup. The samples were excited by a continuous wave (cw) IK series He-Cd laser (325 nm, 25 mW) and 266 nm line of solid state Nd:YAG cw laser(25 mW, model FQCW 266-CryLaS). Set of optical components (reflection mirrors and focused lenses) were used to guide and focus the laser beam on the investigated sample. The luminescence from the sample was collected and focused onto the entrance slit of the spectrograph (iHR320) after passing through interference filter to block the laser beam. The spectrograph contains 3 kinds of gratings with different densities of grooves. The dispersed light was collected using a charge coupled devices CCD detector (syncerity CCD). The experimental setup of the PL is shown in fig (2.17).

In case of **low temperature PL measurement (LTPL)**, samples were paste on holder attached to cold-finger in opened-cycle N₂-cryostat. The samples can be cold down to 77 K and the temperature can be controlled by heat controller till 298 K. The cryostat was pumped down to 1×10^{-3} torr.

In case of **power dependence PL experiment**, set of neutral density filters are used in front of laser beam allowing us to attenuate the laser power.

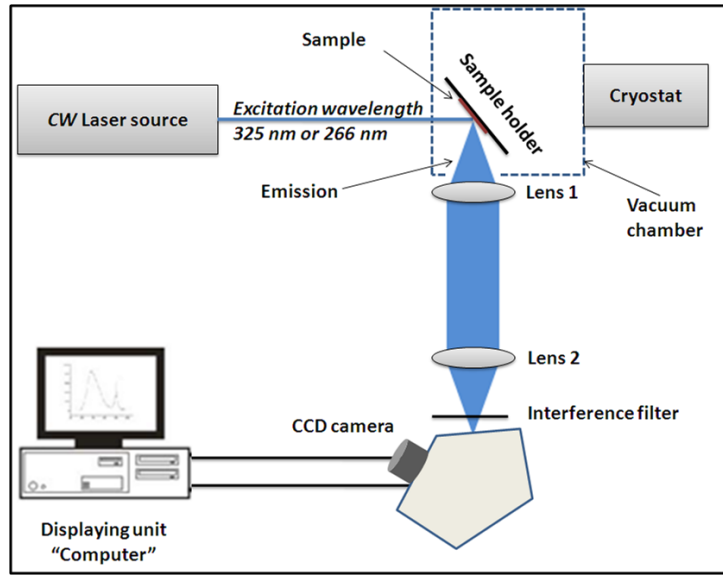


Fig. (2.17): Photoluminescence experimental setup for room and low temperature measurements.

➤ Time resolved photoluminescence (TRPL)

Photoluminescence kinetics is analyzed by studying the time dependence of the PL intensity. The method is called time-resolved photoluminescence (TRPL). The careful probing of the rise and decay of PL intensity with time results in a time-dependent PL signal. Fitting the decay part of the curve can lead to quantitative values of the recombination rates. Examination of the rise time may provide information about the energy transfer mechanisms. In this work the average fluorescence lifetimes (τ) have been estimated using the following equation:[119-120]

$$\tau = \frac{\int_0^{\infty} t I(t) dt}{\int_0^{\infty} I(t) dt}, \quad (2.3)$$

where $I(t)$ is the intensity at time t . Practically speaking, the excitation source in TRPL experiment should be pulsed with pulse duration and repetition rate less than the investigated dynamics of the material, as depicted in fig (2.18). This is in order to correctly de-convolute the contribution of the excitation source signal from the detected signal corresponding to the dynamics in the material. In addition, it is favorable that excitation pulse is not too intense in order not to saturate the excited state population.

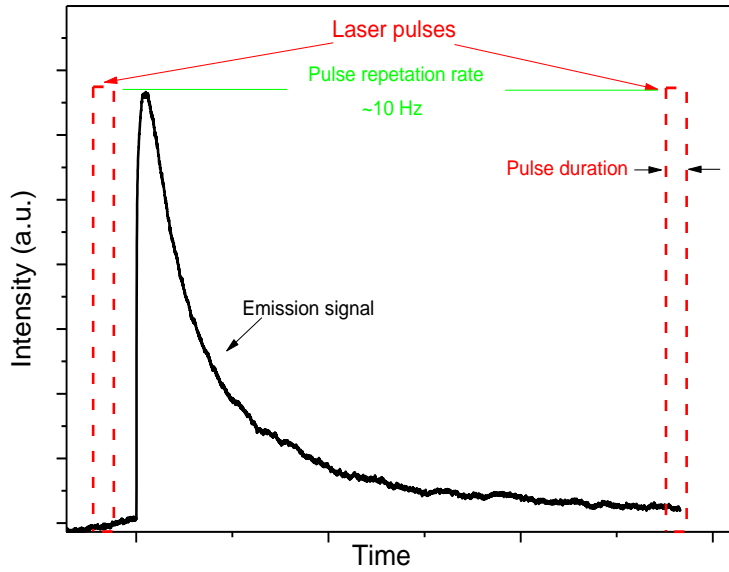


Fig. (2.18): Schematic figure showing the dynamics parameters of time resolved photoluminescence experiment.

In TRPL experiment, the samples were pumped by the 355 nm line corresponding to the third harmonic frequency of a Nd:YAG pulsed laser. The laser pulse was characterized by a repetition rate of 10 Hz, pulse energy ~ 10 mJ and pulse duration 10 ns. The emitted light was collected and focused on a monochromator (model Triax 190) equipped with photomultiplier tube (PMT), as shown in fig (2.19).

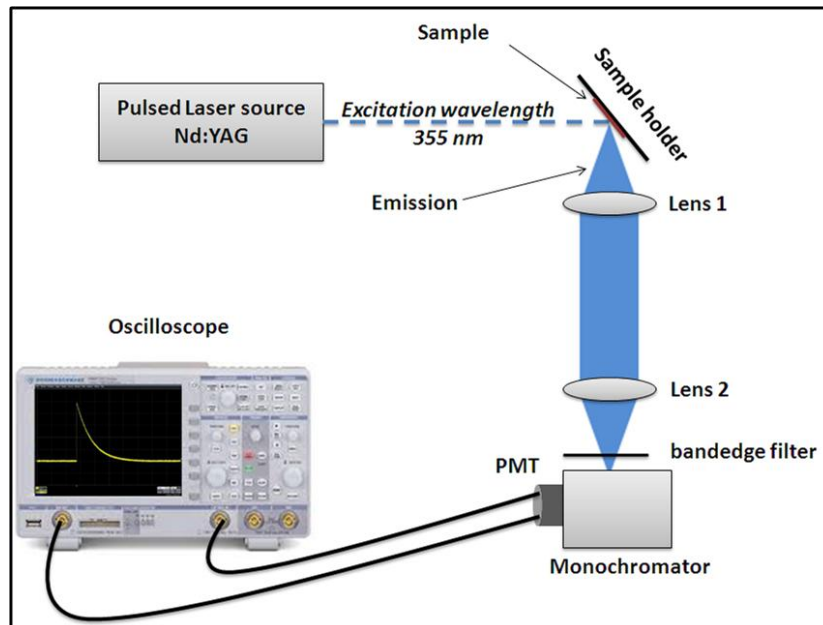


Fig. (2.19): Time resolved photoluminescence experimental setup.

The resolution of the setup is equal to 1 ns, corresponding to the transit time of electrons in the PMT. The signal is analyzed by a GHz Oscilloscope. A band edge filter is placed in front of the monochromator to cut the excitation wavelength. The monochromator is used to analyze the rise and decay time signal at a given emission wavelength. An Oscilloscope was used to record the detected signal in time scale. The PMT converts the optical signal to electrical current corresponding to the PL intensity. Then, the current (I) induces a voltage difference (V) by passing through a resistance (R) following Ohm's relation ($V=IR$). This voltage difference is measured and displayed on the oscilloscope's monitor analog to the PL intensity. Based on that, for samples with low PL intensity, higher resistance can be used to enhance the signal/noise ratio (S/N). On the other side, the response of the PMT is proportional to the characteristic response time τ of the internal capacitance C ($\tau=RC$). This means that, increasing the resistance to enhance S/N ratio results in increasing the characteristic response time τ as well. This will lead to increase the lowest detection limit of time scale of the system. Thus, samples with decay times shorter than the characteristic response time τ of the system cannot be determined due to the overlapping between the two decay times. Therefore, it is important to compromise between the S/N ratio and the characteristic decay time of the system with respect to the decay time of sample, especially in samples with low PL intensity and fast decay rates. In addition, the S/N ratio can be strongly improved by accumulating and averaging the detected signal up to hundreds of times.

➤ **Photoluminescence excitation (PLE)**

In order to explore the optical excitation mechanism of luminescent material, photoluminescence excitation (PLE) experiment is considered a useful tool in this regard. PLE is a specific type of photoluminescence experiment, in which the electronic levels of the material can be probed. In such experiment, the excitation wavelength is varied and the emission intensity is monitored at certain emission wavelength. The bands in the PLE spectra can be considered as absorption bands that contribute in excitation of certain emission wavelength.

The experimental setup of PLE is similar to the PL setup with some modifications as depicted in fig. (2.20). A xenon Lamp with broad emission spectrum is used as excitation source. Two monochromators are used, one (called excitation monochromator) works in scanning mode to disperse the excitation light to separate successive wavelengths. The second is called emission monochromator and adjusted to detect only the monitored emission wavelength.

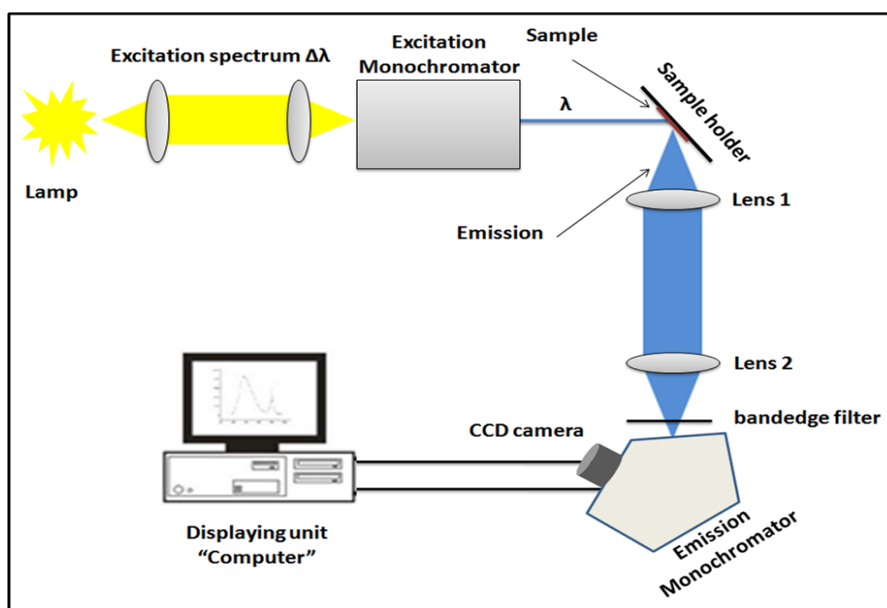


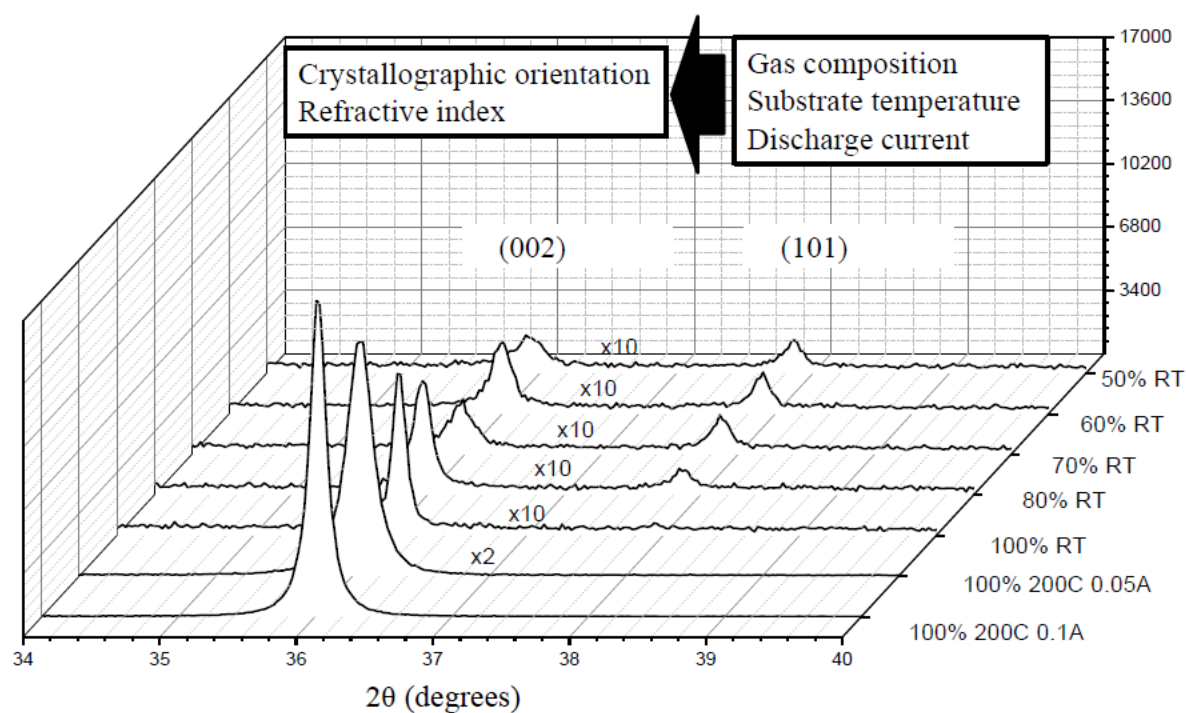
Fig. (2.20): Photoluminescence excitation experimental setup.

The PLE experiment was performed using Fluorescence Steady State Spectrofluorometer (Fluorologhoriba). A 450 W Xe lamp is used as excitation source. The light from the Xe lamp passes through a scanning monochromator, and then falls onto the investigated sample. The luminescence light from sample is collected and focused on the emission monochromator coupled with a silicon based CCD camera for light detection. It is worth to mention that all the spectrometers, used in this work, have been calibrated by quartz tungsten-halogen lamp.

Chapter III

Synthesis and characterizations of AlN thin films

Graphical abstract



Abstract

Although the main purpose of this thesis is to investigate the optical behavior of rare earth-doped AlN thin films, it is convenient to begin the study by having some practical experience about the host "undoped AlN" properties before the doping step. It is really important to explore the structure and the optical properties of prepared AlN thin film to be used as a reference and compare the changes after embedding the RE. Therefore, this chapter is dedicated to examine the structure and the optical properties of AlN thin film prepared by reactive magnetron sputtering technique. The strategy of this chapter will be as follows: First, brief introduction on the correlation of the sputtering conditions and the functional properties of AlN is given. Secondly, the correlation between the sputtering conditions, the crystallographic orientation, the morphology, the microstructure and the optical properties will be discussed. Third, the optimum experimental conditions that will be used during this work are presented. Finally, chapter's conclusion is stated.

1-Introduction

It has been found that sputtering conditions have a strong impact on the functional properties of AlN films.[121-123] For instance, the residual stress of AlN films is influenced by the total pressure such that the films usually undergo stress transition from compressive to tensile mode when the gas pressure is increased.[124] Hardness and elastic modulus of AlN films have been found to be affected by the total pressure as well.[125] Moreover, the surface roughness that has a direct influence on the performance of the surface wave propagation in acoustic wave devices is also affected by the sputtering conditions. Takeuchi et al.[126]demonstrated that increasing the sputtering power leads to rougher film surface. Furthermore, the optical and acoustic performances of AlN films are strongly depending on the crystallographic orientation. Taniyasu et al.[40] found that the UV emission intensity from AlN films is improved by 25 times in a-plane AlN configuration rather than c-plane configuration. In contrast, Zhang et al.[127] showed that c-axis is required for high d_{33} piezoelectric coefficient. Lobl, et al.[128] further reported that highly c-axis oriented AlN also provides strong piezoelectric coupling needed in SAW devices. Thus, producing AlN with high texture degree deposited at reduced temperature is required from a technological point of view. The relative degree of preferred orientation among the crystal planes can be expressed by using the texture coefficient.[129-130] This method takes into account the standard intensities of the crystallographic planes compared with the measured intensities of the grown

samples and used to confirm the preferred orientation of one plane over the others. For deep further analysis of the crystal quality, rocking curve measurement can be used as useful tool to indicate the perfection of the crystallographic orientation along a specific plane.[131-132] Therefore, understanding the correlation between the sputtering conditions and the preferred orientation of AlN thin film has established itself as an important topic of interest in research.[133] Currently, *c*-axis oriented AlN films are intensively studied for use in opto-acoustic devices as they exhibit optical and acoustic properties similar to those of single-crystal AlN films.[132] Thus, a comprehensive study about the influence of growth conditions on microstructure development in AlN thin films is one of the objectives of this chapter.

The manipulation of optical properties of this optically transparent material represents an important challenge for future applications, especially in optical quantum circuits. Three functional properties are of primary importance for this purpose. First, *c*-axis out of plane orientation of AlN thin film is essential for exploiting its largest second order nonlinearity for wavelength conversion and electro-optical effects. Second, the high ordinary refractive index (typically 2.1) of AlN deposited on Si wafer is a prerequisite for realizing low loss in silicon integrated AlN photonic circuits.[42] This high refractive index allows to strongly confine the light for long distance leading to the emergence of a non-linear optical effect on chip scale.[12] Third, the wide range of AlN transparency (bandgap close to 6 eV) can be exploited for wide operation band devices from UV to IR wavelengths. Combining the above features together, AlN is an excellent candidate for integrated nonlinear optics.

In this regard, this chapter is devoted to obtain highly textured AlN films deposited on silicon and sapphire substrates. In addition, manipulation of AlN optical properties, in particular, the optical constants; extinction coefficient "*k*" and refractive index "*n*" will be discussed. The optical anisotropy properties of AlN thin films will also highlighted.

In this chapter, we mostly present results related to the growth of AlN using reactive DC magnetron sputtering but conclude with results obtained using reactive RF magnetron sputtering to serve as a basis for next chapters. The first allows a good control on the electrical parameters during growth enabling to finely correlate the microstructure to the growth conditions but, with the DC power supply used, the maximum power dissipated by the target was rather low, leading to low deposition rates. Hence, based on previous works, RF sputtering was finally selected as a method of choice for the growth of RE-doped AlN films although it is difficult to extract precisely the influence of the electrical parameters on the

microstructure development without calling to advanced plasma characterization tools in this case. A comparison between the properties obtained using these two methods will validate this approach.

2-Sputtering conditions

During this work different sputtering parameters have been screened in order to explore the correlation between these parameters and the film growth mechanisms. In order to probe the influence of each sputtering parameter on the growth mechanisms of the film, set of samples were prepared such that all the parameters are kept constant and changed only the one under investigation. Such dedicated study brought massive information that enhanced our understanding of the correlation between the processing and growth of AlN. Herein, we present one series of this study concerning the influence of sputtering gas composition on the crystallography and microstructure as well as the optical properties of AlN coatings. Table (3.1) summarizes the experimental sputtering parameters in DC discharge mode that used during this study.

Table (3.1): contains the sputtering conditions used in the present study with DC discharge mode.

Sputtering parameters	DC-mode
Gas ratio ($N_2/Ar+N_2$)	50 to 100%
Target-substrate distance	5 cm
Discharge Current	0.05 A, 0.1 A
Discharge Voltage	320-420 V
Discharge power	18- 20 W
Base vacuum	1×10^{-6} Pa
Working pressure	4.4 mtorr
Substrate heating	RT, 200 C
Deposition time	4 hr

2.1- Crystallographic orientations

X-ray diffractogram (XRD) has been used in order to determine the preferential crystallographic orientation of AlN thin films. Figure (3.1) shows the X-ray diffractograms of the AlN thin films deposited on (100) Si and c-sapphire substrates prepared at total pressure 4.4 mtorr for various compositions of the gas phase $N_2\%$ under DC sputtering mode.

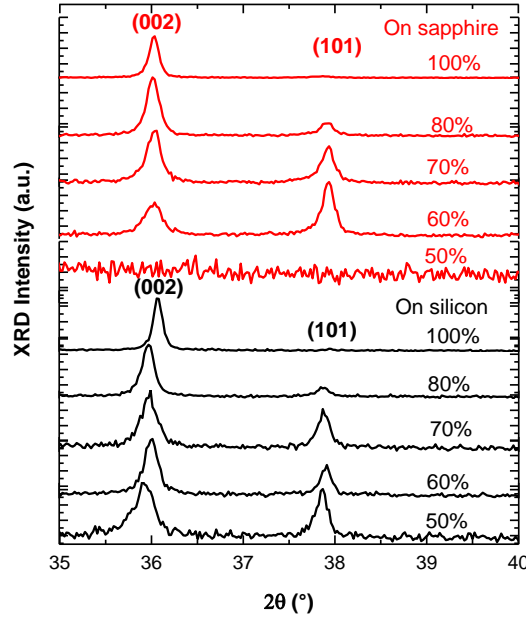


Figure (3.1): X-ray diffractograms, in symmetric θ - 2θ configuration, of c-AlN films synthesized using different $N_2\%$ gas ratio on silicon and sapphire substrates.

The substrates were placed facing the target axis at 5 cm distance and the deposition was performed without intentional heating the substrates. It is worth noting that the base pressure was managed to be $\sim 3 \times 10^{-6}$ Pa and the gas composition is defined as

$$N_2\% = \frac{N_2 sccm}{(N_2 + Ar) sccm} \times 100, \text{ where } sccm \text{ stands for standard cubic centimeters per minute.}$$

Two peaks are visible on the diffractograms except for $N_2\% = 100$ where only one peak is observed. The first and second peaks correspond to the signal from (002) and (101) planes of the hexagonal wurtzite structure of AlN, respectively. It is also observed that the (002) diffraction intensity improves gradually with the $N_2\%$. On contrary, the intensity of the (101) peak deteriorates till the (002) becomes the only detected orientation in the film synthesized under pure nitrogen condition. Strikingly, under 50% N_2 , the film deposited on sapphire, unlike on silicon, exhibits no diffraction signal. This indicates the absence of signal originating from crystallographic planes parallel to the substrate surface. In order to explore

the crystallographic orientation of this sample, XRD in asymmetric geometry configuration with tilting angle equal 1° and TEM image have been collected, see fig (3.2). The (101) peak becomes clearly evident in the X-ray diffractogram and columns are visible on the TEM image but are tilted with respect to the growth direction on the TEM image. Assuming each column is a single crystal, the results indicate columns have mostly (101) planes perpendicular to their long axis but this long axis is tilted with respect to the growth direction. This explains the absence of signal in the x-ray diffractogram measured in symmetric condition that probes only planes parallel to the film surface.

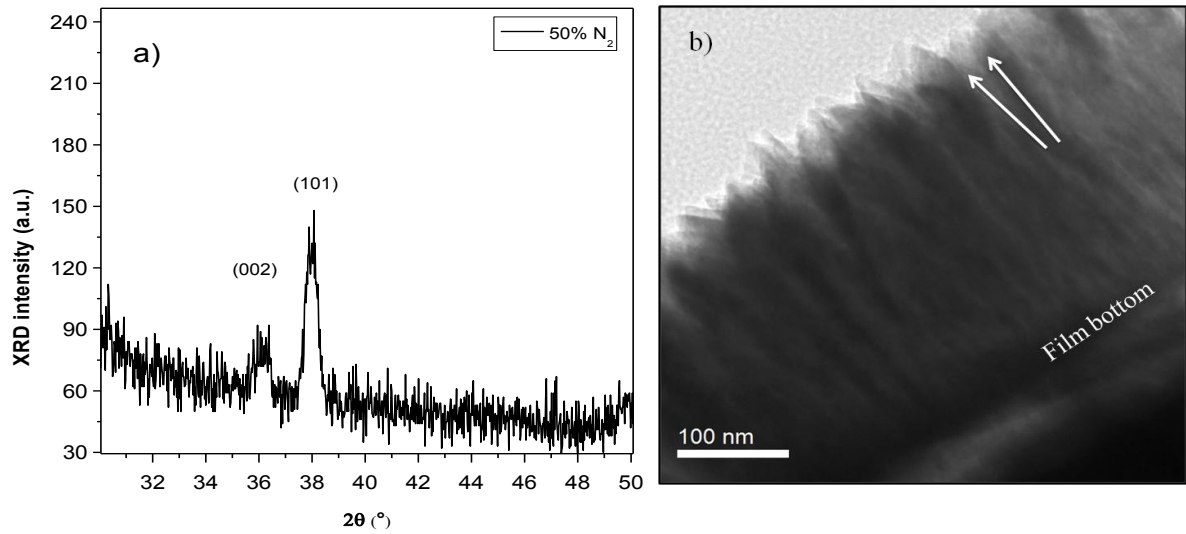


Fig.(3.2): a) Asymmetric XRD and, b) TEM micrograph of sample prepared with 50% N_2 on sapphire.

The texture coefficient T of (002) diffracted planes was calculated from XRD data using the following equation:[129-130]

$$T(002) = \frac{I_{(002)} / I_{0(002)}}{\frac{1}{N} \sum \left[I_{(hkl)} / I_{0(hkl)} \right]}, \quad (3.1)$$

where I is the measured intensity diffracted by different planes, I_0 is standard intensity from a randomly oriented polycrystalline sample (obtained from JCPDS card number 00-025-1133) and N is the number of diffraction peaks corresponding to diffracting hkl planes. Considering the data from fig (3.1), the texture coefficient of (002) is enhanced as a function of $N_2\%$ as observed on fig (3.3). It can be observed that the trend of texture coefficient on both substrates is the same for samples deposited at rich $N_2\% \geq 70\%$ conditions. This means that the substrates have insignificant role in determining the preferential orientation under these conditions. On other hand, films deposited on silicon show higher texture coefficient than on

sapphire for samples deposited under 50% and 60% N_2 , which is coming from the high intensity diffracted by (101) planes of AlN deposited on sapphire. This behavior of AlN on sapphire at lower nitrogen content can be explained by the initial growth mechanism of AlN on sapphire as reported previously [134] if it is considered that the deposition temperature is lower under these conditions as will be verified later. Effectively, although the growth of AlN thin films is generally reported to occur along the c-axis, the deposition of AlN on c-sapphire at low temperature can promote the growth of other planes than (002) parallel to the substrate surface. This is due to a twinning mechanism resulting in the growth of (101) planes, of lower polarity than (002) ones, parallel to the surface. This growth reduces the internal electrostatic field and, thereby, the system energy.

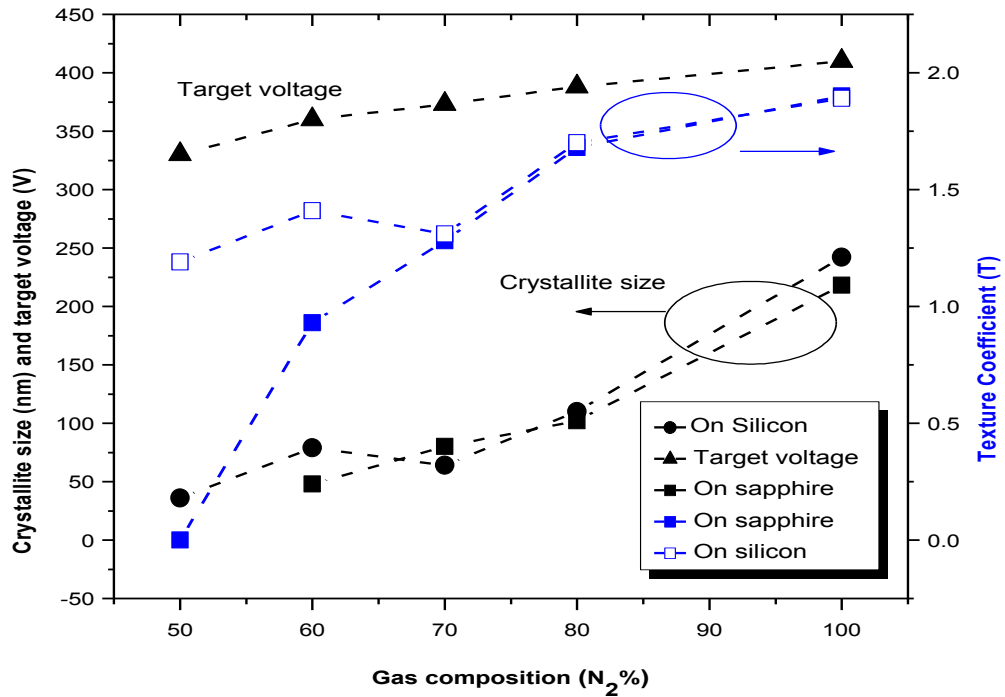


Fig.(3.3): Texture coefficient, average crystallite size along [001] and target voltage as a function of N_2 % deposited on silicon and sapphire substrates.

The average size of crystallites along (002) was calculated from the full width at half maximum of the (002) diffraction peak by using the Scherrer's formula.[135-136] Fig (3.3) shows the size of crystallites increases with N_2 % on both substrates and exhibits a similar trend to the (002) texture coefficient calculated by equation (3.1). This can be confirmed by the monotonic increase of the crystallite size with the texture coefficient, as shown in fig (3.4). The average size of crystallites with (101) orientation was also calculated and ranges from 67 to 87 nm confirming easier growth of crystallites with their c-axis aligned with the growth direction as N_2 % increases.

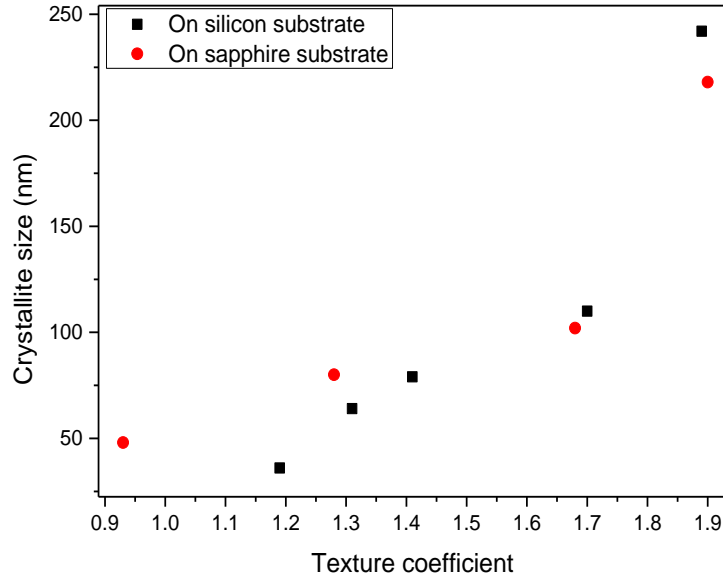


Fig. (3.4): Averaged size of crystallite along [001] with texture coefficient of the AlN thin films deposited on silicon and sapphire substrates.

Although energy dispersive spectroscopy (EDS) could not quantify correctly the nitrogen content, we have performed EDS measurements of the N/Al ratio and did not find sensible variation of this ratio over the entire range of compositions of the gas phase probed in this study. This is not surprising since the large proportion of nitrogen in the gas phase (50 to 100 %) and low sputtering rate must ensure complete reaction of the metallic adatoms with the reactive gas upon growth. Therefore, compositional changes cannot explain the microstructural changes observed.

In order to understand the behavior summarized on figure (3.3), we can refer to the existing literature on the relationship between process parameters and thin films growth, more particularly AlN, using sputtering. The effect of the composition of the gas phase, in particular the role of nitrogen species, on the preferred orientation of AlN thin film has been intensively studied in many reports.[137-139] In some studies, the role of gas composition was linked to the influence of the film deposition rate that is usually reduced at high nitrogen concentration conditions. This phenomenon was explained by the difference in mass of sputtering ions between the Ar^+ ions (heavier) and N_2^+ ions (lighter). As a result, the momentum transferred to the target decreases as the nitrogen content in the gas phase is increased. Thus, the sputtering yield and the deposition rate must decrease. Consequently, the adatoms have more time to rearrange and find the most favorable crystallographic sites. [139] Other reports, are considering the effect of the energy of the adatoms in their

interpretation. Increasing the energy of adatoms either by increasing their mean free path (e.g. working at low pressure) or applying a large substrate bias voltage in radiofrequency sputtering has been investigated.[140] The film-forming adatoms of high energy have sufficient fuel to drive themselves to thermodynamically favorable sites.[132] By combining the above interpretations one can reach the conclusion that it is necessary for the adatoms to have sufficient energy and enough time to find and rest at the most favorable thermodynamic and crystallographic sites.

In our case, the deposition rate was very low (about 1nm/min) and almost constant between all conditions. Hence, all atoms have sufficient time to rearrange after they condensate from the gas phase and the influence of the deposition rate on the type of growth can be ruled out. However, the effect of the kinetic energy of the adatoms was considered as a possible origin to the change in microstructure. Owing to the difference between the atomic radius of Ar gas (large) and the molecular radius of N₂ (small) gas, Al atoms sputtered at higher N₂% are suspected to experience fewer collisions events (i.e. lower scattering probability), increasing their mean free path. The longer mean free path allows the sputtered atoms to keep more energy for the film process.

In addition, the target voltage increases with N₂% as seen in fig (3.3). This is referred to the modification in the plasma conditions and/or the change in target surface composition when the nitrogen content in the gas phase is increased[141]. At high N₂ partial pressure, the Al target is covered by a thin layer of AlN_x. The work function of AlN (5.33 eV) is higher than that of metallic Al (4.08 eV)[142] and the secondary electron emission coefficient is expected to decrease upon target nitriding, explaining why the target voltage increases.[143] Films grown by sputtering process commonly suffer from bombardment by different kinds of high energetic species during growth, such as sputtered, reflected atoms, and highly energetic negative ions[144], see the schematic diagram (2.1) in experimental chapter. According to Thompson distribution,[145] the most common energy of the sputtered species equals half the surface binding energy of the target layer (SBE/2). By taking into account the surface binding energy (SBE) of AlN (10.8 eV) and Al(3.36 eV), sputtered species have higher energy for a nitrided target surface (AlN_x) than for a metallic one (Al).[146-147] Hence, atoms sputtered under nitrogen-rich conditions sputtered can transfer more energy to the film as they impact it. Moreover, the contribution of species backscattered by the target surface species and bombarding the substrate surface should also be considered. Their kinetic energy mainly depends on the mass ratio between the target material and the projectile ions (Ar⁺ and N₂⁺).

The energy of backscattered Ar and N atoms can be calculated from the following equation:[144]

$$E_p = \left(\frac{A-1}{A+1} \right)^2 E_{po}, \quad (3.2)$$

where A is the mass ratio of Al to the projectile ions, and E_{po} is the initial energy of the projectile. The calculated energy of backscattered N atoms ($0.049 E_{po}$) is higher than that of Ar ones ($0.039 E_{po}$). Thus, at higher $N_2\%$, the probability of backscattering N atoms increases due to the high N_2 partial pressure and splitting the N_2^+ molecules into two N atoms. This should deliver more energy to the film surface. Furthermore, with poisoned targets, negative ions that bombard the film surface can play a significant role to increase the mobility of the adatoms, improving the crystallinity of AlN.[148-150] These ions are formed at the target surface, by combination of electronegative sputtered atoms and secondary electrons, and accelerated towards the substrate with a high kinetic energy corresponding to the cathode sheath potential fall, i.e. roughly the discharge voltage. These negative ions hold a large kinetic energy and in extreme cases can promote epitaxial growth near-room temperature, as reported previously in ZnO.[151] Based on the above arguments, depositing AlN at high $N_2\%$ brings more energy to the growing film. The development of c-axis preferred orientation with increasing $N_2\%$ can be explained considering that (002) planes show the highest packing density and the lowest surface energy[35] compared to the other planes.[133, 152] This feature makes the higher energy adatoms and/or the diffused atoms from other planes tend to lower their energy by resting on (002) planes.[153] As mentioned before, at high $N_2\%$ the adatoms gain more energy to diffuse and rearrange. Therefore, grains with (002) planes parallel to the film surface can grow faster than other planes under such conditions. According to the competitive growth mechanism, planes with the highest growth rate tend to envelop the other planes and to become the preferred orientation upon growth.[133, 138] This is consistent with our results. In addition, the size of crystallites increases with $N_2\%$ and texture coefficient, as shown in fig (3.4). This supports the previous hypothesis of improved film crystallinity with enhancing the preferential orientation along the c-axis and is in line with findings reported in.[154]

To confirm our assumptions, a second series of experiments have been performed, in which the substrate was heated to 200 °C for films prepared under 100% N_2 in order to provide some more mobility to the adatoms. Fig. (3.5) reveals that the XRD intensity from the (002) planes

of the AlN films prepared under these conditions increases significantly. It intensifies further when the target current is doubled despite less time is left for the diffusion of adatoms. Raising the target current means increasing in the adatoms flux to the substrate, i.e. more energy delivered to the film per time unit and, thereby, higher self-established temperature at the film.

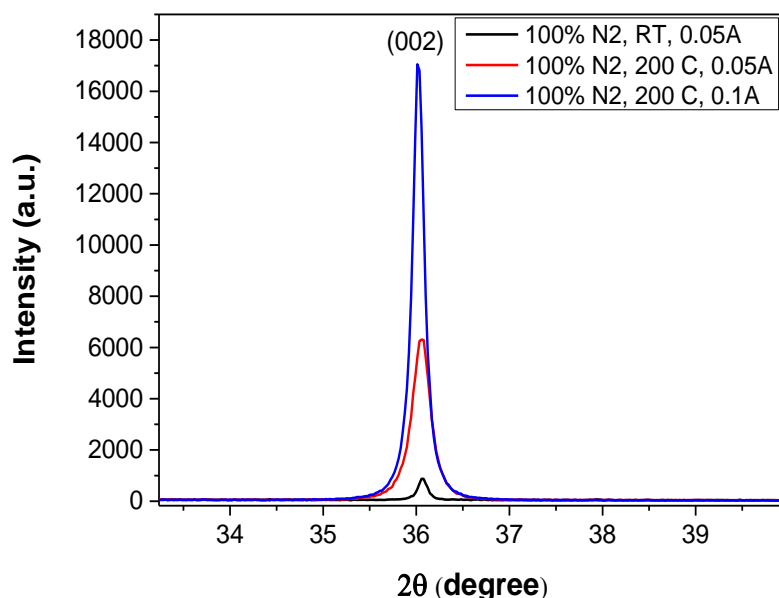


Fig (3.5): XRD of AlN samples deposited at 100% N₂ and different target current and substrate temperature.

Fig. (3.6) shows a schematic diagram representing the preferred orientations under three different sputtering conditions; room temperature growth at discharge current 0.05 A (I. 50% and II. 100% N₂) and thermal assistance growth at 200 °C and 0.1 A (III).

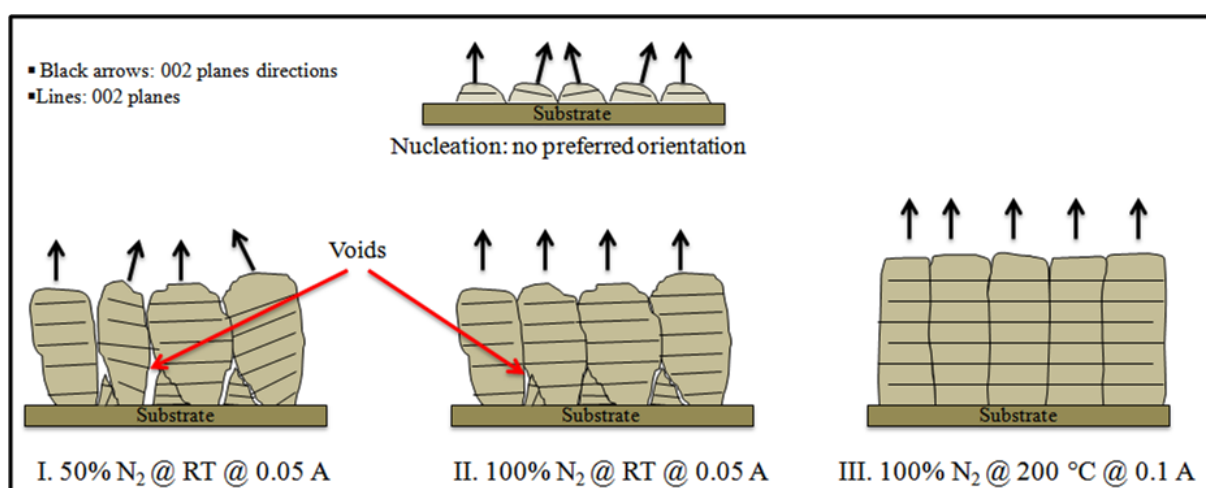


Fig (3.6): schematic diagram of the preferred orientations for samples prepared with and without thermal assistance.

In the initial growth stage (nucleation), if no epitaxial growth occurs, the formed small grains exhibit no preferred orientation. Thus, in the case of sputtering conditions without thermal assistance and low nitrogen content in the gas composition (I), the incoming adatoms hit the substrate and stick on the different grains showing different orientations and some voids between the adjacent columns. This is due to the lack of thermal energy to enhance the diffusion between different grains. Under pure nitrogen conditions (II), the adatom mobility is improved, as described above, resulting in diffusion between the adjacent grains with less voids and enhanced the preferred orientation. On the contrary, the deposition under thermal assistance (III) shows high degree of orientation with lateral smoothening between the columns.

To investigate the influence of the target current on the substrate temperature, the temperature was recorded at the thermal probe as a function of discharge current, see fig (3.7). For more precise temperature measurement, the experiment was established such that the loss in the energy flux (Φ) dissipated by the connected wires is very small compared to the energy flux of the incident species Φ_i and can be neglected, see inset fig (3.7).

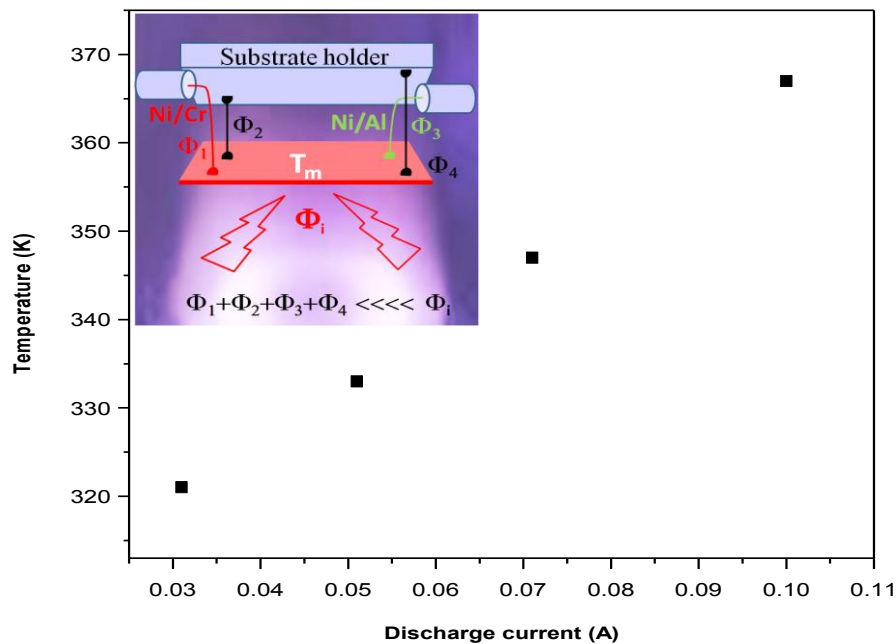


Fig (3.7): Thermal probe temperature as a function of the discharge current. The inset shows the schematic of the home made thermal probe. Φ_i corresponds to the incident energy flux while (Φ_1, Φ_3) and (Φ_2, Φ_4) correspond to the energy dissipated by the thermocouple and holding wires, respectively.

Hence, the measured temperature (T_m) represents the mean thermal energy induced by the incident species. A linear increase in the substrate temperature with the target current with a slope of 670 K A^{-1} was found, which indicates that the higher flux of particles plays a strong role in rising the surface temperature of the growing films. As shown in fig (3.5), the (002) diffraction intensity increases when more energy is brought to the substrate heated at 200 C and raising the discharge current. This is a clear evidence that (002) orientation prefers higher energy of the adatoms.[140]

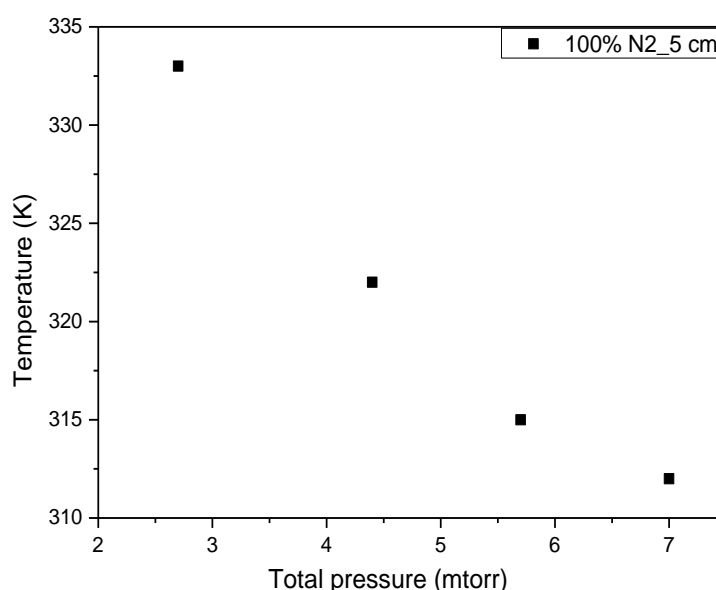


Fig (3.8): The probed substrate temperature as a function of deposition total pressure at 100%N₂ and target-substrate distance 5 cm.

Furthermore, In order to investigate the effect of thermalization (loss of kinetic energy of the sputtered atoms due to collisions), the temperature has been measured at different total pressures while keeping all the other parameters constant as displayed in fig (3.8). The decrease in the substrate temperature with increasing the total pressure is attributed to thermalization effect. High pressure i.e. high density of plasma species is leading to high number of collisions as particles drift from the target towards the film surface that consumed the kinetic energy of the sputtered atoms.

In other words, the flux of particles that induces the substrate heating can be summarized as follows; higher target current leads to higher flux of particles while lower total pressure results in higher flux of particles plus more energetic particles.

2.2-Microstructures and morphology

In order to gain more information on the microstructure, TEM measurements have been performed. All the samples were found to exhibit columnar structure and an average thickness of about 250 nm, see for example the TEM images, fig (3.9 a, b) of samples prepared at 50% and 100% N₂.

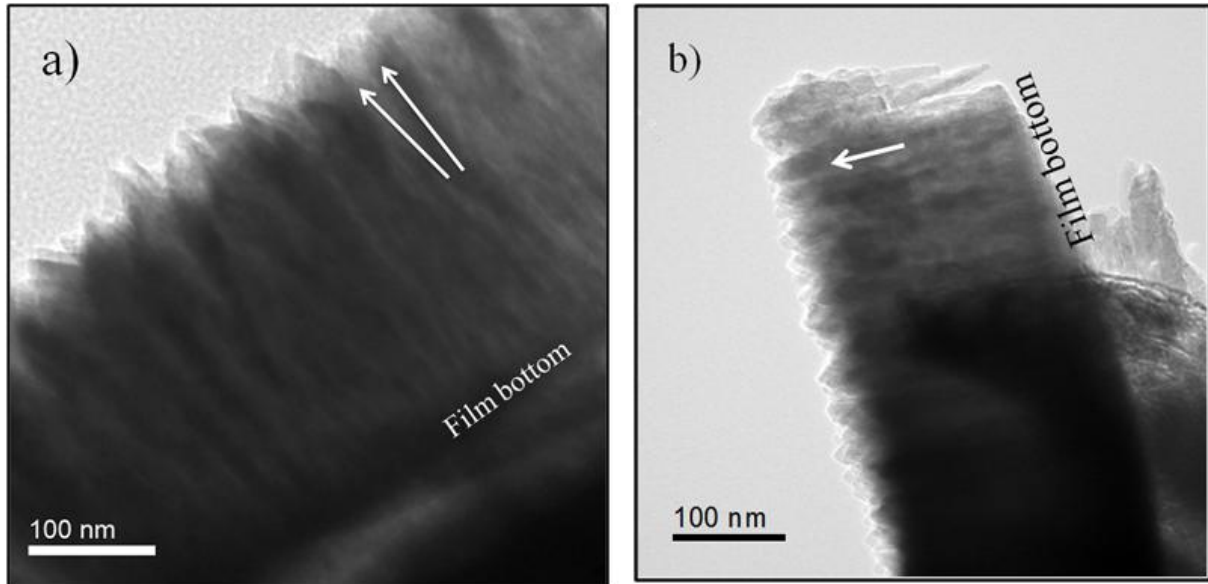


Fig (3.9): TEM images of samples prepared at a) 50%, and b) 100% N₂. The white arrows are to indicate the growth direction.

It can be observed, the good alignment of the columns along the growth direction in sample deposited at 100% N₂. In contrast, the sample prepared at 50% N₂ clearly shows a distribution in the tilting of the column axis with respect to the film growth direction, as shown before in fig (3.2). In addition, it exhibits rougher surface (8 nm) than the 100% N₂ sample (3.3 nm) as confirmed by AFM measurement, see fig (3.10). Decreasing the roughness at pure nitrogen condition indicates a significant change in the growth mechanism and usually refers to increase in the adatoms mobility.[138, 155] This supports the above assumption about enhancement of the adatom mobility at 100% N₂. However, when going deeply inside the 100% N₂ sample using high resolution TEM (HRTEM) fig (3.11), It is found that near the interface with the substrate the film consists of columns slightly tilted with reference to the growth direction and showing a V-shape base that extends over approx. half the film thickness and then stabilizes with uniform shape closer to the surface, fig (3.11 a, b).

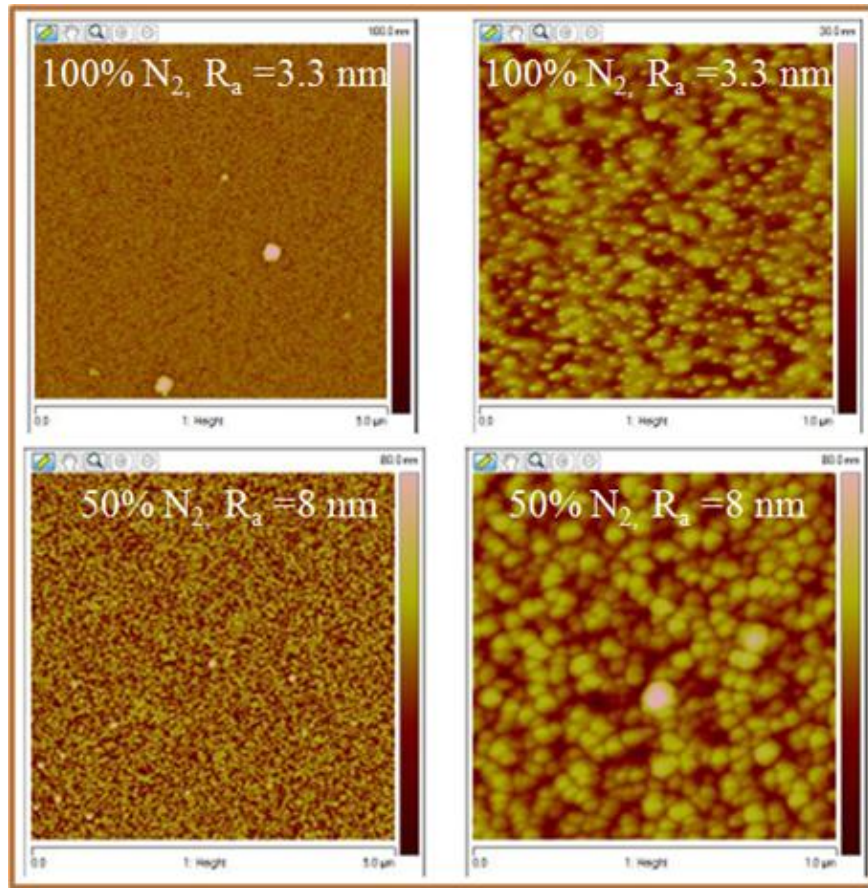


Fig. (3.10): AFM images of AlN samples prepared at 100% N_2 and 50% N_2 .

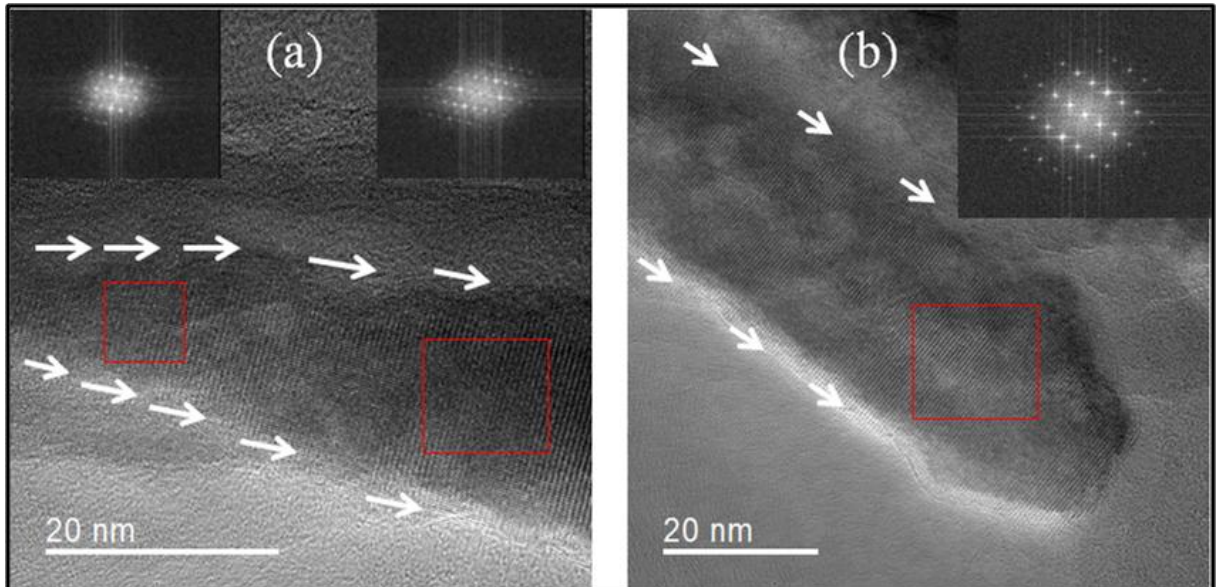


Fig (3.11): HRTEM of 100% N_2 sample close to the substrate (a) and the surface (b). The inset figures are the FFT corresponding to the red squares. The white arrows are to guide the reader to identify the growth direction and the columnar shape.

The FFTs on selected areas close to the surface and the substrate-film interface support evidences a higher crystallinity near the surface. This can be explained by a progressive orientation of the columns along the growth direction that introduces crystal imperfections, in line with the reported work of A.C. Galca et al.[154]

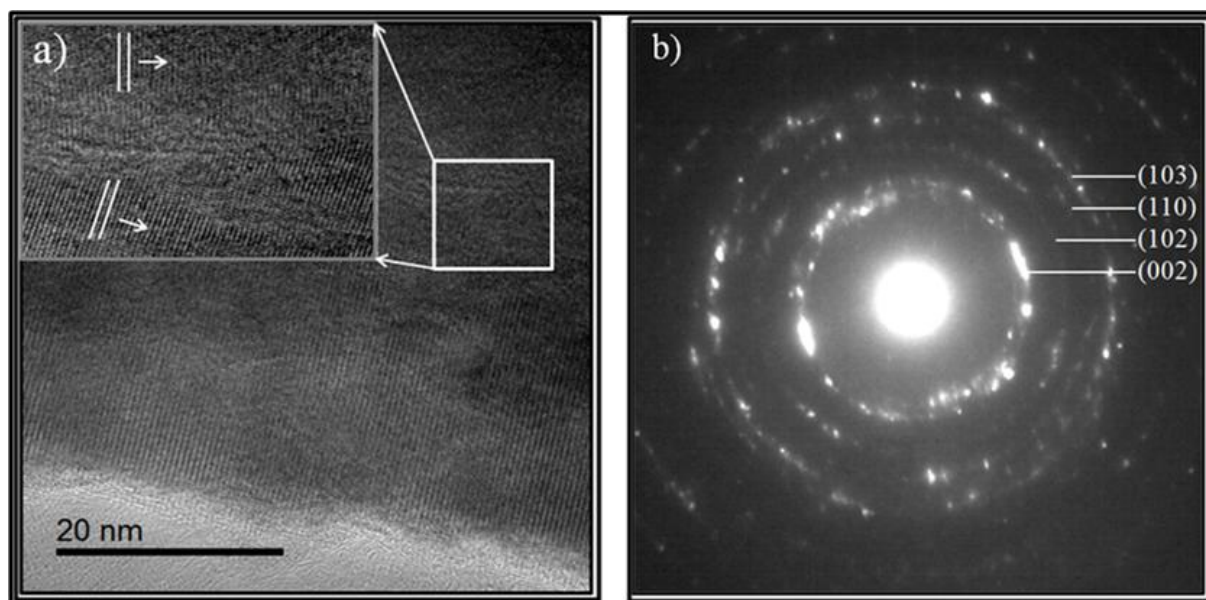


Fig (3.12):a) HRTEM of 100% N₂ sample with magnification of area (white square) between two columns. b) SAED pattern of the same sample collect at low magnification at the center of the film.

Moreover, from the magnified view of area between two columns fig (3.12a), one can distinguish a significant tilt in the growth direction between the two adjacent columns as well as roughness at the lateral edges. This, along with the V-shaped morphology that extends to rather long distances indicate that the competitive growth completes at late growth stages for this film although XRD detected only the (002) orientation. Fig (3.12b) shows selected area electron diffraction (SAED) pattern collected at low magnification. The SAED collected at the center of the film is composed of partial rings, confirming the polycrystalline nature of the film. The signal is brighter along the growth direction at the (002) ring, indicating the crystallites are mostly oriented with (002) planes parallel to the substrate. Nevertheless, the elongation of the spots further confirms the slightly tilting of the columns. On the other hand, Fig (3.13) shows the TEM and SAED of a sample prepared under 100% N₂ with a larger discharge current of 0.1 A, and substrate temperature of 200°C. This sample prepared with thermal assistance exhibits high crystallites order in the low magnification SAED pattern (inset of fig 3.13) characterized by more localized and brighter diffraction spots.

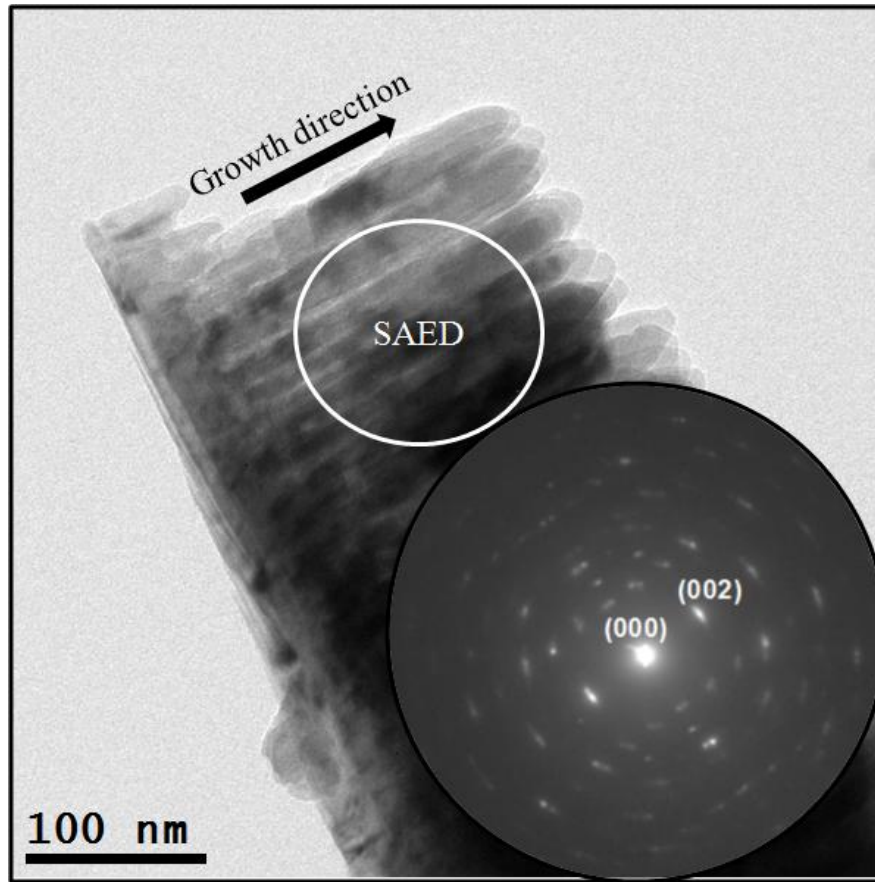


Fig (3.13): TEM of sample deposited at 100% N₂ with target current of 0.1 A and substrate heated to 200 C. Inset: the corresponding SAED collected from the area marked by the circle.

In addition, the HRTEM of two columns of this sample is shown on fig (3.14) and indicates, unlike in fig (3.12a), almost no tilting between the two columns and quasi-continuity of the crystallography is (002) planes between them. This can be explained by earlier termination of the competitive growth that appears to occur in the first 50 nm of the growth. Columns exhibit smooth lateral edges. This agrees well with the higher diffracted intensity measured for this sample by XRD, that probes atomic planes parallel to the film surface in $\theta/2\theta$ configuration. These results are consistent with zones I_c and T in the structure zone model (SZM) proposed by Mahieu, S., et al[156] for films grown without and with thermal assistance, respectively. Looking deeply into the microstructure, the HRTEM images not only show the influence of thermal assistance on the crystallinity of the prepared sample but also give indication on the associated mechanism. It suggests that cross diffusion between the adjacent columns is enhanced at higher mobility condition as shown in the magnified insets of fig (3.14) and in line with common SZM.

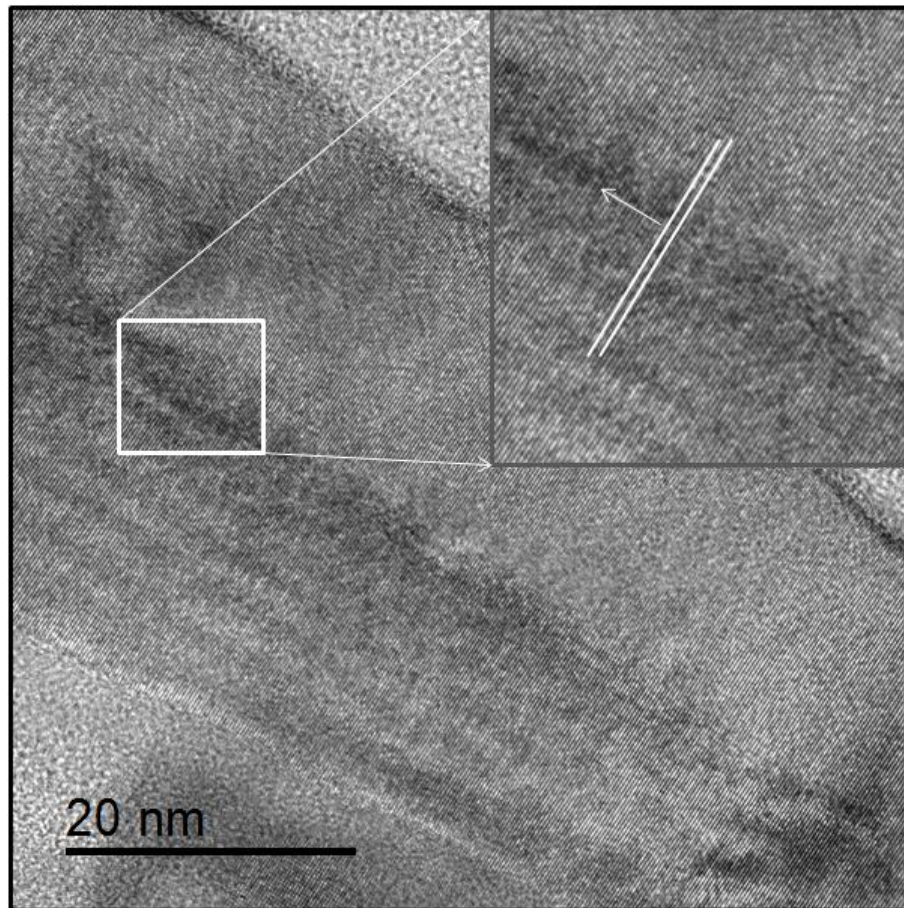


Fig (3.14): HRTEM for sample deposited at 100% N₂ with a target current of 0.1 A and substrate heated to 200 C. The inset: magnification of the area (indicated by the white square) between two columns.

It can be concluded that the progressive alignment during growth[154] is eased by higher adatoms energy and cross diffusion between grains and explained by leading to earlier termination of the competitive growth.

2.3- Optical properties

Enhancement of the crystallinity is supposed to improve the optical properties of the samples. Therefore, the optical transmittance of the AlN films deposited on sapphire substrates was measured in the range from 200 nm (6.45 eV) to 1120 nm (1.10 eV) employing a Woollam M-2000 ellipsometer set to its transmission-mode at normal incidence. Fig.(3.15) shows the UV-VIS transmittance spectra in the 300-800 nm wavelength range. The transmittance is high at around 80% and is almost independent of the nitrogen content in the gas phase. It decreases steeply at the onset of the AlN's fundamental bandgap absorption edge[157] for wavelengths below 250 nm.

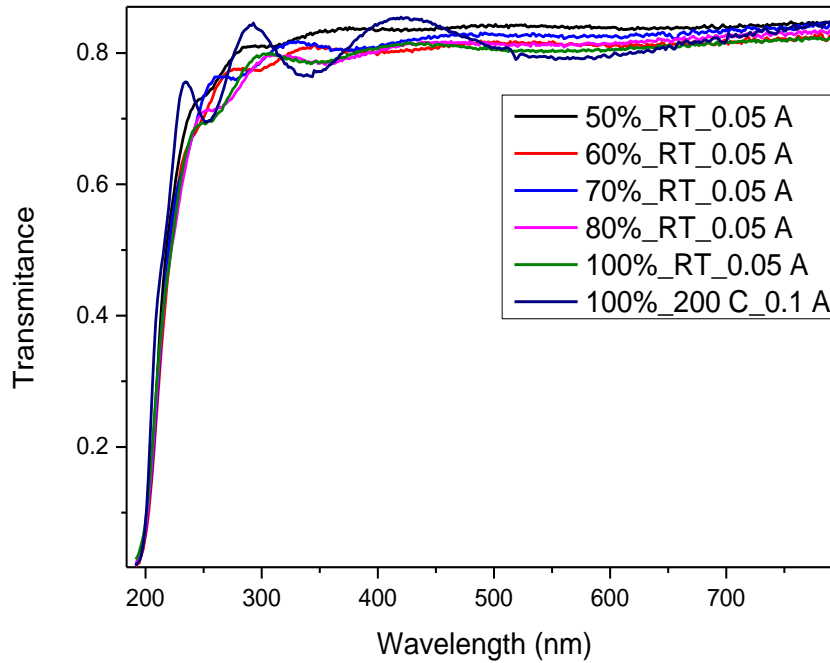


Fig (3.15):UV-VIS transmittance spectra of AlN samples deposited on sapphire substrates.

Fig. (3.16) displays the energy dispersion of the films' optical constants $k(E)$ and $n(E)$ determined by the fitting procedure described in annex A. The extinction coefficient k (fig. 3.16a) remains lower than 0.02 in the visible and infrared wavelength ranges. It exhibits weak absorption bands originating from structural disorder and localized defects. The structural or thermal disorder create states that exponentially extend inside the bandgap and form absorbing shoulder appearing just below the bandgap, called Urbach's tail.[158]

Indeed, appearance of wave-like small amplitudes in $n(E)$ are reflecting the Kramers-Kronig relation between $n(E)$ and $k(E)$.

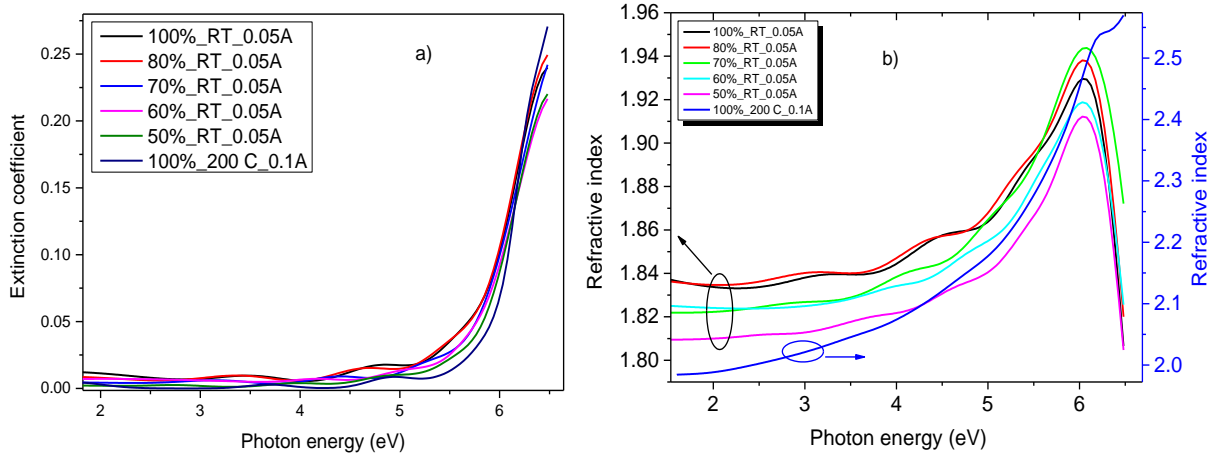


Fig (3.16): a) and b) extension coefficient and refractive index as a function of photon energy, respectively, for all AlN samples prepared at different gas compositions with and without thermal assistance.

The optical bandgap E_g can be deduced from the Tauc's equation that describes the optical absorption in semiconductors having direct electronic transition between their valence and conduction bands:

$$h\nu\alpha = B(h\nu - E_g)^{1/2}, \quad (3.3)$$

where ' $h\nu$ ' and α are the photon energy and the material absorption coefficient calculated.

The bandgap energy found here , $E_g \approx 5.92$ eV, is close to the reported values for polycrystalline AlN films[157]. Apparently, the microstructure and the nitrogen content in the gas phase have no significant effect on the optical band gap that is an intrinsic electronic property of the material. In contrast, the ordinary refractive index n varies appreciably with the amount of N_2 in the gas phase and the thermal assistance, fig. (3.16b).

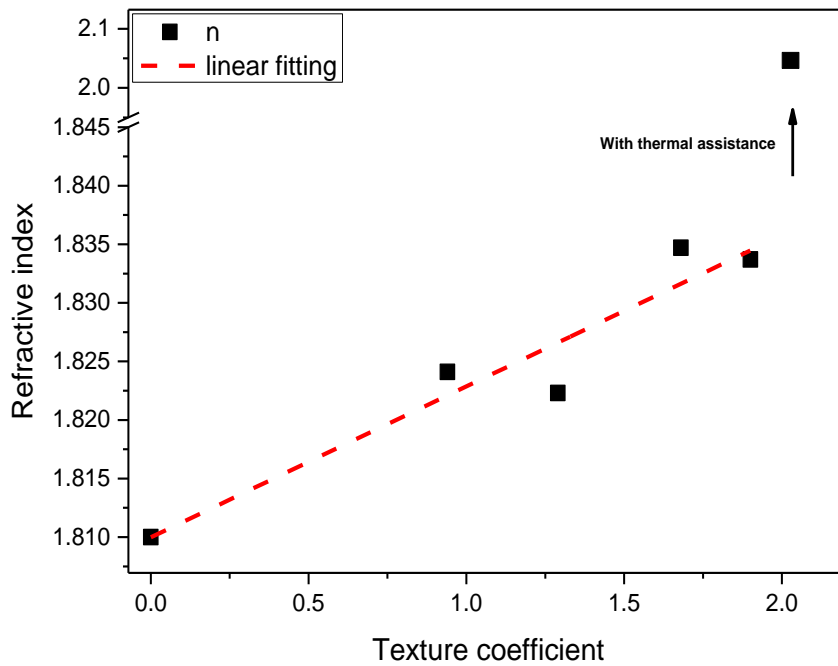


Fig (3.17): The refractive index as a function in texture coefficient.

It increases linearly with the texture coefficient T as shown in fig. (3.17). Hence, controlling the microstructure represents an interesting strategy to adjust the ordinary refractive index of AlN films. The linear dependency may be attributed to less lattice interferences inside the film between crystallites consisting of (002) and (101) planes parallel to the film surface. Consistently with the microstructural analysis from the previous section, the sample deposited with thermal assistance under 100 %N₂ exhibits a very high refractive index, close to 2.1 and to the refractive index of epitaxial AlN.[159]

As better columnar alignment is achieved the density of structural defects decreases as stated before and denser regions are observed in the transverse direction of the films. This increases the ordinary refractive index. To further confirm the strong texture of the film deposited with thermal assistance, rocking curve measurement has been performed at the 002 diffraction peak, see fig (3.18). The narrow FWHM of the rocking curve, about 1.6° , reflects the strong alignment of the c-axis along the growth direction, consistently with the calculated large texture coefficient reported in fig (3.17) and TEM investigations. These results show the possibility to adjust and optimize the refractive index of AlN films deposited on non-matched inexpensive commercial substrates by maximizing the degree of c-axis preferred orientation and crystallinity in soft conditions. It is also shown in annex B that the texturation leads to remarkable anisotropy of the optical properties of AlN films that could serve in several applications.

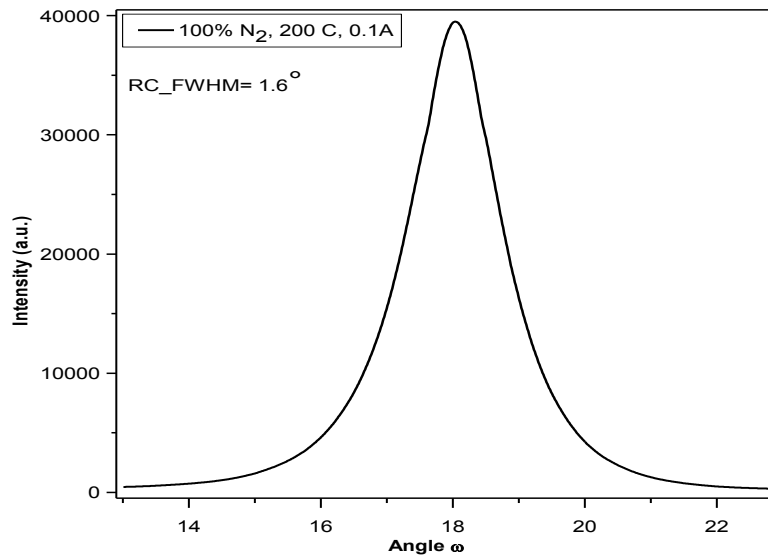


Fig. (3.18): Rocking curve of AlN (001) plane at 002 diffraction peak for sample prepared at 100%N₂ and 0.1 A at 200°C.

3- The optimum deposition conditions

All previous samples were deposited using DC mode of reactive sputtering at very low deposition rate in order to investigate the influence of sputtering conditions on the growth mechanism of AlN. Indeed, DC mode is very suitable for this purpose as it allows easy control and measurement of the sputtering parameters, such as the target current, the voltage or the power in DC mode. Hence, the correlations with the film properties can be more easily established. From the above study, we found that effect of adatoms mobility plays a significant role on the film microstructure, which forced us to use external thermal assistance in order to obtain high texture c-axis AlN.

Due to limitation in the deposition rate using DC associated to very long deposition times to achieve significant thickness for practical applications, it was needed to find an alternative we could apply for the next studies on RE-doped AlN films. While the control of electrical parameters is more difficult using RF sputtering, it is well suited for the growth of thin films in atmospheres containing a large fraction of reactive gases as in our case. Moreover, in RF discharge, there is substantial higher total thermal power to the substrate, compared to DC discharge, that can self-heat the substrate during growth and, thereby, enhance the mobility of adatoms.[160] Finally, the RF discharges can be operated at lower voltages for a similar average power than with DC, enabling a larger discharge current and, consequently, larger

deposition rate. For these reasons, RF sputtering was selected for our studies of the properties of RE-doped AlN films. However, in order to validate the use from the perspective of material properties we have compared the properties obtained using the two modes. As previous studies have been conducted in our group using RF sputtering, we selected optimized conditions that are listed in table (3.2).

Table (3.2): contains the sputtering parameters used in RF discharging mode.

Sputtering parameters	RF- mode
Gas ratio (N ₂ /Ar+N ₂)	65%
Target-substrate distance	5 cm
Discharge Voltage	180-200 V
Discharge power	100 W
Base vacuum	1 x 10 ⁻⁶ Pa
Working pressure	0.7 mtorr
Substrate heating	RT
Deposition time	40 min

The XRD, TEM image and the diffraction pattern typical for samples prepared under these conditions are displayed in fig (3.19). It can be observed that a well crystalline AlN layer with single orientation of the columns along the [002] direction could be synthesized at room temperature. The normalized XRD of sample grown by RF with unheated substrate shows narrower diffraction peak at lower angle compared to the sample grown by DC at substrate temperature 200 °C and discharge current 0.1 A. In addition, the TEM image of AlN_RF exhibits denser film structure than the TEM of AlN_DC shown in fig (3.13). The good crystallinity and denser structure of AlN_RF sample results in high dielectric constant compared to AlN_DC sample, as shown in fig (3.20). The AlN_RF sample shows higher refractive index with value near to 2.1 eV in visible region, which is very close to the reported refractive index of single crystal AlN.

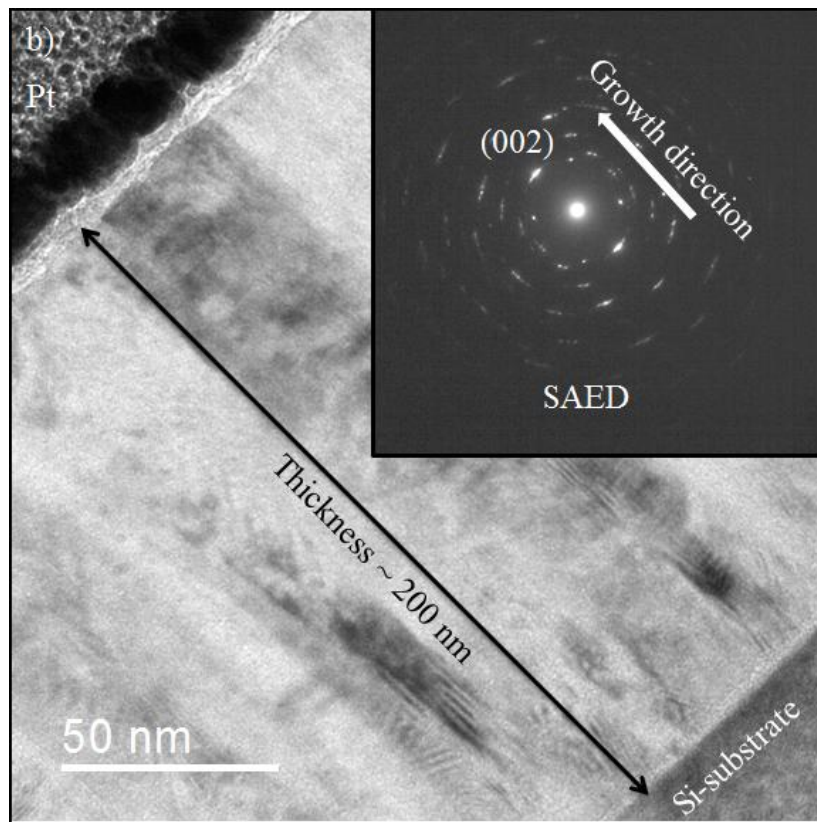
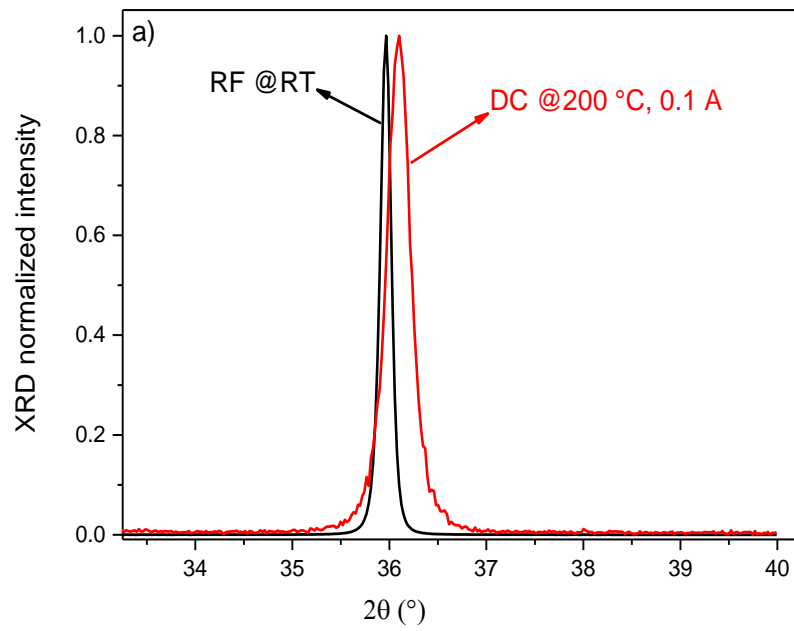


Fig (3.19): a) XRD, and b) TEM with SAED pattern (inset) of AlN sample prepared at 65% N_2 and RF power 100 W and total pressure 0.6 mtorr.

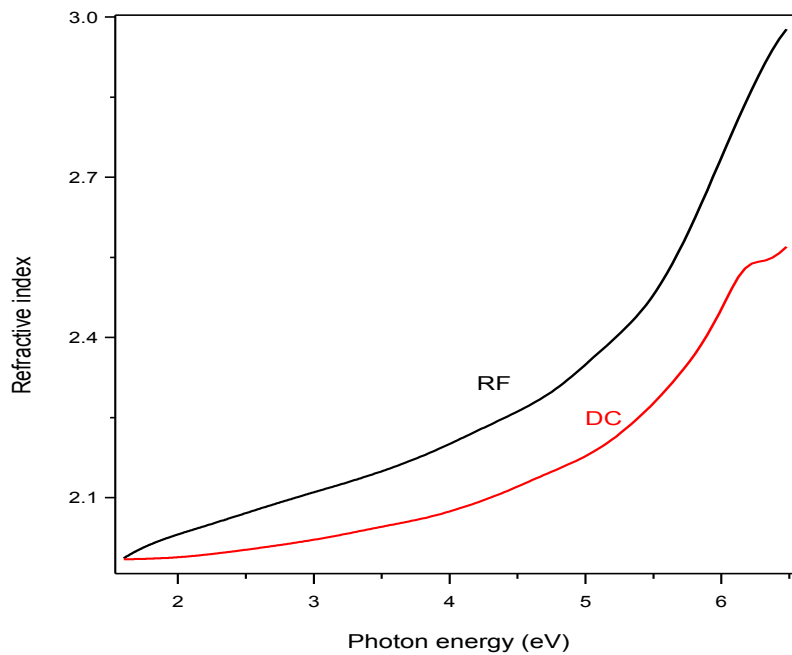


Fig (3.20): The dispersion relation of AlN thin film samples deposited using RF and DC plasma discharge mode.

These good optical and structural properties of AlN_{RF} deposited at room temperature as well as the short deposition time (40 min) meets our preference for using these sputtering conditions in the doping step with rare earth.

4- Conclusion

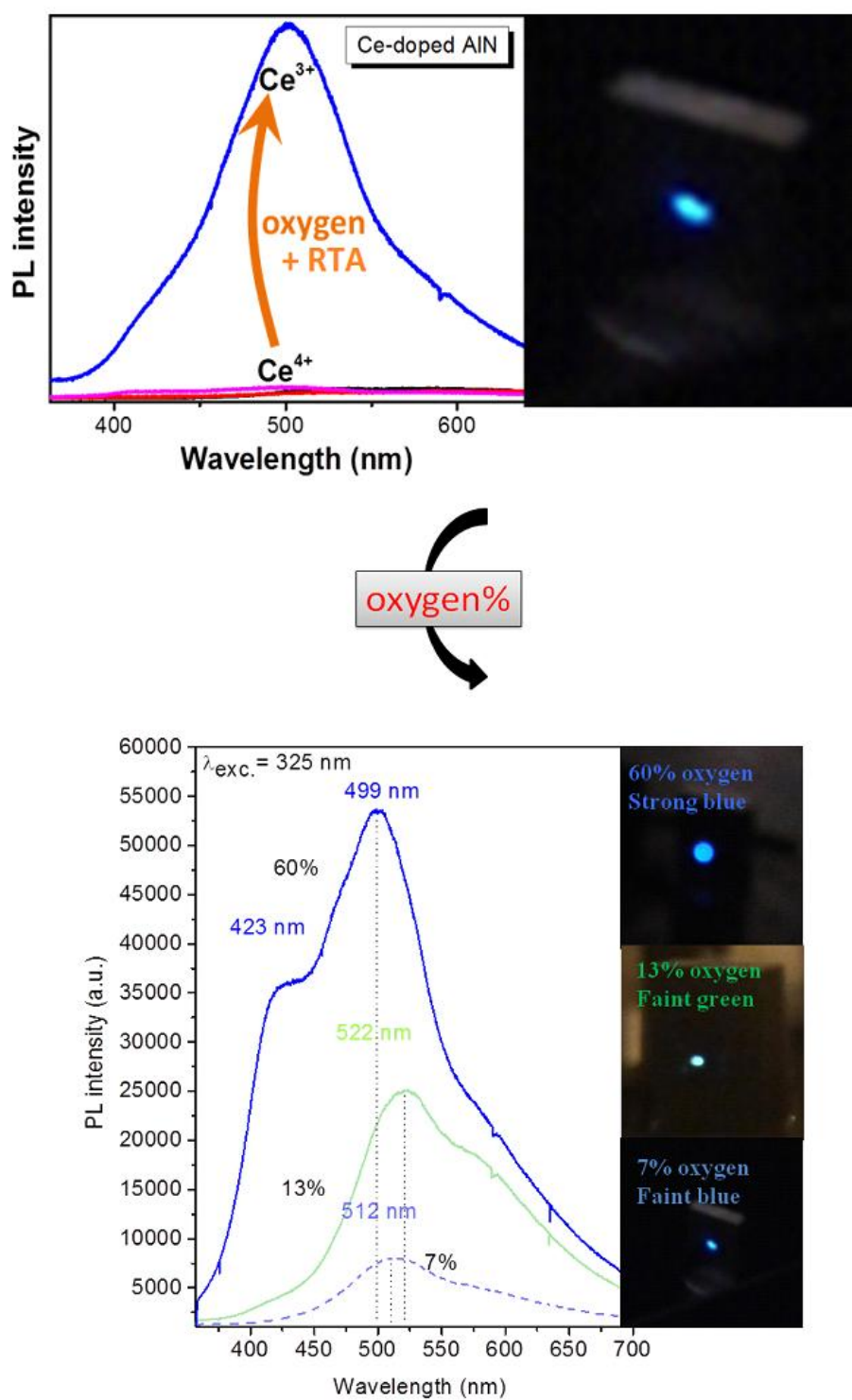
Well crystallized AlN thin films with high degree of c-axis orientation were prepared by reactive magnetron sputtering of an aluminum target. Controlling the preferred orientation by only tuning the N₂% in the gas phase has been achieved. It was found that the synthesis of highly c-axis oriented crystalline AlN is favored by depositing the coatings in nitrogen-rich reactive ambiance. The results have been interpreted on the basis of an improved mobility of adatoms assisted by the bombardment of the films by fast particles. Intentional thermal assistance or increase of the discharge current were found to have similar beneficial influence on the crystallinity of the c-axis oriented films deposited under pure nitrogen conditions. This is explained by thermally-assisted increase in adatoms mobility in both conditions as supported by thermal probe measurement under different discharge currents. The optical constants (n, k) and bandgap of the prepared films have been modeled from spectroscopic ellipsometry measurements in transmission and reflection modes. The results evidence the possibility to tune the refractive index with the crystal orientation while keeping constant the

bandgap. Our findings show that the optical properties of the AlN films can be tuned via their texture which was controlled by the amount of nitrogen in the gas phase. The optimum sputtering conditions that will be used during the rest of this work were stated. Based on high texture, excellent optical properties and fast deposition of AlN prepared using RF reactive magnetron sputtering, RF deposition was selected.

Chapter IV

Cerium-doped AlN

Graphical abstract



Abstract

This chapter is dedicated to investigate the optical behavior of cerium-doped AlN (Ce-AlN) thin films prepared by RF reactive magnetron sputtering. The crystal structure of the prepared samples was investigated by x-ray diffraction (XRD) and transmission electron microscopy (TEM) at low and high resolution (HRTEM). The chemical composition was analyzed by Rutherford backscattering spectrometry (RBS) and Energy-dispersive X-ray (EDX) techniques. The oxidation states of cerium (Ce^{3+} and Ce^{4+}) have been probed using Electron Energy Loss Spectroscopy (EELS). The optical response has been examined by photoluminescence (PL) under different optical excitation wavelengths. Photoluminescence excitations measurements (PLE) have been performed in order to explore the excitation mechanisms. In addition, the PL intensity evolution with low temperature variation was used to gain more information about the PL thermal quenching mechanism. It is found that oxygen plays an important role in the PL response by changing the oxidation state of Ce ions from optically inactive (Ce^{4+}) to the optically active one (Ce^{3+}). In addition, the importance of the oxidation is further confirmed by the excitation mechanisms responsible for blue emission and determined by PLE measurements. This role has been discussed to the light of the correlation between PL, PLE and EELS results. Besides that, the *post*-deposition annealing for our samples is found to be essential for activating the photoluminescence. A comprehensive study is presented to understand the optical mechanisms of Ce-doped aluminum nitride and aluminum (oxy) nitride materials. Based on a proposed approach, PL manipulation has been achieved to offer different emission colors (blue, green and white). Our findings can be used to understand and manipulate the behavior of RE-doped Al(O)N for lightening applications.

1- Introduction

Cerium is a lanthanide element which contains one electron in the 4f-orbital. The luminescence properties of its optically active ion (Ce^{3+}) are characterized by fully allowed electric dipole moment $5d-4f$. [88] Thus, it has large absorption cross-section $\sim 10^{-18} \text{ cm}^2$ compared to the other rare earth $f-f$ transition $\sim 10^{-20} \text{ cm}^2$. [89] In addition, it absorbs in the UV and emits in UV-VIS range, which is suitable for many applications in this range. Furthermore, involving the unshielded outermost d -orbital states in the optical transitions makes the excited electron strongly sensitive to the electric field of the local surrounding environment. This results in the possibility to tune the Ce^{3+} luminescence from UV to blue-

green-yellow by changing the local environment using different host compositions.[90-92] This property is very interesting in terms of luminescence engineering technology. In addition, the ability of Ce to emit blue light is a promising feature for white light generation technology. So, a lot of research efforts have been directed in this regard by using Ce doped in different hosts (glasses, garnet, ceramics and semiconductors).[41, 93-94] Nevertheless, there is little knowledge on Ce-doped AlN material. Amorphous Ce-AlN thin films were prepared by DC magnetron co-sputtering at substrate heated up to 350 C.[99] Their structure and microstructure were studied but the assignment of the PL signal was not clear. Liu et al,[74] studied in more details the blue emission from a polycrystalline powder of AlN phosphor co-activated by Ce^{3+} and Si^{4+} synthesized by gas pressure sintering under high temperature (2050 C for 4 hr) and high nitrogen pressure (0.92 MPa). An intense luminescence at 600 nm from Ce-doped single bulk AlN crystal synthesized by reactive flux method under high pressure/temperature was also reported.[81, 100] Recently, in 2015 and 2016, Majid A. et al[101-102] theoretically demonstrated the modification of the electronic structure of Ce-doped AlN using first principle calculations. More recently, broad band emission from Ce doped AlN ceramic bulk material sintered at (1700 C and 105 MPa) has been reported^[41] but experimental evidence of the influence of Ce oxidation state on the emission of Ce-doped AlN is still missing. Hence, deep investigation of Ce-doped AlN thin films, compatible with the chip technology, is particularly desired.

Based on the above, this work is dedicated to the synthesis and study of the optical properties of crystalline Ce-doped AlN thin films grown at room temperature (RT) by radiofrequency (RF) magnetron sputtering. Strong blue emission has been obtained from the activated Ce ions after rapid thermal annealing (RTA). The origin of the blue emission is investigated by Electron Energy Loss Spectroscopy (EELS), PL and PL excitation (PLE) experiments. The PL thermal quenching mechanism is also investigated.

2- Results and discussion

2.1- Structures and compositions

Ce-doped AlN thin films with different Ce content have been prepared at room temperature using RF discharge sputtering. The sputtering conditions were described in the experimental chapter (II). XRD has been carried out to investigate the effect of Ce concentration on the crystal structure of *as*-deposited Ce-doped AlN films as shown in fig (4.1).

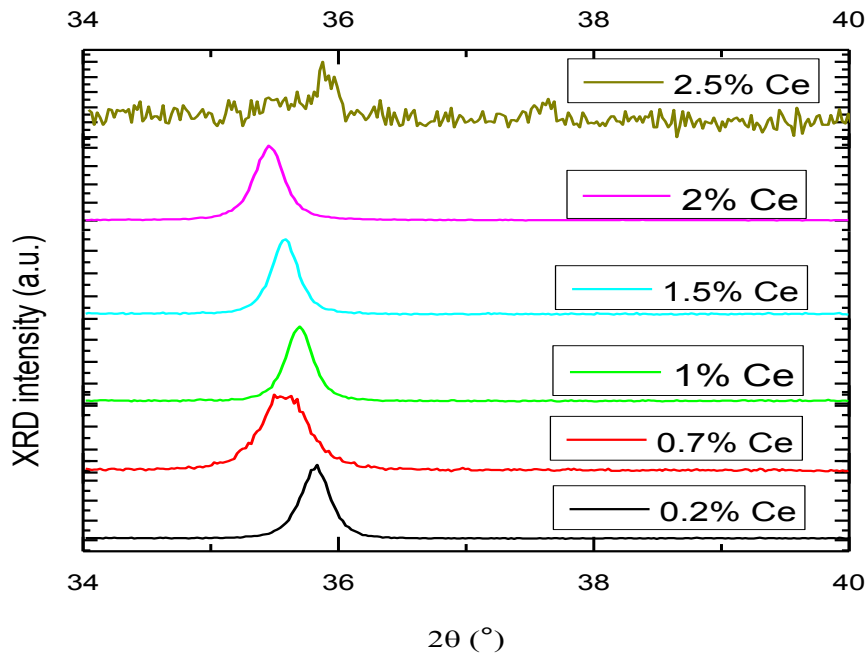


Fig. (4.1): XRD of Ce-doped AlN as-deposited films at different Ce concentrations.

The XRD spectra exhibit only the (002) reflection of the hexagonal wurtzite structure of AlN, indicating (002) planes are parallel to the substrate surface. The shift in the diffraction angle is attributed to the different strains induced in each sample. It can be noticed that sample with the highest Ce content of 2.5 at. % exhibits a strong degradation of the XRD signal, which points to a significant structural modification under high Ce contents. It also tend to indicate that AlN can accommodate Ce ions until 2 at.% without strongly altering the crystal structure of the matrix. Herein, most of our attention during this thesis has been given to the well crystalline samples. It is worth to mention that the concentrations of Ce have been determined using RBS measurements for selected samples. Then, the obtained RBS data were used as a reference for calibrating the EDS measurements for the other samples. Fig. (4.2) shows the RBS spectra performed with a 2 MeV He^+ beam by 5MV accelerator for some samples. The spectra reveal the typical RBS for AlN thin film as reported elsewhere,[161-162] with variation of Ce contents as can be seen at the high energy part of the spectra.

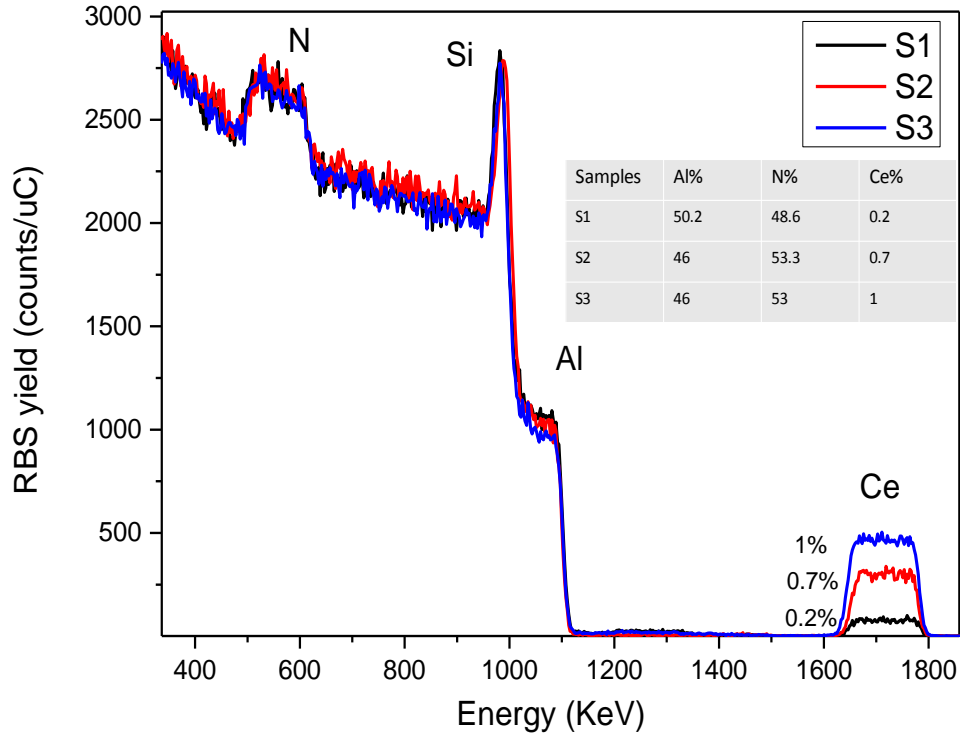


Fig. (4.2): RBS spectra for three selected as-grown Ce-doped AlN films.

In addition, the composition analysis shows a good stoichiometry between Al and N atoms, inset table. It is very common, in RE-doped materials, to perform *post*-deposition annealing in order to optically enhance the activator's luminescence.[112, 163-164] Thus, our samples were divided into small pieces (1 x 1 cm), then underwent a rapid thermal annealing step (RTA) at 1000 °C for 5 minutes under flow of Ar gas. Then, the steady state photoluminescence (PL) have been measured using the 325 nm excitation of a He-Cd laser. The PL spectra of the *post*-deposition annealed samples are displayed in fig (4.3a). All the PL spectra exhibit a broad band extended over the visible range from 400-600 nm with fundamental peak centered at 500 nm and full width at half maximum (FWHM) of about 100 nm. These PL spectra are consistent with the PL features of Ce³⁺ reported elsewhere.[74, 165] Fig (4.3b) shows the evolution of the PL intensity as a function of the Ce concentration. The optimum concentration for highest PL intensity is around 1 at.% (between 0.7 to 1.1%). The PL intensity increases with Ce concentration till 1% of Ce, then decreases at higher concentrations. This PL intensity behavior with RE concentration is common and usually attributed to RE ion-ion interaction process.[75]

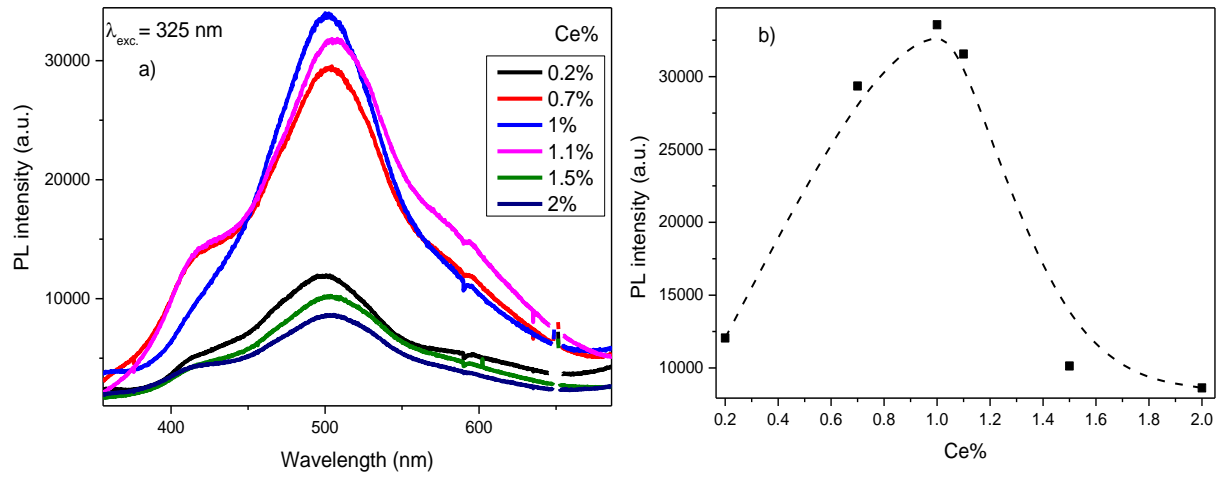


Fig (4.3): a) PL spectra for different Ce concentration. b) PL intensity evolution as a function of Ce%.

At relatively low concentration of Ce, the PL intensity increases as the number of emitting ions increase till it reaches a critical concentration. By further increasing the Ce concentration, the average relative distance between Ce ions is shorten and results in increasing the chance of nonradiative energy transfer between the neighboring ions that weakens the PL intensity. [74] The asymmetry in the PL spectra is sometimes referred to the inhomogeneous in the spin-orbital coupling of the ground states $4f$ [74, 166] and other times to the different lattice locations occupy by Ce ions.[167-168] However, the effect of interference on the PL spectra can't be excluded.

In the following section, we will focus mainly on the sample containing 1% of Ce. Deep structure and optical analyses on this sample will be presented in the following and compared to the results obtained for undoped AlN.

2.2- Structures and optical analyses of Ce-doped AlN

As-deposited 1% Ce-doped AlN sample was divided into two parts; one underwent RTA (1000 °C/5 min) together with undoped AlN under flow of Ar gas, the other was annealed at the same conditions but under flow of forming gas (FG). Annealing in forming gas has been performed to investigate the effect of a reducing atmosphere on the microstructure and the optical properties of the thin films.

2.2.1- X-ray diffraction (XRD)

Fig (4.4) shows the XRD measurements of doped and undoped *as*-deposited (As) and RTA samples. The XRD signals reveal the characteristic peak of (002) plane of the hexagonal

wurtzite structure of AlN, with the basal planes parallel to the substrate surface. No traces of metallic cerium could be observed within the detection limit in the X-ray diffractograms with 2θ angles ranging from 20° to 120° , fig. (4.4a).

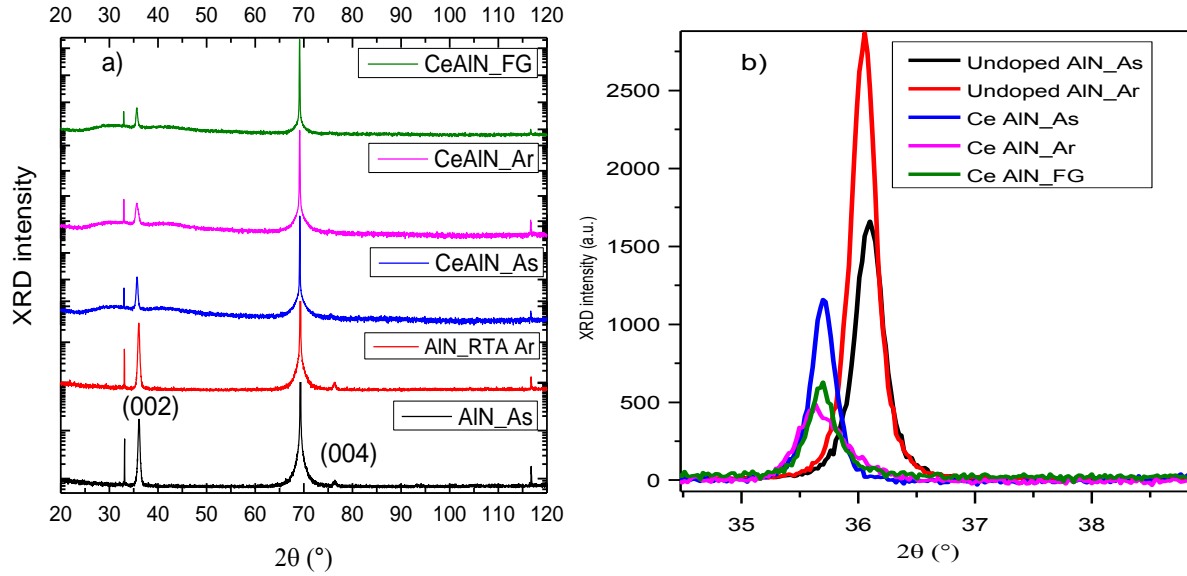


Fig. (4.4): XRD of as-deposited and annealed undoped and Ce-doped AlN films a) is the full range from 20° to 120° . b) is focusing around the 002 peak.

Moreover, metallic cerium was not detected using high resolution TEM at different positions throughout the films. The observed shift in the XRD of the doped samples, fig (4.4b), suggests that Ce incorporation induces modification in the AlN crystal lattice. In particular, the diffraction peaks of doped samples shifted to lower diffraction angles, indicating the incorporation of Ce expands the c -axis parameter, likely due to in-plane compressive stress induced by the large volume of Ce ions.[169] The average c -axis parameters of the prepared samples has been estimated using Bragg's law[170] and is found to be increased from 4.97 \AA to 5.04 \AA for undoped and doped samples, respectively. However, the XRD of the doped samples didn't show any reflection from other planes than (002) related to AlN within the detection limit. This indicates that, although the doping with 1% of Ce, the films exhibit crystallites with c -axis orientation normal to the substrate surface like undoped films.[171] In addition, the annealed undoped AlN sample exhibits higher (002) intensity than the *as*-deposited one. In contrast, doped samples present lower diffraction intensity with respect to the undoped counterpart and, in addition, a further intensity decrease after annealing. This could be attributed to the influence of thermal treatment that can enhance the crystallinity of undoped AlN by curing the material defects.[172] In doped AlN the presence of the foreign

atoms (Ce) inside the lattice could generate more defects under the thermal treatment. This likely occurs by initiating new kind of bonds with the surrounding atoms that degrade the crystal lattice structure. The degradation of XRD intensity in the doped samples in comparison to undoped ones is a familiar effect, particularly when the dopant atoms have larger ionic size than the native atoms. The degradation of the crystallinity is usually attributed to the lattice stress induced by the foreign atoms. In most cases the dopant atoms have either size and/or valance state mismatch with the substituted atoms that disturb the local environment. In our case, the ionic radii of cerium ions Ce^{4+} (101 pm) and Ce^{3+} (115 pm) are much larger than the ionic radius of Al^{3+} (67.5 pm). Effective substitution of Al by Ce leads to local changes in the crystal lattice and, in turn, affects the electronic structure of the material as well.[173] The change in the XRD linewidth and the increase of the c-axis parameter are indicative parameters of the microstructure modifications. For instance, the average strain over whole the thickness of the film (macrostrain) results in change in the c-axis and, in turn, shifting of the XRD signals. A significant shift in the XRD (002) peak position towards lower values in the diffraction angles is observed in the doped samples with respect to undoped ones, see table (4.1). This indicates that incorporation of Ce ions introduces strong macrostrain. The condensation process of the vapor phase itself can lead to macrostrain in undoped coatings with respect to the c-axis parameter for bulk AlN. See annex (C) for microstrain and macrostrain calculations.

Table (4.1): FWHM, XRD peak positions, macrostrain and microstrain values of undoped and Ce-doped AlN samples

	AlN_As	AlN_RTA	Ce-AlN_As	Ce-AlN_FG	Ce-AlN_Ar
FWHM (002)	0.2	0.16	0.18	0.25	0.44
Peak position (°)	36.10	36.06	35.69	35.63	35.61
Macrostrain	- 0.0014	-0.0002	0.0095	0.0113	0.0119
Microstrain	0.083	0.055	0.100	----	----

The microstrain values for undoped AlN films, table (4.1), exhibit a local strain relaxation after annealing the film, while doping with Ce ions induces a significant microstrain. The microstrain values for annealed Ce-doped AlN samples couldn't be determined because the (004) intensity was too small to be used in the microstrain estimation even after long integration time. Moreover, Ce-doped AlN_Ar sample is associated to the weakest diffracted intensity and broadest FWHM with hump at higher angles, which infers microstructural modification occurred after annealing in Ar. On other side, doped samples exhibit a less asymmetric XRD peak after RTA in FG, indicating that annealing in Ar induces a more

substantial modification of the structure. This is in line with the RBS and TEM observations in the next sections.

2.2.2- Fourier Transform Infrared Spectroscopy (FTIR)

FTIR analyses have been performed for all these samples in order to get more information about the vibrational states and the local order of the microstructure. As mentioned in the introduction chapter that the group theory predicts eight optical phonons ($2A_1+2E_1+2E_2+2B_1$) modes for hexagonal wurtzite AlN at the Γ point in the Brillouin zone. Among them A_1 and E_1 are IR active. It was reported that the transverse optical $E_1(\text{TO})$ is the predominant mode and mostly related to the (002) planes parallel to the substrate, while the transverse optical $A_1(\text{TO})$ mode is related to existence of other phases and/or tilting of the (002) planes.[23] In addition, the shifts in FTIR peak positions were linked to the residual stress variation in some studies.[25] FTIR signals of undoped AlN and Ce-doped AlN before and after annealing are depicted in fig (4.5).

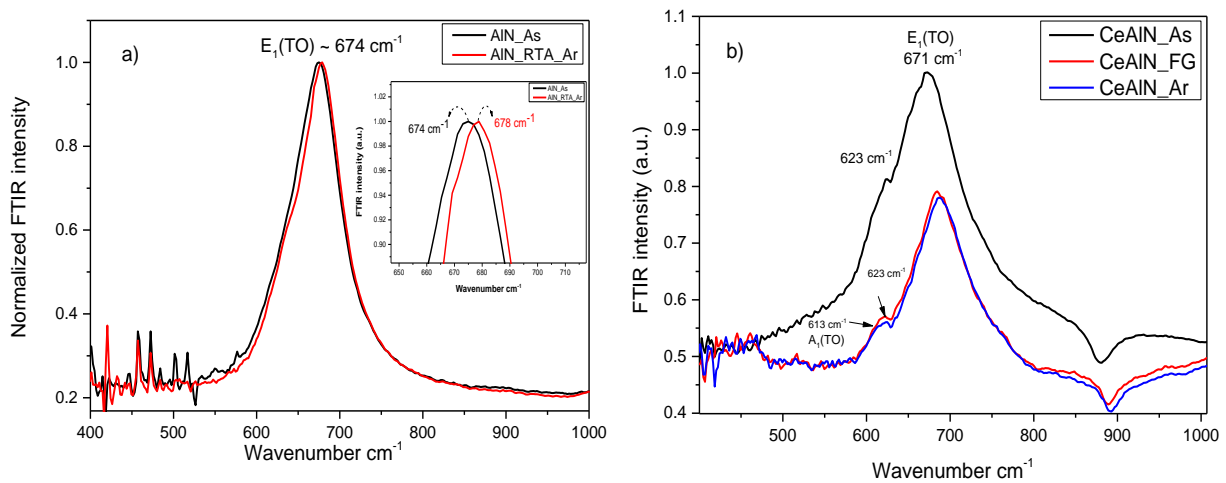


Fig. (4.5): FTIR spectra for as-deposited and annealed a) undoped AlN, and b) Ce-doped AlN

It can be observed that, $E_1(\text{TO})$ at $\sim 674 \text{ cm}^{-1}$ is the only mode in the undoped and doped samples, indicating that these samples are mostly oriented with (002) planes parallel to the surface, consistently with the XRD results. The slight shift in this peak is referred to residual stress as previously reported in.[25] A shift in XRD peaks is also attributed to lattice strain which confirms the assignment of $E_1(\text{TO})$ shift in FTIR to the same reason. In contrast, the $A_1(\text{TO})$ mode is found in the doped samples after annealing, as shown in fig (4.5b). This indicates that some (002) planes are tilted with reference to the film surface and/or the formation of other phases, which will be confirmed later by TEM.[23] The peak at $\sim 623 \text{ cm}^{-1}$ is

a signal from the Si substrate. The FTIR peak intensity at $E_1(\text{TO})$ mode in doped samples is deteriorated after annealing, which could be related to decreased crystallinity and/or loss of some Al-N bonds. All of these FTIR findings are in line with the XRD data presented in fig (4.4), as well as with the TEM results shown in the following sections.

2.2.3- Microstructure and composition

TEM measurements have been performed to get inside the microstructure of the prepared samples. Fig (4.6) shows the TEM images and the corresponding selected area electron diffraction (SAED) for undoped and Ce-doped AlN samples. All samples exhibit columnar structure with columns aligned in the growth direction and c -axis of the wurtzite cell of AlN perpendicular to the surface of the substrate. The SAED of the undoped sample shows that (002) spots are more localized compared to those of doped samples, which are slightly elongated. This indicates the small tilting of the (002) planes with respect to the film surface due to incorporation of the Ce ions. The TEM image of the doped sample after RTA in Ar evidences a bilayer structure, see fig (4.6d). The top layer (about 35 nm-thick) exhibits granular crystallites. This top layer has been found not only in this sample but in all of our Ce-doped AlN samples annealed in Ar atmosphere. A deep look inside this top layer indicates that, it contains voids and clusters with different orientations, as evidenced by the HRTEM and FFT in fig (4.6e). A similar surface modification phenomenon in *post*-deposition annealed films has been reported previously in RE-doped GaN.[174] It was attributed to the release of N surface atoms out of the sample during the annealing at high temperature (above 800°C) leaving N vacancies that could cluster to form voids and change the crystal structure. In addition, at high annealing temperature the partial pressure of residual oxygen inside the oven significantly increased.[175] Hence, as (N) atoms diffuse out of the film, residual oxygen atoms find an open way to substitute the (N) sites and alter the microstructure. To obtain precise information about the composition of the top layer, RBS have been performed for this sample and compared with the results of the *as*-deposited counterpart. Fig (4.7) shows the RBS spectra for *as*-deposited and after RTA in Ar for a Ce-doped sample. The regions corresponding to the different elements are labeled for identification. For each element (N, O, Al, and Ce), the eventual maximum energy of backscattered projectiles is given by the kinematic factor of the collision and corresponds to scattering events occurring at the surface.

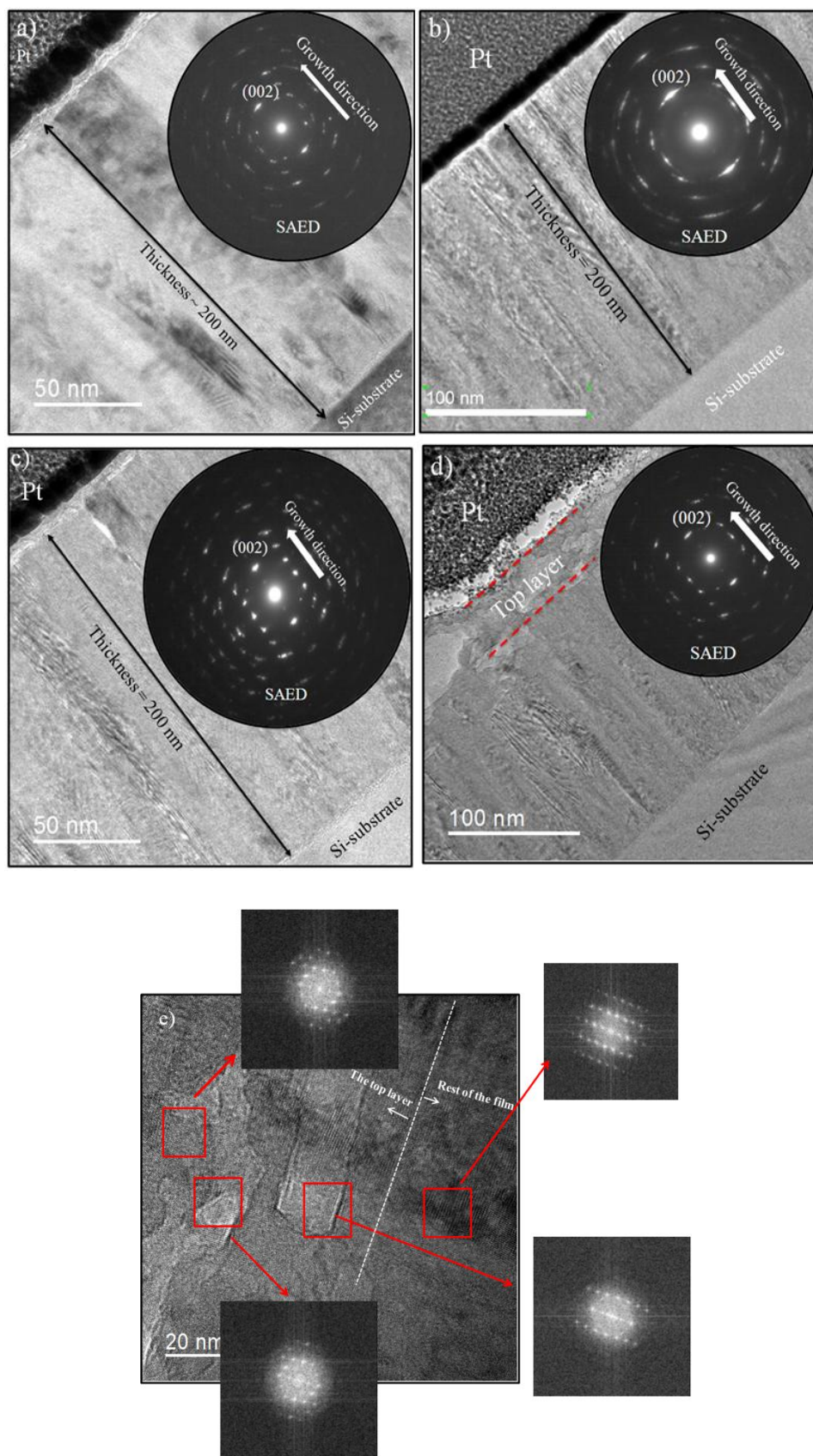


Fig. (4.6): TEM images and corresponding SAED patterns for undoped AlN (a), CeAlN_As (b), CeAlN_FG (c) and CeAlN_Ar (d). (e) HRTEM image with corresponding FFT of different regions at the interface between the top layer and the rest of the film in Ce AlN_Ar sample.

This energy increases with the atomic number of the scattering center. Events (counts) at lower energy correspond to collisions deeper in the sample since part of the projectile energy is lost on the way in and out of the sample. Hence, the broadness and shape of the elemental signals are indication of the film thickness and the elemental profile, respectively. Regarding the substrate signal, the thicker the film the lower the energy onset. Due to the similar atomic mass of Al and Si, the signals from these elements are partially overlapped. Also, since N and O are lighter than Si, their signals appear superimposed to that from the substrate. In the case of the *as*-deposited film, fitting of the RBS spectra indicates a relatively homogeneous film composition over the whole film thickness. However, as mentioned above, annealing in Ar result in a bilayer structure as evidenced from the step in the Ce signal. Here, the decrease in intensity at higher energies reflects a Ce depletion in the near surface region. In parallel, this surface layer is highly oxidized as derived from the appearance of narrow O band that correspond to the near-surface region.

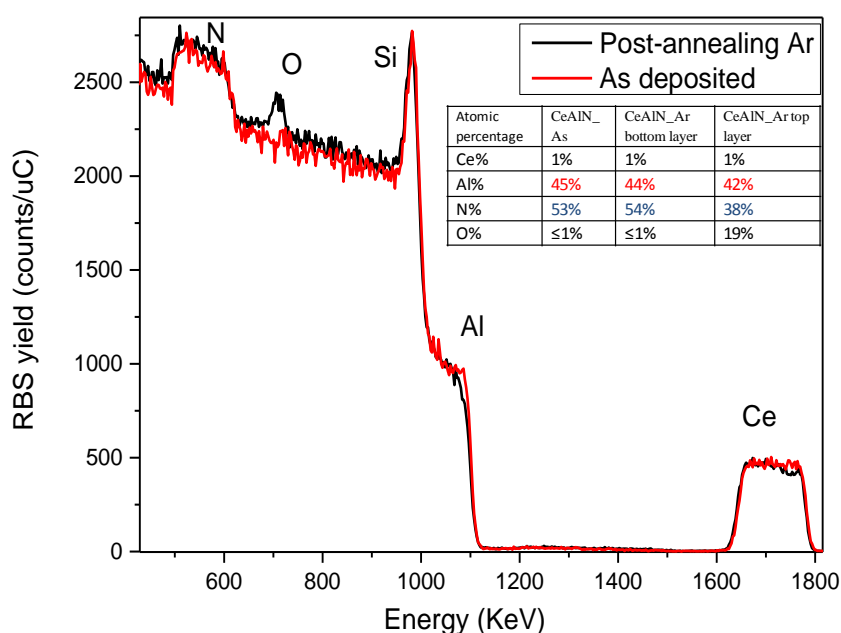


Figure (4.7): RBS signal and fitting data for the CeAlN *as*-deposited and annealed in Ar films. Inset: table with the atomic content of film constitutive elements for the best fitting of RBS data.

This region in the annealed sample also contains a lower N content as compared to the *as*-deposited, see inset table fig. (4.7).

To evaluate the influence of the annealing atmosphere on local bonding, one can consider the following thermodynamic equilibrium equation[175]:

$$\frac{4}{3}AlN + O_2 = \frac{2}{3}Al_2O_3 + \frac{2}{3}N_2, \quad (4.1)$$

that works in the forward direction at high O₂ pressure (case of Ce-doped AlN after RTA in Ar) to stabilize Al-O bonds and in the reverse direction where the N₂ pressure increases to stabilize Al-N bonds (case of Ce-doped AlN after RTA in FG). In addition presence of hydrogen in the forming gas reduces the amount of residual oxygen. Hence, the latter explains why the surface of samples annealed in FG remains smooth. In addition, as noticed from the RBS data, the increase in oxygen content is higher than the decrease in nitrogen one. This is in line with reports indicating that oxygen atoms form Al_{0.66}O as they substitute nitrogen in AlN.[34, 176-177] Therefore, one Al vacancy (V_{Al}) is generated every three O atoms.

2.2.4- Photoluminescence (PL)

In order to study the luminescence behavior of Ce-doped AlN thin films, the undoped and doped samples have been excited by He-Cd laser with 325 nm line and by continuous wave (cw) Nd:YAG laser at the fourth harmonic 266 nm. Figure (4.8) shows the room temperature PL with excitations at 325 nm and 266 nm. The PL shows the same behavior under both excitation wavelengths. Ce-doped AlN sample after RTA in Ar exhibits a strong blue PL intensity as compared to the other samples. The broad PL band is centered at 500 nm and the blue emission can be clearly seen by the naked eye, as shown in the inset of Fig.(4.8a). This PL band is in good agreement with a Ce-related emission. Other samples, undoped and doped (*as-deposited* and after RTA in FG), show one order of magnitude weaker PL intensities than the Ce-AlN sample annealed in Ar, as seen in the inset of fig (4.8a). These weak PL bands (400-600nm) are usually observed in AlN and attributed to defects inside the bandgap. These defects have mostly been assigned to V_{Al} and oxygen related defects.[178-180] The weak PL intensity might also indicated presence of low concentration density of optically activated Ce ions even after annealing in FG. This behavior was similarly observed in all of our samples with different cerium contents.

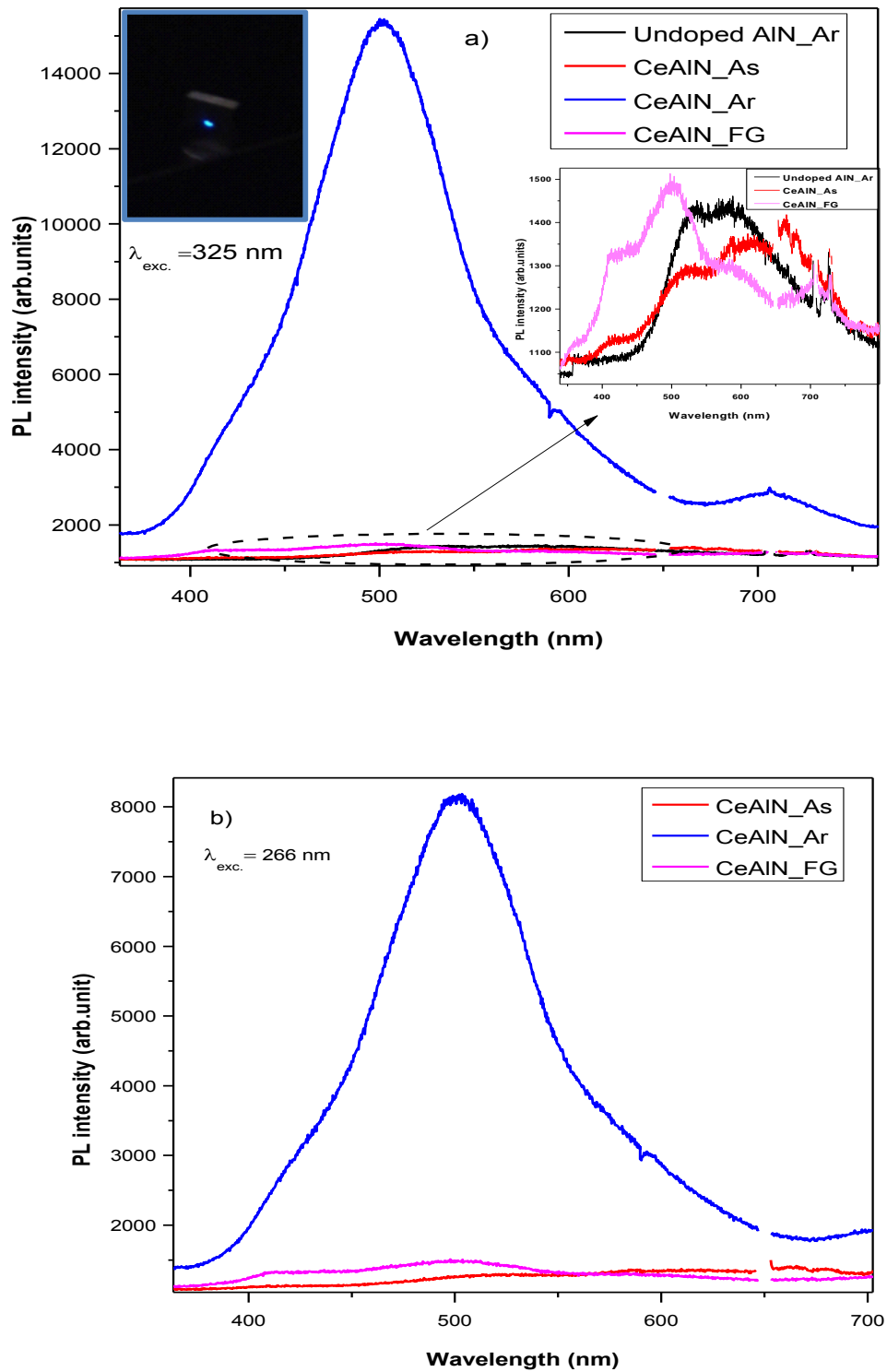


Fig. (4.8): PL of undoped and Ce-doped AlN films excited by a) 325 nm and b) 266 lasers. Inset of fig (4 a): Magnification on the very weak spectra for clarification. Inset photo image: visible blue light emitted from the photo-excited CeAlN_Ar film.

For instance, fig (4.9) shows PL spectra of two samples containing different Ce% (0.7 and 2.5 %) and *post*-deposition RTA annealed in Ar, N₂ and FG. The two samples exhibit weak PL intensity in case of RTA_FG compared to RTA_N₂ and RTA_Ar. This indicates that the PL intensity evolution is linked with the annealing atmosphere and exhibits common behavior in Ce-doped AlN materials independently of the Ce concentration. As indicated above, annealing in Ar results in the formation of a superficial oxidized layer. Therefore, one can suppose that the oxidation plays a role in the photoluminescence. This assumption can be supported by considering the thermodynamic findings of C.-Y. Lin et al[175], who demonstrated that the level of oxidation of AlN annealed in N₂ is higher than annealed in FG because of the difference in the *Gibbs free-energy of oxidation*, ΔG , at around 1000 °C; $\Delta G(N_2) = -581 \text{ kJ/mol} \ll \Delta G(FG) = -491 \text{ kJ/mol}$. This could explain the higher PL intensity in RTA_N₂ than in RTA_FG.

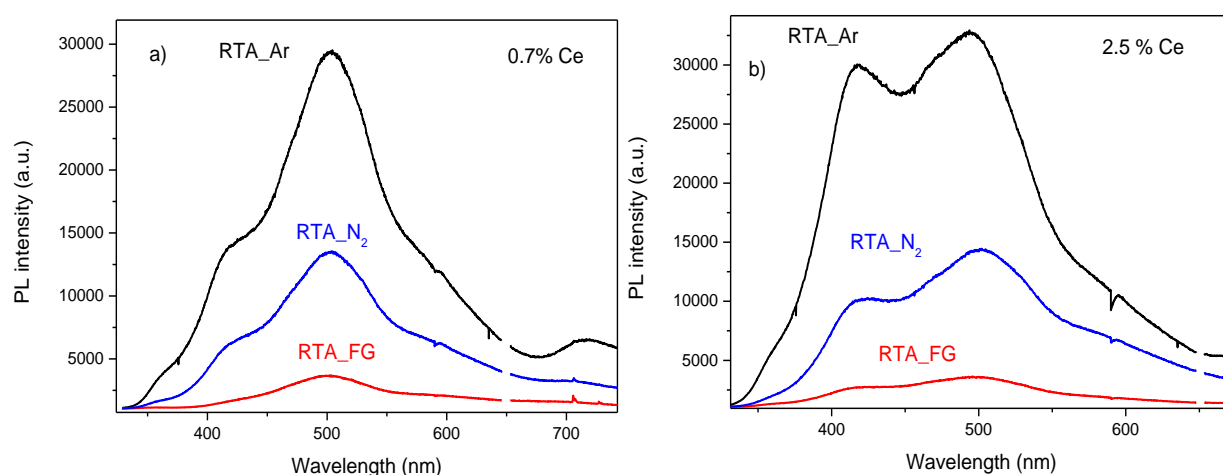


Fig. (4.9): PL spectra of Ce-doped AlN post-deposition annealed at 1000 °C/5 min in Ar, N₂ and FG for two samples a) 0.7% Ce and b) 2.5% Ce.

It has been reported that *post*-deposition annealing of RE-doped phosphors activates the luminescence by modifying the local environment of the RE ions.[181-182] For instance, the thermal annealing (TA) of Sm-, Eu- and Yb-doped amorphous AlN thin films leads to activation of the RE ions by promoting some structural rearrangement and curing the matrix from defects as demonstrated in.[112] In the latter work, it was proposed that the significant improvement of the PL after TA is correlated with the suppression of tail defect states and with the reduction of the probability of non-radiative pathways. Interestingly, the strong PL enhancement in our Ce-doped AlN sample after RTA in Ar, fig (4.8a), is in good agreement with the enhancement factor reported in[112] after TA under the same conditions. This

suggests that AlN films doped with different REs require similar TA treatments to activate a strong PL emission. However, our results show that the PL intensity not only relies on the temperature or duration of the annealing process but also on the type of atmosphere. One can conclude that the *post*-annealing treatment has two contributions. First, thermal assistance reduces the density of non-radiative defects by rearranging the film structure. Second, the annealing environment plays the major role, probably, because it generates and controls the type of defects inside the structure as already reported for other materials.[183-185] Hence, the PL behavior could be understood by considering the activation mechanism of Ce ions. It is known that Ce ions exist in two different stable oxidation states, Ce^{+4} and Ce^{+3} . Ce^{+4} has no electron in its outer shell orbital ($4f^0$). It can therefore be considered as optically inactive while Ce^{+3} has only one electron in its $4f^1$ state that can be responsible for optical emission by $4f$ - $5d$ transitions. Combining the concept of optical activation of Ce ions and the PL intensity correlation with the level of oxidation deduced using different annealing atmosphere; one can guess a link between the oxygen and the activation of Ce ions. Thus, to better understand the PL results and gain information about the oxidation state of Ce, EELS measurements have been performed. EELS is a useful tool to determine the oxidation state of Ce, characterized by two lines referred as M_5 and M_4 band edges at 883 eV and 901 eV, respectively.

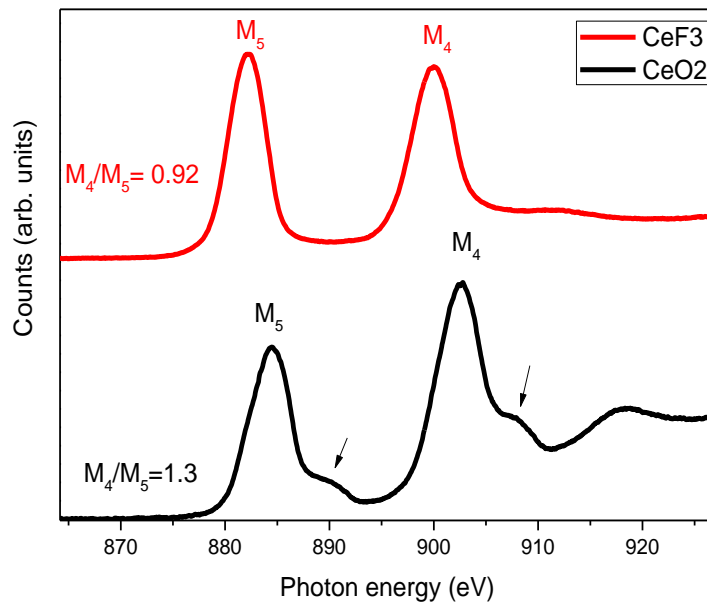


Fig. (4.10): EELS at Ce M-edges peaks for CeO_2 and CeF_3 reference samples.

These features are associated to the orbital splitting of $3d$ - $4f$ transitions. Fig (4.10) shows the EELS spectra for CeO_2 (Ce^{4+}) and CeF_3 (Ce^{3+}) reference samples where the presence of Ce^{4+}

can mainly be distinguished by a shoulder, absent in Ce^{3+} , at 5 eV above those of the two main peaks. In addition, in some reported cases a peak shoulder for Ce^{3+} appears at lower energy in the M_4 peak.¹⁹ Another method developed to evaluate the Ce oxidation state from EELS is the peak intensity ratio between M_4/M_5 . [186] It is found about 0.92 for Ce^{3+} in CeF_3 and 1.3 for Ce^{4+} in CeO_2 in our reference samples. The EELS measurements have been performed for Ce-doped AlN *as*-deposited and annealed samples in order to probe the signal response from Ce ions. Considering all the above methods to determine the Ce oxidation state, we found that all doped samples exhibit EELS spectra corresponding to the Ce ions band edges spectra in agreement with the reported spectra elsewhere. [186-187] Fig (4.11) shows the EELS of Ce-doped AlN films *as*-deposited and after RTA in FG. In both samples, the characteristic peak shoulder for Ce^{4+} that appears at higher energy beside M_4 and M_5 edges.

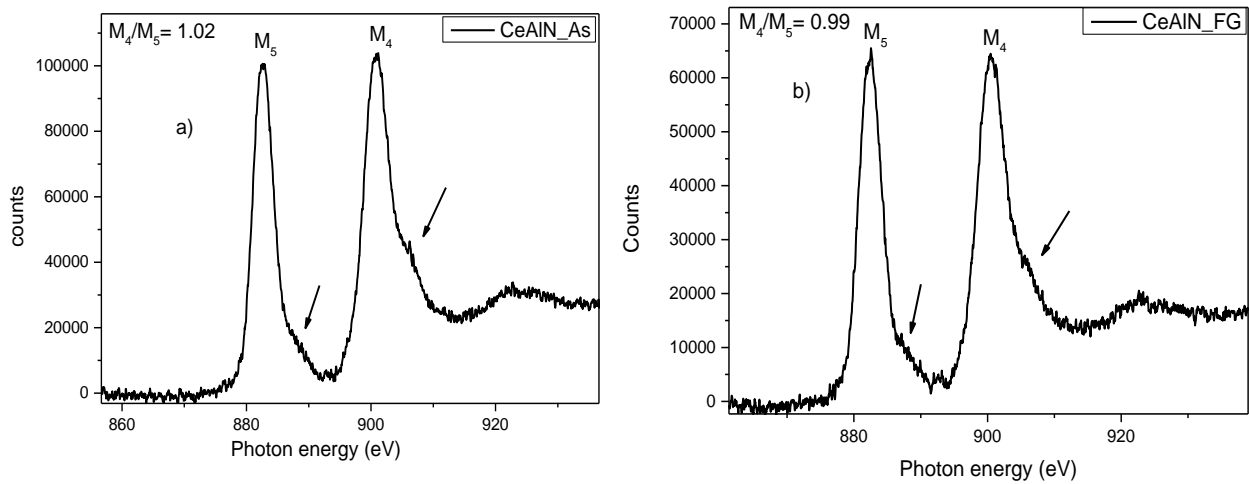


Fig. (4.11): EELS at Ce M-edges peaks for a) CeAlN_As, and b) CeAlN_FG.

This means that both samples exhibit EELS signal close to the signature of Ce^{4+} . That reflects the predominance of 4+ oxidation state of Ce inside these samples. This is consistence with the weak PL response from these samples as the optically inactive Ce ion is the predominant. On the other hand, EELS measurements have also been performed at different areas in the Ce-AlN sample after RTA in Ar, fig (4.12). EELS probed from the top layer (containing oxygen) exhibits very close signal to the Ce^{3+} where the peak shoulder appears above the M_4 and M_5 is absent as well as appearing of peak shoulder before the M_4 band. In contrast, the signal from the rest of the film (bottom layer) shows predominant Ce^{4+} oxidation state. It means that, the presence of oxygen plays a major role in the activation of Ce ions by changing the valence

state from +4 to +3. This is in line with the previous assumption made from the results of PL at different annealing atmosphere and the level of oxidation. Moreover, we can infer that the PL of this sample mostly originates from the top layer, which raises the question about the role of oxygen in the PL behavior.

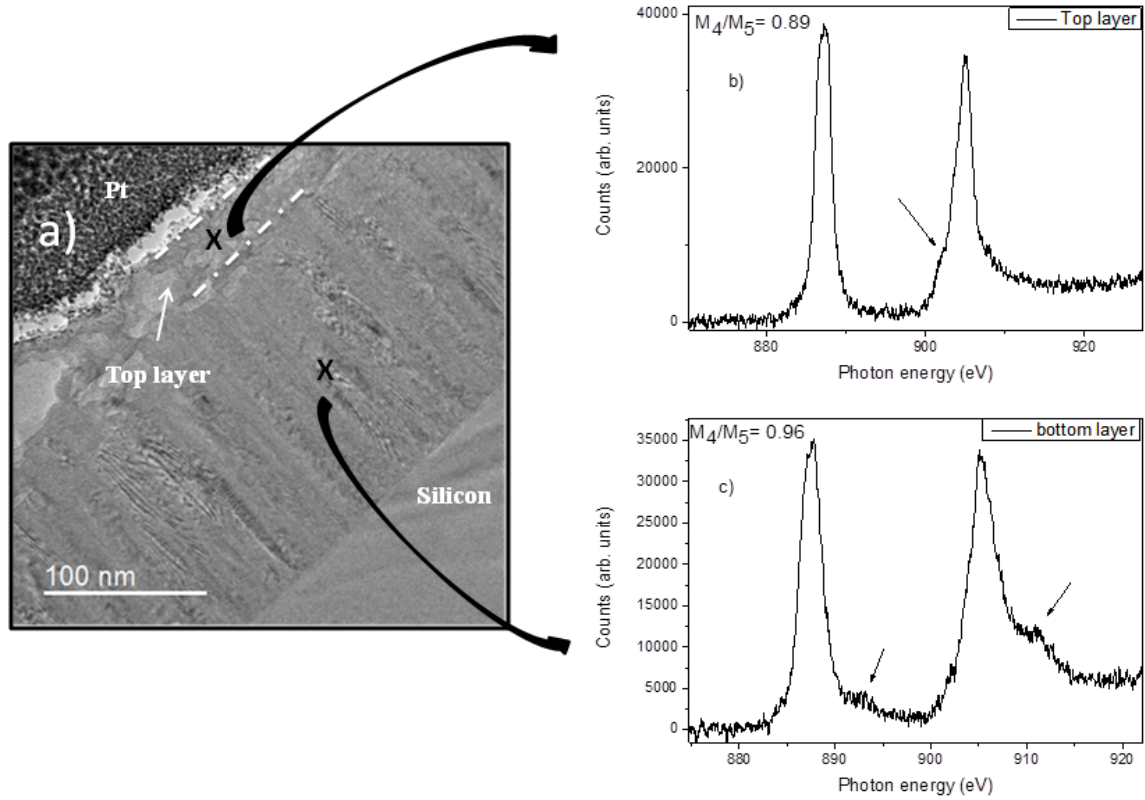


Fig. (4.12): a) TEM image for Ce AlN_Ar labelled with the location of corresponding EELS measurements for Ce M-edges peaks at b) the top layer c) the bottom layer.

2.2.5- The role of oxygen

To understand the role of oxygen, it is convenient to explore what happens when oxygen diffuses inside the AlN matrix. It has been reported that AlN exhibits very large affinity for accommodating oxygen, being the most common impurity in AlN that can't be totally avoided. Therefore, several studies were dedicated to figure out the role of oxygen in AlN. It is widely established that oxygen enters AlN as Al_2O_3 not as AlO. Therefore, the incorporation of oxygen inside AlN proceeds by substituting the nitrogen sites accompanied by formation of aluminum vacancies for charge balance according to the following equation:[188]



In this case, one molecule of $\text{Al}_{0.67}\text{O}$ substitutes one molecule of AlN and leads to constitute this formula $(V_{\text{Al}})_{0.33}\text{Al}_{0.67}\text{O}$, where (V_{Al}) denotes aluminum vacancy. Hence, each three oxygen atoms, one aluminum vacancy is formed.[34, 176] The substituting oxygen atom O_{N}^+ acts as shallow donor with a level at $E_v + 5.85$ eV in AlN . [189] C. Stampfl et al [31] demonstrated that, the formation energy of O_{N}^+ is very low, particularly at low Fermi level as AlN tends to be n-type by attracting impurities forming donor levels. In addition, the triply negatively charged aluminum vacancy V_{Al}^{3-} exhibits the lowest formation energy under high Fermi level conditions. It also lies close to the valence band maximum and acts as a deep acceptor level in AlN . [31] Therefore, V_{Al}^{3-} acts as an effective compensating center for the shallow levels formed by oxygen O_{N}^+ . Moreover, Mäki et al [190] demonstrated by using positron annihilation experiment that all O atoms have a neighboring V_{Al} and suggested that a defect complex related to coupling O_{N}^+ with V_{Al}^{3-} is predominant over isolated V_{Al}^{3-} defect.

Qimin Yan et al, [179] have used hybrid-functional calculations to determine the formation energy, transitions levels and the optical properties of defects in AlN . Their results show that the association of O_{N} and V_{Al} leads to formation of $V_{\text{Al}}\text{-O}_{\text{N}}$ complex and involves electron transfer from O_{N} to V_{Al} . They also demonstrated the formation energy of the most common defects in AlN as a function of Fermi level as displayed in fig (4.13).

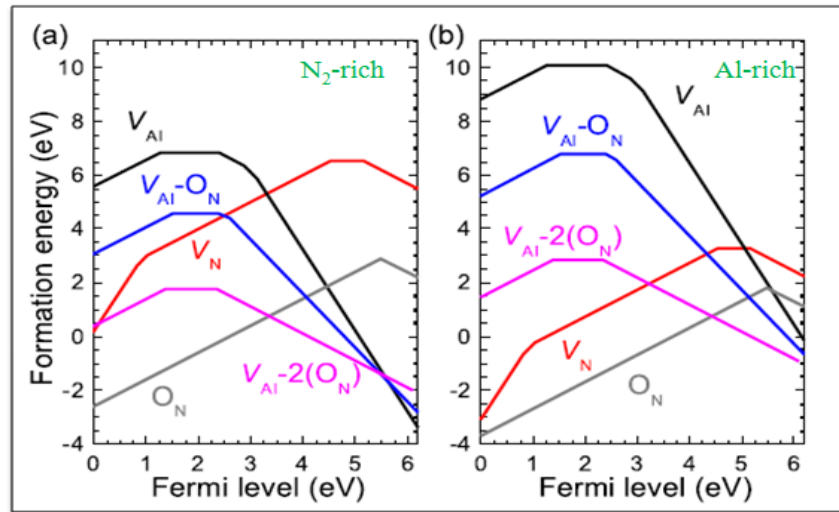


Fig. (4.13): Formation energies as a function of Fermi level for the nitrogen vacancy V_{N} , aluminum vacancy V_{Al} , oxygen impurity O_{N} , and vacancy oxygen complexes $V_{\text{Al}}\text{-O}_{\text{N}}$ and $V_{\text{Al}}\text{-2}(\text{O}_{\text{N}})$, under (a) N-rich and (b) Al-rich conditions.[191]

It can be noticed that the formation energy of aluminum vacancy-oxygen complexes is lower in N-rich than Al-rich conditions. In addition, the formation energy of $V_{\text{Al}}\text{-O}_{\text{N}}$ complex is

found lower than the formation energy of isolated V_{Al} in most of the Fermi level positions. Therefore, it is recognized that there is a strong driving force for Al vacancy to form complex with oxygen impurity. Hence, $(V_{Al})^{3-}$ is likely coupled to O_N^+ to form singly and/or doubly negatively charged $(V_{Al}-O_N)^{2-}$ and $(V_{Al}-2O_N)^{1-}$ complexes depending on the oxygen concentration, which is consistent with previously reported works.[180, 192] Furthermore, these defect complexes are found to contribute in absorption and luminescence processes. B. Berzina et al[193] suggested that, the O_N defect and the coupling between O_N and V_{Al} complex are responsible for the UV-blue PL in AlN. The authors also proposed a model to interpret the concept of luminescence center containing oxygen related defects, where these defects can be excited directly or indirectly through the host material. More precisely, in the same line, it has been reported by using several experimental measurements such as cathodoluminescence and PL that the defect complexes $(V_{Al}-O_N)^{2-}$ and $(V_{Al}-2O_N)^{1-}$ give rise to an absorption band around 3.9 eV and 4.7 eV, respectively.[192, 194-197] Consistently with this experiments, Qimin *et al* [179] found by hybrid-functional calculations that $(V_{Al}-O_N)^{2-}$ in AlN materials is responsible for an absorption band around 3.9 eV (317nm) due to electronic transitions $[(V_{Al}-O_N)^{2-} \Rightarrow (V_{Al}-O_N)^{1-} + e]$ and another electronic transition $[(V_{Al}-2O_N)^{1-} \Rightarrow (V_{Al}-2O_N)^0 + e]$ is responsible for an absorption band at an energy higher than 4.3 eV that depends on the oxygen content.

Based on the abovementioned information, the presence of Ce^{3+} in the oxidized surface layer can be interpreted as follows:

In the *as*-deposited and the Ce-doped AlN samples annealed in forming gas, where the content of oxygen is very low, Ce^{4+} is dominant. In contrast, when oxygen is unintentionally inserted in Ce-doped AlN annealed in Ar atmosphere, Ce^{3+} is dominant. These findings point to the role played by oxygen which can be explained as follows. When, oxygen diffuses in AlN and substitute N site, O_N^+ forms donor level accompanied by the release of one electron. This electron is likely responsible for the valance state change of Ce^{4+} to Ce^{3+} in the oxidized region. Further, Ishikawa et al[81] reported another energetically stable defect complex that involves Ce^{3+} when $(V_{Al})^{3-}$ connects with nearby Ce_{Al} in Ce-doped AlN material. This can also likely happen in the oxidized layer as the density of $(V_{Al})^{3-}$ is increased due to presence of oxygen. Therefore, these kinds of defects may explain the valence state changes of Ce and the predominance of Ce^{3+} in the EELS of the top layer, as well as indicate that strong PL emission can be interpreted by *5d-4f* transition of Ce^{3+} . However, obtaining similar PL excited by two different wavelengths, as in fig (4.8), raises a question about the excitation mechanism of Ce^{3+} . To investigate the excitation mechanism for the Ce-doped AlN sample after RTA in

Ar, PLE has been measured for the emission peak at 500 nm, see fig (4.14). It reveals two broad excitation bands around 3.9 eV and 4.8 eV. This indicates that there are two pathways responsible for the blue emission peak at 500 nm.

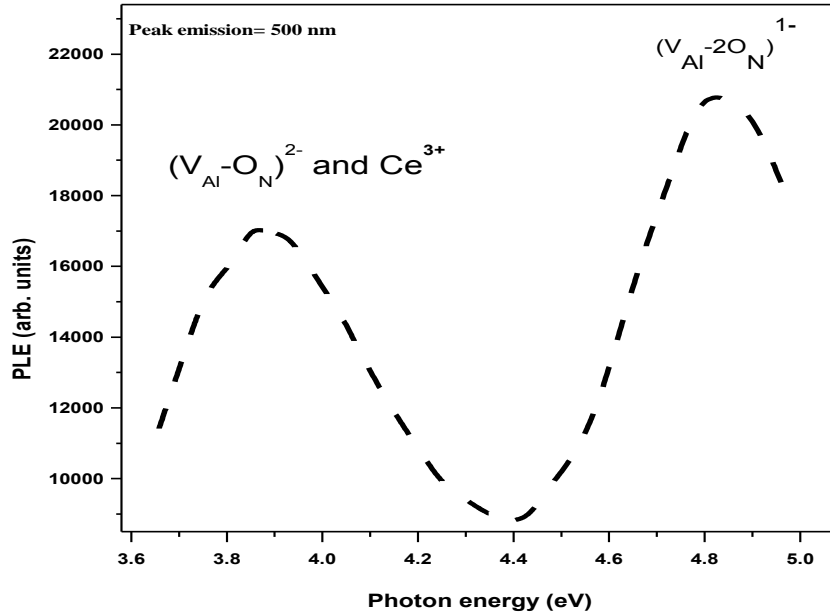


Fig. (4.14): PLE spectra recorded at emission peak 500 nm for the Ce-doped AlN_Ar film.

It is worth noting that, the absorption peak at 3.9 eV is very close to the reported absorption band of Ce^{3+} . [198-200] As well as, it is very close to the electron transition in this defect complex $[(\text{V}_{\text{Al}}-\text{O}_{\text{N}})^{2-} \Rightarrow (\text{V}_{\text{Al}}-\text{O}_{\text{N}})^{1-} + e]$, as demonstrated above. Hence, the first band (3.9 eV) can be assigned either to the defect transition $(\text{V}_{\text{Al}}-\text{O}_{\text{N}})^{2-/1-}$ [179] or to the absorption band of Ce^{3+} . [201-202] The second band (4.8 eV) can be referred to an $(\text{V}_{\text{Al}}-2\text{O}_{\text{N}})^{1-}$ complex at high oxygen concentrations, as reported elsewhere. [34, 179, 190]

Indeed, the excitation mechanism (either direct or indirect) for Ce^{3+} ions, when excited by 325 nm, is then rather difficult to determine due to the overlapping between the excitation bands for Ce^{3+} and $(\text{V}_{\text{Al}}-\text{O}_{\text{N}})^{2-}$ complex at 3.9 eV. Although, the high absorption cross section of Ce^{3+} stimulates the assignment of the band at 3.9 eV mainly to the direct absorption of Ce^{3+} . Nevertheless, the indirect excitation mechanism of Ce^{3+} ions via $(\text{V}_{\text{Al}}-\text{O}_{\text{N}})^{2-}$ complex cannot be excluded from several aspects. First, a good agreement is found between the excitation peak around 3.9 eV in our Ce-doped AlN sample and the reported absorption peak of the $(\text{V}_{\text{Al}}-\text{O}_{\text{N}})^{2-}$ complex in AlN. [179, 194, 196] Second, indirect excitation can be very efficient in several RE-doped III-V semiconductor compounds. [30, 203] Third, the PLE peak at 4.8 eV

demonstrates that Ce^{3+} ions can be efficiently indirectly excited. Furthermore, indirect excitation of Ce was tested by the detection of PL excited by 266 nm laser (4.66 eV) close to the 4.8 eV band and away from the suspected absorption band for Ce^{3+} , see fig (4.8b). Then, when the sample is pumped at 325 nm, direct and indirect excitations can occur simultaneously. Direct excitation arises from the absorption by Ce^{3+} transferring an electron from $4f$ orbital to $5d$ orbital and emitting photons at 500 nm during the relaxation process. Indirect excitation can be achieved via energy transfer from excited $(\text{V}_{\text{Al}}\text{-O}_{\text{N}})^{2-}$ defect to a nearby Ce^{3+} ion.

To emphasize on the role of the defect complexes in the PL, two samples have been prepared: one under Al-rich conditions (formation of V_{Al} is energetically difficult) and the second one under N-rich conditions (formation of V_{Al} is relatively easier, as found in the formation energy diagram of fig (4.13)). These samples have then been annealed in Ar atmosphere. Fig (4.15) shows the PL of these samples excited by 325 nm. The PL intensity of the N-rich sample is stronger than that of Al-rich sample, which is consistent with the excitation mechanisms proposed.

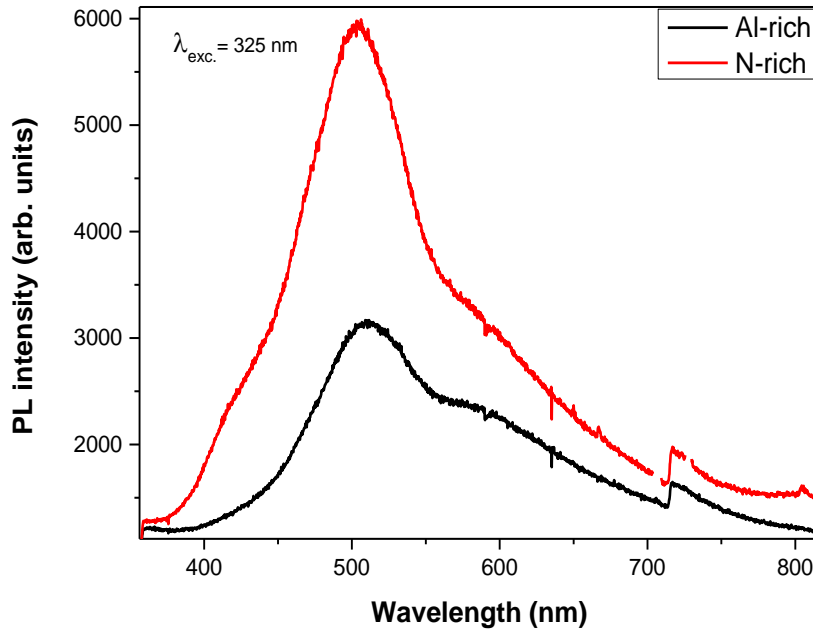


Fig. (4.15): PL of two Ce-doped AlN samples annealed in Ar and prepared at Al-rich and N-rich conditions.

In other words, an increase of the PL intensity can be stimulated by higher density of V_{Al} that leads to more activated Ce^{3+} ions and/or higher density of $\text{V}_{\text{Al}}\text{-O}_{\text{N}}$. This confirms the significant role of V_{Al} -related defects in the PL and supports the previous explanations.

The role of oxygen can be summarized as shown in the following diagram, fig (4.16a).

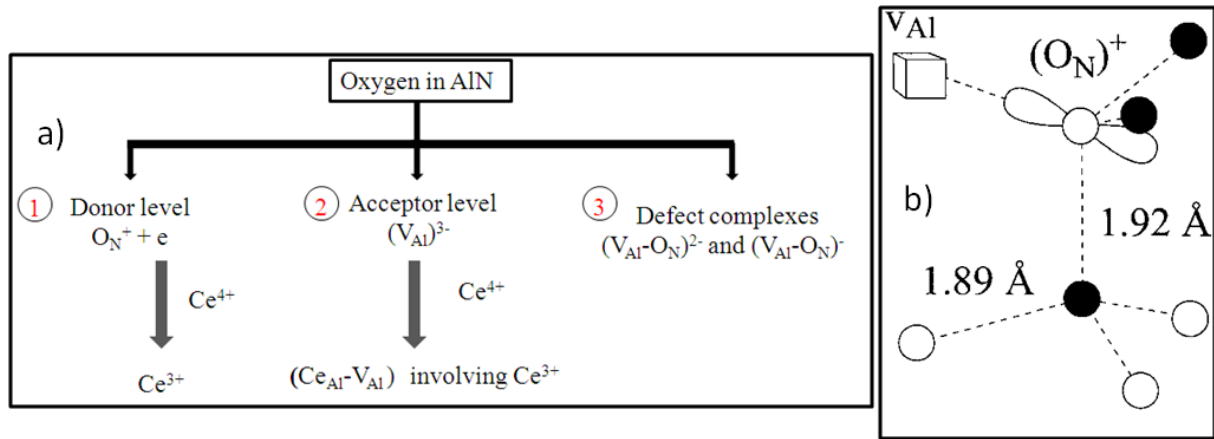


Fig. (4.16): a) Schematic presentation for the different proposed processes occurred in oxygen doped Ce-AlN. b) Schematic model for the formation of the defect complex $V_{Al}-O_N$ in AlN.[204]

When the oxygen diffuses inside AlN, it creates three kinds of defects (donor level O_N^+ , acceptor level V_{Al} and $V_{Al}-O_N$ defect complexes) which contribute significantly in the photoluminescence. Both O_N and V_{Al} defects contribute in the valance state change of Ce^{4+} to Ce^{3+} . In addition, a nearby O_N and V_{Al} defects interacts to form the defect complex $V_{Al}-O_N$, as depicted in fig (4.16b), which participates in the excitation mechanism, as assigned in the PLE fig (4.14). The previous findings clearly show the essential role of oxygen in the photoluminescence of Ce-doped AlN. To confirm our previous interpretation oxygen has been intentionally introduced during the growth of Ce-doped AlN films.

2.3- Intentionally doping oxygen during Ce-AlN growth

To incorporate oxygen during the growth of Ce-doped AlN, a flow rate of oxygen was applied using a very fine tuning valve that allows controlling the partial pressure of oxygen before the deposition. The partial pressure of oxygen was set to 0.1×10^{-6} torr, while keeping the total pressure almost unchanged. This results in Ce-doped aluminum (oxy)-nitride (Ce-Al(O)N) films with oxygen content of about 7% as measured by EDS and calibrated by RBS. Then, the sample underwent to *post*-deposition annealing in the FG and Ar atmospheres. The photoluminescence of the films has been measured using excitation wavelength 325 nm. Fig (4.17) shows the PL spectra of *as*-deposited and annealed samples.

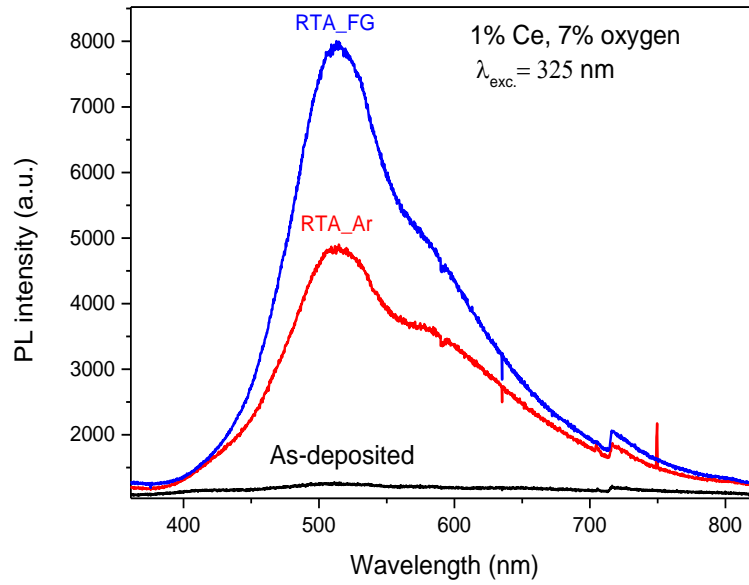


Fig. (4.17): PL spectra for as-deposited, Ar, and FG annealed 1% Ce-doped Al(O)N sample with oxygen content 7%.

The PL spectra show that, the sample annealed in forming gas exhibits intense PL intensity, higher than the one annealed in Ar. In addition, the *as-deposited* sample reveals very weak PL signal even if it contains 7% oxygen. This result clearly confirms that oxygen and *post-deposition* annealing are required to activate the photoluminescence from Ce-doped AlN material. In the previous section, it was found that beside the electronic modifications in Ce oxidation state and the formation of defect complexes, *unintentional* oxygen induces structural modifications. Thus, the following section is focusing on the structure and the electronic picture of *intentional* incorporation of oxygen in Ce-doped AlN. Fig (4.18) shows the XRD of the prepared Ce-doped AlN and Ce-doped Al(O)N samples. It is observed that incorporation of oxygen drastically degrades the (002) diffraction peak. This points to the strong modification occurring in the lattice structure. Therefore, TEM and EDS measurements have been performed to have a deep look on the microstructure and composition of Ce-doped Al(O)N sample. Fig (4.19) shows the TEM images of *as-deposited* and annealed (in Ar and FG) 1% Ce-doped Al(O)N. The oxygen contents for different areas throughout the cross section of the layer are measured by EDS and indicated in table (4.2).

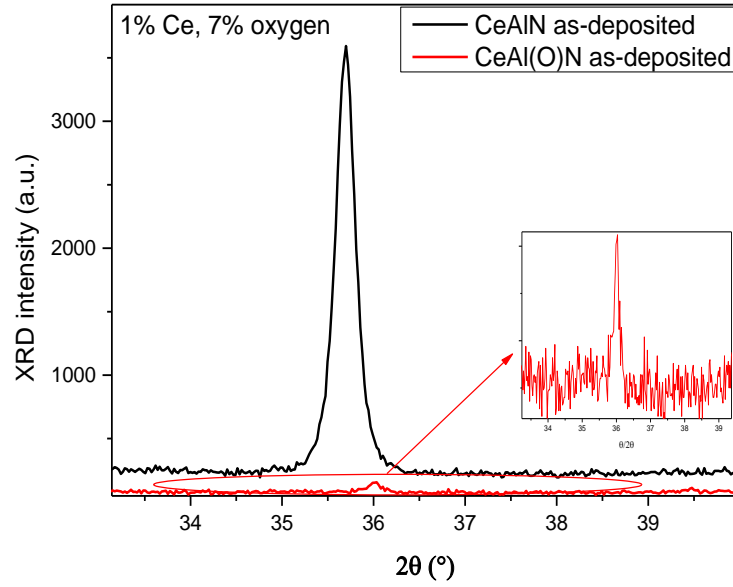


Fig. (4.18): XRD of *as*-deposited Ce-doped AlN and Ce-doped Al(O)N samples.

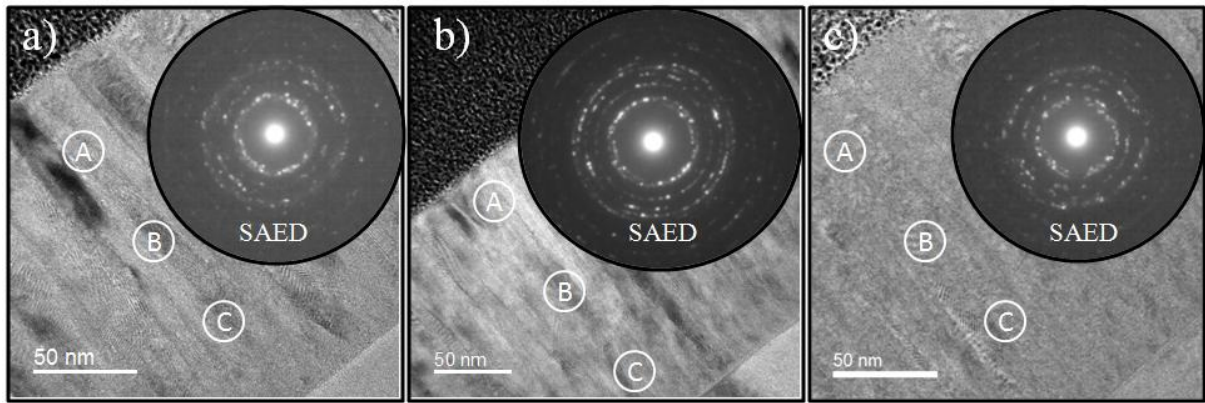


Fig. (4.19): a), b), and c) are TEM images with corresponding SAED patterns for Ce doped Al(O)N of 7% oxygen as deposited, FG, and Ar annealed samples, respectively.

Table (4.2): EDS results for oxygen content at A, B, C regions as indicated in the TEM images of fig (4.19)

	As-deposited	RTA_FG	RTA_Ar
A	7.5%	8%	13%
B	7%	7%	10%
C	7.5%	7%	8%

It can be observed that all samples exhibit films with polycrystalline structure, as evidenced by the corresponding SAED patterns. EDS data show the oxygen content at different regions labeled A, B and C in each sample. The average content of oxygen in *as*-deposited and RTA_FG samples is about 7% whereas it is slightly higher at 13% in RTA_Ar sample near the film surface and gradually decreases down to the bottom. This further confirms our

findings about the diffusion of oxygen inside the layer during the *post*-deposition annealing in Ar. On the other hand, to figure out the oxidation state of Ce ions in these samples, EELS has been performed at different points in each sample. Fig (4.20) shows the EELS spectra for the *as*-deposited, RTA_Ar and RTA_FG samples. All samples reveal EELS signals very close to the signature of Ce^{3+} , which means a majority of optically active ions are present in these samples even in the *as*-deposited sample.

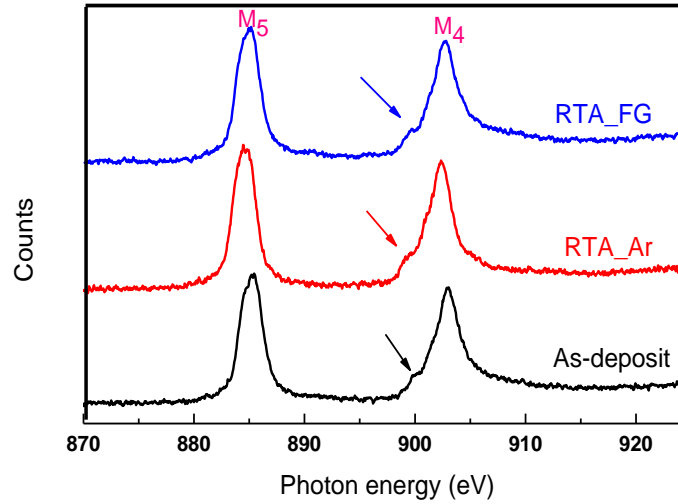


Fig. (4.20): EELS at Ce M-edges peaks for *as*-deposit and annealed Ce-doped Al(O)N.

These results strongly evidence that, incorporation of oxygen in AlN is responsible for the valence state change in Ce ions from +4 to +3. In addition, it indicates that RTA is needed to stimulate the PL even with presence of Ce^{3+} , as found in the case of *as*-deposited sample exhibiting very weak PL signal although it contains mostly Ce^{3+} .

Hence, the above results drive to this conclusion:

- The major valence state of Ce in AlN is Ce^{4+} (optically inactive)
- The major valence state of Ce in Al(O)N is Ce^{3+} (optically active)
- However, to sensitize the PL from Ce-doped Al(O)N thin film, the post-deposition annealing is necessary.

Then, the findings can be summarized as follows: Oxygen without RTA or RTA without oxygen raise to the same "weak PL". The two processes are needed together for initiating the PL. The specific role of annealing in this regard will be discussed later. Two remaining questions could be raised in order to draw a complete picture about the behavior of oxygen and Ce inside AlN.

The first: Can the role of oxygen (O_N)⁺ as donor level be played by other impurities in AlN?

The second: What is the reason behind the stability of Ce^{4+} in AlN, in absence of oxygen, even after annealing at high temperature in FG?

The first question can be addressed by considering the work published by T.-C. Liu et al[74] about the blue emission from Ce co-doped with Si in AlN powder. The authors reported about the absence of PL from Ce-doped AlN powder without the co-doping with Si^{4+} ions. Although the authors couldn't determine the exact role of Si^{4+} in the PL of Ce-doped AlN, the valence state change approach can be used to interpret this behavior. Knowing that Si^{4+} favorably substitutes Al atoms from an energetical point of view and forms a donor level, Si_Al^+ , which releases an electron for charge compensation.[31] This electron is likely captured by Ce^{4+} ion to form the optically active Ce^{3+} , hence the PL can be activated. This observation supports our interpretation about the role of donor level played by oxygen in our case. Hence, one can reach to a general conclusion that Ce^{4+} is stable inside the AlN matrix and, in order to activate the photoluminescence, introduction of donor levels is needed to generate electrons for reducing Ce^{4+} in to Ce^{3+} . Thus, the reply to the first question is: the role of oxygen is a functional role related to the electronic state "donor level" generated by substituting the nitrogen sites. However, in our opinion, using oxygen to play this role in AlN could be better than other impurities due to the ease to dope AlN with oxygen. Oxygen is considered as a permanent impurity inside AlN, especially in industrial field and in large scale production. In that case, the difficulty to free AlN from oxygen can be turned into advantage to activate the PL in Ce-doped AlN.

Regarding the second question, the stability of the high oxidation state Ce^{4+} in AlN can be attributed to presence of a large number of N^{3-} ions surrounding it in the AlN crystal. In more details, Landrum, G.A.,[205] demonstrated that Ce^{4+} exists even in CeN that "formally" contains Ce^{3+} . Their findings were attributed to the substantial *d* character of the remaining electron in Ce^{3+} that delocalizes in the direction of the Ce-Ce interaction instead of being localized in the *f* states. In Contrast, in Ce-doped Al(O)N samples, the presence of oxygen breaks the local structure and electronic symmetry around Ce ions by altering the bonding system in different ways either with O atoms or by formation of V_Al .

It is worth noting that the PL intensity of Ce-doped Al(O)N sample annealed in FG is higher than for the same sample annealed in Ar as shown in fig (4.17), despite the later one exhibits more oxygen particularly near the surface. The diffusion of oxygen into the film surface during annealing in Ar is associated with a diffusion of nitrogen out of the film as described

above in the case of *unintentional* diffusion of oxygen. This in/out diffusion process results in structure disturbance that can produce voids and some nitrogen vacancies which can play the role of nonradiative defect centers and reduce the PL intensity. As described by C. Stampfl et al [31], the formation energy of positively charged nitrogen vacancy (V_N^{3+}) is low and this defect likely forms at high temperature. Thus, it can be proposed that (V_N^{3+}) combines rapidly with the generated (V_{Al}^{3-}) to form voids and reduces the chance to form Ce^{3+} by interacting with (V_{Al}^{3-}). On the other hand, using RTA in FG where the diffusion of oxygen is avoided, the probability to produce such defects is low. In addition, the hydrogen in forming gas probably passivates the nonradiative centers.

In order to investigate on the microstructural modifications induced by oxygen, HRTEM of Ce-doped Al(O)N sample has been performed and compared with that of Ce-doped AlN sample, see fig (4.21). The HRTEM images of both samples show local structural defects indicated by the red arrows in fig (4.21a, b), likely induced by dopant atoms. More precisely, the HRTEM of Ce-AlN_{As} shows some random local structure disorder (as indicated by the red arrows, fig (4.21a)) that may be due to incorporation of Ce ions. This local disorder in the microstructure leads to significant microstrain, as mentioned above (see annex C) and reported in.[206] However, the crystallites are mostly oriented along the [002] direction of AlN (see, the direction of the white arrows) as also evidenced by the intense localized spots in the diffraction pattern, as show in fig (4.6a). The HRTEM image of Ce-Al(O)N_{As} sample reveals a higher density of structural defects. In particular, some regions appear with amorphous-like structure (indicated by the red arrows fig (4.21b)) and lateral discontinuity in the atomic arrangements near the grain boundaries (white arrays of arrows) is observed. In addition, crystallites present different crystalline orientations along the growth direction resulting in the presence of partial rings in the SAED pattern, fig (4.19a). Despite some of these defects could be attributed to the presence of Ce ions due to the large ionic radius of Ce that induces microstrain in the crystal lattice, we mainly ascribe these structural modifications to oxygen incorporation.

Such structural modifications have been generally observed in all of our samples with intentionally incorporating oxygen, compared to Ce-doped AlN with a very low oxygen content of about 2%.

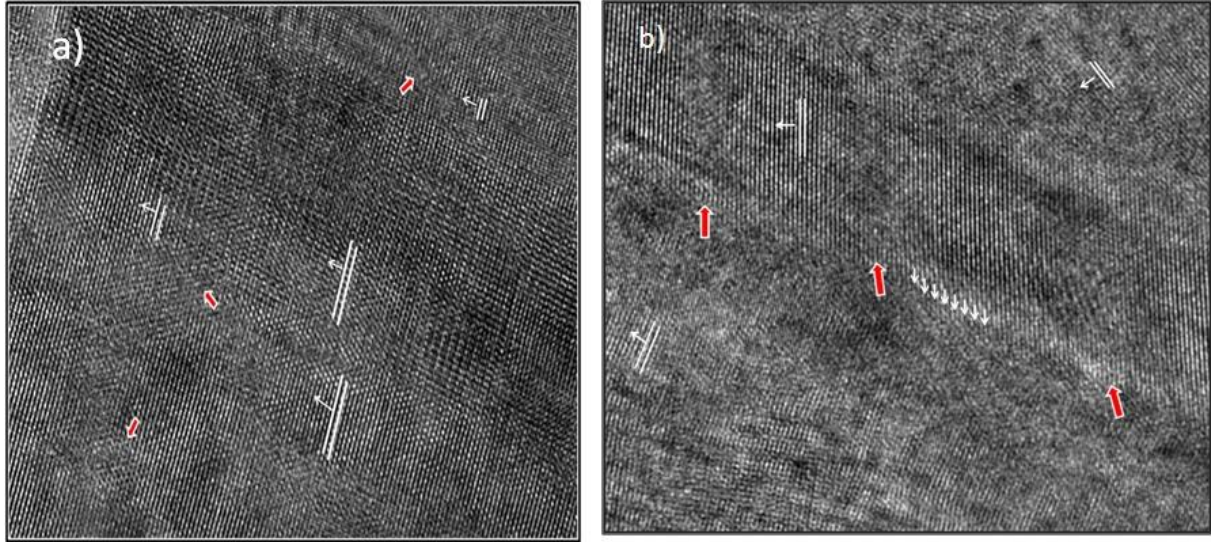


Fig. (4.21): HRTEM of a) 1% Ce-doped AlN, and b) 1% Ce-doped Al(O)N with 7% oxygen.

- **The effect of higher oxygen content and the role of annealing**

Emphasizing on the role of oxygen, two other samples with higher concentration of oxygen were prepared and annealed in FG. One sample contains 13% of oxygen (Ce-Al(O)N_13%). The second sample contains 60% oxygen and is nanocrystalline with α -Al₂O₃ as shown in fig (4.22). The cerium content is 1 at.% in both samples. Fig. (4.22) shows HRTEM image and the corresponding Fast Fourier Transform pattern (FFT) for 1% Ce-doped Al_xO_y containing 60% oxygen. The HRTEM image displays very small nanocrystals of Al₂O₃ that can be observed by the highlighted lattice planes and identified to Al₂O₃ by indexing the FFT (JCPDS 46-1212). Hence, this sample can be considered as the oxide counterpart to our set of Ce-Al(O)N samples.

The PL spectra of these samples, as depicted in fig (4.23), show increase in the PL intensity with the oxygen content. This can be attributed to the increase in the number of the optically active, Ce³⁺, ions as well as oxygen offers better local environment for efficient excitation and emission pathways. In addition a shift in the PL peak positions is observed with oxygen content. Interestingly, this shift in the PL peaks is sufficient to change the observed emission color from faint blue to faint green, then to strong blue as seen the photos of fig (4.23).

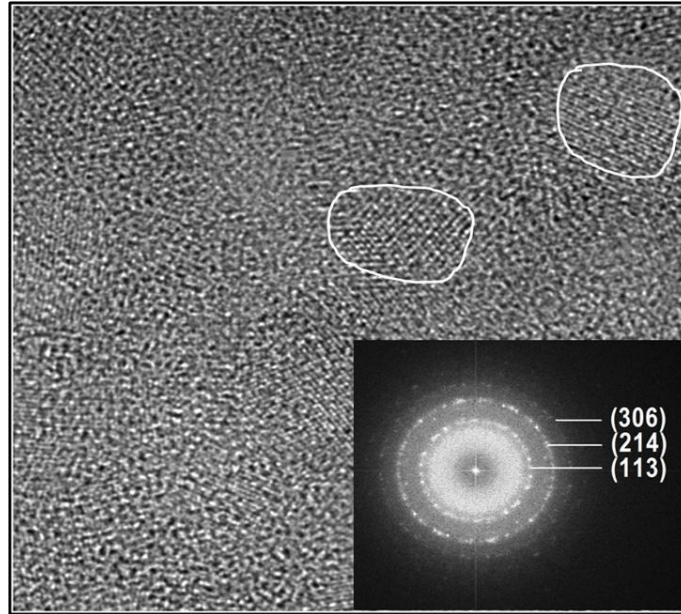


Fig. (4.22): HRTEM image and FFT pattern of 1% Ce-doped Al_xO_y contains 60% oxygen sample.

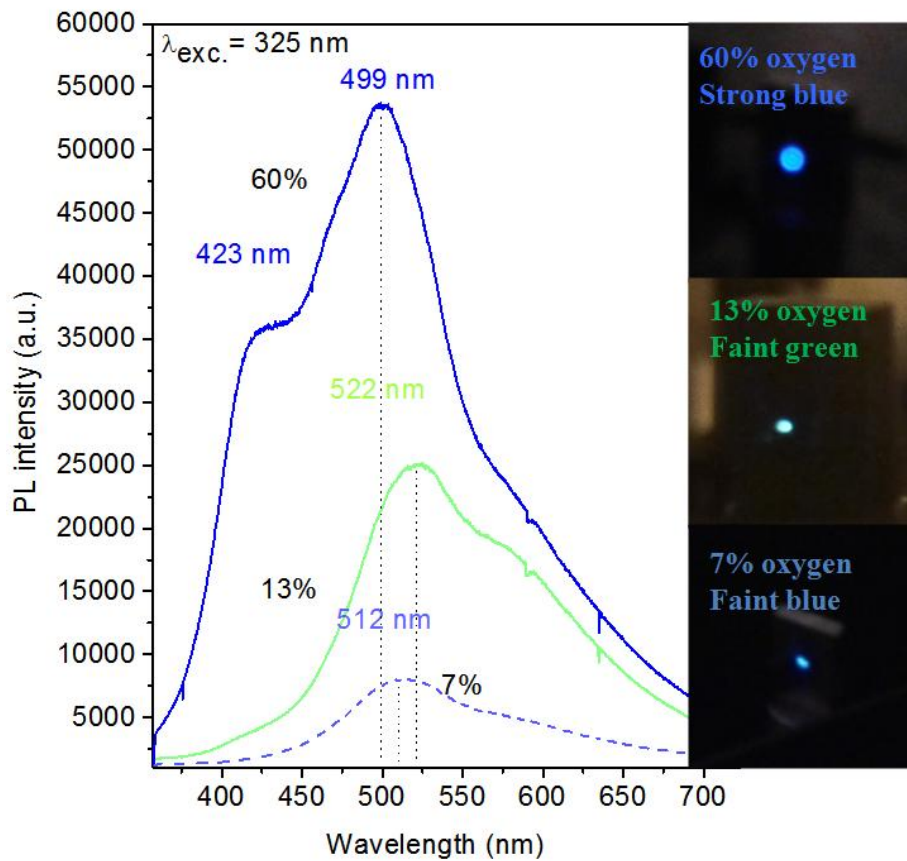


Fig. (4.23): PL spectra with the corresponding eye observed emission photos of *post*-deposition annealed Ce-doped Al(O)N at oxygen contents of 7%, 13% and Ce-doped Al_xO_y -60%.

The change in color is realized because the PL peaks lay between two adjacent color regions (end of blue at 500 nm and beginning of green at 522 nm). This evolution can be explained by

modification of the local environment around Ce^{3+} ions. More precisely, it has been reported that changing the local coordination ratio between oxygen and nitrogen around Ce^{3+} modifies the energy position of the excited $5d$ -level of Ce.[168] In addition, the difference in the formal charge between N^{3-} and O^{2-} ions as well as the difference in their electronegativity values (3.04 for N and 3.44 for O) induces a significant modification in the local fields that surround the excited $5d$ -level of Ce^{3+} when the O/N ratio is changed. This opens the possibility to tune the emission color from Ce^{3+} by modifying the local environment of the host material. This is considered as a unique character of Ce^{3+} over all the other RE^{3+} . [168] To the best of our knowledge this is the first demonstration of such effect in Ce-doped AlN.

It is worth to mention that only the annealed Ce-doped Al(O)N sample exhibits a strong PL despite as-deposited Ce-doped Al(O)N also contains a majority of Ce in the optically active Ce^{3+} state in the EELS fig (4.20). This reveals the presence of Ce^{3+} is not the only condition to activate PL but that it must be accompanied by a *post*-deposition annealing step. The role of annealing in this regard is not clear yet, but it is believed it can reduce the density of non-radiative defects acting as PL quenching centers.[112] Moreover, annealing at such high temperature can provide sufficient energy to initiate new local bonds between oxygen with Al and/or Ce atoms. In order to gain information about the influence of annealing on the bonding structure, EELS at the Al $L_{2,3}$ -edges were measured in Ce-doped AlN, Ce-doped Al(O)N, and compared to Ce-doped Al_xO_y sample, fig (4.24). It can be observed that major changes are detected in EELS spectra around 80 eV and 124 eV bands. The shape of the 80 eV band, consisting of three sub-bands, is the same for AlN and Al(O)N hosts, while it is different in the case of Al_xO_y . Hence, this band can be used as a sign to the general phase transition from AlN to Al_xO_y , as reported elsewhere.[207] On the other hand, the band at 124 eV is practically absent in AlN and as-deposited Al(O)N while it is intense in Al_xO_y and annealed Al(O)N. This band is also a feature of the electronic structure of Al_2O_3 . [207] This infers that the annealed Al(O)N exhibits some Al_xO_y characters even if the material is mostly AlN, which can be explained by the local formation of Al-O bonds in annealed Al(O)N.

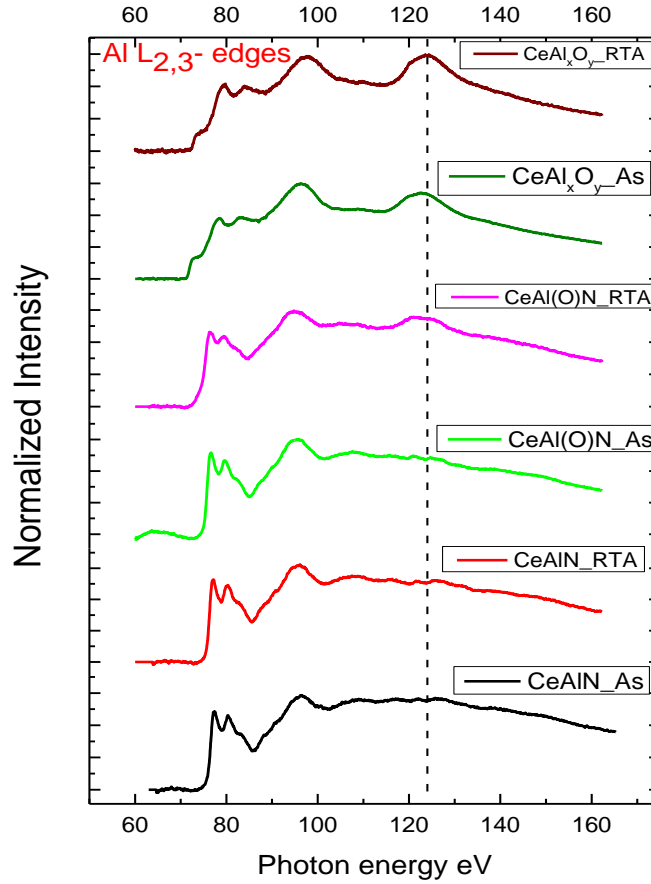


Fig. (4.24): EELS at the Al $L_{2,3}$ -edges of as-deposited and annealed Ce-doped AlN, Ce-doped Al(O)N, and Ce-doped Al_xO_y samples.

Photoluminescence excitation (PLE) of the annealed samples has been measured in order to get more information about the excitation mechanism and figure out why annealing activates the PL. Fig (4.25) displays the PLE spectra for Ce-doped Al(O)N_FG samples incorporating 7 and 13 at.% oxygen and annealed aluminum oxide one. The PLE spectra of the oxynitrides reveal two main broad bands located around 3.74-3.86 eV and 4.9 eV. On the other hand, aluminum oxide exhibits only one broad excitation band centered at 3.99 eV, which highlights a significant difference in the excitation mechanism between oxynitrides and the oxide. The assignments of the PLE bands have been reported previously.[34, 177, 191] The absorption peaks around 3.7 to 4 eV can be referred to the overlapping between the absorption band of Ce^{3+} and the absorption band of the specific stable defect complex $(V_{Al}-O_N)^{2-}$ in the Al(O)N matrix. The absorption band from 4.6 to 5 eV is usually referred to another defect complex $(V_{Al}-2O_N)^-$ found at higher oxygen content.

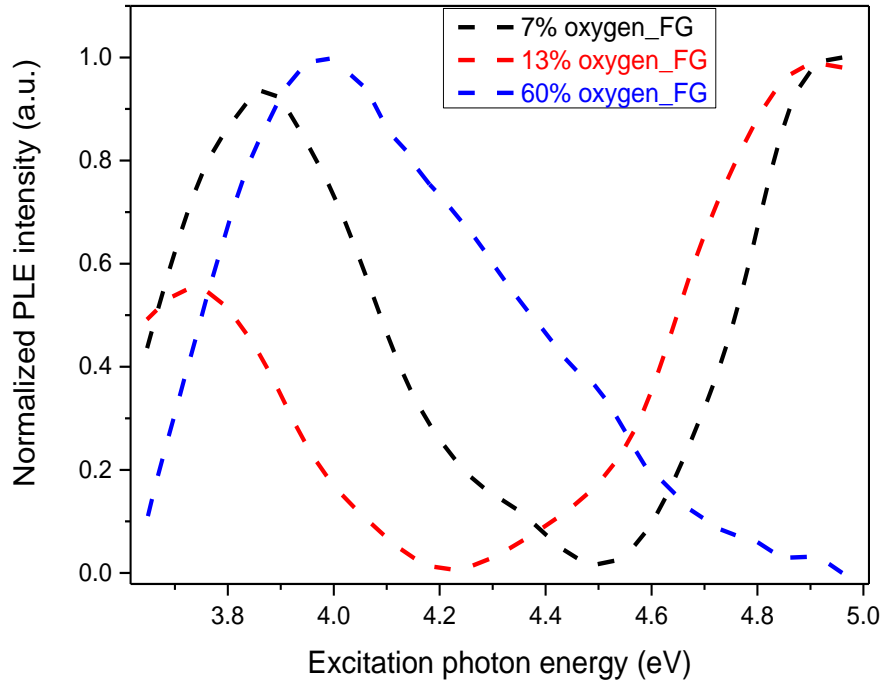


Fig. (4.25): PLE spectra for Ce-doped Al(O)N and Al_xO_y with 7%, 13%, and 60% oxygen annealed samples.

This defect complex acts as a donor (D) - acceptor (A) pair (D: Oxygen, A: V_{Al}) and participates to the energy transfer from the host to the emitting ions.[72] As annealing generates Al-O bonds and triggers the formation of V_{Al}, its role on PL activation through both excitation routes appears evident. Nevertheless, under excess of oxygen, as in the Al_xO_y-60% sample, the PLE band close to 5 eV is drastically quenched. Upon incorporation of a large amount of oxygen, the density of V_{Al} is likely decreased due to the coupling of the excess of oxygen over V_{Al} and occupancy of the V_{Al} sites by O atoms, as reported by Kita, T. et al[72] in the case of Gd-doped AlN. Hence, the density of V_{Al}-2O_N defect complex is reduced and the energy transfer path from this defect to the activator "Ce³⁺" is blocked. In addition, the PLE band at 4 eV became broader and blue shifted, probably due to the absorption of high number of activated Ce ions. It also can be concluded that Ce³⁺ in Al₂O₃ sample is directly excited.

2.4- Low temperature photoluminescence dependence (LTPL)

The PL behavior of rare earth-doped semiconductor at low temperature is a significant tool used to give information about the optical mechanisms. At low temperature, the non-radiative processes induced by phonon interactions are reduced. This leads to the modification of the PL signal due to a competition between the radiative and non-radiative processes. These modifications can be manifested in the PL intensity, position and spectral shape. Finding the good correlation between these PL evolutions with temperatures will lead to better understanding the excitation and recombination processes. Generally speaking, the PL intensity is commonly enhanced with cooling down the temperature of the material, due to the reduction of the non-radiative phonon interactions with the emitting species. However, the PL intensity evolution with the temperature can't be easily predicted. In some cases, where the excitation process depends on non-radiative energy transfer, lowering the temperature deactivate the energy transfer process and results in reduction of the PL intensity. In other cases, some emitting states exhibit thermal activation behavior that stimulates the radiative recombination, hence the PL intensity increases.

In the following, the PL has been studied as a function of temperature for 1% Ce-doped Al(O)N sample with oxygen content of 7%. The PL signals were recorded at different temperature values from 78 K to 295 K under excitation wavelengths 325 nm. Fig (4.26) shows the PL spectra recorded at different temperature.

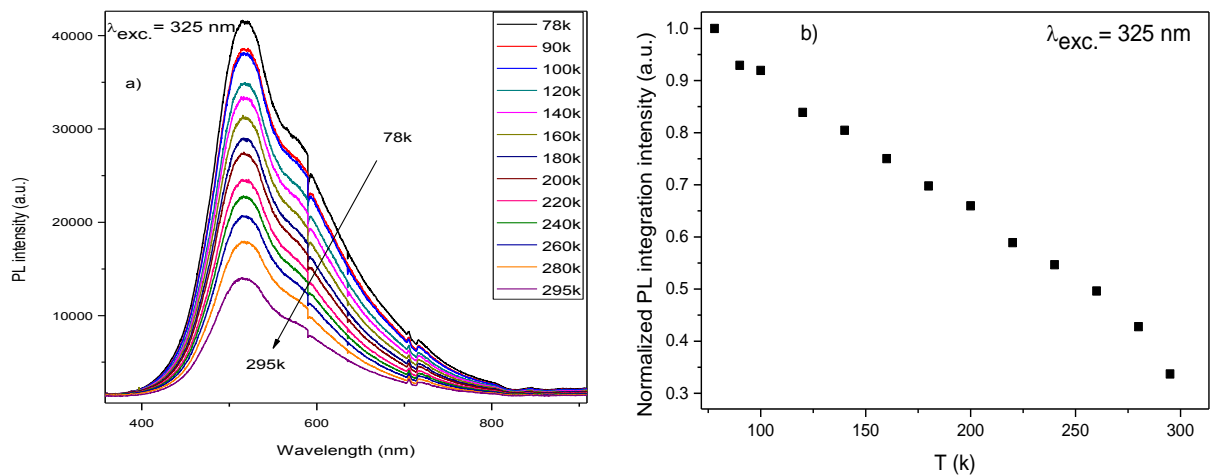


Fig. (4.26): a) PL spectra as a function of temperature of 1% Ce-doped Al(O)N with 7% oxygen sample performed by excitation wavelength 325 nm. b) Normalized PL integration intensity as a function of temperature.

It can be observed that the PL intensity decreases with increasing the temperature. More precisely, the PL evolution with temperature exhibits PL thermal quenching from 78 K to 295 K by 65%, as seen in fig (4.26b). For more quantitative analysis of the PL (T) results, the thermal dependence of the PL intensity can be generally described by Arrhenius equation (4.3) using the single[208] or double exponential terms[117-118]:

$$I(T) = \frac{I_0}{1 + c_1 \exp\left(-\frac{E_{A1}}{k_B T}\right) + c_2 \exp\left(-\frac{E_{A2}}{k_B T}\right)}, \quad (4.3)$$

where $I(T)$ is the PL intensity at the temperature of T , I_0 is the integrated PL intensity at 78 K, E_{A1} and E_{A2} are the activation energies, c_1 and c_2 are fitting constants and k_B is Boltzmann's constant. Therefore, the exponential decay behavior of $(\frac{I_0}{I} - 1)$ versus T^{-1} can be used as a guide for Arrhenius fitting.

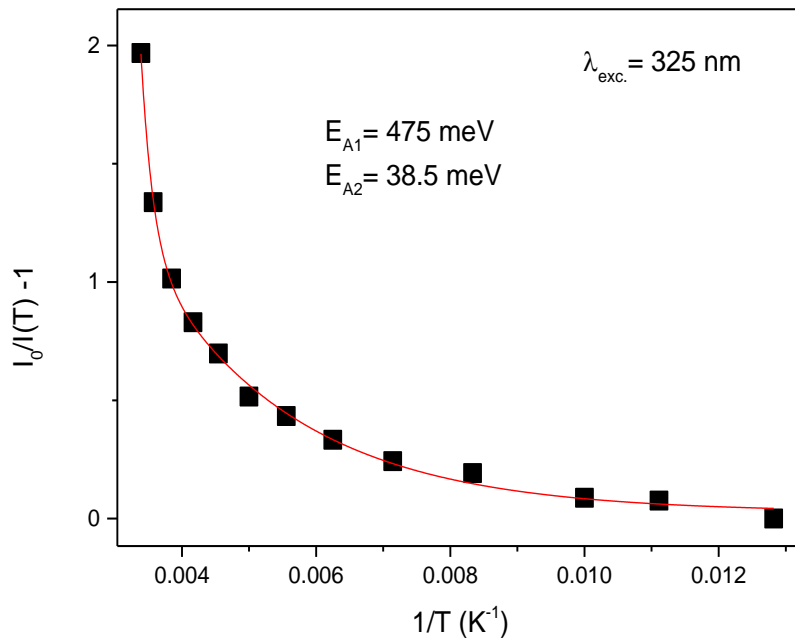


Fig. (4.27): $(\frac{I_0}{I(T)} - 1)$ versus T^{-1} for Arrhenius guiding of 1% Ce-doped Al(O)N with 7% oxygen sample under excitation wavelength 325 nm.

The best fit for data for $(\frac{I_0}{I} - 1)$ versus T^{-1} is given by a double exponential function, see fig (4.27). Two activation energies E_{A1} and E_{A2} (about 475 meV and 38.5 meV, respectively) can be extracted. The mechanisms of the PL thermal quenching of Ce^{3+} in wide bandgap materials has been discussed previously in.[209] The most consistent mechanism for Ce^{3+} thermal quenching is the thermal ionization process via activating electron transfer from the excited $5d$ level of Ce to the conduction band of the host material.[209-210] This mechanism based

on the relative location of the excited $5d$ level of Ce to the conduction band minimum (CBM) of the host. In thermal quenching process, upon excitation of electron from $4f$ to $5d$ levels and increasing the temperature, this electron is likely transferred to the CB if enough thermal energy is gained to cross the $5d$ to CB barrier. The value of this energy is called "thermal activation energy E_A " and depends on the relative energy distance between the excited $5d$ and the conduction band minimum (CBM) of the host, which varies according to the host material.

It is established that, Ce^{3+} in crystalline hosts undergoes crystal field which induces splitting of the $5d$ level into two main sub-levels; lowest excited state $5d_1$ and highest excited state $5d_2$. [209, 211] Therefore, the possible pathways for the electron transition to the CB have been proposed either in one step process (directly from $5d_2$ -CB) or in two steps process (from $5d_1$ to $5d_2$ then $5d_2$ - CB), see schematic fig (4.28). This is greatly depending on the excitation and activation energy, as reported in. [209] At low excitation energy, the electron excites to the lowest $5d_1$ and may follow the two steps quenching process. On the contrary, at higher excitation energy, when the electron is excited to the highest $5d_2$ state, it likely follows the one step quenching process. Because of the closer position of $5d_2$ than $5d_1$ to the CBM, the activation energy for the electron transfer from $5d_2$ -CBM should be lower than the activation energy for $5d_1$ -CBM transition.

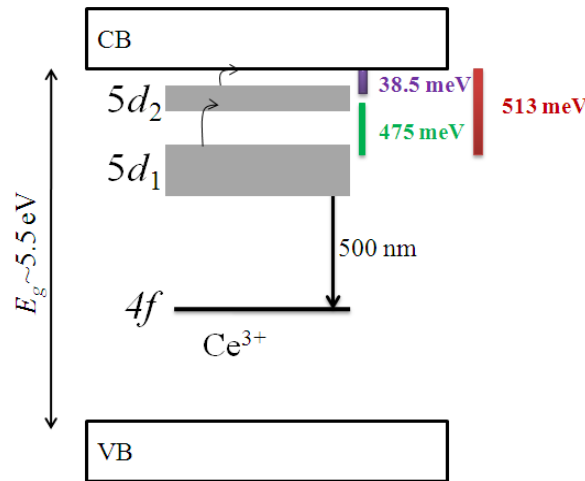


Fig. (4.28): Schematic diagram illustrating the thermal quenching process in Ce-doped Al(O)N with the indication of the calculated activation energies.

Based on the abovementioned physical meaning for the PL thermal quenching approach of Ce^{3+} in wide bandgap material, the estimated activation energies from our sample can be interpreted as follows: Considering the location of lowest $4f$ states of Ce^{3+} at around 2.5 eV in the AlN bandgap as reported in. [212-213] The energy difference between the emitting state

($5d_1$) and the ground state of Ce^{3+} in our sample can be determined from the emission peak at around 500 nm (2.47 eV). Hence, the location of the $5d_1$ state in the AlN bandgap is estimated to be around 4.97 eV (2.5+2.47 eV). By knowing that the bandgap of Ce-doped Al(O)N is around 5.5 eV as determined from the ellipsometry measurement, see fig (4.29). The energy difference $5d_1$ -CBM is around 530 meV, which is very close to the summation of E_{A1} and E_{A2} (475+38.5= 513.5 meV). It is worth to mention that, in the case of the reported thermal quenching of Ce-doped YAG material[209], the $5d_1$ - $5d_2$ energy difference calculated from the activation energy was found to be around 420 meV; while the $5d_2$ - CB difference was 80 meV. By similarity, the $5d_1$ - $5d_2$ energy difference in our Ce-Al(O)N can be considered around 475 meV for $5d_2$ - CBM is around 38.5 meV for $5d_2$ -CBM. The higher $5d_1$ - $5d_2$ energy difference value (475 meV) in our sample than the one in Ce-doped YAG is in line with crystal field strength that supposed to be larger in nitrides than in oxides.

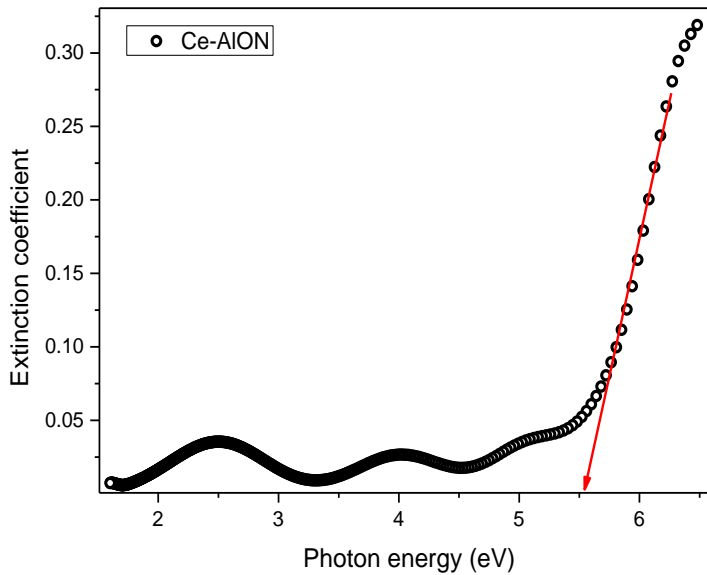


Fig. (4.29): Extinction coefficient as a function in photon energy for Ce-doped Al(O)N sample.

Based on the that, the thermal quenching of Ce^{3+} in Al(O)N host can be probably occurs in two cumulative steps as shown in schematic fig (4.28). The first one via transition of some excited electrons from $5d_2$ to CBM with activation energy equal (38.5 meV). The second is by transition of part of the electrons from $5d_1$ to $5d_2$ with activation energy equal (475 meV), then to CBM with the 38.5 meV.

3- Application perspective

- **White light approach**

Based on our findings, one can realize that the PL of Ce-doped Al(O)N can be manipulated and engineered to increase the intensity or change the emitted light color by modifying the local composition around Ce^{3+} ions. This luminescence behaviors of Ce inside Al(O)N matrix, stimulate us to exploit the ability of tuning the PL color in order to obtain broad spectrum that can be used in white light generation. The possibility to use Ce based materials such as Ce-doped YAG in white light been well established.[209, 214] The most widely used technique in this regard is the phosphor-converted w-LED (pc-LED). For instance, Ce-doped YAG was integrated with InGaN-based blue LED to obtain w-LED.[209, 214] Therefore, generation of white light based pc-LED became a hot topic in the last decades and is still nowadays. This is because white LED is a promising approach to replace conventional fluorescent lamps. In addition, the w-LEDs are highly demanded from technological point of view to produce smart-phones, computer screens and TVs....etc. It is known that bright white light can be obtained from the combination of the three RGB colors.[215] Thus, two common methods have been developed to create w-LEDs. First, the multi-LED chips that contain three individual LEDs with blue, green and red colors which mixing results in white light. The second is the phosphor conversion LED that contains blue or ultraviolet (UV) emitters with yellow or multicolor phosphors. From technical point of view, the challenges in white light production are summarized in three main obstacles: first, fabrication of high quality crystalline material. Second, the need to achieve high quality of color mixing (blue-green-red or blue-yellow phosphors) and, third, the thermal stability of the material under high power and long working times.

Most of these issues can be addressed by finding a way to generate white light free from multi-phosphors to avoid the color mixing problems. Moreover, in a host material with a strong crystal structure and exhibiting high thermal conductivity in order to dissipate the unwanted heat is highly sought for the high power and long operation time. This is what recently proposed by A.T. Wieg et al.[41] The authors were able to obtain white light emission from Ce-doped AlN bulk ceramic material under UV excitation. AlN matrix is an excellent material exhibiting high thermal conductivity, chemical resistance and high transparency in UV-VIS range. Thus, it shows promising properties to be used as a host material for white light phosphors. Although, Wieg et al demonstrated the possibility of

“color-mixing free” white light from bulk Ce-doped AlN ceramic, such white light from Ce-doped AlN thin film is missing. This is highly desired to integrate white light in optoelectronic microchips technology (chip-on-board). In this section, we demonstrate the generation of eye-observed white light excited by 325 nm laser from 5 micron thickness Ce-doped Al(O)N thin film prepared by RF magnetron reactive sputtering. Using the present approach of laser driven white light emission opens the way to achieve high power white light sources. In addition, we believe that, the simplicity and low cost as well as the industrial favorability of magnetron sputtering technique will push this approach forward to reduce the technological cost on large scale production. We hope these findings will act as a seed for generating new and cheap white light sources.

Therefore, a 1% Ce-doped Al(O)N sample of about 5 μ m thickness and containing about 7% of oxygen was prepared. The idea behind increasing the film thickness is to offer several different local environments around Ce ions throughout the film thickness. As the film thickness increases, the crystallite size and the total number of defects are expected to increase too. Fig (4.30), displays the PL spectrum of this sample carried out using 325 nm laser as excitation wavelength.

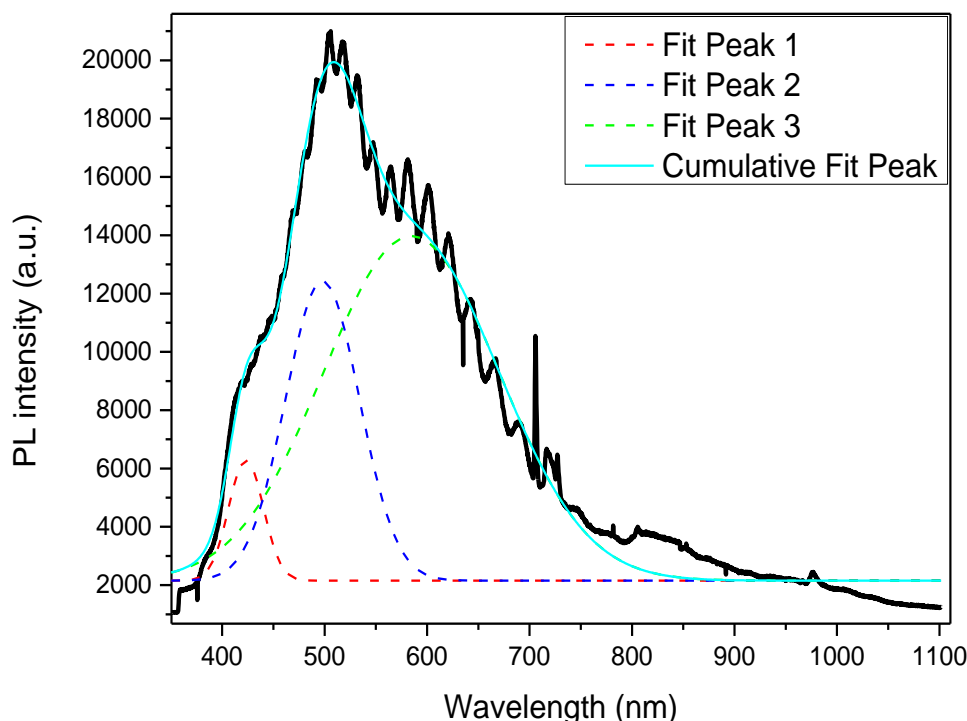


Fig. (4.30): PL spectrum of annealed 1% Ce-doped Al(O)N of 7% oxygen and 5 μ m thickness.

It is observed that the PL spectrum consists of broad band that can be de-convoluted into three sub-bands peaked at 422 nm (in the blue light region), 497 nm (end of the blue light region),

and 585 nm (end of yellow region). This broad band can be explained by considering the effect of film thickness as follows:

Due to the large thickness of the film, Ce^{3+} ions have the opportunity to experience different environment, for instance when located inside the grains or in the grain boundaries. Moreover, the total number of defects in 5 μm -thick film is much higher than in 200 nm-thick films. Such different locations of Ce ions and higher total number of defects offer different local environment around Ce ions in different areas throughout the film. Since the d -level of Ce^{3+} is very sensitive to the environment, the energy position of the emitting states can be shifted, as described before. This stimulates slight different PL bands from different locations of Ce along the film thickness. This is in line with our previous PL of different colors (blue and green) obtained from oxynitride hosts, see (fig 4.23). In addition, a significant PL intensity from the radiative defects of AlN in such large thickness should be considered. The combination of emissions from Ce and defects from the entire film thickness of AlN results in broad emission[41] and strong white light emission occur and can be seen by the naked eye, see fig (4.31).

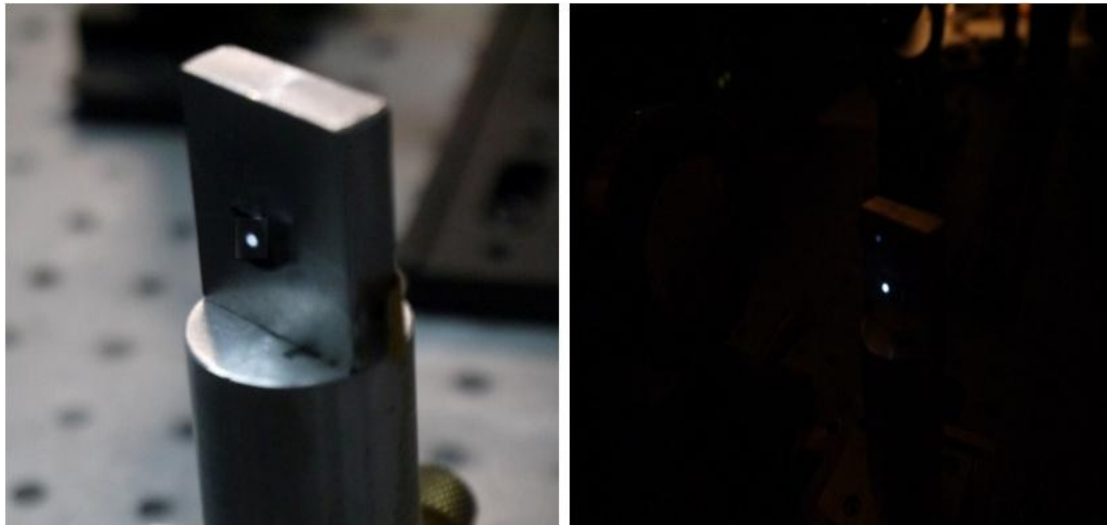


Fig (4.31): White emission photos with bright and dark background from 1% Ce-doped Al(O)N of 7% oxygen and 5 μm thickness excited by a 325 nm laser.

For better understanding this sample, TEM and EDS measurements have been performed. The TEM image shows columnar structure with column width about 200 nm near to the surface, see fig (4.32a). This column width is decreased when moving down to the substrate direction due to the V-shape of the columnar growth. The local compositional analyses are done by performing local EDS map on a part of the film shown in fig (4.32b). The corresponding EDS

map for Ce, fig (4.32c), exhibits almost homogeneous distribution of Ce elements in the bulk grains and grain boundaries. On the contrary, accumulation of oxygen is observed in the grain boundaries, as depicted in fig (4.32d).

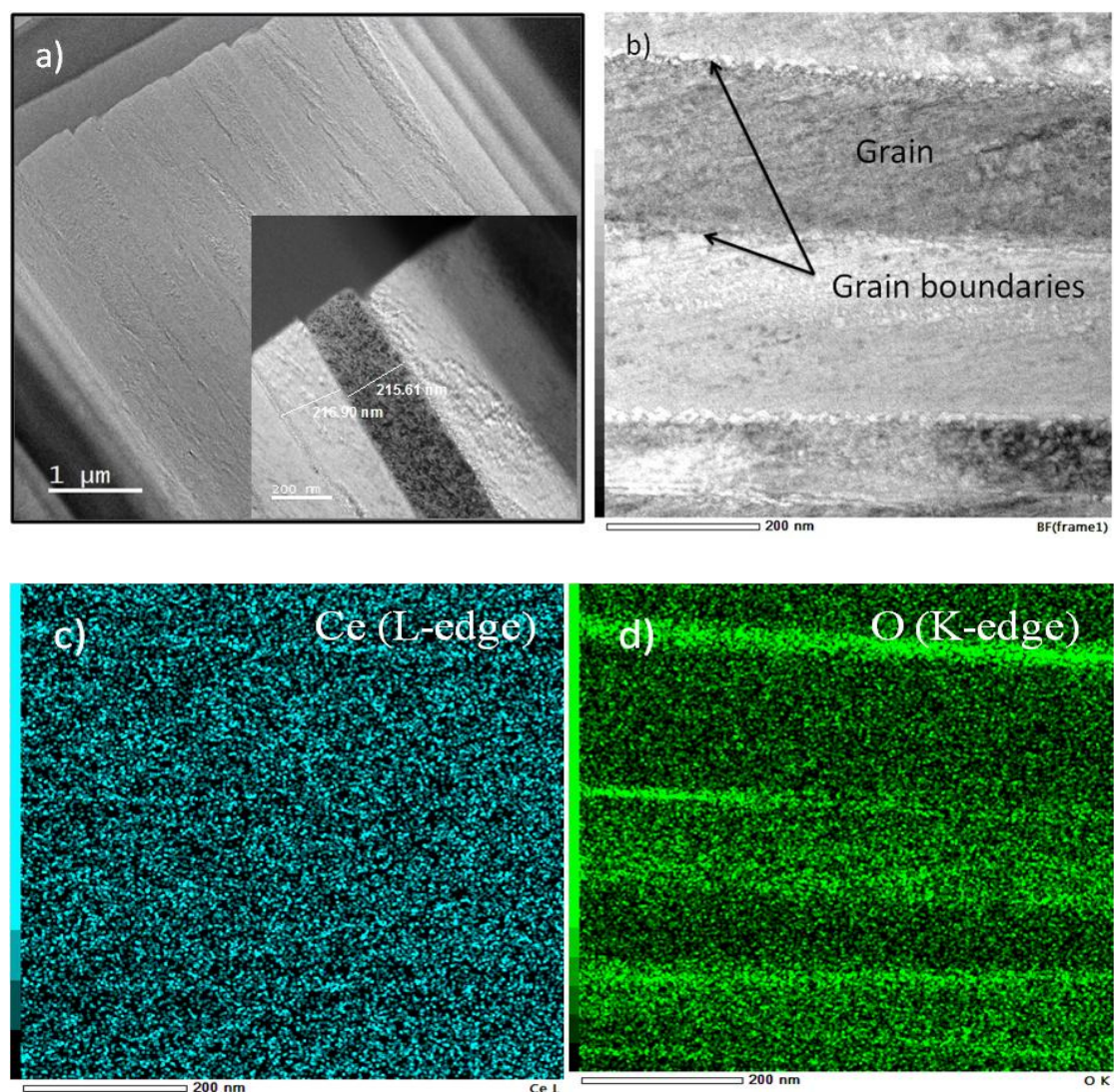


Fig. (4.32): TEM and EDS map images for sample that emits white light. a) TEM image at low and high (inset) magnification, b) The selected part of the film underwent EDS analyses, c) and d) are the corresponding EDS map probing Ce L and O K edges; respectively.

This inhomogeneity in the oxygen distribution supports the previous hypothesis regarding the different local environments around Ce ions. We believe that, this approach of white light generation free from multi-phosphors colors and conducted in thin film is of great interest for the field of solid state optoelectronics.

4- Conclusion

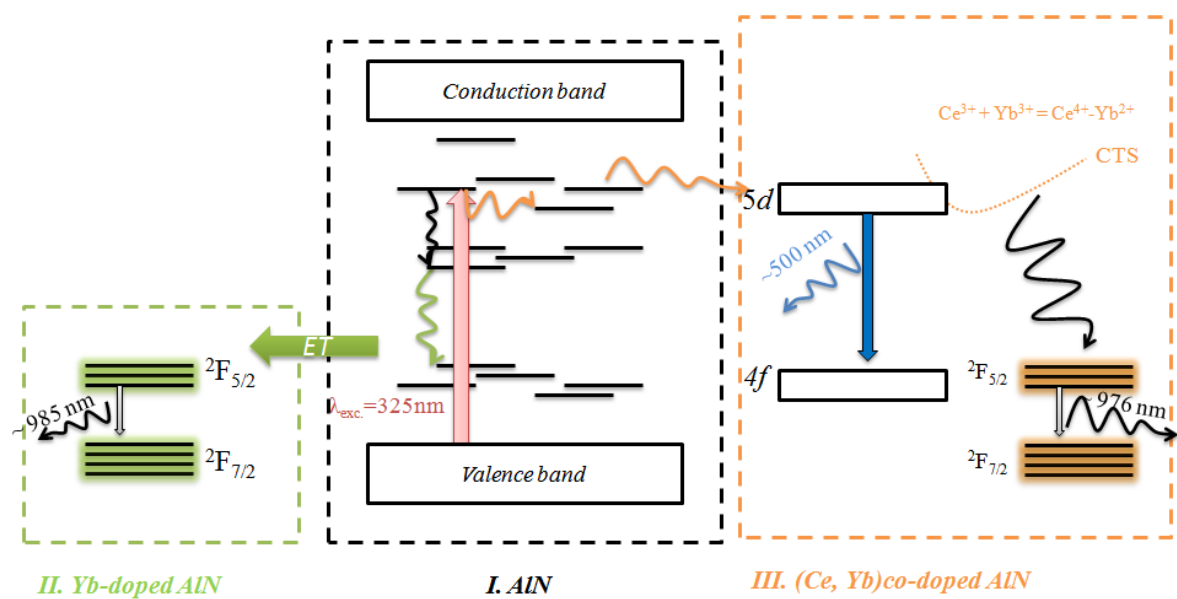
This chapter was focusing on understanding the optical behavior of Ce doped AlN thin films. The correlation between the structure/compositions and the optical behavior has been discussed in details during all the study. Crystalline thin films of undoped and Ce-doped AlN were prepared using reactive magnetron sputtering technique. The crystal structures of the prepared samples and the compositions have been examined by TEM, RBS, EDS and EELS. It was found that presence of oxygen in "Ce-doped AlN" is essential for sensitizing the photoluminescence. Oxygen has been found playing major role not only in converting Ce ions from the optically inactive state +4 to the optically active one +3, but also leads to the formation of defect complexes with Al vacancies. These defect complexes were found to contribute in the excitation mechanism. This double role of oxygen is confirmed by EELS (for oxidation state of Ce identification) and PLE measurements (for defect complexes assignments). Therefore, an optical excitation and emission mechanisms have been proposed based on the role of oxygen. Then, Ce^{3+} ions are suggested to be excited directly and/or indirectly by energy transfer from the host defects. This proposed mechanism was found consistent with the interpretation of the PL results as well as confirmed by testing the PL behavior at higher concentration of oxygen. In addition, the role of annealing in the PL has been discussed and referred to generating local Al-O bonds and suppressing the nonradiative defect centers. Based on that, manipulation of the PL was achieved and different colors (blue, and green) were clearly observed by the naked eye. In addition, PL thermal quenching mechanism has been proposed by studying the temperature dependent PL behavior. The PL thermal quenching was proposed based on thermal ionization mechanism by electron transfer from the $5d$ levels of Ce^{3+} to the conduction band. Moreover, white light approach has been presented and strong eye observed white light was obtained.

We hope that this dedicated study offers better understanding of the luminescence properties of Ce-based aluminum nitride, (oxy)-nitride, and oxide compounds that can be used in solid state lightening applications.

Chapter V

Yb-doped AlN and (Ce, Yb) co-doped AlN

Graphical abstract



Abstract

This chapter is devoted to study the optical mechanisms of Yb-doped Al(O)N and (Ce, Yb) co-doped AlN thin films. The main goal of this part of work with Yb in AlN is to establish a comparative study between two different rare earth ions doped in AlN in order to explore the similarities and the discrepancies, particularly in the optical behaviors. We believe that this kind of comparison will lead to better understanding the optical properties of RE-doped AlN compound and result in enhancing our knowledge in phosphor based nitride applications. The reasons behind the selection of Yb element have been stated in the beginning of this thesis, motivation part, which can be summarized as follows:

- Yb^{3+} has different luminescence electronic states properties ($f-f$) than Ce^{3+} ($f-d$). This gives a wide view about the different electronic properties of RE^{3+} .
- Yb^{3+} emits in NIR region, while Ce^{3+} emits in UV-Vis region: So, this study will cover wide range of light spectrum for different lighting applications.
- The co-doping between Yb and Ce exhibits great attraction nowadays in down conversion applications.
- There are very few works reported on either Ce or Yb in AlN.

The microstructures and the compositions of the prepared samples have been investigated. The optical properties have been examined, at room temperature, using the steady state PL, PLE, and time resolve photoluminescence (TRPL). The PL thermal quenching mechanism for Yb and (Ce, Yb) co-doped Al(O)N is studied by probing the PL evolution at low temperatures. In addition, energy transfer (ET) mechanism between Ce and Yb has been established. A comparison is made with the optical mechanisms in Ce-doped Al(O)N.

1- Introduction

Ytterbium (Yb) is a rare earth element which contains completely filled $4f^{14}$ orbital. Although Yb^{3+} is the common oxidation state of ytterbium, Yb^{2+} can be found under certain circumstances. The electronic configuration of Yb^{3+} ($[\text{Xe}] 4f^{13} 6s^0$) is ended by $4f$ orbital filled with 13 electrons. Thus, it is considered as the last RE^{3+} ion exhibiting incomplete $4f$ orbital. Free Yb^{3+} ion has relative simple electronic configuration compared to other RE^{3+} . It consists of two energy terms $^2F_{5/2}$ and $^2F_{7/2}$ and is considered as a two energy levels system. Thanks to this electronic simplicity, Yb^{3+} placed in different host matrices constitutes a good platform to extract useful information about $f-f$ transitions in RE^{3+} . Hence, it attracts extensive

investigations, in particular on theoretical calculations. In addition, the energy separation between the ground and excited states of Yb^{3+} equals ~ 1.23 eV and related transitions emit photons in near infrared region NIR (~ 1000 nm). This makes Yb^{3+} competitive with the well-known Nd^{3+} ion that emits in the same region and is widely used in solid state lightening devices. Although Nd^{3+} is widely used, from spectroscopic point of view, Yb^{3+} exhibits some advantages over Nd^{3+} . [216] More precisely, the simpler structure of energy levels minimizes the cross relaxation, the up-conversion and excited-state absorption processes that lead to luminescence quenching in Nd ion systems. Hence, the possibility to higher output power can be obtained by reaching higher concentration of Yb than Nd before quenching occurs. In addition, the longer lifetime of upper excited states of Yb^{3+} ($\sim 1\text{ms}$) than Nd^{3+} ($\sim 300\mu\text{s}$) provides a better storage of the pump energy, which is desirable in laser systems. However, the simple energy terms $^2\text{F}_{5/2}$ and $^2\text{F}_{7/2}$ of Yb^{3+} becomes more complex when the ions experience strong crystal field interaction with the host material. This crystal electric field induces Stark splitting of the energy levels resulting in sub-band electronic transitions. Furthermore, in some cases, additional electronic transition lines that can't be explained by the influence of the crystal field have been found. This suggests the existence of Yb^{3+} in different optically active centers involving complexes with defects. [78] This stimulates many studies to understand and exploit the behavior of Yb^{3+} for lightening solid state application.

The energy separation between the ground and excited states of Yb^{3+} (1.23 eV) higher than bandgap of silicon (1.12 eV), makes Si is not a suitable host for Yb. Therefore, researchers turned their attention to other host materials. III-V semiconductors appear the most promising hosts. They are characterized by a wide optical bandgap (above 2 eV) and excellent integration with silicon technology. Thus, many works were directed to investigate the optical properties of Yb-doped III-V semiconductors [217-220], with few attentions to Yb-doped III-nitrides, particularly to GaN. [111, 221-222] So far, Yb hasn't been given enough attention to be investigated as optically active ion in crystalline AlN. [78] Zanatta, A.R. et al, [112, 223] have investigated the effect of thermal annealing on the optical properties of amorphous/nanocrystalline AlN thin films considering Yb among other RE ions. Koubaa, T., et al [78] theoretically studied the spectral and energy levels of Yb in crystalline AlN thin films based on cathodoluminescence measurements. However, a dedicated study of the optical excitation and emission mechanisms of Yb in crystalline AlN is missing. This lack in the available information stimulates us to perform this systematic study on Yb-doped crystalline AlN thin films.

Part I: Yb-doped Al(O)N

2- Structures and compositions

Yb-doped Al(O)N thin films have been prepared using RF reactive magnetron sputtering. For comparison purpose with the previous Ce-Al(O)N study, the Yb-Al(O)N samples have been prepared with about ~ 7% of oxygen. Chemical analyses have been performed using RBS mainly to probe the Yb content. Fig (5.1) shows RBS spectra for the different prepared films.

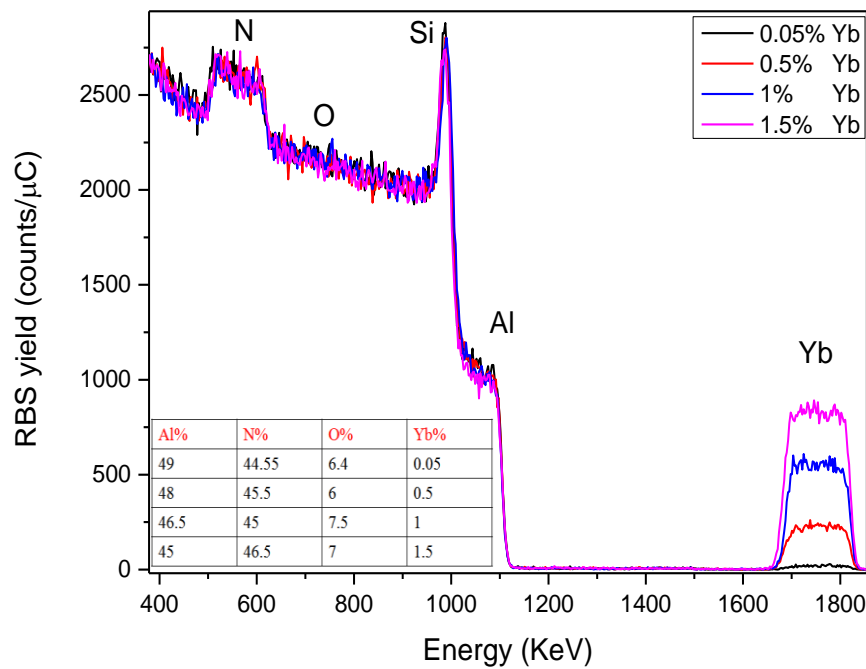


Fig. (5.1): RBS fitting data for the prepared Yb-doped Al(O)N samples at different Yb%.

In the RBS spectra, the regions corresponding to the different elements are labeled (Yb, Al, Si, O, N). The content of each element is indicated in the inset table. There is no significant change in the elemental composition of the host (Al, N, and O) between the four samples. On the other side, different contents of Yb% (0.05, 0.5, 1, and 1.5%) can be clearly noticed.

The crystal structure of samples has been primarily investigated by XRD. Figure (5.2) shows the XRD of the prepared Yb-Al(O)N samples with different Yb% contents. The prepared films exhibit a single diffraction peaks around 36° , which is characteristic of (002) planes of the hexagonal wurtzite structure of AlN. It suggests the crystallites are mostly oriented with the [002] direction aligned with the growth direction. The shift in the diffraction peak position can be related to the lattice strains due to Yb incorporation. The effect of doping by REs on

the lattice strains of AlN has been discussed in the previous chapter with Ce-doped AlN and reported in.[224]

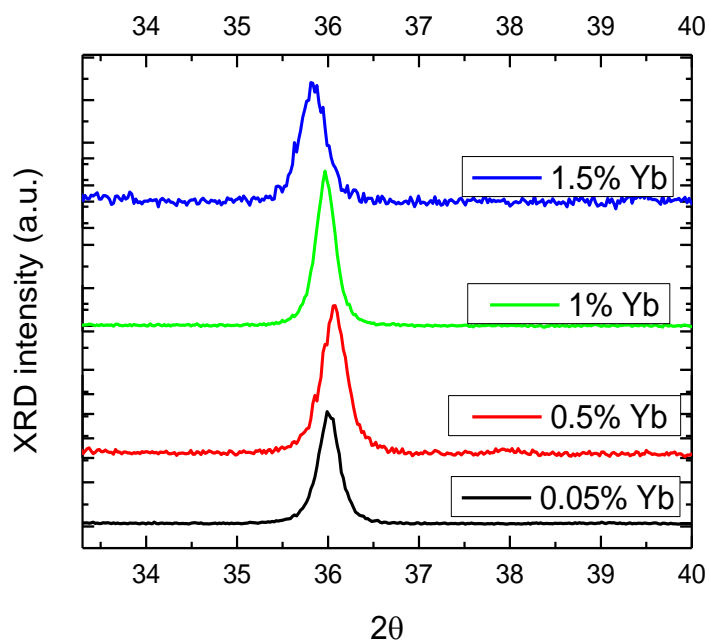


Fig. (5.2): XRD of Yb-doped AlN samples at different Yb%;

Fig (5.3), shows the TEM and corresponding SAED of 1% Yb-doped Al(O)N *as-deposited*. The film exhibits columnar structure and the partial electron diffraction rings with localized bright spots is consistent with the polycrystalline nature of this sample with preferred orientation along [002]. Herein the results will be generally shown for sample 1% Yb-doped Al(O)N.

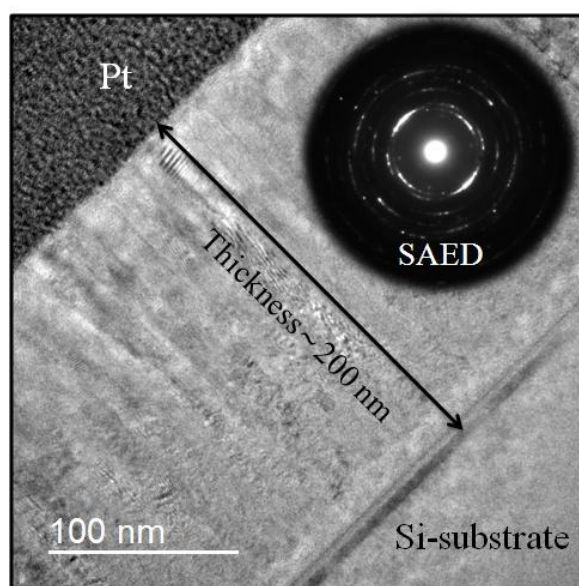


Fig. (5.3): TEM image and the corresponding SAED pattern for 1% Yb-Al(O)N *as-deposited*.

3- Photoluminescence (PL)

PL of 1% Yb-doped Al(O)N *as*-deposited and *post*-deposition annealed (RTA) samples has been performed at RT using the 325 nm excitation line of a He-Cd laser. Near infrared (NIR) PL signals have been detected at around 985 nm, see fig (5.4). The PL spectra can be divided into two main PL regions: broad bands in the visible region (~ 400-550 nm) and sharper NIR bands in the NIR region (~ 900-1050 nm). The bands in visible region are attributed to the radiative defects in AlN. Similar bands in visible region have been found in the PL of undoped AlN sample, (see inset fig (4.8a), chapter_IV) and reported in.[225]

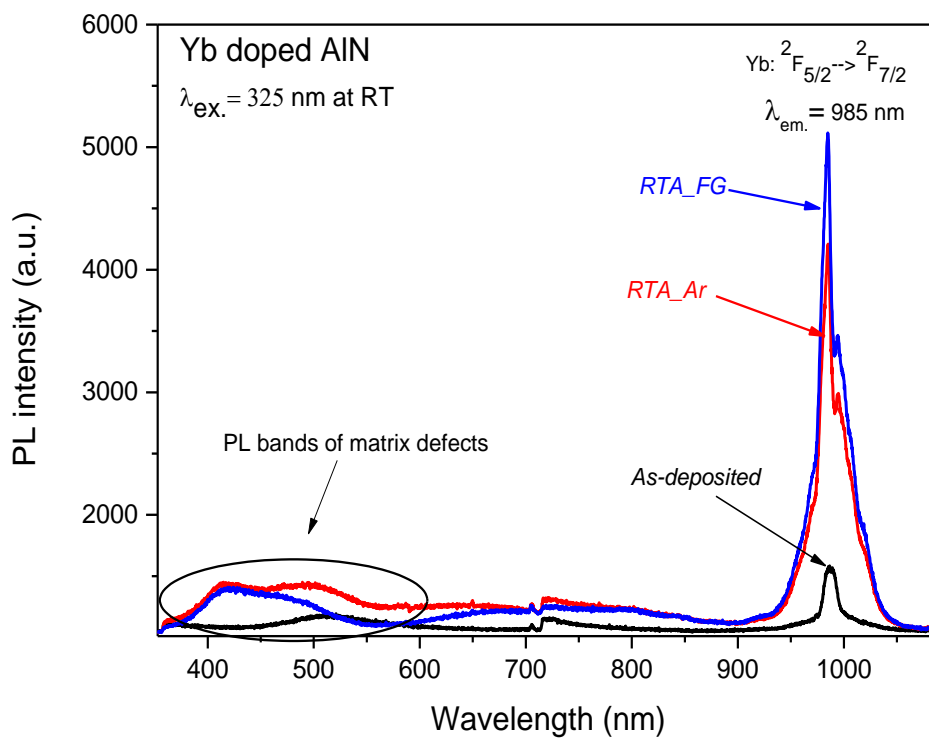


Fig. (5.4): PL spectra of 1% Yb-doped Al(O)N *as*-deposited, RTA_Ar, and RTA_FG.

No PL related to Yb³⁺ ions have been reported in this region. NIR emission bands are characteristic luminescence signals of Yb³⁺ usually accounted around (967- 1030 nm), as reported elsewhere.[78, 226] These bands are centered at 985 nm and assigned to the optical transitions from ²F_{5/2} to ²F_{7/2}. For better analysis, spectra magnification of the NIR region is shown in fig (5.5). It can be observed that the PL spectral shapes of samples annealed in Ar and FG are similar but are different to that of the *as*-deposited sample. The *as*-deposited sample exhibits a symmetrical non-splitting weak PL band centered around 987 nm. Annealed samples display asymmetrical splitting intense PL peaking at 985nm. The PL consists mainly

of well resolved peak at 985 nm, shoulder at 970 nm, a small peak at 994 nm with other small humps observed at (1000, 1005, and 1020 nm).

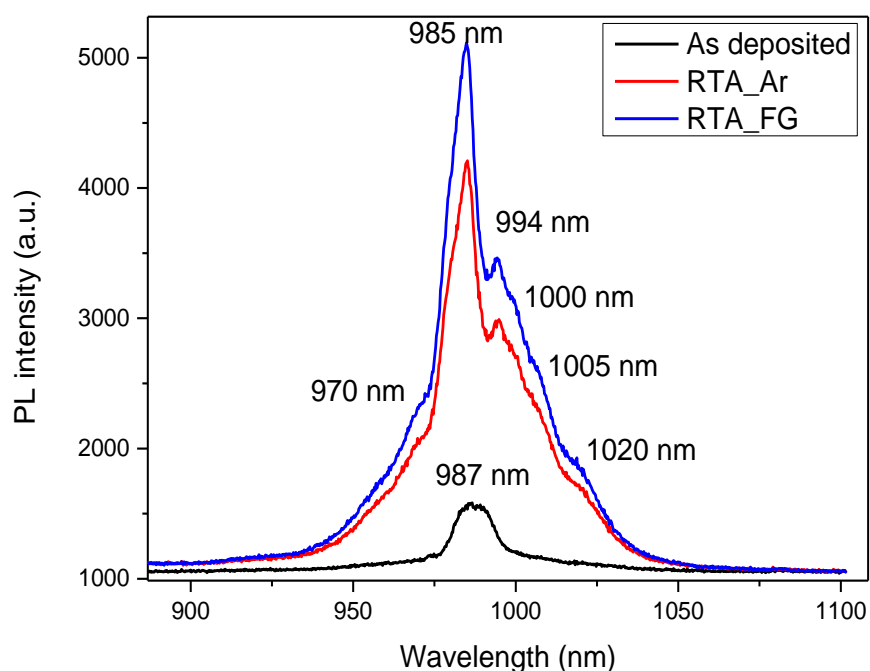


Fig. (5.5): Zoom in graph on the NIR_PL of 1% Yb-Al(O)N *as-deposited* and annealed samples.

In addition, a broad background at the base of the emission spectra can be observed, which is likely due to overlapping between unresolved spectral lines.

Regarding the excitation of Yb^{3+} , it was reported that the absorption cross section of Yb^{3+} ions located in NIR region around 980 nm overlapped with the emission spectra.[227-230] This makes the only possible way to excite Yb^{3+} ions is directly pumped by using NIR wavelength such as 981 nm.[231-232] However, the direct excitation of Yb^{3+} exhibits a weak cross section due to the lying of the $4f$ orbital in the core of the valence band. This is why much efforts have been spent to find an indirect more efficient way to excite Yb^{3+} by energy transfer via another ion such as Ce, Nd.....etc.[233-236] In our case, intense NIR emission from Yb^{3+} has been obtained by 325 nm excitation whereas Yb^{3+} has no known absorption band in the UV-Visible regions. This evidences an efficient indirect excitation from the host AlN to Yb^{3+} ions. Moreover, as the 325 nm is fairly below the bandgap energy of AlN (~ 210 nm), this evidences that the energy transfer from AlN to Yb^{3+} is mediated by matrix defects. This process appears to be enhanced by annealing. In order to test another pumping scheme, Yb-Al(O)N_FG sample has been excited by higher photon energy at 266 nm and compared with the PL obtained by 325 nm excitation, fig (5.6). It can be observed that the PL exhibits similar

spectral features under the two different excitation wavelengths. This shows the possibility to use different pumping schemes for the indirect excitation of Yb^{3+} ions in AlN.

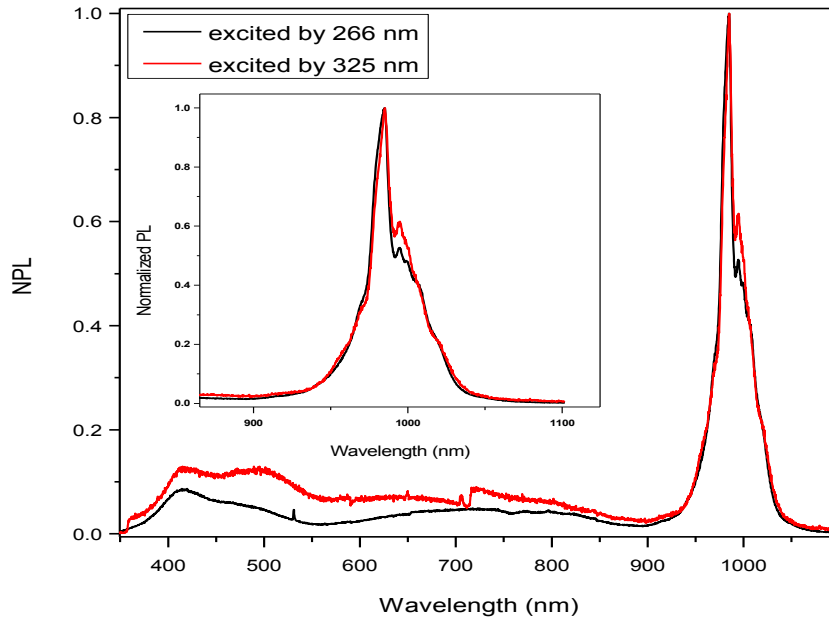


Fig. (5.6): PL spectra of 1% Yb-Al(O)N annealed in FG and excited by 325 nm and 266 nm. Inset is the magnification on the NIR region.

These findings open the door for realizing room temperature NIR emission from Yb-based solid state devices excited by UV sources. In order to probe the excitation mechanisms, PLE measurements have been carried out by monitoring the PL peak at 985 nm, see fig (5.7a). Surprisingly, the positions of the appeared two PLE bands are located at photon energies (~ 3.9 and 4.8 eV) very close to the PLE bands positions of Ce-doped Al(O)N, as shown in fig (5.7b).

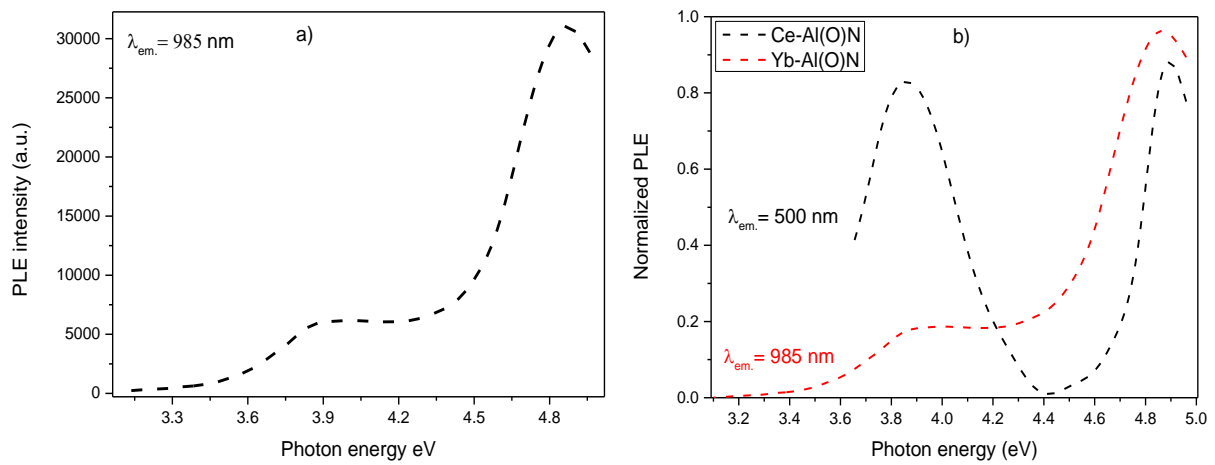


Fig. (5.7): a) PLE spectra for 1% Yb-doped Al(O)N monitored at 985 nm, and b) normalized PLE for both 1% Yb-Al(O)N and 1% Ce-doped Al(O)N samples monitored at 985 nm, 500 nm; respectively.

Hence, the assignment for these two PLE bands could be done in the light of the previous assignment of the PLE of Ce-doped Al(O)N samples. Based on that, these bands can be ascribed to the host defects, more precisely to defect complexes involving Al-vacancy with oxygen, as proposed for Ce-doped Al(O)N. However, in the case of Yb, the PLE band around 4 eV exhibits much lower relative intensity than the band at 5 eV whereas, in the case of Ce, both the bands have comparable intensities. The higher intensity of the 4 eV band of in Ce-doped samples can be attributed to the overlapping between the Ce^{3+} and $(\text{V}_{\text{Al}}\text{-O}_{\text{N}})$ defect complex absorption bands, see the previous PLE discussion in chapter IV. The PLE result for Yb-doped Al(O)N further suggest that defects in the host matrix provide an efficient pathway in the RE^{3+} excitation mechanisms. In this regard, two theoretical models have been proposed for the optical excitation mechanisms of the f - f transition of RE^{3+} in wide bandgap III-V semiconductors.[78, 86] The first assumes changes in the valence of the RE^{3+} by charge transfer. The second one is based on mediation through electron-hole pair that localizes on, or very close to, a RE-isoelectronic trap. The second one is the most commonly accepted and is supported by experimental observations. When REs incorporate in III-V compounds or alloys, it usually substitutes the III ions and generates isoelectronic traps due to the size and electronegativity mismatch between the RE and the substituted III ions. This trap is electrically active and captures a charge carrier, which subsequently binds to opposite charge carrier by coulomb interaction for e-h pair formation. Alternatively, this RE-trap can couple to a vicinity e-h pair (free or bound exciton).[87, 237] Upon excitation, the trapped or the vicinity e-h pair becomes excited and energy transfer can occur from the e-h pair to the core f - f transition in the RE. Hence, based on the abovementioned models and our PLE findings, the optical excitation of Yb-doped Al(O)N can be understood through an energy transfer from a vicinity $\text{V}_{\text{Al}}\text{-O}_{\text{N}}$ defect complex to the $4f$ levels of Yb^{3+} . This kind of defect complexes acts as donor-acceptor pair that, excited by 325 nm or 266 nm, transfer energy to the Yb^{3+} . Subsequently, excited Yb^{3+} ions relax to the ground state and emit light around 985 nm. It is worth to mention that, the large Stokes shift between the absorbed photons at 325 nm or 266 nm and the emitted photons at 985 nm can be accommodated by phonon interactions and/or dissipation through non-radiative centers.

Precise assignment of the PL peaks/shoulders in fig (5.5) is very difficult with the present PL data due to the strong overlapping between the transition lines. Thus, in order to gain more information about these transition lines, PL at low temperature (LTPL) was carried out down to 78 K. At low temperature, the thermal motion of the carriers is supposed to be reduced

resulting in their localization at the transition levels. This is expected to bring more precise information on the energy sub-levels structure.

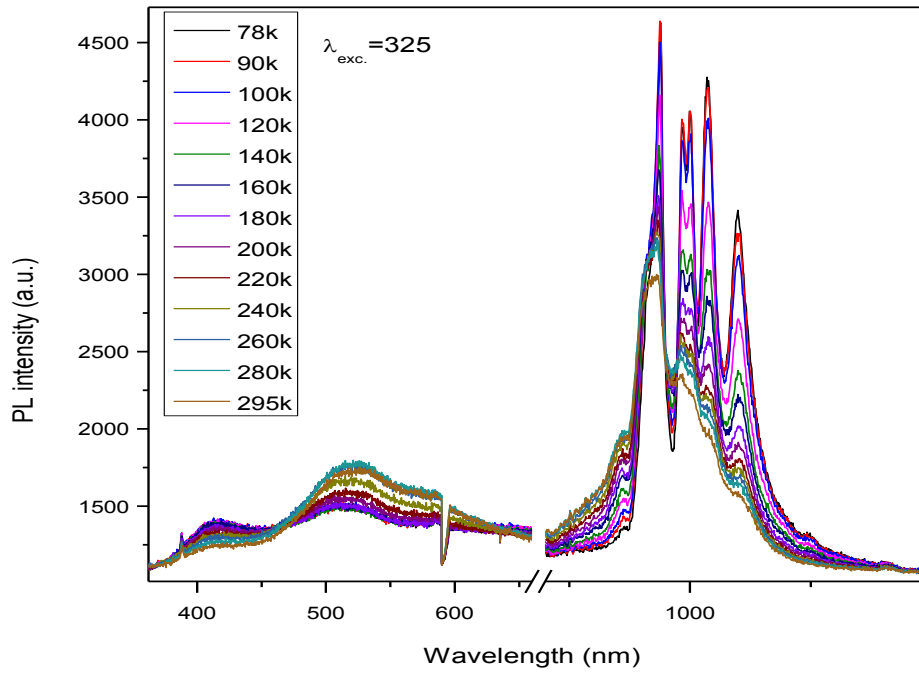


Fig. (5.8): PL spectra of 1% Yb-doped Al(O)N film for different temperatures from 78K to 295K

Fig (5.8) shows the PL spectra for Yb-doped Al(O)N sample excited by 325 nm and measured from 78 k to 295 K. It can be observed that the PL spectra reveal significant changes in the PL intensity and the shape. Changes appear both in the NIR and visible regions. For better contrasting these changes, the PL spectra for 78 K and 295 K are plotted together, see fig (5.9a, b) for 325 nm and 266 nm excitations.

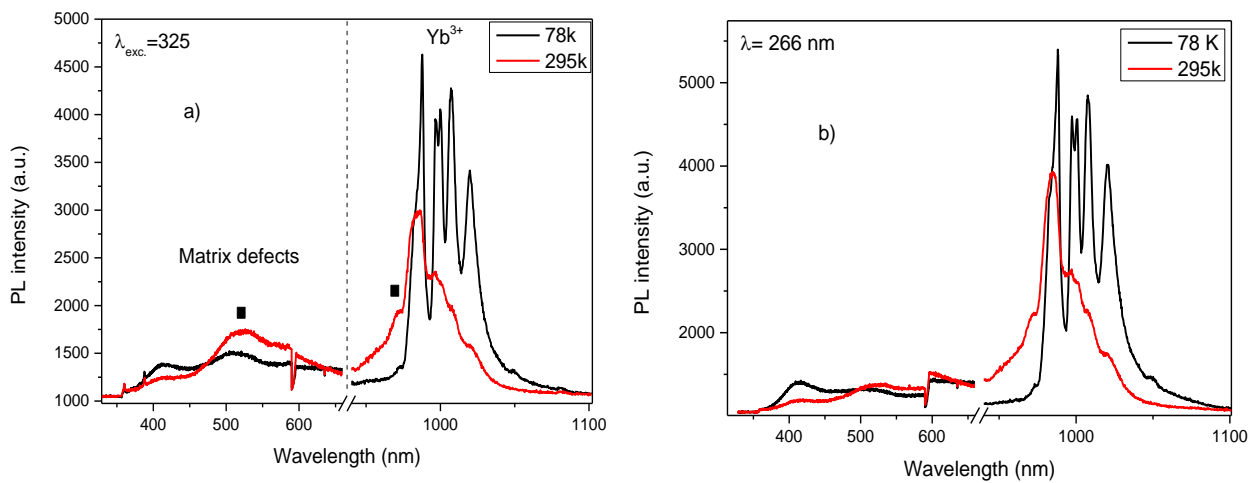


Fig. (5.9): PL of 1% Yb-doped Al(O)N sample carried out at 78K and 295K under excitation wavelength a) 325 nm and b) 266 nm.

While temperature little affects the shape of the visible bands, NIR peaks are much better resolved at low temperature. All lines and bands show increase in PL intensity from 295 K to 78 K except the small bands indicated by the black square ■. The PL intensity of these two bands are thermally activated (populated), unlike other lines/bands that are thermally quenched. In the thermally quenched lines in NIR spectrum, it can be also observed the significant suppression of the lower energy lines compared to the higher energy lines when the temperature increased. This is an expected behavior due to higher temperature favors higher energy transitions. Very similar spectra have been obtained under excitation with 266 and 325 nm excitation. This means PL follows the same temperature response regardless the two excitation pathways.

It is well established that the energy levels of RE ions undergo spectral splitting into "Stark levels" due to coulomb, spin orbital, and crystal field interactions. However the crystal field plays the most significant contribution in this regard particularly in RE-doped crystalline materials. Because of incorporation of RE³⁺ ions into crystalline matrix, the energy states of 4fⁿ electrons experience a disturbance due to the applied crystal electric field. The effect of this crystal field on the energy levels of REs ions can be probed by low temperature PL measurements due to the reduction of the thermal motion of the carriers. Although the crystal field strength doesn't significantly change with temperature, at room temperature the phonon interactions induce overlapping in the energy levels' wavefunctions, which hides the influence of the crystal field. The strength and number of the splitting levels is depending on the strength of the local crystal field and on the crystal symmetry around the lattice location of the RE³⁺; respectively. This is the physical reason behind the observed spectral splitting in many RE³⁺ ions such as Pr³⁺, [238] Sm³⁺, [239] Tm³⁺, [240] and Nd³⁺. [241] Yb³⁺ also exhibits similar behavior in crystalline materials as reported several times in GaN host. [222, 226, 242] However, to the best of knowledge, there is only one published article to date dealing with the energy levels of Yb in crystalline AlN. [78] The authors reported on the calculation of the crystal field energy levels of Yb-doped AlN thin films using crystal field theory. Their theoretical results have been based on the cathodoluminescence of the prepared sample. The cathodoluminescence (CL) measurements (at 11 K) exhibits a CL spectrum contains up to 25 emission lines/shoulders/humps. The authors couldn't explain such complicated CL spectrum by assuming only the substitution of Yb³⁺ in the Al (Yb_{Al}), and other different sites had to be proposed. They assumed another possible site for Yb³⁺ associated with nitrogen vacancy V_N to form a defect complex (V_N-Yb) resulting in a good agreement between the measured and

calculated energy levels. They also emphasized on the role of defects in the PL of Yb^{3+} . Yb^{3+} ions interact with the defects and produce binding photo-generated carriers or excitons, which participate in the energy transfer to the $4f$ -shell electrons.

In our case, the careful examination of the PL at 78k reveals 9 transitions manifested in lines, shoulders, and humps, see fig (5.10).

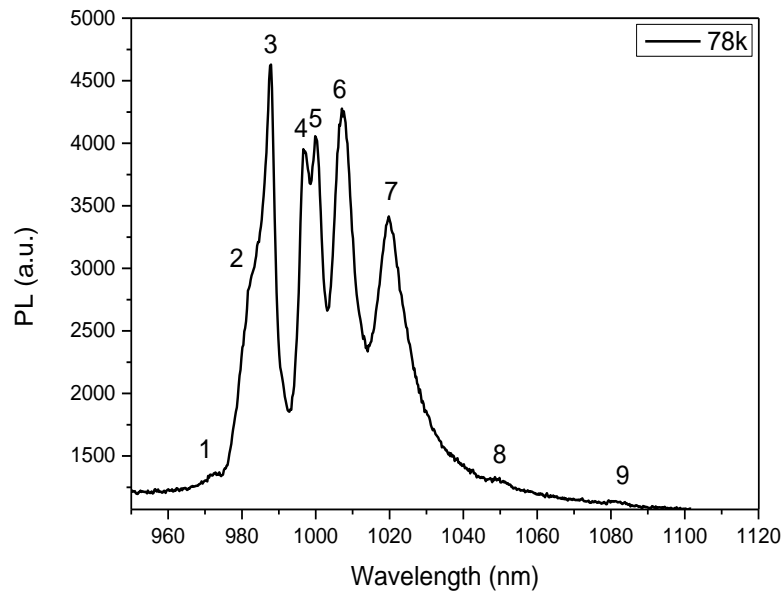


Fig. (5.10): Zoom in for the NIR emission carried out at 78K.

The wavelength positions of the observed PL transition lines are reported in table (5.1):

Table (5.1): Precise wavelengths positions of NIR emission lines measured at 78k.

PL Transition number	1	2	3	4	5	6	7	8	9
Wavelength (nm)	972.2	981.7	987.7	996.6	999.8	1007	1019.7	1049	1080

The number of PL lines (9 transitions) from our samples is much lower than the reported CL transitions (25 transitions) from Yb in AlN[78] or the PL of Yb in GaN (25 transitions).[226] This suggests that Yb^{3+} ions are located on a single site in our samples, likely substituting on the Al- site (Yb_{Al}). Therefore, the two spin orbit manifolds $^2F_{7/2}$ and $^2F_{5/2}$ are splitting into at most $(2j+1)/2$ sublevels, resulting in four and three crystal field levels (doublets).[221] Based on that, at least four PL transitions are expected if these transitions are considered only from the lowest excited level in $^2F_{5/2}$, and twelve if transitions from other sublevels are also considered, see the schematic diagram (5.11) and the corresponding table. The positions of

the energy levels (in cm^{-1}) have been used from the calculated energy levels reported in[78] for Yb^{3+} substituting on the Al- site (Yb_{Al}).

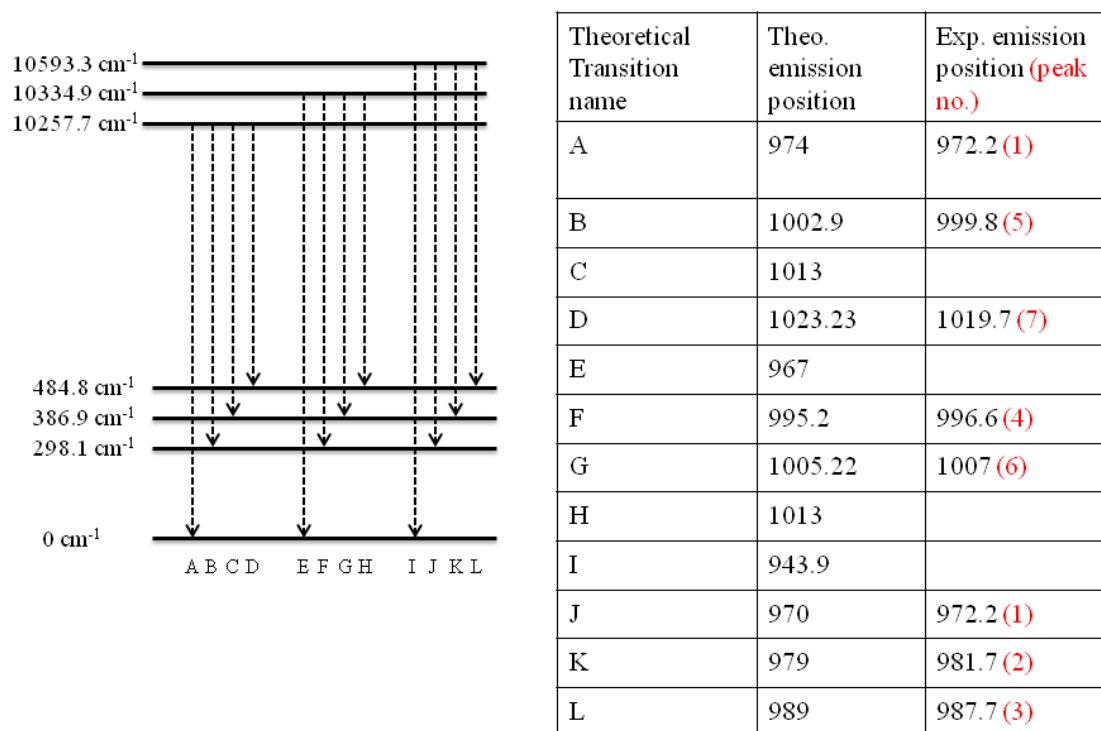


Fig. (5.11): Calculated energy level diagram for Yb^{3+} ions in Al substitutional site (Yb_{Al}) in AlN (on left). The theoretical (Theo.) and experimental (Exp.) transition lines positions (on right).

All the measured emission transitions can be assigned by the calculated energy diagram with small shifts; except the two small transitions at 1049 nm and 1080 nm. The slight shift between the calculated and measured values can be attributed to the different crystal field strength between the two studies, different preparation and different excitation methods. It is established that the local site symmetry, the crystal field strength, and the ligand arrangements are considerable parameters that significantly control the energy level values and the transition probabilities from the sublevels.[240] These parameters are mostly related to the matrix properties that modify the optical response of the Yb in different materials as well as in the same material by local structure modifications. Hence, when the local environment around Yb-site is changed, the strength and the excitation cross section as well as the branching ratio of the transition lines are expected to be altered. Regarding the two small peaks at 1049 nm and 1080 nm, the former one has been observed at very close value in Yb-doped GaN[226] without any clear assignment specified. However, the latter one is reported for the first time here. These two small peaks could be explained by the occupancy of another site occupied by

Yb ions.[78] However, based on their very small intensity, the density of such state must be very low compared to Yb_{Al}.

As mentioned before, fig (5.9), two opposite PL behaviors are found in the PL evolution with temperature. Transition bands indicated by black squares ■ (one in visible and one in NIR regions) are thermally activated (populated), unlike all other observed transitions, which are thermally quenched (de-populated).

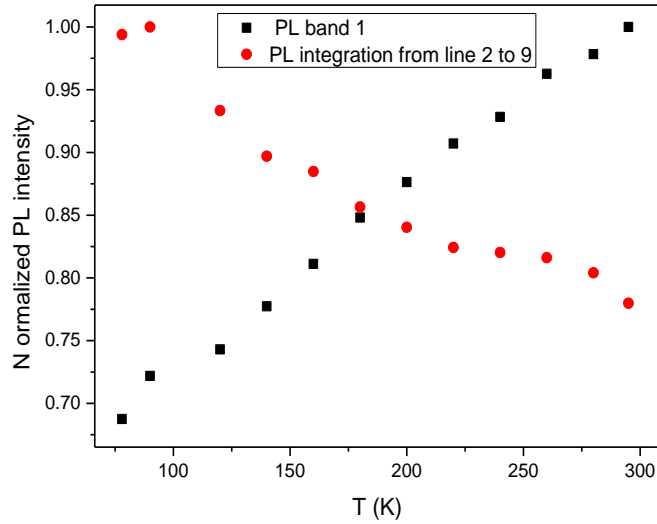


Fig. (5.12): Normalized PL as a function of temperature for band number 1 and integrated intensity for lines from 2 to 9 in fig (5.10).

The PL intensity evolutions as a function of temperature for NIR band ■ (thermally activated) and integrated intensity for all thermally quenched lines from 2 to 9 are shown in fig. (5.12). The integrated signal for lines 2 to 9 shows thermal quenching by about 23% while peak no. 1 shows PL enhancement by 30%.

PL thermal quenching can be explained considering the following arguments. It is widely accepted that the excitation of $4f-4f$ transitions in RE is achieved by energy transfer via a mediator. This mediator can be the host material (e.g. defects) or another ion (e.g. RE or transition metal). The PL thermal quenching pathways can be generally proposed through two channels:[86, 243] In the first channel, the gained thermal energy is partially absorbed by the excited mediator and leads to dissociation of its carriers before it transfers the excitation energy to the core localized $f-f$ levels of the RE. In this case, the characteristic time of the quenching process should be shorter than the time of energy transfer to the $f-f$ levels. In the second channel, the gained thermal energy is partially absorbed by the generated carriers from the $f-f$ levels and leads to dissociation of these carriers before it recombines. The later can

occur by back energy transfer to the mediator or to another defect that subsequently loses the energy either by radiative or nonradiative processes. This requires that the back energy transfer process is faster than f - f recombination process. It is worth mentioning that, any energy mismatch in the energy transfer process can be accommodated by phonons assistance.

The quantitative analysis of the PL evolution with temperature is performed using the Arrhenius equation, see equation (4.3) in the previous chapter. Fig (5.13) shows the data along with the best fit to the Arrhenius plot of integrated PL intensity for thermally depopulated peaks 2 to 9 in fig (5.10). From the fitting, two activation energies can be estimated, $E_{a1} = 11.2$ meV and $E_{a2} = 1200$ meV. In order to understand the physical meaning behind the two activation energies, the approach proposed in[117] can be used. The authors noticed that the thermal quenching in the PL emission lines of Er in GaN is accompanied with thermal activation (population) of other lines called "hot lines". In addition, they found that the estimated activation energy is very close to the energy mismatch (energy displaced) between hot and quenched lines. Following the same approach in our case, it is found that the energy displaced between the transition of highest energy within the quenched lines, peak 2 at 981.7 nm (1262 meV), and the thermally activated lines (■) at 972.2 nm (1274.6 meV) and 500 nm (2479 eV) equals 12.2 and 1217 meV, respectively. It is very consistent with the activation energies E_{a1} and E_{a2} , respectively.

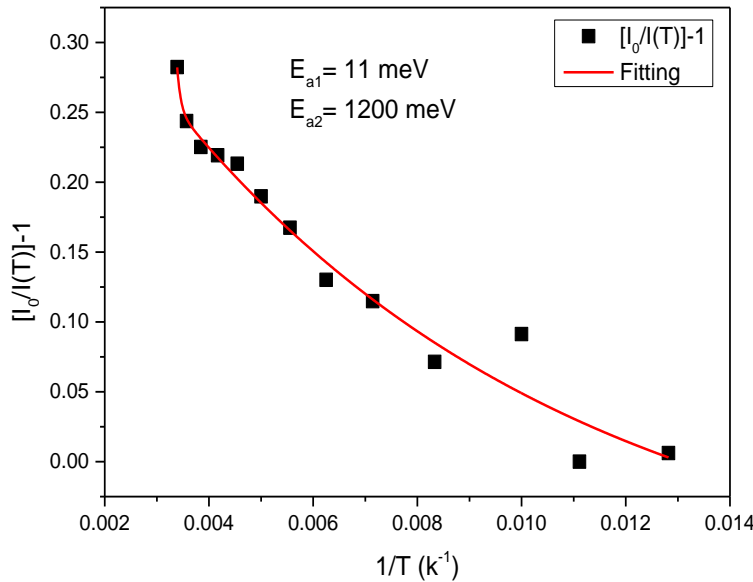


Fig. (5.13): $(\frac{I_0}{I(T)} - 1)$ versus T^{-1} for Arrhenius guiding of Yb-doped Al(O)N with 7% oxygen sample under excitation wavelength 325 nm.

This infers that, the thermal quenching of Yb^{3+} NIR emission in our samples occurs via energy transfer to thermally populated levels (■) at 500 nm and 972.2 nm. These two thermally populated levels lose the gained energy by radiative recombination. It can be considered that part of the population of these two levels (■) is enhanced by phonon-assisted energy transfer from the quenched PL lines in NIR region.

Part II: (Ce, Yb) co-doped Al(O)N

The similarity between the PLE of Yb-doped Al(O)N and Ce-doped Al(O)N, fig (5.7b), stimulates us to investigate the possible energy transfer between the two ions in co-doped AlN. It is also interesting to do so not only for curiosity but for practical applications. Recently, this RE system (Ce, Yb) has attracted great attention for energy down conversion. In down conversion (DC), the energetic UV-VIS photons are converted to less energetic photons in the IR. This approach can be realized via energy transfer mechanism based on quantum cutting or down shifting phenomena. Quantum cutting (QC) is refereeing to splitting of one energetic UV/visible photon into two IR photons, while down shifting (QS) is a process of converting one energetic photon into one photon of lower energy. Specific attention is given to QC for the high quantum efficiency that could be obtained. A particular attention is given to down conversion in solar cell field. Effectively, the spectral mismatch of Si-solar cell with the solar emission spectrum significantly limits the cell efficiency because a significant part of the solar spectrum in UV-Visible is not efficiently used and is thermally dissipated.

The NIR emission of Yb has been integrated in this field coupled with different ions such as Nd[244], Er[245], Tm[246], and Pr.[247] However, coupling Yb with Ce shows some interesting features pushing up the expectation level to increase the quantum efficiency conversion to the NIR signal close to 200%. This high expectation has been based on the unique optical properties of Ce of large UV/visible absorption cross-section with emission at 500 nm (20000 cm^{-1}) equal to the double of energy required for the Yb excitation (less than 10000 cm^{-1}). This means that one Ce ions can transfer its energy to two neighboring Yb ions. In addition, due to the absence of energy sub-levels in Ce ions, the back energy transfer from Yb to Ce is expected to be minimized. Therefore, the large UV-Visible absorption property of Ce can be exploited to absorb the solar emission in this region, then transfer the energy to Yb ions. Fortunately, the emission spectrum of Yb around 1000 nm (1.2 eV) is in good match with the bandgap of silicon 1.1 eV. Consequently, energy transfer from Yb to silicon can

occur. Therefore, coating silicon solar cell by a transparent layer containing Ce, Yb in down conversion coupling is expected to increase the solar cell efficiency.

However, this coupling system (Ce, Yb) has never been reported in AlN, which motivate us to go forward with this study. In addition, AlN is highly transparent in the UV- VIS. Therefore, it can efficiently transmit the solar emission and acts as a good protective layer for the cell. Moreover, using sputtering technique is an additional advantage since it is used for large scale coatings suitable for solar cell production.

The main goal of this part is to investigate on the influence of co-doping on the optical mechanisms of Yb ions. Therefore, (Ce, Yb) co-doped Al(O)N thin films have been prepared. The concentration of Ce was fixed to 1.5 at. % and the Yb content was varied between 0 and 1.5 at. %.

4- Structure of (Ce, Yb) co-doped Al(O)N sample

The crystalline structure of (1.5% Ce, 1% Yb) co-doped Al(O)N is examined by XRD, TEM and SAED, fig. (5.14). The XRD shows predominance of the (002) reflection evidences the wurtzite crystalline structure of AlN. The microstructure consists of columnar grains with the c-axis aligned with the growth direction as indicated by the TEM and the localized spots in the SAED pattern; respectively.

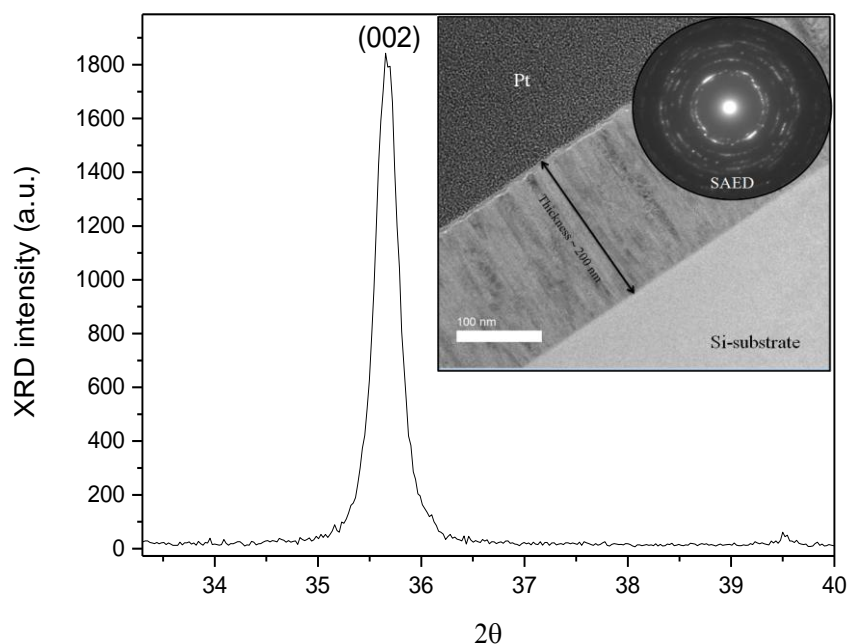


Fig. (5.14): XRD of (1.5% Ce, 1% Yb) co-doped Al(O)N sample. Inset: corresponding TEM and SAED images.

5- Photoluminescence

The PL of (1.5% Ce, 1% Yb) co-doped Al(O)N sample has been carried out using 325 nm and 266 nm *cw* lasers, as shown in fig (5.15).

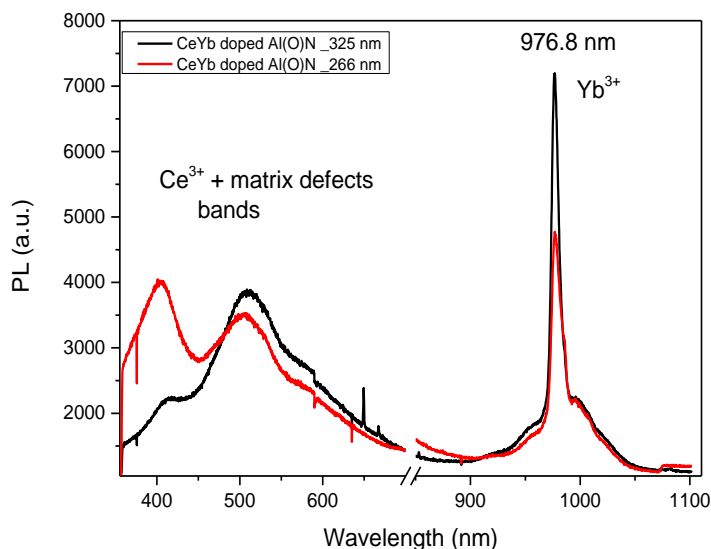


Fig. (5.15): PL spectra of (1.5% Ce, 1% Yb) co-doped Al(O)N sample excited by 325 nm and 266 nm wavelengths.

It is observed that the NIR emission related to Yb ions exhibits the same spectral shape under two excitation wavelengths and is characterized by single and sharp peak centered at 976.8 nm. In addition, small wide band at the base of the spectra is found, which usually referred to the overlapping of unresolved lines. In the visible region, two bands centered around 400 nm and 500 nm are detected. These bands can be ascribed to the emission of Ce^{3+} and radiative defects from the matrix that emit in the same region. The two PL contributions from Ce and defects are difficult to be de-convoluted due to the overlapping between the two emission spectra. Under 325 excitation the band at 500 nm is more intense than the band at 400 nm but the situation is reversed under excitation at 266 nm. This may indicate different excitation mechanisms and/or modulation of the contribution from the matrix defects in the PL process. Excitation by higher photon energy is supposed to increase the probability to involve more transition states in the emission process. For easier analysis and for comparison purposes, the PL spectra of Ce and Yb single-doped and co-doped Al(O)N are plotted together in fig (5.16).

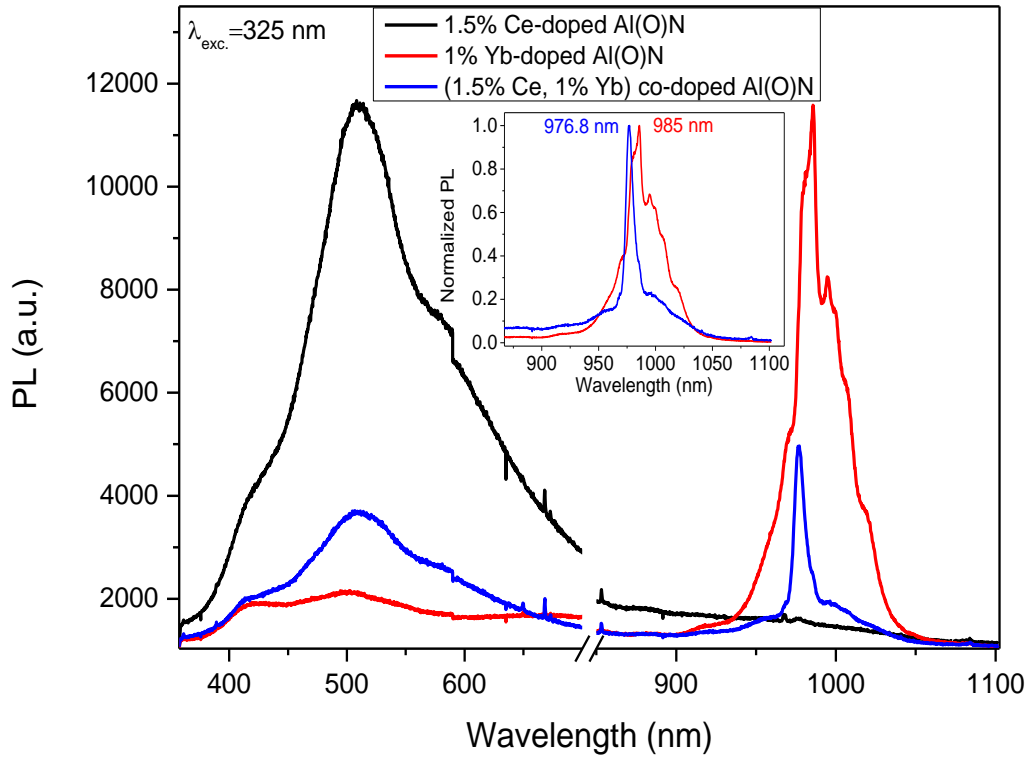


Fig. (5.16): PL spectra of Ce and Yb single doped and co-doped in Al(O)N samples. Inset: normalized PL of the NIR emission.

All samples have been measured under the same experimental conditions in the same run, such that we can compare the different contributions. The PL spectra of all samples reveal the different contribution of REs-related emissions as well as the matrix defects emission. From the visible part of the PL, one can realize the relative contribution of matrix defects and Ce^{3+} on the visible PL bands in Ce Al(O)N and (Ce, Yb) AlN samples. In addition, the spectra show the difference in the NIR emission related to Yb^{3+} ions. In Yb-doped Al(O)N sample, the NIR region exhibits a broad PL spectrum with significant appearance of small peaks and humps around the main peak centered at 985 nm. On the other hand, in (Ce, Yb) co-doped sample, the NIR emission exhibits a single peak centered at 976.8 nm surrounded at the base by small humps.

Hence, some remarks can be observed in this fig (5.16):

- Change in the spectral shape of the NIR signal in (Ce, Yb) co-doped with respect to Yb single doped sample.
- Shift in the fundamental NIR emission peak from 985 nm in Yb single doped Al(O)N to 976.8 nm in (Ce, Yb) co-doped sample.

- The NIR emission intensity related to Yb ions exhibits lower intensity in co-doped sample compared with Yb-doped Al(O)N.
- The visible PL band related to Ce and matrix defects in co-doped sample shows decrease in the intensity compared to Ce-doped Al(O)N.

All these spectral modifications in the co-doped sample point to a significant role that might be played by the interaction of Ce with Yb ions. In order to explore this kind of interaction, information about the excitation mechanism in the co-doped sample should be considered. Hence, PLE measurements have been done. Figure (5.17a) shows the PLE spectra recorded for the maximum NIR emission in Yb-doped Al(O)N (at 985 nm) and (Ce, Yb) co-doped Al(O)N (at 976 nm) samples. The PLE (@ 985 nm) for Yb-doped Al(O)N sample as described previously mainly consists of the two bands around 3.8 eV and 4.8 eV and is dominated by the second one. Both bands were assigned to defect complexes of oxygen coupled with aluminum vacancy ($V_{Al}-O_N$). In contrast, the PLE of NIR emission (@ 976 nm) in (Ce, Yb) co-doped Al(O)N is dominated by the band at 3.8 eV. In addition, the PLE band at 3.8 eV in the co-doped sample is slightly broader with higher contribution at the lower energy band tail as shown in the normalized PLE spectra, inset fig (5.17a). This could be related to the absorption by Ce^{3+} around 3.8 eV. These modifications in the PLE of the NIR emission band are indicative of the contribution of Ce in the NIR emission.

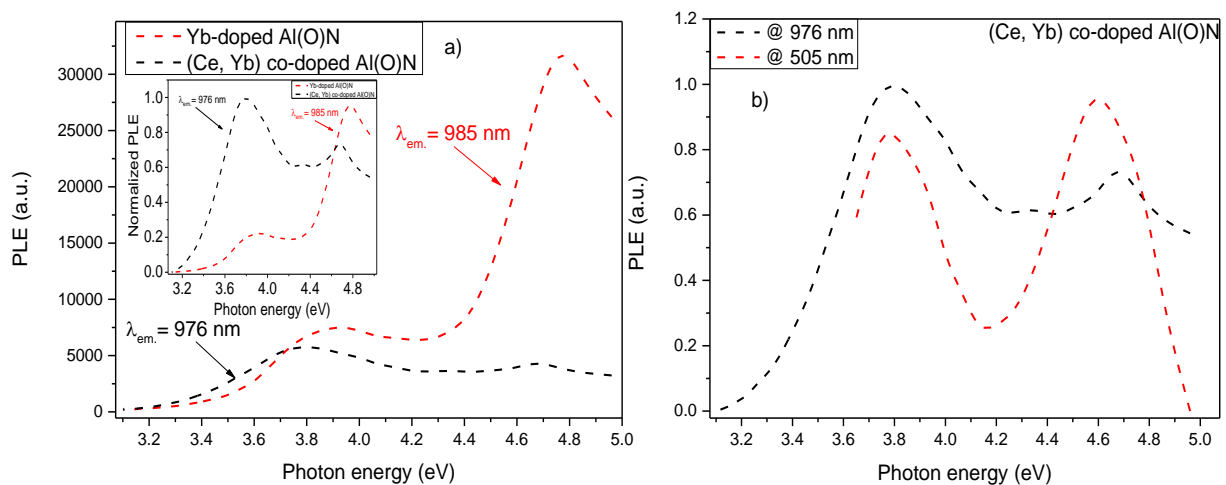


Fig. (5.17): PLE spectra a) at NIR emission from 1% Yb-doped and (1.5 Ce, 1% Yb) co-doped samples. b) at NIR and visible emissions of (1.5 Ce, 1% Yb) co-doped sample.

Moreover, the PLE of the co-doped sample shows similar band shape at 3.8 eV for visible (505 nm) and NIR (976 nm) emissions, see fig (5.17b). This similarity in the shape between the excitation band of Ce^{3+} and Yb^{3+} at 3.8 eV is considered as a direct evidence for the energy transfer between the two ions.[234, 248] Thus, one can suggest that, the absorption of Ce contributes in the NIR emission of Yb^{3+} . For further investigation of the energy transfer, (Ce, Yb) co-doped Al(O)N system has been examined using different concentration of Yb. The PL of these set of samples is presented in fig (5.18).

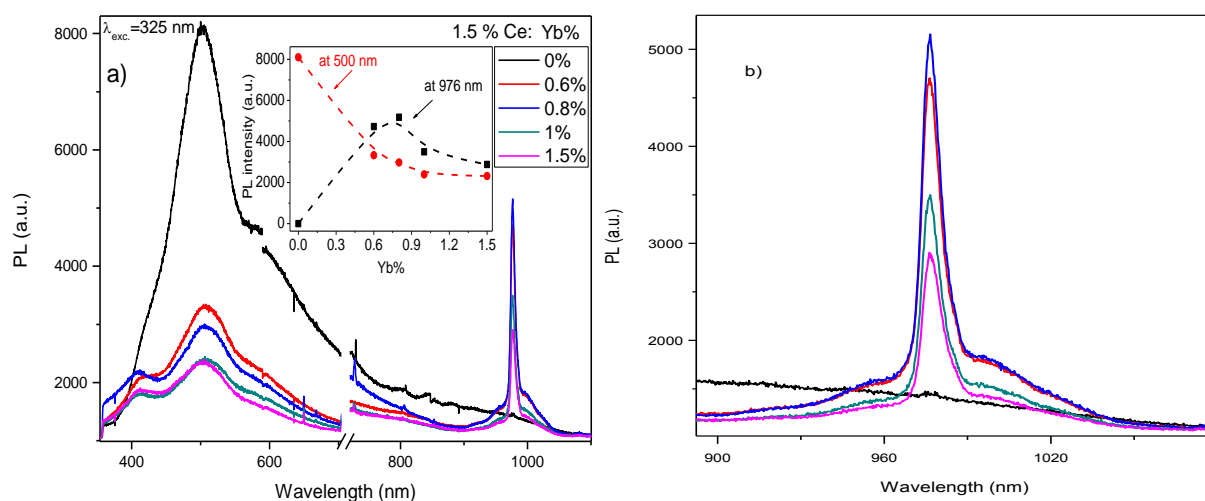


Fig. (5.18): a) PL spectra of (Ce, Yb) co-doped Al(O)N samples at different Yb concentrations. b) Zoom in the NIR spectra.

The PL spectra show a specific behavior that points to energy transfer from Ce to Yb ions as shown in the inset fig (5.18a). At 0% of Yb, we have only the visible PL band related to Ce ions. When the Yb% increases, the NIR emission appears and starts increasing. In the same time the visible PL band decreases. Further increasing the Yb content above 0.8 at. % reduces the NIR emission. This behavior can be ascribed to energy transfer from Ce to Yb.[211, 248-250] The decrease in the NIR emission at higher Yb% is attributed to concentration quenching phenomenon.[251] The mechanism of concentration quenching can be described by resonant energy migration between the Yb ions that leads to non-radiative energy transfer between excited and un-excited Yb ions. Moreover, incorporation of higher concentrations of Yb generates more lattice defects/impurities that could act as quenching centers for the PL.

This Ce-Yb interactions might be the reason behind the appearance of the single PL peak at 976 nm in the co-doped rather than the several PL peaks/shoulders around 985 nm in single Yb-doped Al(O)N sample. This likely indicates that, the energy transfer from Ce ions results

in selective excitation to specific excited state in Yb^{3+} and suppresses the other sublevels. This behavior suggests a cooperative energy transfer mechanism from one Ce ion to two Yb ions, which induces emission of two NIR photons with the same energy. However, further investigations are required to justify or decline this expected cooperative mechanism.

Therefore, time resolved photoluminescence (TRPL) measurements have been performed for further clarifying the energy transfer process. Unfortunately, evolution of Ce decay times couldn't be followed because of the very fast decay time of Ce and the limitation of our excitation and detection systems. However, the decay time of Yb ions could be probed and brought some information in this regard. Fig (5.19) shows the TRPL of the NIR emission of Yb in Yb-doped Al(O)N and (Ce, Yb) co-doped Al(O)N.

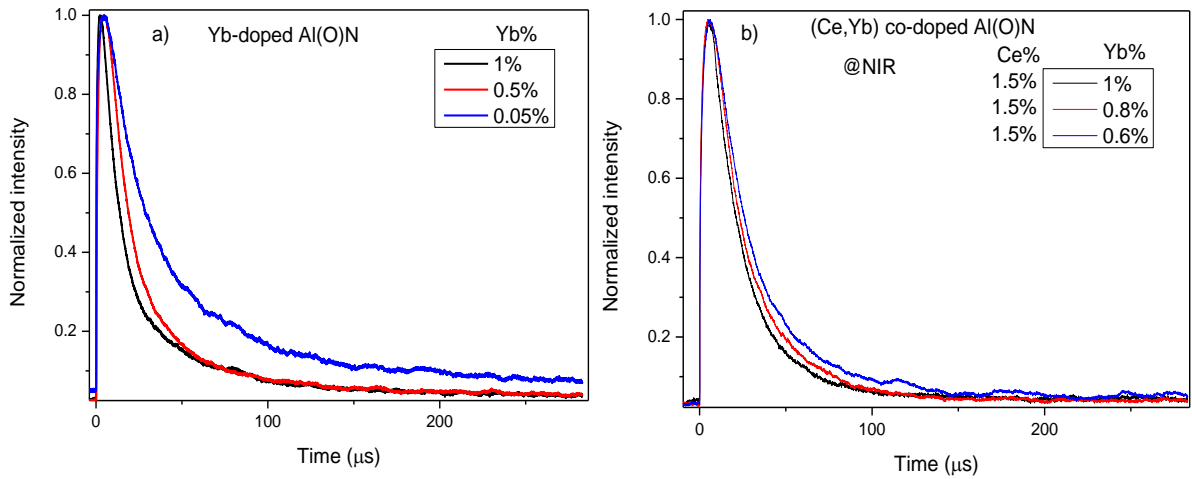


Fig. (5.19): TRPL for the NIR emission of a) Yb-doped Al(O)N, b) (Ce, Yb) co-doped Al(O)N.

It can be observed that both sets of single and co-doped samples exhibit a decrease in the decay rate with Yb concentrations in line with the concentration quenching phenomenon. The average fluorescence lifetime of Yb ions (τ) in single and co-doping samples have been estimated using the following equation:[119-120]

$$\tau = \frac{\int_0^{\infty} t I(t) dt}{\int_0^{\infty} I(t) dt}, \quad (5.1)$$

where $I(t)$ is the intensity at time t . It is found that the average lifetime of Yb^{3+} in single and co-doped samples exhibit insignificant changes and it is equal $\sim 63\text{-}70 \mu\text{s}$ in all samples. This indicates that the presence of Ce has no significant influence on the decay time of Yb^{3+} . However, the careful observation of the rise times in single and co-doped samples reveals a

slower response rate in the co-doped as shown in fig (5.20). This strongly suggests the energy transfer mechanism mediated by Ce ions that stretches the excitation process of Yb^{3+} .

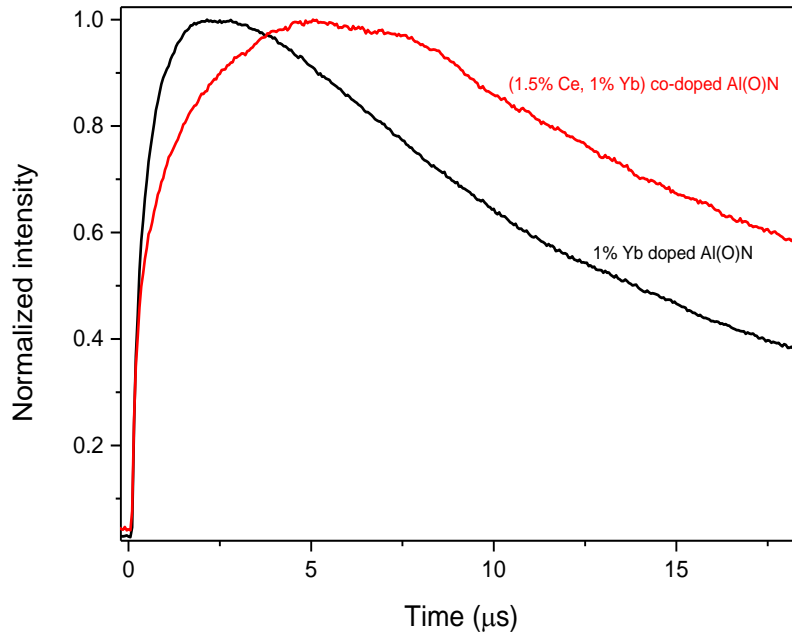


Fig. (5.20): Rising time response curves for single and co-doped Al(O)N sample.

It is found that the rise time response curve for the co-doped sample is best fitted by a double exponential growth function and results in two rise time components ($\tau_1 = 3.5 \mu\text{s}$, $\tau_2 = 0.5 \mu\text{s}$). In contrast, the rise time of Yb in single doped sample is best fitted by a single exponential growth function with rise time value equal $0.4 \mu\text{s}$. It is worth noting that, the rise time in single doped sample exhibits single component with value close to the second component in co-doped sample. Since the rise time is considered as a sign for the excitation pathways, this suggests that the excitation of Yb ions in co-doped system can be proposed via two pathways, unlike the excitation of Yb in single doped system that can occur via one pathway. Therefore, the excitation of Yb in single doped sample can be considered by energy transfer from one mediator, which is likely the host defect band located in the PLE spectral range from 3.4 to 4.2 eV and assigned to oxygen related defects, see PLE fig (5.17). In co-doped samples, some Yb ions are excited by the same mediator as in single doped case (exhibit close rise time values, around $0.5 \mu\text{s}$) and other Yb ions are excited by a different mediator with longer rise time, probably involving the Ce ions. This is consistent with the assignment of the PLE band, centered at 3.8 eV, to the overlapping between the absorption of Ce and the host defects.

In all cases the rise time is found to be longer than the expected decay time of Ce, which is about few nanoseconds. If the energy transfer from Ce to Yb was a direct process, the rise time should correspond to the relaxation time from the $5d$ levels in Ce^{3+} to the $^2\text{F}_{7/2}$ of Yb^{3+} . [250] The long rise times obtained suggest that the energy transfer for Ce^{3+} to Yb^{3+} is not achieved through a direct process. J. Ueda et al, [250] considered that, the longer rise time of Yb in (Ce, Yb) system than the decay time of Ce is due to a slow nonradiative relaxation from a charge transfer state (CTS) to the $^2\text{F}_{5/2}$ of Yb^{3+} . In this case the energy transfer is achieved via one-to-one photon through CTS mechanism and not through cooperative mechanism (one-to two photons).

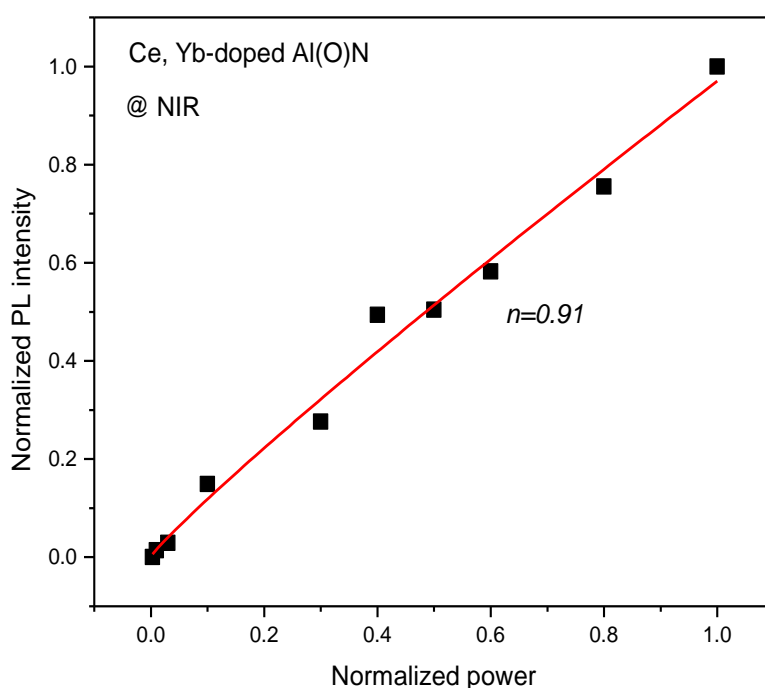


Fig. (5.21): Power dependence of Yb emission of a (1.5% Ce, 1% Yb) co-doped sample excited by 325 nm.

Moreover, power dependent PL is used to figure out the type of the energy transfer mechanism. Excitation power measurements allow determining the origin of the down-conversion (DC) process. [252-253] A power law ($I_{PL} \propto P^n$) is used, where I_{PL} is the PL intensity, P is the excitation power and n is corresponding to the number of transferred photons that produce one NIR photon. [252-254] The power dependence measurement for the (Ce, Yb) co-doped system shows a near linear dependence, where n is close to 1, as shown in fig (5.21). This further confirms the lifetime findings that the energy transfer from Ce to Yb occurs through CTS mechanism, i.e. one-to-one photon.

CTS is usually attributed to electron transfer mechanism among between Ce and Yb ($Ce^{3+} + Yb^{3+} = Ce^{4+} + Yb^{2+}$). We see from the above that Yb-doped Al(O)N and Ce-doped Al(O)N are efficiently excited by UV light through host defects than Ce. Then, a question can be raised about the significance of co-doping Al(O)N with Ce and Yb ions for down conversion (DC) applications. The answer can be as follows:

The emission intensity of 1% Yb in single doped system is found to be higher than 1% Yb in the co-doped one. However, there is uncertainty about doing such comparison. Despite having the same Yb content in both systems, the total concentration of REs ions in co-doped system (Ce+Yb) is higher (about 2.5%). This large amount of foreign dopants probably results in the generation of a high density of defects, which may act as quenching centers. So, if we need to compare the absolute PL intensity of NIR emission of Yb in this co-doped sample, the correct comparison could be done with Yb-doped Al(O)N sample containing about 2.5% of Yb. The reason that forced us to assume such uncertainty is the significant role of defects in the PL quenching behavior of our samples, as described above.

Nevertheless, for such DC application for which the spectral shape of the NIR emission is not so important but the absolute emission intensity is critical (e.g. Si-solar cell), Yb single-doped Al(O)N could be the good choice. On the other side, for applications mainly interesting in a narrow NIR spectrum (lasers, waveguiding), (Ce, Yb) co-doped Al(O)N could be of interest. For instance, the effective emission cross section multiplied by the radiative lifetime ($\sigma_e\tau_r$) of Yb is an important parameter in laser applications.[216, 227, 255] This parameter can be calculated by applying Füchtbauer–Ladenburg method[227] on the emission spectra of Yb^{3+} (see annex D). A large value of this parameter minimizes the absorption loss and lowers the threshold gain of the active medium of laser. In our samples, the ($\sigma_e\tau_r$) value in (Ce, Yb) co-doped system ($1.12 \times 10^{-20} \text{ cm}^2 \text{ ms}$ @ 976 nm) is found to be larger than the value in Yb single doped system by 1.5 times ($0.74 \times 10^{-20} \text{ cm}^2 \text{ ms}$ @ 985 nm).

In addition, simultaneously intense and narrow NIR emission of Yb can be achieved in our (Ce, Yb)-doped aluminum oxide sample. In order to exploit the advantage of high PL intensity observed in Ce-doped aluminum oxide (see chapter IV), a (Ce, Yb) co-doped aluminum oxide film was prepared. The PL of this sample is presented in fig. (5.22).

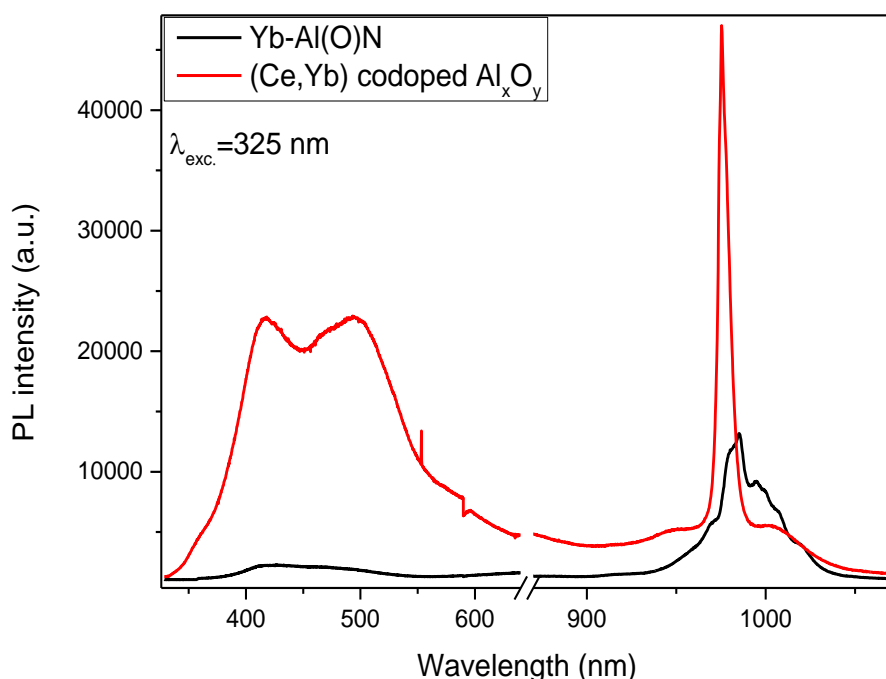


Fig. (5.22): PL spectra of (1.5% Ce, 1% Yb) co-doped aluminum oxide sample and Yb-doped Al(O)N.

In the oxide case, the NIR emission exhibits a very intense signal compared to Yb-doped Al(O)N as well as a narrow spectral shape as in (Ce, Yb) Al(O)N. So, the spectral properties can be modified depending on the desired application by modifying selecting the appropriate RE ion(s) and changing the local chemistry of the matrix.

There remains a chance to increase the NIR emission intensity significantly in (Ce, Yb) Al(O)N by achieving cooperative energy transfer. This can be done by finding a way to avoid or minimize the CTS process.[251] This could be achieved by searching for the optimum Ce and Yb concentrations, modifying the composition of the Al(O)N material, or doping with a third mediator.[234] This requires a dedicated study that could be interesting for a future work.

All the above findings confirm the energy transfer from Ce to Yb via CTS mechanism. Thus, the previously our proposed reason behind the narrow NIR spectral shape in co-doped system, based on selective cooperative energy is not realistic. The reason may be related to the strength of the local crystal field around Yb ions, which is likely reduced by the presence of Ce or Ce and oxygen together. Measuring the PL of the co-doped system at low temperature can help us to clarify this.

6-Low temperature photoluminescence (LTPL)

The PL of (Ce, Yb) co-doped sample has been measured as a function of temperature from 78 K to 295 K in order to explore the influence of the crystal field as well as the thermal PL quenching mechanisms, as displayed in fig (5.23).

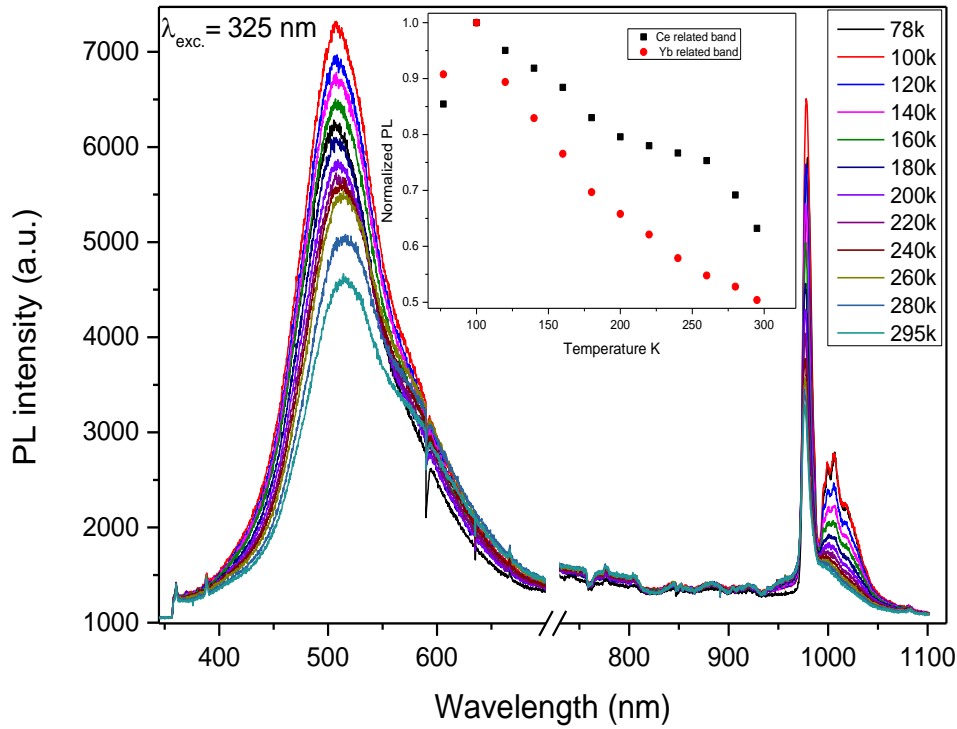


Fig. (5.23): PL as a function of temperature from 78K to 295K for (Ce, Yb) co-doped Al(O)N sample. Inset fig is the PL evolution with temperature for the Ce and Yb related peaks.

It can be observed that both Ce and Yb emission bands follow similar PL evolution. When the temperature rises up to 295 K, the PL band related to Ce ions at the visible region exhibits thermal quenching by 40% from its maximum intensity value. In the same time, the NIR emission related to Yb^{3+} is quenched by 50%. In addition, the spectral shape changes with temperature. PL at 78 K and 295 K are plot on fig (5.24a) for more clarity.

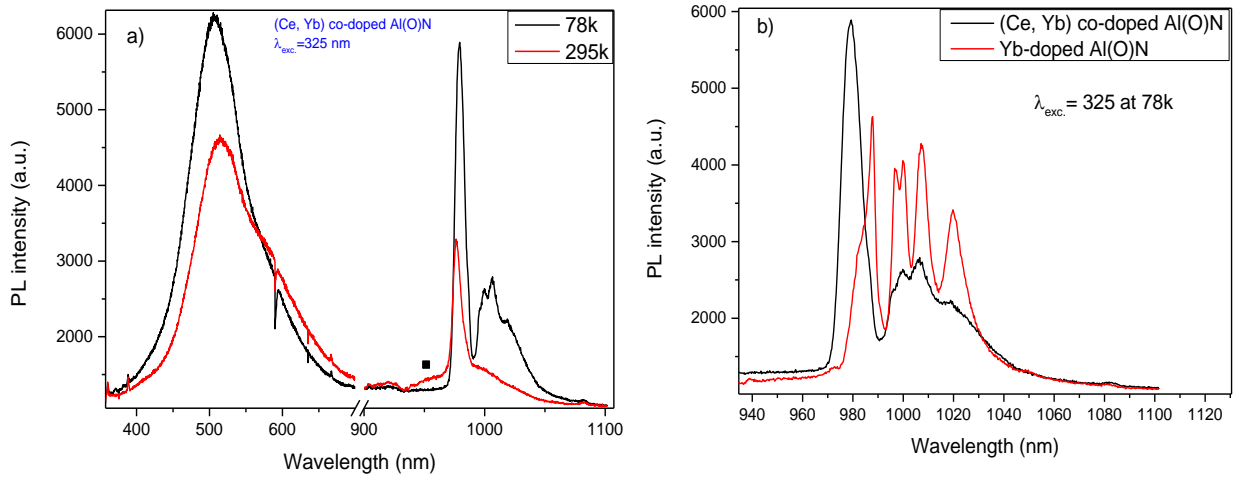


Fig. (5.24): a) PL spectra of (Ce, Yb) co-doped Al(O)N carried out at 78k and 295k. b) NIR emission spectra for (Ce, Yb) co-doped and Yb-doped samples carried out at 78k.

The NIR emission peak at 976 nm is increased and slightly red-shifted when the temperature is decreased down to 78k. Moreover, a broad sub-band overlapped with small peaks starts to appear at the lower energy tail of the main peak at 976 nm. The higher PL intensity and appearance of new splitting peaks at low temperature have been discussed in the previous section of LTPL for Yb-doped Al(O)N. However, the splitting strength of the sub-levels in the NIR emission of (Ce, Yb) co-doped is rather weaker than in the case of Yb-doped Al(O)N, fig (5.24b). This can be attributed to presence of Ce ions and/or Ce with oxygen that likely reduces the crystal field strength of the host around Yb ions by screening or distorting the local surrounding environment. This could be considered as the reason behind the single peak shape of NIR emission in co-doping system.

The quantitative analysis of the PL evolution with temperature can be obtained from Arrhenius plot, fig (5.25a, b). The thermal quenching of NIR emission exhibits only one activation energy about 28.5 meV unlike for single Yb-doped Al(O)N that showed two activation energies. However, the same thermal quenching mechanism can be used in our interpretation. Effectively, the PL thermal quenching behavior for the peak at 976 nm (1270 meV) can be explained by the thermal activation of small pre-hump (■) at 953 nm (1300 meV), fig (5.24a). The energy mismatch between the two transitions is equal to 30 meV, which is very close to the calculated activation energy 28.5 meV, fig (5.25a). This indicates that the thermal de-population in the fundamental peak at 976 nm is accompanied by thermal population of another radiative state at 953 and the energy mismatch is compensated by the thermal activation energy of 28.5 meV.

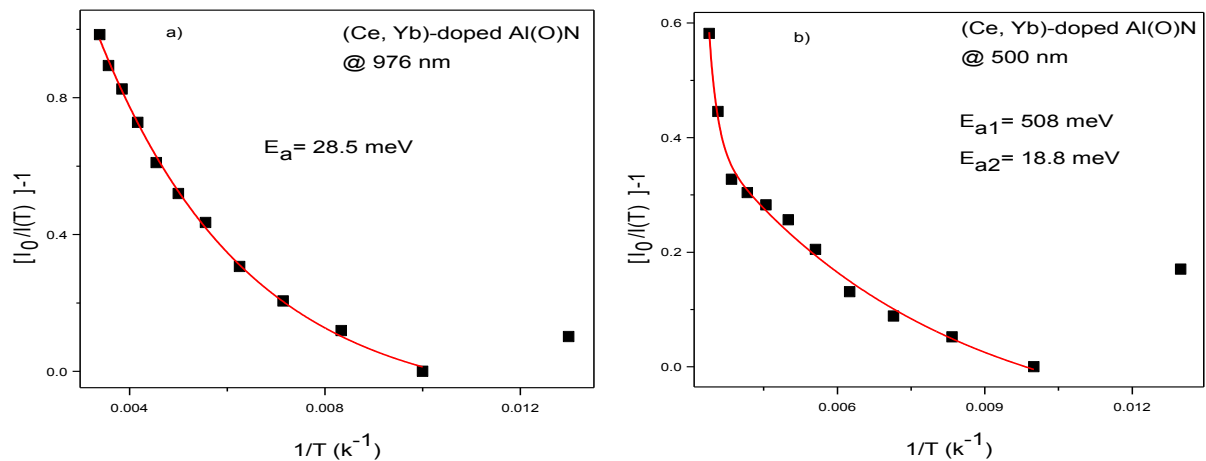


Fig. (5.25): $(\frac{I_0}{I(T)} - 1)$ versus T^{-1} for Arrhenius guiding of (Ce, Yb) co-doped Al(O)N sample calculated for the NIR (a) and visible emission (b).

On the other hand, the PL thermal quenching behavior of the visible emission related to Ce ions exhibits two activation energies 18.8 meV and 508 meV as shown in fig (5.25b). The summation of these two activation energy values (526.5 meV) is close to the summation of activation energy values for the single Ce-doped Al(O)N sample (513.5 meV) and both are very close to the energy difference between $5d_1$ and the conduction band maximum of about 530 meV. Hence, the thermal quenching mechanism can be considered via electron transfer from the excited $5d$ levels in Ce to the conduction band of the host, see the schematic fig (4.28) in the previous chapter.

7- Conclusion

In this chapter, Yb-doped and (Ce, Yb) co-doped Al(O)N films were prepared. The crystal structures and compositions of the prepared samples have been investigated by XRD, TEM and RBS measurements. Indirect optical excitation of the NIR emission of Yb ions has been obtained. The excitation mechanisms of the NIR and visible emission of single and co-doped samples have been discussed. A comparison with the excitation mechanism of Ce single doped in Al(O)N was presented. It was found that the similarity between the PLE spectra of the PL of Ce and Yb results in the possibility of achieving energy transfer between the two ions in the co-doping system. The energy transfer mechanism is manifested in the discrepancy between the NIR emission by Yb in co-doped and single-doped samples. In addition, the PL rise time associated to Yb stretches in co-doped Al(O)N, which is considered as a strong sign for the energy transfer between Ce and Yb. Results are consistent with a one-to-one down conversion scheme via charge transfer state mechanism. The PL thermal quenching has been

studied by following the PL evolution with low temperatures. The thermal quenching mechanism of Yb ions is proposed via back energy transfer to thermally populate other radiative states. In addition, we proposed that the reason behind the narrow NIR emission peak in the co-doped system is the reduction of the crystal field around Yb ions by Ce and O.

General conclusion

This project is dedicated to study the optical properties of rare earth-doped aluminum nitride thin films. More particularly, the work is oriented to investigate the luminescence mechanisms of selected RE elements incorporated in AlN thin films to be used as a candidate for lighting devices. Rare earth-doped III-V compounds attracted great attention since it shows direct and large optical bandgap in the range 2 eV to 6 eV, providing good opportunity to host the RE ions emit in ultraviolet-visible (UV-Vis) range. Also, it offers the possibility of the integration with semiconductor microelectronics. Among III-V compounds, hexagonal wurtzite AlN exhibits the largest direct optical bandgap (6 eV). In addition, it exhibits very interesting chemical and physical properties such as strong chemical resistance and large thermal conductivity. Thus, it is a promising candidate for integration in devices working at high power operation. Nevertheless, the optical mechanism of RE-doped AlN is still under debate, which motivates us to start this study in order to explore the optical behavior of this system.

For undoped AlN, well crystallized AlN thin films with high degree of c-axis orientation were prepared by reactive magnetron sputtering of an aluminum target. Controlling the preferred orientation by only tuning the $N_2\%$ in the gas phase has been achieved. It was found that, the synthesis of highly c-axis oriented crystalline AlN is favored by depositing the coatings in nitrogen-rich reactive ambiance. The results have been interpreted on the basis of an improved mobility of adatoms assisted by the bombardment of the films by fast particles. Intentional thermal assistance or increase of the discharge current were found to have similar beneficial influence on the crystallinity of the c-axis oriented films deposited under pure nitrogen conditions. This is explained by thermally-assisted increase in adatoms mobility in both conditions as supported by thermal probe measurement under different discharge currents. The optical constants (n , k) and bandgap of the prepared films have been modeled from spectroscopic ellipsometry measurements in transmission and reflection modes. This evidenced the possibility to tune the refractive index with the crystal orientation while keeping constant the bandgap. Our findings suggest that, the optical properties of the AlN films can be tuned via their crystallographic orientation which, in turn, varied by the amount of nitrogen in the gas phase. Moreover, some of the AlN optical anisotropy has been

discussed. Significant birefringence and dichroism have been found in our prepared c-axis AlN, which point to the possibility of using AlN for efficient waveguide devices.

For doped AlN, crystalline Ce-doped AlN were prepared using RMS technique. The crystal structure of the prepared samples and the compositions have been examined by TEM, RBS, EDS and EELS analyses. It was found that, presence of oxygen in this material is essential for sensitizing the photoluminescence. Oxygen has been found playing major role not only in converting Ce ions from the optically inactive state +4 to the optically active one +3, but also led to the formation of defect complexes with Al vacancies. These defect complexes were found contributed in the excitation mechanism of Ce ions. This double role of oxygen is confirmed by EELS (for identification of the oxidation state of Ce) and photoluminescence excitation (PLE) measurements (for defect complexes assignments). Therefore, an optical excitation and emission mechanisms have been proposed based on the role of oxygen. This proposed mechanism was found consistent with the interpretation of the PL results, as well as confirmed by testing the PL behavior at higher concentration of oxygen. Based on that, manipulation of the PL was achieved and different colors (blue, and green) were clearly observed by the naked eye. In addition, PL thermal quenching mechanism has been proposed by studying the temperature dependent of the PL. The PL thermal quenching was proposed based on thermal ionization mechanism by electron transfer from the 5d levels of Ce³⁺ to the conduction band. Moreover, white light emission approach has been presented and strong eye observed white light was obtained.

Yb-doped and (Ce, Yb) co-doped Al(O)N systems are prepared. The crystal structures and compositions of the prepared samples have been investigated by XRD, TEM and RBS measurements. Indirect optical excitation of the NIR emission of Yb ions is achieved. The excitation mechanisms of the NIR and visible emission of single and co-doped samples are discussed. A comparison with the excitation mechanism of Ce single doped in Al(O)N is presented. It is found that, the similarity between the PLE spectra of Ce and Yb results in the possibility of achieving energy transfer between the two ions in the co-doping system. The energy transfer mechanism is manifested in the discrepancy of the NIR emission of Yb in co-doped sample than the Yb emission in single doped sample. In addition, elongation of the rise and decay time of the PL of Yb in co-doped is considered as a strong sign to the energy transfer. The type of energy transfer mechanism is found consistent with the one-to-one down conversion via charge transfer state mechanism. The PL thermal quenching has been

studied by following the PL evolution with low temperatures. The thermal quenching mechanism of Yb ions is proposed via back energy transfer to thermally populate other radiative states.

Hopefully, this dedicated study offers better understanding to luminescence properties of Ce and Yb based aluminum nitride, (oxy)-nitride, and oxide compounds that can be used in solid state lightening applications.

Future perspectives

This work is not the end of the story, like any scientific research when you reach to what looks like the complete picture a lot of new and missing parts start to appear. Here, I would like to point to some of these parts hopefully to help me or someone else to build up on the present study.

Indeed, understanding the optical behavior of undoped and doped AlN materials opens the door to many future works that can better exploit the functional properties of such materials. For instance, the undoped AlN shows very promising anisotropic features (birefringence and dichroism) which can be controlled by the experimental conditions. These features are of great importance in nonlinear optics applications. Therefore, we believe that a dedicated study to these nonlinear properties (e.g. second order nonlinear susceptibility) will provide new channels to apply AlN thin films in nonlinear chip-scale technology.

For Ce-doped AlN study, with our proposed approach, the manipulation of the photoluminescence is quite well controlled and understood. However, deep analysis for the defects characterization which play the major role in this PL is still missing. This will be part of our future interest by exploring such characterizations by using for example thermoluminescence technique. As well as, the scintillation properties of this material is not figured out yet. In addition, the electrical excitation (electroluminescence) of Ce-doped AlN thin films, which is needed for optoelectronic applications, is challenging due to the some insulation properties of AlN. Achieving the electroluminescence from Ce-doped AlN will be our main target in the near future.

For Yb and (Ce, Yb) co-doped AlN study, we think that this study still in the beginning stage, particularly the co-doped system, and more effort is needed to well understand the energy transfer between Ce and Yb ions. For instance, great potentials can be directed to find the

optimum conditions for achieving down conversion via cooperative energy transfer (quantum cutting) at different REs concentrations and/or host compositions.

Annexes

Annex A

Fitting procedure that used to determine the dispersion relations of $n(\lambda)$ and $k(\lambda)$ from transmission measurements

Attempts to describe the refractive index either by Cauchy's or Sellmeier's empirical dispersions result in oscillations which are referring to AlN defects. The fact that these dispersions models are well suited to highly transparent films,[256-258] makes relevant to these samples the use of multiple Kramers-Kronig consistent Gaussian oscillators to express the dispersions of $n(\lambda)$ and $k(\lambda)$. The Woollam-WVase software has been used to fit three oscillator's parameters, i.e. the central wavelength (or energy position), strength and broadening. Excellent fits have been obtained with appreciably low mean-squared errors (maximum likelihood estimators) between 0.10-0.13 as shown in the inset fig (A.1). The good quality of these fits is further confirmed by the randomly distributed differences between the modeled and measured transmittance close to zero without any systematic trend. Table (A.1) displays the best-fit oscillator parameters with their error (90% confidence limits). The center energy of first and the last oscillators were fixed at their extreme possible wavelengths to avoid parameter correlations. The reasonably low error values also attest the validity of the assumed optical model for our AlN films. Moreover, the fitted film thickness is close to that obtained from both in situ reflectometry and TEM.

Table (A.1): the best-fit oscillator parameters used to model transmission measurements.

Oscillator Number	Amplitude	Center energy (eV)	Broadening (eV)	ϵ_1 offset	Thickness (nm)
1	0.85 ± 0.01	6.5 (fixed)	0.76 ± 0.01	3.27 ± 0.03	209 ± 3
2	0.143 ± 0.006	5.68 ± 0.02	0.68 ± 0.03		
3	0.064 ± 0.001	4.81 ± 0.01	0.86 ± 0.03		
4	0.029 ± 0.002	3.53 ± 0.03	2.34 ± 0.19		
5	0.047 ± 0.001	1.5 (fixed)	3.27 ± 0.03		

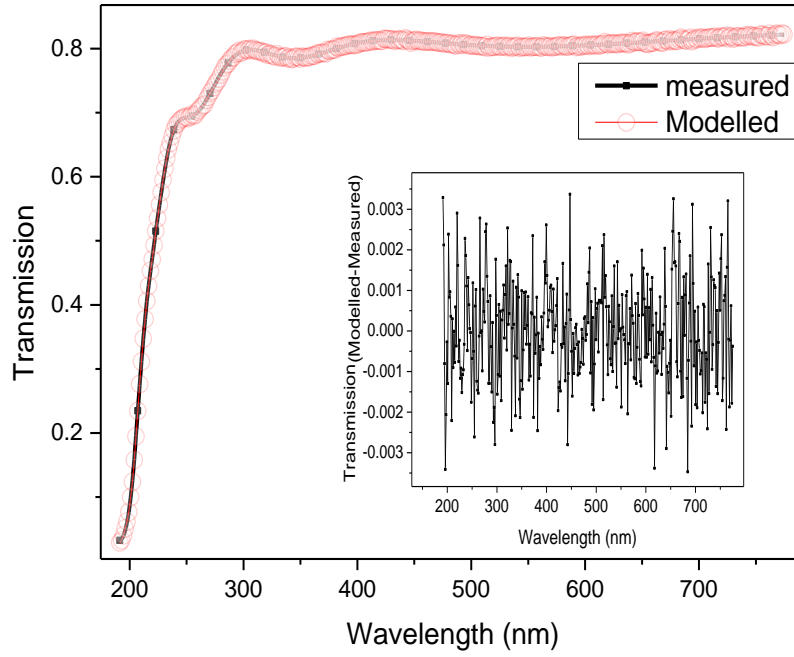


Fig (A.1): Example for the fitting of the measured transmittance. Inset: the error deviation between them.

Annex B

Anisotropic optical properties of AlN

Hexagonal wurtzite AlN is characterized by intrinsic uniaxial anisotropic properties. The specific stacking sequence of atoms in hexagonal wurtzite structure results in structural and optical anisotropy between the directions parallel and normal to the c-axis. This attracts high attention, particularly, in the field of optoelectronics. The optical anisotropy "Birefringence", that corresponds to the difference in magnitude between the ordinary (n_o) and the extraordinary (n_e) refractive indices has been early reported for AlN in [259] based on transmission-reflection measurements. It plays an important role in integrated based-waveguide optics. Controlling the birefringence of AlN is of great importance, especially in the field of integrated optics. For instance, conventional linear integrated optics are based mostly on single mode waveguides, while realizing nonlinear and quantum integrated optics requires control of multimode dispersions. Thus, manipulating the optical anisotropy of AlN can be used for this purpose. It was found that, in waveguide applications, the propagation of guided light is controlled by the confinement efficiency in both transverse electric (TE) and

transverse magnetic (TM) Polarizations.[42] Knowing that, the TE-mode is determined by n_0 and TM-mode by n_e . [12, 260] Adjustment of these refractive indices can enhance the guiding efficiency. Furthermore, thanks to the significant large birefringence and high 2nd order nonlinear susceptibility, AlN attracts great attention in non-linear photonic circuits. R. Martin et al, [261] displayed the potential use of AlN for nonlinear optical applications based on quasi-phase matching by adjusting the optical anisotropic parameters of polar AlN films. In addition, M. Stegmaier et al[12] reported on the applicability of using AlN waveguides for frequency mixing on chip scale. For instance, one of the well known frequency mixing processes is the second harmonic generation (SHG). Thanks to the high second order of c-axis AlN, this SHG process can be realized.[262]

In order to get through the optical anisotropy of our AlN samples, spectroscopic ellipsometry (SE) has been performed. SE is a powerful tool in determining the ordinary and extraordinary refractive indices with high accuracy. In this regard, S. Shokhovets et al[263] demonstrated that SE is an excellent method that can be used for determining the optical anisotropy of thin film layer and overcomes on the limitations of the other methods like (prism coupling technique).

Herein, the anisotropic analyses are focused on sample 100% N_2 deposited at room temperature that exhibits good c-axis orientation (002) perpendicular to the substrate in the XRD, see fig (3.1). For comparison, the sample deposited at 80% N_2 , that shows small reflection contribution of (101) plane, has been also investigated. The three layers model system air/isotropic and uniform film/silicon substrate has been used to fit the modeled reflection (generated) to the measured data. Fig (B.1) shows the measured and generated ellipsometry parameters Δ and Ψ for samples 100% and 80%.

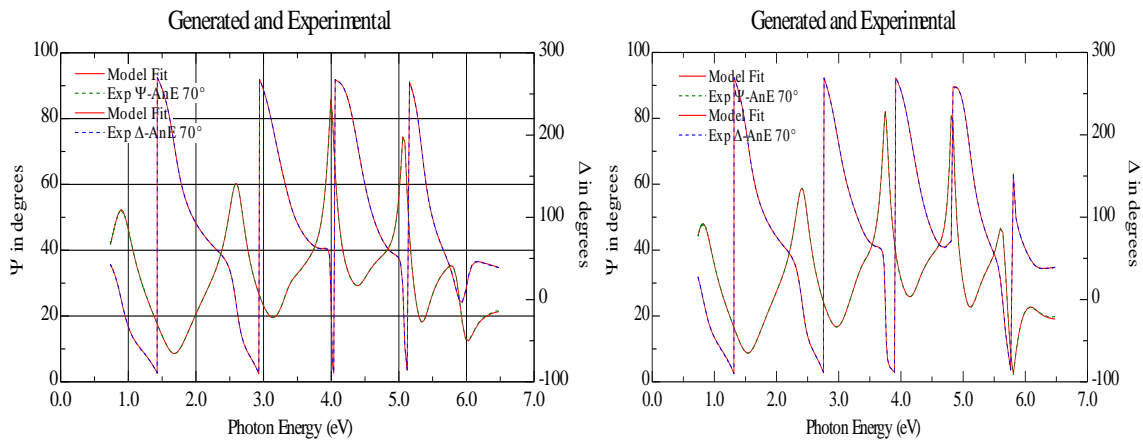


Fig (B.1): Experimental and fitting ellipsometry parameters Δ and Ψ for samples prepared at 100% N_2 (on left) and 80% N_2 (on right).

Very good fit to the measured data has been obtained with about zero error deviations. The dispersion relation of n_o and n_e refractive indices has been extracted and plotted for both samples, as shown in fig (B.2a, b). It is observed that n_e is always larger n_o . This is in line with the positive birefringence for hexagonal wurtzite AlN reported by V.I. Gavrilenko et al. [264]. The dispersion behavior of the birefringence Δn can be given as shown in (B.2c). The birefringence value of 100% N_2 sample is higher than for 80% N_2 sample and the difference in the visible is significant at about 0.02, which highlights the role of texture on the anisotropic optical properties of AlN. This birefringence shows dependency to the incident photon energy (wavelength). For example, in sample deposited at 100%, the birefringence changes from 0.056 (@1770 nm IR) to 0.1 (@350 nm UV) as seen in fig (B.2c).

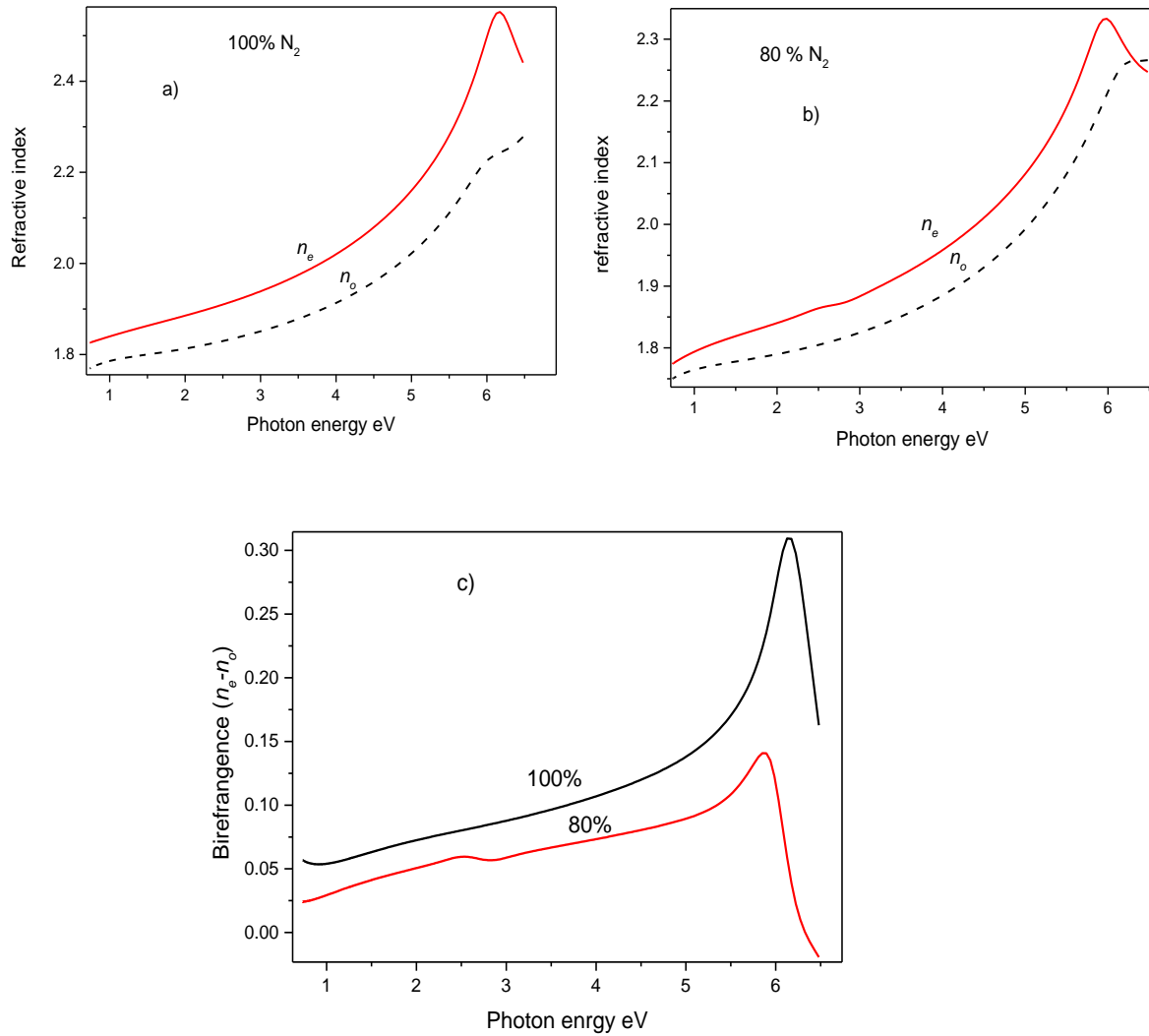


Fig (B.2): a) and b) the refractive index dispersion relation for samples 100% and 80%, respectively. c) the birefringence as a function in the photon energy for both samples.

AlN offers efficient wavelength conversion due to its high second order nonlinearity, hence second harmonic generation (SHG) can be achieved. This requires fulfilling the phase matching conditions between the pump and the SHG wave, which can be realized by adjusting n_0 and n_e in c-axis AlN.

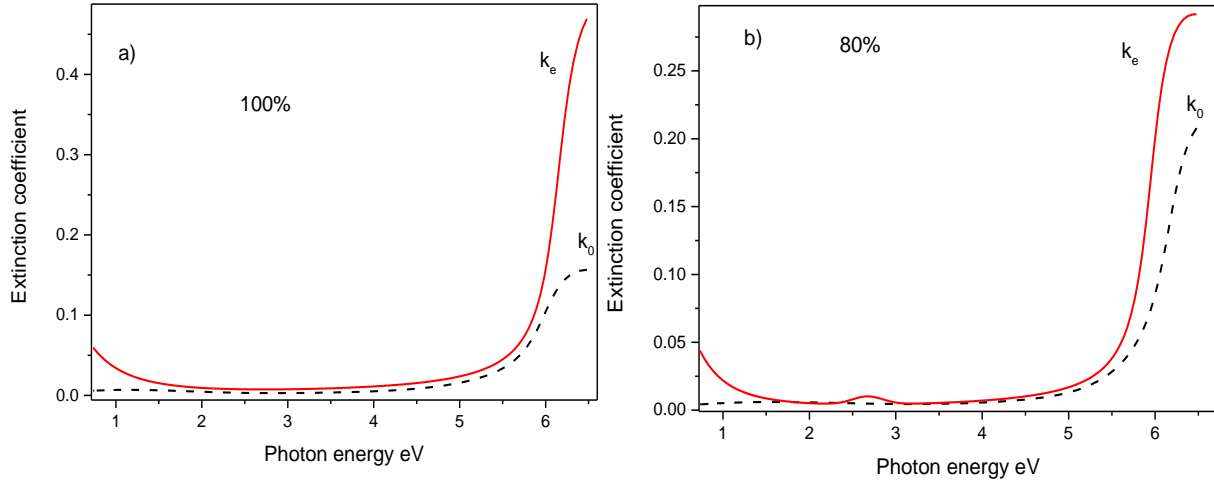


Fig (B.3): The extinction coefficient as a function in photon energy for samples a) 100% and b) 80%.

The polarization-dependent ordinary (k_0) and extraordinary (k_e) extinction coefficients are shown in fig (B.3) as a function of photon energy for both samples. It can be noticed that the absorption is very weak in the transparent region and starts to have significant values above 5 eV near the bandgap edge of AlN. In addition, a dependence of near bandgap absorption on the polarized light can be seen strongly in sample 100% N_2 and with less strength in 80% N_2 , as depicted in fig. (B.3). Around 6 eV, the polarization parallel to the c-axis, which corresponds to the extraordinary axis, shows higher absorption intensity than the polarization perpendicular to the c-axis. This results in the dispersion near the bandgap edge. This anisotropy in the absorption is called "dichroism". Hexagonal structure of wurtzite AlN exhibits negative crystal field energy, unlike wurtzite GaN and InN that produce positive crystal field. This leads to a different band structure arrangement for AlN. This negative crystal field induces splitting in the valence band maximum (VBM) around the Γ point of the Brillouin zone into three states labeled from the uppermost of the VB as Γ_{7+} , Γ_9 and Γ_{7-} . On the contrary, the positive crystal field in GaN and InN makes Γ_9 the uppermost state in the valence band.[265-266]

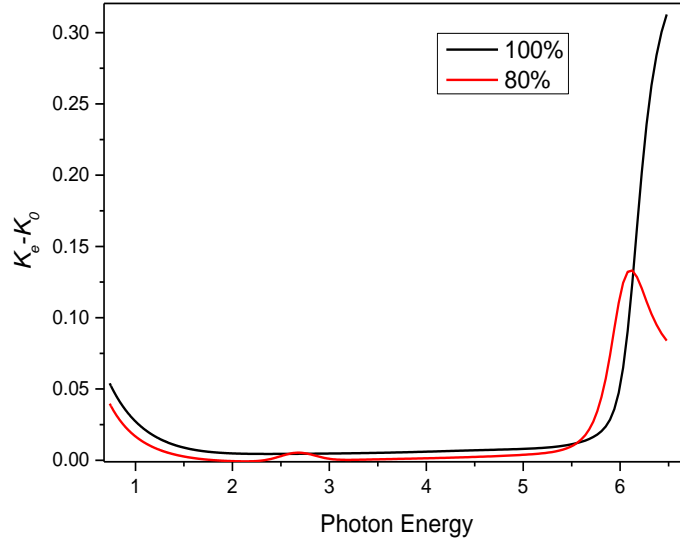


Fig (B.4): Dichroism for samples 100% and 80% N₂ as a function of the photon energy.

Three optical transitions have been proposed from the conduction band Γ_7 to the valence band as follows: A (Γ_7 - Γ_{7+}), B (Γ_7 - Γ_9), and C (Γ_7 - Γ_{7-}) with energy positions 6.05 eV, 6.24 eV and 6.26 eV respectively. In addition, these transitions have been found not only to exhibit different energy positions, but also their transition probabilities (oscillator strength) are polarization dependence. It was reported that the transition probability of A is high for the polarized light with electric field parallel to the c-axis ($E \parallel c$) and weak for perpendicular polarization ($E \perp c$). The opposite behavior has been seen for the C transition. Moreover, B transition is only observed for ($E \perp c$). M. Feneberg et al, [265-266] demonstrated that, the dichroism near the bandgap edge is dominated by excitonic interactions (free exciton, exciton-phonon complex and exciton continuum). These anisotropic features near the bandgap are believed to be responsible for the anisotropy in the visible region. This is consistent with our observations of birefringence and dichroism in AlN. The 100%N₂ sample that shows strong dichroism near the bandgap edge also exhibits larger birefringence in the visible region as observed in fig (B.4). Y. Taniyasu et al, found that the extraction of emission light at 210 nm along the a-axis from AlN p-n junction in light emitting diode[267] is 25 times higher than the extraction of light along the c-axis.[40] They attributed this remarkable result to the optical anisotropy of AlN. This is in line with our findings of higher extinction coefficient along the c-axis than a-axis that should imply less intense extraction of light along the c-axis due to the large absorption in this direction.

Annex C

Estimation of microstrain and macrostrain of Ce-doped AlN samples

The macrostrain along the c -axis is calculated for all samples using the following expression:

$$(c-c_0)/c_0, \quad (C.1)$$

where $c_0 = 4.978 \text{ \AA}$ is the c -axis value of the unstrained sample and c is calculated from the position of the (002) reflection.[268] On the other hand, the FWHM broadening of XRD is associated to the local structure (microstrain) induced by structure disorders, boundaries and dislocations as well as the small size of crystallites.[268-269] Hence, the FWHM broadening is considered as a combination of the small crystal size and the microstrain. In this regard, Williamson-Hall (WH) method can be used to determine the microstrain by considering two integral line breadth components at 002 and 004 diffraction angles, see fig (C.1).

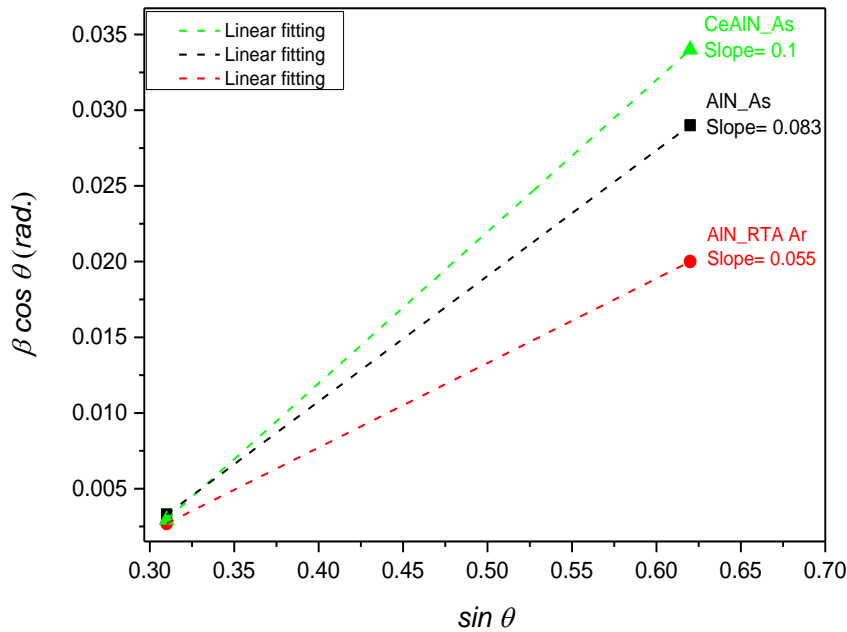


Fig. (C.1): Williamson-Hall (WH) plot for as- deposited AlN, annealed AlN_Ar, and as deposited Ce-doped AlN.

This figure represents the Williamson-Hall (WH) plot to determine the microstrain of AlN and Ce-doped AlN thin films using the following relation:

$$\beta \cos \theta = (\lambda/L) + \langle \epsilon^2 \rangle^{1/2} \sin \theta, \quad (C.2)$$

where β is the integral breadth after subtracting the instrumental breadth line, θ is the diffraction angle, λ is the x-ray wavelength, L is the average crystallites size normal to the crystal planes, and $\langle \epsilon^2 \rangle^{1/2}$ is the local root-mean-square strain (microstrain). Hence, WH plots

$\beta \cos \theta$ versus $\sin \theta$ at 002 and 004 reflections. From the line's slope, the microstrain " $\langle \epsilon^2 \rangle^{1/2}$ " can be determined.

Annex D

Determination of the laser parameter emission cross section x radiative lifetime

The effective emission cross section ($\sigma_e(\lambda)$) multiplied by radiative lifetime (τ_{rad}) is important parameter for the assessment of a laser performance. Knowledge of this parameter is essential in evaluating other laser parameters such as saturation intensity and threshold pump power. Füchtbauer–Ladenburg method is applied to calculate ($\sigma_e \tau_{rad}$) from the emission spectra of 1% Yb- doped Al(O)N and (1.5 Ce, 1% Yb) co-doped Al(O)N.

Füchtbauer–Ladenburg relationship can be expressed as:

$$\sigma_e(\lambda) = \frac{1}{8\pi n^2 c \tau_{rad}} \frac{\lambda^5 I(\lambda)}{\int \lambda I(\lambda) d\lambda} \quad (D.1)$$

Where σ_e is the emission cross-section, τ_{rad} is the radiative lifetime, λ is the emission wavelength, and $I(\lambda)$ is the emission intensity. The parameter $\sigma_e(\lambda) \tau_{rad}$ as a function of emission wavelength can be presented as shown in fig (D.1).

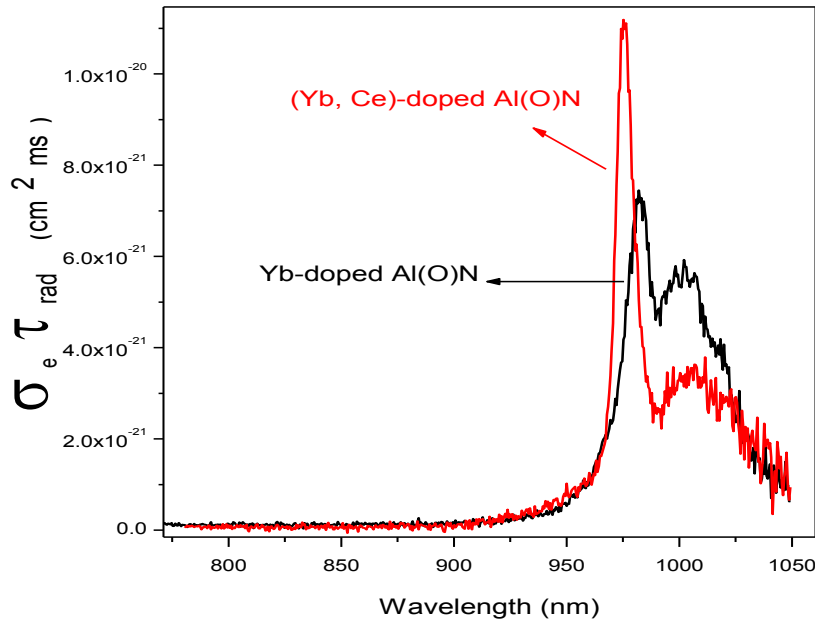


Fig. (D.1): The calculated $\sigma_e \tau_{rad}$ parameter as a function of wavelength.

Bibliography

1. Kenyon, A.J., *Recent developments in rare-earth doped materials for optoelectronics*. Progress in Quantum Electronics, 2002. **26**(4): p. 225-284.
2. Park, M.-H. and S.-H. Kim, *Thermal conductivity of AlN thin films deposited by RF magnetron sputtering*. Materials Science in Semiconductor Processing, 2012. **15**(1): p. 6-10.
3. Carsten, H., et al., *Preparation of Bulk AlN Seeds by Spontaneous Nucleation of Freestanding Crystals*. Japanese Journal of Applied Physics, 2013. **52**(8S): p. 08JA06.
4. Suehiro, T., et al., *Synthesis of Aluminum Nitride Nanopowder by Gas-Reduction–Nitridation Method*. Journal of the American Ceramic Society, 2003. **86**(6): p. 1046-1048.
5. Assouar, M.B., et al., *STUDY OF ACOUSTICAL AND OPTICAL PROPERTIES OF ALN FILMS FOR SAW AND BAW DEVICES: CORRELATION BETWEEN THESE PROPERTIES*. Integrated Ferroelectrics, 2006. **82**(1): p. 45-54.
6. Caliendo, C., P. Imperatori, and E. Ciani, *Structural, morphological and acoustic properties of AlN thick films sputtered on Si(001) and Si(111) substrates at low temperature*. Thin Solid Films, 2003. **441**(1–2): p. 32-37.
7. Kecik, D., et al., *Layer- and strain-dependent optoelectronic properties of hexagonal AlN*. Physical Review B, 2015. **92**(16): p. 165408.
8. Yang, M., et al., *Optoelectronic properties of GaN, AlN, and GaAlN alloys*. Optik - International Journal for Light and Electron Optics, 2015. **126**(22): p. 3357-3361.
9. Hanada, T., *Basic Properties of ZnO, GaN, and Related Materials*, in *Oxide and Nitride Semiconductors: Processing, Properties, and Applications*, T. Yao and S.-K. Hong, Editors. 2009, Springer Berlin Heidelberg: Berlin, Heidelberg. p. 1-19.
10. Morkoç, H., *General Properties of Nitrides*, in *Handbook of Nitride Semiconductors and Devices*. 2009, Wiley-VCH Verlag GmbH & Co. KGaA. p. 1-129.
11. Cervenka, J., et al., *Nucleation and Chemical Vapor Deposition Growth of Polycrystalline Diamond on Aluminum Nitride: Role of Surface Termination and Polarity*. Crystal Growth & Design, 2013. **13**(8): p. 3490-3497.
12. Stegmaier, M. and W.H.P. Pernice, *Mode control and mode conversion in nonlinear aluminum nitride waveguides*. Optics Express, 2013. **21**(22): p. 26742-26761.
13. Zhang, J.X., et al., *Growth of AlN films on Si (100) and Si (111) substrates by reactive magnetron sputtering*. Surface and Coatings Technology, 2005. **198**(1–3): p. 68-73.
14. <https://arxiv.org/abs/1507.08113v1>.
15. Wolff, P.A., *Electronic Structure of Semiconductors*, in *Electronic Materials*, N.B. Hannay and U. Colombo, Editors. 1973, Springer US: Boston, MA. p. 1-40.
16. Kobayashi, A., et al., *Semiempirical tight-binding band structures of wurtzite semiconductors: AlN, CdS, CdSe, ZnS, and ZnO*. Physical Review B, 1983. **28**(2): p. 935-945.
17. Ruiz, E., S. Alvarez, and P. Alemany, *Electronic structure and properties of AlN*. Physical Review B, 1994. **49**(11): p. 7115-7123.
18. Nwigboji, I.H., et al., *Ab-initio computations of electronic and transport properties of wurtzite aluminum nitride (w-AlN)*. Materials Chemistry and Physics, 2015. **157**: p. 80-86.
19. Gorczyca, I., et al., *Optical phonon modes in GaN and AlN*. Physical Review B, 1995. **51**(17): p. 11936-11939.
20. Carlone, C., K.M. Lakin, and H.R. Shanks, *Optical phonons of aluminum nitride*. Journal of Applied Physics, 1984. **55**(11): p. 4010-4014.
21. McNeil, L.E., M. Grimsditch, and R.H. French, *Vibrational Spectroscopy of Aluminum Nitride*. Journal of the American Ceramic Society, 1993. **76**(5): p. 1132-1136.
22. Debieu, O., et al., *Structural and optical characterization of pure Si-rich nitride thin films*. Nanoscale Research Letters, 2013. **8**(1): p. 31.

23. Khan, S., et al., *Texture of the nano-crystalline AlN thin films and the growth conditions in DC magnetron sputtering*. Progress in Natural Science: Materials International, 2015. **25**(4): p. 282-290.
24. Jagannadham, K., et al., *Structural characteristics of AlN films deposited by pulsed laser deposition and reactive magnetron sputtering: A comparative study*. Journal of Vacuum Science & Technology A, 1998. **16**(5): p. 2804-2815.
25. Sanz-Hervás, A., et al., *Influence of crystal properties on the absorption IR spectra of polycrystalline AlN thin films*. Diamond and Related Materials, 2003. **12**(3–7): p. 1186-1189.
26. https://en.wikipedia.org/wiki/Crystallographic_defect.
27. <http://www.iue.tuwien.ac.at/phd/wittmann/node7.html>.
28. Fourmond, E., et al., *Electrical properties of boron, phosphorus and gallium co-doped silicon*. Energy Procedia, 2011. **8**: p. 349-354.
29. Sobolev, N.A., *Defects and their influence on the luminescence of rare-earth ions implanted in single crystal Si*. Physica B: Condensed Matter, 2001. **308–310**: p. 333-336.
30. Kenyon, A.J., *Recent developments in rare-earth doped materials for optoelectronics*. Progress in Quantum Electronics, 2002. **26**(4–5): p. 225-284.
31. Stampfl, C. and C.G. Van de Walle, *Theoretical investigation of native defects, impurities, and complexes in aluminum nitride*. Physical Review B, 2002. **65**(15): p. 155212.
32. Sedhain, A., et al., *Photoluminescence properties of AlN homoepilayers with different orientations*. Applied Physics Letters, 2008. **93**(4): p. 041905.
33. Bickermann, M., et al., *Point defect content and optical transitions in bulk aluminum nitride crystals*. physica status solidi (b), 2009. **246**(6): p. 1181-1183.
34. Slack, G.A., et al., *Some effects of oxygen impurities on AlN and GaN*. Journal of Crystal Growth, 2002. **246**(3–4): p. 287-298.
35. He, M., et al., *Preparation of nearly oxygen-free AlN thin films by pulsed laser deposition*. Journal of Vacuum Science & Technology A, 1998. **16**(4): p. 2372-2375.
36. Vispute, R.D., et al., *Epitaxial growth of AlN thin films on silicon (111) substrates by pulsed laser deposition*. Journal of Applied Physics, 1995. **77**(9): p. 4724-4728.
37. Mizuho, M., et al., *Epitaxial Growth of Aluminum Nitride on Sapphire Using Metalorganic Chemical Vapor Deposition*. Japanese Journal of Applied Physics, 1981. **20**(1): p. 17.
38. Xie, J.L. and S. Wickramanayaka. *Effect of process pressure on PVD AlN thin film*. in *Electronics Packaging Technology Conference (EPTC), 2014 IEEE 16th*. 2014.
39. Copyright, in *Handbook of Silicon Based MEMS Materials and Technologies*. 2010, William Andrew Publishing: Boston. p. iv.
40. Taniyasu, Y., M. Kasu, and T. Makimoto, *An aluminium nitride light-emitting diode with a wavelength of 210 nanometres*. Nature, 2006. **441**(7091): p. 325-328.
41. Wieg, A.T., et al., *Broadband white light emission from Ce:AlN ceramics: High thermal conductivity down-converters for LED and laser-driven solid state lighting*. APL Materials, 2016. **4**(12): p. 126105.
42. Xiong, C., W.H.P. Pernice, and H.X. Tang, *Low-Loss, Silicon Integrated, Aluminum Nitride Photonic Circuits and Their Use for Electro-Optic Signal Processing*. Nano Letters, 2012. **12**(7): p. 3562-3568.
43. Barrett, S.D. and S.S. Dhesi, *The Structure of Rare-Earth Metal Surfaces*. 2001, World Scientific.
44. Atwood, D.A., ed. *The Rare Earth Elements: Fundamentals and Applications*. 2012, Wiley. 624.
45. Cotton, S., *The Lanthanides - Principles and Energetics*, in *Lanthanide and Actinide Chemistry*. 2006, John Wiley & Sons, Ltd. p. 9-22.
46. Mezdrogina, M.M., E.Y. Danilovskii, and R.V. Kuz'min, *Emission from rare-earth ions in GaN wurtzite crystals*. Inorganic Materials, 2011. **47**(13): p. 1450-1469.
47. Judd, B.R., *Optical Absorption Intensities of Rare-Earth Ions*. Physical Review, 1962. **127**(3): p. 750-761.

48. Ofelt, G.S., *Intensities of Crystal Spectra of Rare-Earth Ions*. The Journal of Chemical Physics, 1962. **37**(3): p. 511-520.
49. Dieke, G.H., *Spectra and Energy Levels of Rare Earth Ions in Crystals*, H. Crosswhite and H.M. Crosswhite, Editors. 1968, Interscience.
50. <https://en.wikipedia.org/wiki/Luminescence>.
51. Aydin, M. and D.L. Akins, *Vibroelectronic Properties of Functionalized Single-Walled Carbon Nanotubes and Double-Walled Boron Nitride Nanotubes*, in *Physical and Chemical Properties of Carbon Nanotubes*, S. Suzuki, Editor. 2013, InTech: Rijeka. p. Ch. 03.
52. <https://en.wikipedia.org/wiki/Phosphorescence>.
53. Uitert, L.G.V. and L.F. Johnson, *Energy Transfer Between Rare-Earth Ions*. The Journal of Chemical Physics, 1966. **44**(9): p. 3514-3522.
54. Dexter, D.L., *A Theory of Sensitized Luminescence in Solids*. The Journal of Chemical Physics, 1953. **21**(5): p. 836-850.
55. https://en.wikipedia.org/wiki/Spontaneous_emission.
56. Stachowicz, M., et al., *Crystal field analysis of rare-earth ions energy levels in GaN*. Optical Materials, 2014. **37**: p. 165-174.
57. Steckl, A.J., J.H. Park, and J.M. Zavada, *Prospects for rare earth doped GaN lasers on Si*. Materials Today, 2007. **10**(7–8): p. 20-27.
58. Park, J.H. and A.J. Steckl, *Site specific Eu³⁺ stimulated emission in GaN host*. Applied Physics Letters, 2006. **88**(1): p. 011111.
59. Gan, L., et al., *Multiple doping structures of the rare-earth atoms in [small beta]-SiAlON:Ce phosphors and their effects on luminescence properties*. Nanoscale, 2015. **7**(26): p. 11393-11400.
60. Wang, C.-M., et al., *Grain Boundary Films in Rare-Earth-Glass-Based Silicon Nitride*. Journal of the American Ceramic Society, 1996. **79**(3): p. 788-792.
61. Sourty, E., *Atomic-scaled investigation of structure-dependent luminescence in Sialon:Ce phosphors*. Applied Physics Letters, 2012. **101**(16): p. 161904.
62. Takeda, T., R.-J. Xie, and N. Hirosaki, *Local Structure Analysis in Nitride and Oxynitride Phosphors*. ECS Journal of Solid State Science and Technology, 2013. **2**(2): p. R3132-R3137.
63. Shinn, M.D., et al., *Optical transitions of Er³⁺ ions in fluorozirconate glass*. Physical Review B, 1983. **27**(11): p. 6635-6648.
64. Miniscalco, W.J., *Erbium-doped glasses for fiber amplifiers at 1500 nm*. Journal of Lightwave Technology, 1991. **9**(2): p. 234-250.
65. Nicoara, I., N. Pecingina-Garjoaba, and O. Bunoiu, *Concentration distribution of Yb²⁺ and Yb³⁺ ions in YbF₃:CaF₂ crystals*. Journal of Crystal Growth, 2008. **310**(7–9): p. 1476-1481.
66. Vila, L.D.d., et al., *Mechanism of the Yb–Er energy transfer in fluorozirconate glass*. Journal of Applied Physics, 2003. **93**(7): p. 3873-3880.
67. Hinojosa, S., et al., *Energy back transfer, migration and energy transfer (Yb-to-Er and Er-to-Yb) processes in Yb,Er:YAG*. Journal of Luminescence, 2003. **102–103**: p. 694-698.
68. Wang, L., et al., *Energy transfer in Ce, Nd, and Yb co-doped YAG phosphors*. Chinese Optics Letters, 2013. **11**(6): p. 061604.
69. Chen, J., et al., *Near-infrared quantum cutting in Ce³⁺, Yb³⁺ co-doped YBO₃ phosphors by cooperative energy transfer*. Optical Materials, 2010. **32**(9): p. 998-1001.
70. <https://en.wikipedia.org/wiki/Silicon>.
71. Li, T., M. Mastro, and A. Dadgar, eds. *III–V Compound Semiconductors: Integration with Silicon-Based Microelectronics*. 2010, CRC Press. 603.
72. Kita, T., et al., *Thermal annealing effects on ultra-violet luminescence properties of Gd doped AlN*. Journal of Applied Physics, 2015. **117**(16): p. 163105.
73. Lozykowski, H.J., et al., *Luminescence and excitation mechanism of Pr, Eu, Tb and Tm ions implanted into AlN*. Microelectronics Journal, 2005. **36**(3–6): p. 453-455.
74. Liu, T.-C., et al., *Blue Emission by Interstitial Site Occupation of Ce³⁺ in AlN*. Chemistry of Materials, 2012. **24**(17): p. 3486-3492.

75. Wang, W., et al., *Bifunctional AlN:Tb semiconductor with luminescence and photocatalytic properties*. RSC Advances, 2015. **5**(110): p. 90698-90704.
76. Weingärtner, R., et al., *Thermal activation, cathodo- and photoluminescence measurements of rare earth doped (Tm, Tb, Dy, Eu, Sm, Yb) amorphous/nanocrystalline AlN thin films prepared by reactive rf-sputtering*. Optical Materials, 2006. **28**(6–7): p. 790-793.
77. Wieg, A.T., et al., *Nd:AlN polycrystalline ceramics: A candidate media for tunable, high energy, near IR lasers*. Applied Physics Letters, 2016. **109**(12): p. 121901.
78. Koubaa, T., et al., *Spectra and energy levels of Yb3+ in AlN*. Journal of Applied Physics, 2009. **106**(1): p. 013106.
79. Zanatta, A.R., C.T.M. Ribeiro, and U. Jahn, *Optoelectronic and structural characteristics of Er-doped amorphous AlN films*. Journal of Applied Physics, 2005. **98**(9): p. 093514.
80. Merkle, L.D., et al., *Fluorescence of Er3+:AlN polycrystalline ceramic*. Optical Materials Express, 2012. **2**(1): p. 78-91.
81. Ishikawa, R., et al., *Atomic Structure of Luminescent Centers in High-Efficiency Ce-doped w-AlN Single Crystal*. Scientific Reports, 2014. **4**: p. 3778.
82. Lavi, R., et al., *Efficient pumping scheme for neodymium-doped materials by direct excitation of the upper lasing level*. Applied Optics, 1999. **38**(36): p. 7382-7385.
83. Sangla, D., F. Balembois, and P. Georges, *Nd:YAG laser diode-pumped directly into the emitting level at 938 nm*. Optics Express, 2009. **17**(12): p. 10091-10097.
84. Vantomme, A., B. De Vries, and U. Wahl, *Lattice Location of RE Impurities in IIINitrides*, in *Rare Earth Doped III-Nitrides for Optoelectronic and Spintronic Applications*, K. O'Donnell and V. Dierolf, Editors. 2010, Springer Netherlands: Dordrecht. p. 55-98.
85. Faulkner, R.A. and J.J. Hopfield, *Isoelectronic Impurities in Semiconductors*, in *Localized Excitations in Solids*, R.F. Wallis, Editor. 1968, Springer US: Boston, MA. p. 218-238.
86. Lozykowski, H.J., *Kinetics of luminescence of isoelectronic rare-earth ions in III-V semiconductors*. Physical Review B, 1993. **48**(24): p. 17758-17769.
87. Braud, A., *Excitation Mechanisms of RE Ions in Semiconductors*, in *Rare Earth Doped III-Nitrides for Optoelectronic and Spintronic Applications*, K. O'Donnell and V. Dierolf, Editors. 2010, Springer Netherlands: Dordrecht. p. 269-307.
88. Guerbous, L. and O. Krachni, *The 4f-5d luminescence transitions in cerium-doped LuF3*. Journal of Modern Optics, 2006. **53**(14): p. 2043-2053.
89. Mares, J., et al., *Energy transfer mechanisms between Ce3+ and Nd3+ in YAG : Nd, Ce at low temperature*. Rev. Phys. Appl. (Paris), 1987. **22**(2): p. 145-152.
90. Suresh, K., N.V. Poornachandra Rao, and K.V.R. Murthy, *Blue excitable green emitting Ce3+ doped CaS phosphor for w-LEDs*. Luminescence, 2016. **31**(1): p. 179-182.
91. Parganiha, Y., et al., *Near UV–blue emission from Ce doped Y2SiO5 phosphor*. Materials Science in Semiconductor Processing, 2015. **31**: p. 715-719.
92. Jang, H.S., et al., *Mechanism for strong yellow emission of Y3Al5O12:Ce3+ phosphor under electron irradiation for the application to field emission backlight units*. Applied Physics Letters, 2007. **90**(7): p. 071908.
93. Kindrat, I.I., et al., *Spectroscopic properties of the Ce-doped borate glasses*. Optical Materials, 2016. **59**: p. 20-27.
94. Nikl, M., et al., *Defect Engineering in Ce-Doped Aluminum Garnet Single Crystal Scintillators*. Crystal Growth & Design, 2014. **14**(9): p. 4827-4833.
95. Marchand, R., et al., *Nitrides and oxynitrides: Preparation, crystal chemistry and properties*. Journal of the European Ceramic Society, 1991. **8**(4): p. 197-213.
96. Rong-Jun, X. and H. Naoto, *Silicon-based oxynitride and nitride phosphors for white LEDs—A review*. Science and Technology of Advanced Materials, 2007. **8**(7-8): p. 588.
97. He, X.-H., et al., *Dependence of luminescence properties on composition of rare-earth activated (oxy)nitrides phosphors for white-LEDs applications*. Journal of Materials Science, 2009. **44**(18): p. 4763-4775.
98. <https://www.ntt-review.jp/archive/ntttechnical.php?contents=ntr201008sf2.html>.

99. Aldabergenova, S.B., et al., *Blue, green and red emission from Ce³⁺, Tb³⁺ and Eu³⁺ ions in amorphous GaN and AlN thin films*. Journal of Non-Crystalline Solids, 2002. **299–302, Part 1**: p. 709-713.
100. Ishikawa, R., et al., *Direct Observation of Dopant Atom Diffusion in a Bulk Semiconductor Crystal Enhanced by a Large Size Mismatch*. Physical Review Letters, 2014. **113**(15): p. 155501.
101. Dar, A. and A. Majid, *DFT study of cerium doped aluminum nitride*. Eur. Phys. J. Appl. Phys., 2015. **71**(1): p. 10101.
102. Majid, A., et al., *Role of nitrogen vacancies in cerium doped aluminum nitride*. Journal of Magnetism and Magnetic Materials, 2016. **412**: p. 49-54.
103. Brenier, A., *A new evaluation of Yb³⁺-doped crystals for laser applications*. Journal of Luminescence, 2001. **92**(3): p. 199-204.
104. Wang, C., et al., *Ceramic planar waveguide laser of non-aqueous tape casting fabricated YAG/Yb:YAG/YAG*. Scientific Reports, 2016. **6**: p. 31289.
105. Atar, G., et al., *Yb/Al-codoped fused-silica planar-waveguide amplifier*. Optical Materials, 2016. **55**: p. 49-54.
106. Ma, C., et al., *Longitudinally diode-pumped planar waveguide YAG/Yb:LuAG/YAG ceramic laser at 1030.7 nm*. Optics Letters, 2016. **41**(14): p. 3317-3319.
107. Minelly, J.D., et al., *Diode-array pumping of Er/sup 3+//Yb/sup 3+ Co-doped fiber lasers and amplifiers*. IEEE Photonics Technology Letters, 1993. **5**(3): p. 301-303.
108. Meijer, J.-M., et al., *Downconversion for solar cells in $\text{YF}_3\text{:Nd}^{3+}$, Yb^{3+}* . Physical Review B, 2010. **81**(3): p. 035107.
109. Florêncio, L.d.A., et al., *Efficiency enhancement in solar cells using photon down-conversion in Tb/Yb-doped tellurite glass*. Solar Energy Materials and Solar Cells, 2016. **157**: p. 468-475.
110. Li, J., et al., *Efficient Near-Infrared Downconversion and Energy Transfer Mechanism of Ce³⁺/Yb³⁺ Codoped Calcium Scandate Phosphor*. Inorganic Chemistry, 2015. **54**(10): p. 4806-4810.
111. Lorenz, K., et al., *Defect studies and optical activation of Yb doped GaN*. Journal of Physics: Conference Series, 2010. **249**(1): p. 012053.
112. Zanatta, A.R., *Effect of thermal annealing treatments on the optical properties of rare-earth-doped AlN films*. Journal of Physics D: Applied Physics, 2009. **42**(2): p. 025109.
113. Ellmer, K. and T. Welzel, *Reactive magnetron sputtering of transparent conductive oxide thin films: Role of energetic particle (ion) bombardment*. Journal of Materials Research, 2012. **27**(5): p. 765-779.
114. Mahieu, S. and D. Depla, *Correlation between electron and negative O⁻ ion emission during reactive sputtering of oxides*. Applied Physics Letters, 2007. **90**(12): p. 121117.
115. <http://www.microscopy.ethz.ch/TEMED.htm>.
116. Olhero, S.M., F.L. Alves, and J.M.F. Ferreira, *Last Advances in Aqueous Processing of Aluminium Nitride (AlN) - A Review*, in *Advances in Ceramics - Synthesis and Characterization, Processing and Specific Applications*, C. Sikalidis, Editor. 2011, InTech: Rijeka. p. Ch. 10.
117. Ho, V.X., et al., *Photoluminescence quantum efficiency of Er optical centers in GaN epilayers*. 2017. **7**: p. 39997.
118. Fang, Y., et al., *Investigation of temperature-dependent photoluminescence in multi-quantum wells*. 2015. **5**: p. 12718.
119. Li, L., et al., *Temperature Dependent Energy Transfer in Ce³⁺-Yb³⁺ Co-Doped YAG Phosphors*. ECS Journal of Solid State Science and Technology, 2016. **5**(9): p. R146-R149.
120. Jia, Y., et al., *Synthesis and photoluminescence properties of Ce³⁺ and Eu²⁺-activated Ca₇Mg(SiO₄)₄ phosphors for solid state lighting*. Physical Chemistry Chemical Physics, 2012. **14**(10): p. 3537-3542.
121. Barth, S., et al., *Sputter deposition of stress-controlled piezoelectric AlN and AlScN films for ultrasonic and energy harvesting applications*. IEEE Transactions on Ultrasonics, Ferroelectrics, and Frequency Control, 2014. **61**(8): p. 1329-1334.

122. Miao, X.S., Y.C. Chan, and Z.Y. Lee, *Optical Properties and Reactive Sputtering Conditions of AlN and AlSiN Thin Films for Magneto- Optical Applications*. Journal of Electronic Materials, 1997. **26**(1): p. 21-24.
123. Makoto, O., T. Hiroto, and F. Hiroyuki, *Effect of sputtering pressure on crystalline quality and residual stress of AlN films deposited at 823 K on nitrided sapphire substrates by pulsed DC reactive sputtering*. Japanese Journal of Applied Physics, 2016. **55**(5S).
124. Huffman, G.L., et al., *Stress dependence of reactively sputtered aluminum nitride thin films on sputtering parameters*. Journal of Vacuum Science & Technology A, 1989. **7**(3): p. 2252-2255.
125. Wei, Q.-p., et al., *Effects of sputtering pressure on nanostructure and nanomechanical properties of AlN films prepared by RF reactive sputtering*. Transactions of Nonferrous Metals Society of China, 2014. **24**(9): p. 2845-2855.
126. Takeuchi, H., M. Ohtsuka, and H. Fukuyama, *Effect of sputtering power on surface characteristics and crystal quality of AlN films deposited by pulsed DC reactive sputtering*. physica status solidi (b), 2015. **252**(5): p. 1163-1171.
127. Zhang, M., et al., *Research on the Piezoelectric Properties of AlN Thin Films for MEMS Applications*. Micromachines, 2015. **6**(9): p. 1236.
128. Lobl, H.P., et al. *Piezo-electric AlN and PZT films for micro-electronic applications*. in *Ultrasonics Symposium, 1999. Proceedings. 1999 IEEE*. 1999.
129. Navaladian, S., et al., *A Rapid Synthesis of Oriented Palladium Nanoparticles by UV Irradiation*. Nanoscale Research Letters, 2009. **4**(2): p. 181-186.
130. Shah, H.N., R. Jayaganthan, and D. Kaur, *Effect of sputtering pressure and temperature on DC magnetron sputtered CrN films*. Surface Engineering, 2010. **26**(8): p. 629-637.
131. Kumada, T., M. Ohtsuka, and H. Fukuyama, *Influence of substrate temperature on the crystalline quality of AlN layers deposited by RF reactive magnetron sputtering*. AIP Advances, 2015. **5**(1): p. 017136.
132. Iriarte, G.F., J.G. Rodríguez, and F. Calle, *Synthesis of c-axis oriented AlN thin films on different substrates: A review*. Materials Research Bulletin, 2010. **45**(9): p. 1039-1045.
133. Kajikawa, Y., S. Noda, and H. Komiyama, *Comprehensive perspective on the mechanism of preferred orientation in reactive-sputter-deposited nitrides*. Journal of Vacuum Science & Technology A, 2003. **21**(6): p. 1943-1954.
134. Liu, T., et al., *Nucleation and growth of (10⁻¹¹) semi-polar AlN on (0001) AlN by Hydride Vapor Phase Epitaxy*. Scientific Reports, 2016. **6**: p. 26040.
135. Amirhoseiny, M., et al., *Characterizations of InN Thin Films Grown on Si (110) Substrate by Reactive Sputtering*. Journal of Nanomaterials, 2011. **2011**: p. 7.
136. Akiyama, M., et al., *Preparation of highly oriented AlN thin films on glass substrates by helicon plasma sputtering and design of experiments*. Thin Solid Films, 1999. **350**(1-2): p. 85-90.
137. Choudhary, R.K., et al., *Structural and Optical Properties of Aluminum Nitride Thin Films Deposited by Pulsed DC Magnetron Sputtering*. ISRN Materials Science, 2013.
138. Deniz, D., T. Karabacak, and J.M.E. Harper, *Competitive growth mechanisms of aluminum nitride thin films deposited by off-normal reactive magnetron sputtering*. Journal of Applied Physics, 2008. **103**(8): p. 083553.
139. Jin, H., et al., *Deposition of c-axis orientation aluminum nitride films on flexible polymer substrates by reactive direct-current magnetron sputtering*. Thin Solid Films, 2012. **520**(15): p. 4863-4870.
140. Clement, M., et al., *Influence of sputtering mechanisms on the preferred orientation of aluminum nitride thin films*. Journal of Applied Physics, 2003. **94**(3): p. 1495-1500.
141. Depla, D., et al., *Target voltage behaviour during DC sputtering of silicon in an argon/nitrogen mixture*. Vacuum, 2002. **66**(1): p. 9-17.
142. Musarrat Hasan, et al., *Dual-Metal-Gate Work Function by Controlling Metal Gate Thickness and Composition*. Electrochemical and Solid-State Letters, 2008. **11**(5).

143. Wang Tao, et al., *Target voltage behaviour of a vanadium-oxide thin film during reactive magnetron sputtering*. Chin. Phys. B, 2011. **20**(3).
144. Ellmer, K. and T. Welzel, *Reactive magnetron sputtering of transparent conductive oxide thin films: Role of energetic particle (ion) bombardment*. Journal of Materials Research, 2012. **27**(05): p. 765-779.
145. Horwat, D. and A. Anders, *Ion acceleration and cooling in gasless self-sputtering*. Applied Physics Letters, 2010. **97**(22): p. 221501.
146. Chernow, F., J.A. Borders, and D.K. Brice, eds. *Ion Implantation in Semiconductors 1976. 1977*, Springer US: Boston, MA. 21-29.
147. Kubart, T., T. Nyberg, and S. Berg, *Modelling of low energy ion sputtering from oxide surfaces*. Journal of Physics D: Applied Physics, 2010. **43**(20): p. 205204.
148. Iborra, E., et al., *Effect of particle bombardment on the orientation and the residual stress of sputtered AlN films for SAW devices*. IEEE Trans. Ultrason., Ferroelect., Freq. Control, 2004. **51**(3): p. 352-358.
149. Kikuo, T., et al., *High-Energy Particles in AlN Film Preparation by Reactive Sputtering Technique*. Japanese Journal of Applied Physics, 1983. **22**(3R): p. 418.
150. G.F. Iriarte, J.G.R., F. Calle, *Effect of substrate-target distance and sputtering pressure in the synthesis of AlN thin films*. Microsystem Technologies, 2011. **6**: p. 2011.
151. Chamorro, W., et al., *Near-room temperature single-domain epitaxy of reactively sputtered ZnO films*. Journal of Physics D: Applied Physics, 2013. **46**(23): p. 235107.
152. Shi, S.-C., et al., *Structural evolution of AlN nano-structures: Nanotips and nanorods*. Chemical Physics Letters, 2006. **418**(1–3): p. 152-157.
153. Knuyt, G., et al., *A model for texture evolution in a growing film*. Surface and Coatings Technology, 1995. **76–77, Part 1**: p. 311-315.
154. Galca, A.C., et al., *Structural and optical properties of c-axis oriented aluminum nitride thin films prepared at low temperature by reactive radio-frequency magnetron sputtering*. Thin Solid Films, 2012. **524**: p. 328-333.
155. Feng, Y., et al., *Competitive growth mechanisms of AlN on Si (111) by MOVPE*. Scientific Reports, 2014. **4**: p. 6416.
156. Mahieu, S., et al., *Biaxial alignment in sputter deposited thin films*. Thin Solid Films, 2006. **515**(4): p. 1229-1249.
157. Joo, H.-Y., et al., *Spectrophotometric analysis of aluminum nitride thin films*. Journal of Vacuum Science & Technology A, 1999. **17**(3): p. 862-870.
158. Zanatta, A.R. and I. Chamboleyron, *Absorption edge, band tails, and disorder of amorphous semiconductors*. Physical Review B, 1996. **53**(7): p. 3833-3836.
159. Joo, H.Y., et al., *The optical and structural properties of AlN thin films characterized by spectroscopic ellipsometry*. Thin Solid Films, 2000. **368**(1): p. 67-73.
160. Klaus, E., *Magnetron sputtering of transparent conductive zinc oxide: relation between the sputtering parameters and the electronic properties*. Journal of Physics D: Applied Physics, 2000. **33**(4): p. R17.
161. Fatemeh, H., et al., *Optical Properties of Amorphous AlN Thin Films on Glass and Silicon Substrates Grown by Single Ion Beam Sputtering*. Japanese Journal of Applied Physics, 2010. **49**(9R): p. 095802.
162. Khan, S., et al., *Effect of substrate biasing and temperature on AlN thin film deposited by cathodic arc ion*. Materials Science in Semiconductor Processing, 2013. **16**(3): p. 640-646.
163. Guerra, J.A., et al., *Erratum: Effect of thermal annealing treatments on the optical activation of Tb 3+ -doped amorphous SiC:H thin films (2016 J. Phys. D: Appl . 49 375104)*. Journal of Physics D: Applied Physics, 2016. **49**(40): p. 409601.
164. Fialho, M., et al., *Effect of AlN content on the lattice site location of terbium ions in Al_xGa_{1-x}N compounds*. Semiconductor Science and Technology, 2016. **31**(3): p. 035026.
165. Ma, Y.Y., et al. *Luminescence properties of cerium doped silicon nitride with MgO additive*. in *2013 IEEE 5th International Nanoelectronics Conference (INEC)*. 2013.

166. Hu, L., et al., *Luminescence of Ce³⁺ in lanthanum silicon oxynitride*. Chinese Physics B, 2010. **19**(12): p. 127807.
167. Li, L., et al., *Luminescence of Ce³⁺ in Different Lattice Sites of La₂CaB₁₀O₁₉*. The Journal of Physical Chemistry C, 2008. **112**(35): p. 13763-13768.
168. van Krevel, J.W.H., et al., *Long wavelength Ce³⁺ emission in Y-Si-O-N materials*. Journal of Alloys and Compounds, 1998. **268**(1-2): p. 272-277.
169. Yokoyama, T., et al., *Effect of Mg and Zr co-doping on piezoelectric AlN thin films for bulk acoustic wave resonators*. IEEE Transactions on Ultrasonics, Ferroelectrics, and Frequency Control, 2014. **61**(8): p. 1322-1328.
170. Nilsson, D., E. Janzén, and A. Kakanakova-Georgieva, *Lattice parameters of AlN bulk, homoepitaxial and heteroepitaxial material*. Journal of Physics D: Applied Physics, 2016. **49**(17): p. 175108.
171. Liu, F.S., et al., *Visible and infrared emissions from c-axis oriented AlN:Er films grown by magnetron sputtering*. Journal of Applied Physics, 2006. **99**(5): p. 053515.
172. Liu, B., et al., *Preparation and rapid thermal annealing of AlN thin films grown by molecular beam epitaxy*. Solid State Communications, 2009. **149**(17-18): p. 715-717.
173. Mao, C., et al., *Effect of Er doping on microstructure and optical properties of ZnO thin films prepared by sol-gel method*. Journal of Materials Science: Materials in Electronics, 2015. **26**(11): p. 8732-8739.
174. Lorenz, K., et al., *Influence of the Annealing Ambient on Structural and Optical Properties of Rare Earth Implanted GaN*. MRS Proceedings, 2005. **892**.
175. Lin, C.-Y. and F.-H. Lu, *Oxidation behavior of AlN films at high temperature under controlled atmosphere*. Journal of the European Ceramic Society, 2008. **28**(3): p. 691-698.
176. Slack, G.A., *Nonmetallic crystals with high thermal conductivity*. Journal of Physics and Chemistry of Solids, 1973. **34**(2): p. 321-335.
177. Rosa, J. and I. Tale, *Mechanism of thermoluminescence in AlN:O*. Czechoslovak Journal of Physics B, 1979. **29**(7): p. 810-824.
178. Berzina, B., et al., *Luminescence mechanisms of oxygen-related defects in AlN*. Radiation Effects and Defects in Solids, 2002. **157**(6-12): p. 1089-1092.
179. Yan, Q., et al., *Origins of optical absorption and emission lines in AlN*. Applied Physics Letters, 2014. **105**(11): p. 111104.
180. Sedhain, A., et al., *The origin of 2.78 eV emission and yellow coloration in bulk AlN substrates*. Applied Physics Letters, 2009. **95**(26): p. 262104.
181. Vila, M., et al., *Intense luminescence emission from rare-earth-doped MoO₃ nanoplates and lamellar crystals for optoelectronic applications*. Journal of Physics D: Applied Physics, 2014. **47**(35): p. 355105.
182. Sakaguchi, I., et al., *Effect of post-annealing on structural and optical properties, and elemental distribution in heavy Eu-implanted ZnO thin films*. Journal of the Ceramic Society of Japan, 2010. **118**(1383): p. 1087-1089.
183. Chin, W.C. and K.Y. Cheong, *Effects of post-deposition annealing temperature and ambient on RF magnetron sputtered Sm₂O₃ gate on n-type silicon substrate*. Journal of Materials Science: Materials in Electronics, 2011. **22**(12): p. 1816.
184. Rao, T.P., S.G. Raj, and M.C.S. Kumar, *Effect of Annealing Atmosphere on Structural and Optical Properties of Nd:ZnO Thin Films*. Procedia Materials Science, 2014. **6**: p. 1631-1638.
185. Zhang, Q.Y., et al., *Influence of annealing atmosphere and temperature on photoluminescence of Tb³⁺ or Eu³⁺-activated zinc silicate thin film phosphors via sol-gel method*. Chemical Physics Letters, 2002. **351**(3-4): p. 163-170.
186. Wu, L., et al., *Oxidation state and lattice expansion of CeO_{2-x} nanoparticles as a function of particle size*. Physical Review B, 2004. **69**(12): p. 125415.
187. Cheng, S., et al., *Quantification of the boron speciation in alkali borosilicate glasses by electron energy loss spectroscopy*. Scientific Reports, 2015. **5**: p. 17526.

188. Youngman, R.A. and J.H. Harris, *Luminescence Studies of Oxygen-Related Defects In Aluminum Nitride*. Journal of the American Ceramic Society, 1990. **73**(11): p. 3238-3246.
189. Jones, R. and B. Hourahine, *Theoretical Modelling of Rare Earth Dopants in GaN*, in *Rare Earth Doped III-Nitrides for Optoelectronic and Spintronic Applications*, K. O'Donnell and V. Dierolf, Editors. 2010, Springer Netherlands: Dordrecht. p. 1-24.
190. Mäki, J.M., et al., *Identification of the $V_{Al}-O_N$ defect complex in AlN single crystals*. Physical Review B, 2011. **84**(8): p. 081204.
191. Yan, Q., et al., *Origins of optical absorption and emission lines in AlN*. Applied Physics Letters, 2014. **105**(11): p. 111104.
192. Sedhain, A., et al., *Photoluminescence properties of AlN homoepilayers with different orientations*. Applied Physics Letters, 2008. **93**(4): p. 041905.
193. Berzina, B., et al., *Spectral characterization of bulk and nanostructured aluminum nitride*. Journal of Nanophotonics, 2009. **3**(1): p. 031950-031950-16.
194. Nepal, N., et al., *Photoluminescence studies of impurity transitions in AlGaIn alloys*. Applied Physics Letters, 2006. **89**(9): p. 092107.
195. Nam, K.B., et al., *Deep impurity transitions involving cation vacancies and complexes in AlGaIn alloys*. Applied Physics Letters, 2005. **86**(22): p. 222108.
196. Hoshi, T., et al., *Correlation between the violet luminescence intensity and defect density in AlN epilayers grown by ammonia-source molecular beam epitaxy*. physica status solidi (c), 2008. **5**(6): p. 2129-2132.
197. Lu, P., et al., *Different optical absorption edges in AlN bulk crystals grown in m- and c-orientations*. Applied Physics Letters, 2008. **93**(13): p. 131922.
198. Paul, A., M. Mulholland, and M.S. Zaman, *Ultraviolet absorption of cerium(III) and cerium(IV) in some simple glasses*. Journal of Materials Science, 1976. **11**(11): p. 2082-2086.
199. Herrmann, A., et al., *Spectroscopic properties of cerium-doped aluminosilicate glasses*. Optical Materials Express, 2015. **5**(4): p. 720-732.
200. Brandily-Anne, M.-L., et al., *Specific absorption spectra of cerium in multicomponent silicate glasses*. Journal of Non-Crystalline Solids, 2010. **356**(44-49): p. 2337-2343.
201. He, X., et al., *Effects of local structure of Ce^{3+} ions on luminescent properties of $Y_3Al_5O_{12}:Ce$ nanoparticles*. Scientific Reports, 2016. **6**: p. 22238.
202. Dierre, B., et al., *Blue emission of Ce^{3+} in lanthanide silicon oxynitride phosphors*. Journal of Materials Research, 2007. **22**(7): p. 1933-1941.
203. O'Donnell, K. and V. Dierolf, eds. *Rare-Earth Doped III-Nitrides for Optoelectronic and Spintronic Applications*. Vol. 124. 2010, Springer Netherlands.
204. Schweizer, S., et al., *Investigation of Oxygen-Related Luminescence Centres in AlN Ceramics*. physica status solidi (b), 2000. **219**(1): p. 171-180.
205. Landrum, G.A., et al., *Electronic Structure and Bonding in Cerium (Nitride) Compounds: Trivalent versus Tetravalent Cerium*. Chemistry – A European Journal, 1999. **5**(2): p. 515-522.
206. Giba, A.E., et al., *Strong room-temperature blue emission from rapid-thermal annealed cerium-doped aluminum (oxy)nitride thin films*. ACS Photonics, 2017.
207. Fan, X.J., et al., *Al L core edge fine structure in Al, AlN and α -Al₂O₃ : A comparison of microelectron energy loss spectra with theory*. Acta Physica Sinica (Overseas Edition), 1998. **7**(3): p. 214.
208. Ma, C., et al., *High reliable and chromaticity-tunable flip-chip w-LEDs with Ce:YAG glass-ceramics phosphor for long-lifetime automotive headlights applications*. Optical Materials, 2017. **69**(Supplement C): p. 105-114.
209. Ueda, J., et al., *Insight into the Thermal Quenching Mechanism for $Y_3Al_5O_{12}:Ce^{3+}$ through Thermoluminescence Excitation Spectroscopy*. The Journal of Physical Chemistry C, 2015. **119**(44): p. 25003-25008.
210. Ueda, J., K. Aishima, and S. Tanabe, *Temperature and compositional dependence of optical and optoelectronic properties in Ce^{3+} -doped $Y_3Sc_2Al_3-xGa_xO_{12}$ ($x=0, 1, 2, 3$)*. Optical Materials, 2013. **35**(11): p. 1952-1957.

211. Liu, X., et al., *Broadband conversion of visible light to near-infrared emission by Ce³⁺, Yb³⁺-codoped yttrium aluminum garnet*. Optics Letters, 2009. **34**(22): p. 3565-3567.
212. Dorenbos, P. and E.v.d. Kolk, *Location of lanthanide impurity levels in the III-V semiconductor GaN*. Applied Physics Letters, 2006. **89**(6): p. 061122.
213. Dorenbos, P. and E.v.d. Kolk, *Lanthanide impurity level location in GaN, AlN, and ZnO in Gallium Nitride Materials and Devices II*. 2007, SPIE Proceedings. p. 647313-1.
214. Shvaleva, M.A., et al., *Ce³⁺:YAG doped glass-ceramics for white light-emitting diode*. Optical Review, 2014. **21**(5): p. 683-686.
215. Xie, R.-J., et al., *Nitride Phosphors and Solid-State Lighting*. 2011, CRC Press
216. Haumesser, P.-H., et al., *Determination of laser parameters of ytterbium-doped oxide crystalline materials*. Journal of the Optical Society of America B, 2002. **19**(10): p. 2365-2375.
217. Ennen, H., G. Pomrenke, and A. Axmann, *Luminescence of the rare-earth ion ytterbium in InP, GaP, and GaAs*. Journal of Applied Physics, 1985. **57**(6): p. 2182-2185.
218. Ishiyama, T., et al., *4f-shell configuration of Yb in InP studied by electron spin resonance*. Journal of Applied Physics, 1997. **82**(9): p. 4457-4460.
219. Godlewski, M., et al., *Excitation and recombination processes of Yb in InP and InAsP*. Journal of Alloys and Compounds, 1995. **225**(1): p. 564-566.
220. Lozykowski, H.J., A.K. Alshawa, and I. Brown, *Kinetics and quenching mechanisms of photoluminescence in Yb-doped InP*. Journal of Applied Physics, 1994. **76**(8): p. 4836-4846.
221. Jadwisieniczak, W.M. and H.J. Lozykowski, *Optical properties of Yb ions in GaN epilayer*. Optical Materials, 2003. **23**(1-2): p. 175-181.
222. Dammak, M., et al., *Theoretical investigations of the optical spectra and EPR parameters for Yb³⁺ ions in GaN epilayer*. Journal of Alloys and Compounds, 2007. **432**(1-2): p. 18-22.
223. Weingärtner, R., et al., *Thermal activation, cathodo- and photoluminescence measurements of rare earth doped (Tm,Tb,Dy,Eu,Sm,Yb) amorphous/nanocrystalline AlN thin films prepared by reactive rf-sputtering*. Optical Materials, 2006. **28**(6): p. 790-793.
224. Giba, A.E., et al., *Strong Room Temperature Blue Emission from Rapid Thermal Annealed Cerium-Doped Aluminum (Oxy)Nitride Thin Films*. ACS Photonics, 2017. **4**(8): p. 1945-1953.
225. Sun, J., et al., *Photoluminescence and its time evolution of AlN thin films*. Physics Letters A, 2001. **280**(5-6): p. 381-385.
226. Koubaa, T., et al., *Crystal field and Zeeman parameters of substitutional Yb³⁺ ion in GaN*. Journal of Alloys and Compounds, 2010. **496**(1-2): p. 56-60.
227. Dong, J., et al., *Dependence of the Yb³⁺ emission cross section and lifetime on temperature and concentration in yttrium aluminum garnet*. Journal of the Optical Society of America B, 2003. **20**(9): p. 1975-1979.
228. Krishnaiah, K.V., et al., *Fluorescence and Spectroscopic Properties of Yb³⁺-Doped Phosphate Glasses*. Physics Procedia, 2012. **29**: p. 109-113.
229. Takaichi, K., et al., *Yb³⁺-doped Y₃Al₅O₁₂ ceramics – A new solid-state laser material*. physica status solidi (a), 2003. **200**(1): p. R5-R7.
230. Lacovara, P., et al., *Room-temperature diode-pumped Yb:YAG laser*. Optics Letters, 1991. **16**(14): p. 1089-1091.
231. Batay, L.E., et al., *Efficient tunable laser operation of diode- pumped Yb,Tm:KY(WO₄)₂ around 1.9 μm*. Applied Physics B, 2002. **75**(4): p. 457-461.
232. Balembois, F., et al., *Line competition in an intracavity diode-pumped Yb:KYW laser operating at 981nm*. Journal of the Optical Society of America B, 2011. **28**(1): p. 115-122.
233. Wang, Q., et al., *NIR Enhancement Based on Energy Transfer Process of Ce³⁺–Yb³⁺ in Inverse Opal Photonic Crystals*. Journal of the American Ceramic Society, 2016. **99**(3): p. 911-916.
234. Kumar, K.S., et al., *Enhancement of the near-infrared emission of Ce³⁺-Yb³⁺ co-doped Y₃Al₅O₁₂ phosphors by doping Bi³⁺ ions*. RSC Advances, 2017. **7**(40): p. 24674-24678.
235. Zhou, L., et al., *Spectral Properties and Energy Transfer between Ce³⁺ and Yb³⁺ in the Ca₃Sc₂Si₃O₁₂ Host: Is It an Electron Transfer Mechanism?* The Journal of Physical Chemistry A, 2016. **120**(28): p. 5539-5548.

236. Artizzu, F., et al., *Controlling Nd-to-Yb energy transfer through a molecular approach*. Journal of Materials Chemistry C, 2015. **3**(43): p. 11524-11530.
237. Thonke, K., et al., *On excitation and decay mechanisms of the Yb 3+ luminescence in InP*. Semiconductor Science and Technology, 1990. **5**(11): p. 1124.
238. Gruber, J.B., et al., *Crystal-field splitting of Pr³⁺ (4f²) energy levels in GaN*. Journal of Applied Physics, 2001. **89**(12): p. 7973-7976.
239. Gruber, J.B., et al., *Spectroscopic properties of Sm³⁺(4f⁵) in GaN*. Journal of Applied Physics, 2002. **91**(5): p. 2929-2935.
240. Gruber, J.B., et al., *Spectra and energy levels of Tm³⁺ (4f¹²) in AlN*. Physical Review B, 2004. **70**(24): p. 245108.
241. Gruber, J.B., et al., *Crystal field and Zeeman splittings for energy levels of Nd³⁺ in hexagonal AlN*. Optical Materials Express, 2012. **2**(9): p. 1176-1185.
242. Kallel, T., et al., *Optical studies and crystal field calculation of GaN nanorods doped with Yb³⁺ ions*. Journal of Alloys and Compounds, 2014. **609**: p. 284-289.
243. Lozykowski, H.J. and W.M. Jadwisieniczak, *Thermal quenching of luminescence and isovalent trap model for rare-earth-ion-doped AlN*. physica status solidi (b), 2007. **244**(6): p. 2109-2126.
244. Chen, D., et al., *Ultraviolet-blue to near-infrared downconversion of Nd³⁺-Yb³⁺ couple*. Optics Letters, 2010. **35**(2): p. 220-222.
245. Aarts, L., et al., *Downconversion for the Er³⁺, Yb³⁺ couple in KPb₂Cl₅—A low-phonon frequency host*. Journal of Luminescence, 2011. **131**(4): p. 608-613.
246. Lin, H., et al., *Down-Conversion From Blue to Near Infrared in Tm³⁺-Yb³⁺ Codoped Y₂O₃ Transparent Ceramics*. IEEE Photonics Technology Letters, 2010. **22**(12): p. 866-868.
247. Xu, Y., et al., *Efficient Near-Infrared Down-Conversion in Pr³⁺-Yb³⁺ Codoped Glasses and Glass Ceramics Containing LaF₃ Nanocrystals*. The Journal of Physical Chemistry C, 2011. **115**(26): p. 13056-13062.
248. Liu, Z., et al., *Efficient near-infrared quantum cutting in Ce³⁺-Yb³⁺ codoped glass for solar photovoltaic*. Solar Energy Materials and Solar Cells, 2014. **122**: p. 46-50.
249. Chen, D., et al., *Quantum cutting downconversion by cooperative energy transfer from Ce³⁺ to Yb³⁺ in borate glasses*. Journal of Applied Physics, 2008. **104**(11): p. 116105.
250. Ueda, J. and S. Tanabe, *Visible to near infrared conversion in Ce³⁺-Yb³⁺ Co-doped YAG ceramics*. Journal of Applied Physics, 2009. **106**(4): p. 043101.
251. Lin, H., et al., *Near infrared quantum cutting in heavy Yb doped Ce_{0.03}Yb_{3x}Y(2.97-3x)Al₅O₁₂ transparent ceramics for crystalline silicon solar cells*. Journal of Applied Physics, 2010. **107**(4): p. 043107.
252. Streck, W., P. Deren, and A. Bednarkiewicz, *Cooperative processes in KYb(WO₄)₂ crystal doped with Eu³⁺ and Tb³⁺ ions*. Journal of Luminescence, 2000. **87**: p. 999-1001.
253. Stręk, W., A. Bednarkiewicz, and P.J. Dereń, *Power dependence of luminescence of Tb³⁺-doped KYb(WO₄)₂ crystal*. Journal of Luminescence, 2001. **92**(3): p. 229-235.
254. Terra, I.A.A., et al., *Down-conversion process in Tb³⁺-Yb³⁺ co-doped Calibo glasses*. Journal of Luminescence, 2012. **132**(7): p. 1678-1682.
255. Jiang, C., Q. Zeng, and F. Gan. *Dependence of spectroscopic properties on ytterbium ion concentration in glasses*. 2000.
256. Dirk, P. and S. Philippe Frederic, *Methods for the determination of the optical constants of thin films from single transmission measurements: a critical review*. Journal of Physics D: Applied Physics, 2003. **36**(15): p. 1850.
257. Joo, H.-Y., et al., *Spectrophotometric analysis of aluminum nitride thin films*. Journal of Vacuum Science & Technology A: Vacuum, Surfaces, and Films, 1999. **17**(3): p. 862-870.
258. Fujiwara, H., *Spectroscopic Ellipsometry: Principles and Applications*, in *Spectroscopic Ellipsometry*. 2007, John Wiley & Sons, Ltd.
259. Roskovicová, I., J. Pastrňák, and R. Babušková, *The Dispersion of the Refractive Index and the Birefringence of AlN*. physica status solidi (b), 1967. **20**(1): p. K29-K32.

-
260. Dogheche, E., et al., *Growth and optical characterization of aluminum nitride thin films deposited on silicon by radio-frequency sputtering*. Applied Physics Letters, 1999. **74**(9): p. 1209-1211.
 261. Martin, R., et al., *Optical characterization of Al- and N-polar AlN waveguides for integrated optics*. Applied Physics Express, 2015. **8**(4): p. 042603.
 262. Fujii, Y., et al., *Nonlinear optical susceptibilities of AlN film*. Applied Physics Letters, 1977. **31**(12): p. 815-816.
 263. Shokhovets, S., et al., *Determination of the anisotropic dielectric function for wurtzite AlN and GaN by spectroscopic ellipsometry*. Journal of Applied Physics, 2003. **94**(1): p. 307-312.
 264. Gavrilenko, V.I. and R.Q. Wu, *Linear and nonlinear optical properties of group-III nitrides*. Physical Review B, 2000. **61**(4): p. 2632-2642.
 265. Rossbach, G., et al., *Influence of exciton-phonon coupling and strain on the anisotropic optical response of wurtzite AlN around the band edge*. Physical Review B, 2011. **83**(19): p. 195202.
 266. Feneberg, M., et al., *Anisotropic absorption and emission of bulk $\overline{100}$ AlN*. Physical Review B, 2013. **87**(23): p. 235209.
 267. Taniyasu, Y. and M. Kasu, *Surface 210 nm light emission from an AlN p–n junction light-emitting diode enhanced by A-plane growth orientation*. Applied Physics Letters, 2010. **96**(22): p. 221110.
 268. Stan, G.E., et al., *Highly textured (001) AlN nanostructured thin films synthesized by reactive magnetron sputtering for SAW and FBAR applications*. Digest Journal of Nanomaterials and Biostructures, 2010. **5**(4).
 269. Balzar, D., *X-Ray Diffraction Line Broadening: Modeling and Applications to High-T(c) Superconductors*. Journal of Research of the National Institute of Standards and Technology, 1993. **98**(3): p. 321-353.

Abstract

Rare earth-doped aluminum nitride thin films for optical applications

This project is dedicated to study the optical properties of rare earth-doped aluminum nitride thin films. In particular, to investigate the luminescence mechanisms of selected RE elements incorporated in AlN thin films. Reactive magnetron sputtering (RMS) technique is used to synthesize the undoped and doped AlN thin films. The effect of sputtering conditions on the structure and optical properties of the prepared samples are investigated. In addition, the optimum experimental conditions that will be used during this work are determined. The structure and composition analyses have been investigated by several means, such as transmission electron microscopy (TEM), Energy-dispersive X-ray spectroscopy (EDS), and Rutherford backscattering spectrometry (RBS). The optical properties of the films are characterized by UV-Visible transmission, Ellipsometry spectroscopy, and Photoluminescence spectroscopy. For undoped AlN, well crystallized AlN thin films with high degree of c-axis orientation were prepared. Controlling the preferred orientation by only tuning the $N_2\%$ in the gas phase has been achieved. It was found that, the synthesis of highly c-axis oriented crystalline AlN is favored by depositing the coatings in nitrogen-rich reactive ambiance. The results have been interpreted on the basis of an improved mobility of adatoms assisted by the bombardment of the films by fast particles. The optical constants (n , k) and bandgap of the prepared films have been modeled from spectroscopic ellipsometry measurements in transmission and reflection modes. It is found that the refractive index can be tuned with the crystal orientation while keeping constant the bandgap. Our findings suggest that, the optical properties of the AlN films can be tuned via their crystallographic orientation which, in turn, varied by the amount of nitrogen in the gas phase.

For doped AlN, crystalline Ce-doped AlN were prepared. The crystal structure of the prepared samples and the compositions have been examined by TEM, RBS, EDS and EELS analyses. It was found that, presence of oxygen in this material is essential for sensitizing the photoluminescence. Oxygen has been found playing major role not only in converting Ce ions from the optically inactive state +4 to the optically active one +3, but also led to the formation of defect complexes with Al vacancies. These defect complexes were found contributed in the excitation mechanism of Ce ions. Therefore, an optical excitation and emission mechanisms have been proposed based on the role of oxygen. Based on that, manipulation of the PL was achieved and different colors (blue, and green) were clearly observed by the naked eye. In addition, white light emission approach has been presented and strong eye observed white light was obtained. Yb-doped and (Ce, Yb) co-doped Al(O)N systems are prepared. The crystal structures and compositions of the prepared samples have been investigated. Indirect optical excitation of the NIR emission of Yb ions is achieved. The excitation mechanisms of the NIR and visible emission of single and co-doped samples are discussed. It is found that, the similarity between the PLE spectra of Ce and Yb results in the possibility of achieving energy transfer between the two ions in the co-doping system. The type of energy transfer mechanism is found consistent with the one-to-one down conversion

via charge transfer state mechanism. The PL thermal quenching has been studied by following the PL evolution with low temperatures.

Keywords: AlN thin films, rare earth doped AlN, optical properties, magnetron sputtering

Résumé

Films minces de nitrure d'aluminium dopés par des terres rares pour applications optiques

Ce projet est dédié à l'étude des propriétés optiques des couches minces de nitrure d'aluminium dopé aux terres rares. En particulier, pour étudier les mécanismes de luminescence des éléments RE sélectionnés incorporés dans des films minces AlN. La technique de pulvérisation cathodique magnétron réactif (RMS) est utilisée pour synthétiser les films minces d'AlN dopés et non dopés. L'effet des conditions de pulvérisation sur la structure et les propriétés optiques des échantillons préparés est étudié. En outre, les conditions expérimentales optimales qui seront utilisées au cours de ce travail sont déterminées. Les analyses de structure et de composition ont été étudiées par plusieurs moyens, tels que la microscopie électronique à transmission (TEM), la spectroscopie à rayons X à dispersion d'énergie (EDS) et la spectrométrie de rétrodiffusion Rutherford (RBS). Les propriétés optiques des films sont caractérisées par une transmission UV-visible, une spectroscopie d'ellipsométrie et une spectroscopie par photoluminescence.

Pour l'AlN non dopé, des films minces d'AlN bien cristallisés avec un degré élevé d'orientation de l'axe c ont été préparés. Le contrôle de l'orientation préférée en réglant seulement le pourcentage de N₂ dans la phase gazeuse a été atteint. Il a été trouvé que la synthèse d'AlN cristallin fortement orienté sur l'axe c est favorisée en déposant les revêtements dans une ambiance réactive riche en azote. Les résultats ont été interprétés sur la base d'une mobilité améliorée des adatoms assistée par le bombardement des films par des particules rapides. Les constantes optiques (n, k) et la bande interdite des films préparés ont été modélisées à partir de mesures d'ellipsométrie spectroscopique en modes transmission et réflexion. On trouve que l'indice de réfraction peut être réglé avec l'orientation cristalline tout en gardant constant le bandgap. Nos résultats suggèrent que les propriétés optiques des films AlN peuvent être ajustées par leur orientation cristallographique qui, à son tour, varie en fonction de la quantité d'azote dans la phase gazeuse.

Pour l'AlN dopé, l'AlN dopé au Ce cristallisé a été préparé. La structure cristalline des échantillons préparés et des compositions a été examinée par des analyses TEM, RBS, EDS et EELS. Il a été constaté que la présence d'oxygène dans ce matériau est essentielle pour sensibiliser la photoluminescence. On a trouvé que l'oxygène joue un rôle majeur uniquement dans la conversion des ions Ce de l'état optiquement inactif +4 à l'optiquement actif +3, mais conduit aussi à la formation de complexes défectueux avec des lacunes d'Al. Ces complexes de défauts ont été trouvés contribuer au mécanisme d'excitation des ions Ce. Par conséquent, des mécanismes d'excitation et d'émission optiques ont été proposés sur la base du rôle de

l'oxygène. Sur cette base, la manipulation du PL a été réalisée et différentes couleurs (bleu et vert) ont été clairement observées à l'œil nu. De plus, une approche d'émission de lumière blanche a été présentée et une lumière blanche fortement observée dans les yeux a été obtenue. Des systèmes Al (O) N dopés Yb et (Ce, Yb) sont préparés. Les structures cristallines et les compositions des échantillons préparés ont été étudiées. L'excitation optique indirecte de l'émission NIR des ions Yb est obtenue. Les mécanismes d'excitation du NIR et l'émission visible d'échantillons uniques et co-dopés sont discutés. On constate que la similarité entre les spectres PLE de Ce et Yb permet d'obtenir un transfert d'énergie entre les deux ions dans le système de co-dopage. Le type de mécanisme de transfert d'énergie se trouve consistance avec la conversion un-à-un bas via le mécanisme d'état de transfert de charge. La trempe thermique PL a été étudiée en suivant l'évolution du PL à basse température.

Mots-clefs : Films minces de nitrure d'aluminium, AlN dopé par une terre rare, propriétés optiques, pulvérisation cathodique

Zusammenfassung

Dieses Projekt widmet sich der Untersuchung der Lumineszenzmechanismen von Cerium-(Ce) und Ytterbium-Ionen (Yb), die in Aluminiumnitrid-Dünnschichten (AlN) einzeln und co-dotiert sind. Die reaktive Magnetronsputter-Technik (RMS) wird verwendet, um die undotierten und dotierten AlN-Dünnschichten zu synthetisieren. Die Auswirkung der Prozessbedingungen und der Konzentrationen von Ce und Yb auf die Struktur und die optischen Eigenschaften der hergestellten Proben werden untersucht. Die Struktur- und Zusammensetzungsanalysen wurden mit verschiedenen Methoden wie Transmissionselektronenmikroskopie (TEM), energiedispersive Röntgenspektroskopie (EDS) und Rutherford-Rückstreu-Spektrometrie (RBS) durchgeführt. Die optischen Eigenschaften der Filme wurden durch Spektralphotometrie, Ellipsometrie und Photolumineszenz-Spektroskopie (PL) charakterisiert. Ein vorgeschlagener Mechanismus zur Verbesserung und Löschung der PL wird diskutiert. Zusätzlich wurde ein Energieübertragungsprozess zwischen Ce- und Yb-Ionen erreicht. Basierend auf dem vorgeschlagenen Mechanismus konnten wir die Emission dieses Materials manipulieren, um blaue, grüne und weiße Farben zu erhalten. Unser Befund kann als Richtlinie zum besseren Verständnis des optischen Verhaltens von Seltenerdionen in AlN verwendet werden.